U.PORTO
FEUP FACULDADE DE ENGENHARIA
UNIVERSIDADE DO PORTO

Nanostructured Architectures Based on Metal Oxides with Direct Wide Band-gap for the Engineering of Photocatalytic Reactions

Thesis submitted in partial fulfillment of the requirements for the degree of Doctor of Philosophy in Chemical and Biological Engineering, at the Faculty of Engineering, University of Porto

Maria José Fernandes Sampaio

LABORATÓRIO ASSOCIADO
LSRE LABORATORY OF SEPARATION AND REACTION ENGINEERING
Laboratório Associado de Materiais icm

Supervisors:
Professor Doctor Joaquim Luís Bernardes Martins de Faria
Doctor Cláudia Sofia Castro Gomes da Silva
Doctor Adrián Manuel Tavares da Silva

Aos meus pais, Manuel e Deolinda
Ao meu Helder e ao meu pequeno Tomás

Abstract

Heterogeneous photocatalysis is an active area of research regarding the oxidation and mineralization of a wide range of organic pollutants present in waste waters. The illumination of a semiconductor (normally TiO_2 or ZnO) with radiation of energy equal or greater than its band gap generates electron-hole pairs (e^-/h^+), which diffuse to the surface and react with adsorbed species promoting the degradation of the organic contaminants.

The undesirable recombination of the e^-/h^+ pairs, the problems arising from the use of the photocatalysts as suspensions, and the need of an artificial irradiation source, are some of the limitations in photocatalytic processes. To overcome these issues, the present research work was focused on the development of materials with superior photocatalytic performance. This was achieved by increasing their absorption in the visible range, the use of glass supports for immobilization of the photocatalyst and the utilization of irradiation sources to simulate solar ligth.

In the first part of this work, glass raschig rings were coated with different types of TiO_2, namely Aeroxide® P25 (EP), anatase TiO_2 from Sigma–Aldrich (SA), and TiO_2 obtained from a sol–gel procedure (SG). The efficiency of the coating was evaluated on phenol degradation, in a recirculation reactor system, operating under simulated solar light irradiation.

Regardless the material tested, phenol degradation gradually increases with the number of TiO_2 layer coatings. SA-coated glass rings showed the highest efficiency for phenol degradation, but do lose activity when reused due to particle disaggregation from the support. Rings coated with EP were the most stable over 3 cycles. Their efficiency was evaluated by comparing the apparent first order reaction rate (*r*) as a function of several operating conditions. The reaction conversion was mainly influenced by the initial phenol concentration, the number of TiO_2-coated rings, the irradiation intensity and the hydrogen peroxide concentration. Also is minimally affected by the solution's flowrate. A kinetic model was developed for the determination of *r* as a function of the operating parameters.

The EP-coated rings were used for the treatment of a synthetic effluent consisting of a solution with a mixture of seven phenolic derivatives: protocatechuic acid, 4-hydroxybenzoic acid, 4-methoxyphenol, 4-hydroxyphenethyl alcohol, benzoic acid, gallic acid and phenol. A relationship between the extent of photocatalytic degradation and the activating/deactivating nature of the aromatic ring substituents was proposed.

In order to increase the TiO_2 photo-efficiency, hydration–dehydration (HD) and sol-gel (SG) methods were used to prepare TiO_2/multiwalled carbon nanotube (TiO_2/CNT) composites with different carbon contents using functionalized (CNT_f) and pristine carbon nanotubes (CNT). The TiO_2 based materials were immobilized on glass slides by using the doctor blade technique. The photocatalytic activity of the films was tested in the degradation of methylene blue by near-UV to visible irradiation. Depending on the nature of TiO_2, the composites containing different amounts of CNT evidenced distinct spectroscopic, morphological and textural properties. In addition, it was shown that the introduction of oxygen surface groups in CNT is crucial to prepare TiO_2/CNT composites with high photoactivity, promoting the dispersion of TiO_2 particles and inducing the CNT action as a photosensitizer.

The composites prepared by sol-gel and using CNT_f were tested in the photocatalytic degradation of 4 *para*-substituted phenols: 4-aminophenol, 4-methoxyphenol, 4-chlorophenol and 4-nitrophenol. A relationship between the Hammett constant of each *para*-substituted phenol compound and its degradability by photocatalysis was obtained. A beneficial effect of the introduction of CNT in the matrix of TiO_2 was mainly observed for the degradation of 4-aminophenol and 4-methoxiphenol.

Becase of the beneficial effect of the introduction of CNT into the TiO_2 matrix, composites using graphene oxide (GO) and nanodiamonds (ND) as carbon phase were also synthetized and tested in the degradation of a cyanobacterial toxin, microcystin-LA (MC-LA), under both visible and simulated solar light irradiation. It was noticed that the photocatalytic efficiency is different depending on the carbon phase, following the order: GO-TiO_2-4 > ND-TiO_2-15 > CNT-TiO_2-4. The high photocatalytic activity of GO-TiO_2-4 was attributed to the optimal assembly and interfacial coupling between the TiO_2 nanoparticles and the GO sheets that can effectively inhibit e^-/h^+ recombination. Reaction intermediates of MC-LA photocatalytic degradation using GO-TiO_2-4 composite were also identified by mass spectrometry LC/Q-TOF and LC/MS/MS, most of them resulting from the attack of hydroxyl radicals to the MC-LA molecule.

The effect of the introduction of carbon materials, namely nanotubes (CNT), nanofibers(CNF), nanodiamonds (ND), fullerene (C_{60}) and graphene (FLG) on ZnO synthesized by chemical vapor deposition (CVD) was evaluated. The photocatalytic efficiency of the carbon/ZnO composites was tested in phenol degradation under simulated solar light irradiation. In general, the carbon materials enhance the efficiency

of ZnO, and the composite containing nitrogen-doped carbon nanotubes (N-CNT/ZnO) showed the highest photocatalytic activity. Photoluminescence analysis confirms the presence of efficient electron transfer between the carbon phase and the ZnO. Both ZnO and N-CNT/ZnO show high stability after reuses.

A beneficial effect on photocatalytic activity was observed when noble metal (Au and Ag) nanoparticles were deposited on different ZnO materials. The best activity for phenol oxidation was obtained with the Au-loaded on ZnO samples produced by CVD (Au/ZnO-cvd), and by thermal decomposition of zinc acetate (Au/ZnO-t). The efficiency of the ZnO materials was influenced by the gold nanoparticle dimensions and by the irradiation wavelength used. In case of the Ag/ZnO materials the efficiency was related to the ZnO type and Ag load. The best activity was obtained with ZnO prepared by thermal decomposition of zinc acetate with 0.25 *at%* Ag (0.25%Ag/ZnO-t). Selective trapping of photogenerated holes and radicals by specific scavengers show that holes are crucial, but free radicals do also participate on the phenol photodegradation pathway.

Finally, the ZnO-t and 0.25%Ag/ZnO-t materials were tested in a mixture containing phenolic compounds (4-methoxyphenol, 4-chorophenol, phenol, and resorcinol), using a batch and recirculation reaction systems with the catalyst in powder form and immobilized on glass raschig rings, respectively. Faster conversion was obtained when Ag particles were present in the photocatalyst.

Resumo

A fotocatálise heterogénea é uma área de investigação muito ativa no que respeita à conversão e mineralização de uma grande variedade de poluentes orgânicos presentes em águas residuais. O processo baseia-se na formação de pares eletrão-buraco (e^-/h^+), quando materiais semicondutores derivados de óxidos metálicos (como TiO_2 e ZnO) são ativados com radiação de energia igual ou superior à sua energia de hiato. Esses pares e^-/h^+ difundem para a superficie do sólido onde reagem com as espécies adsorvidas promovendo a degradação dos contaminantes orgânicos presentes no meio.

A recombinação indesejável dos pares e^-/h^+ gerados, a difícil recuperação do catalisador no final da reação e necessidade de fontes de irradiação artificiais, respresentam algumas das desvantagens do processo. Com vista a superar essas limitações este trabalho de investigação concentrou-se no desenvolvimento de fotocatalizadores altamente activos. A estratégia usada consistiu em aumentar a sua absorção na zona do visível, imobilizar os catalisadores em superficies, e utilizar fontes de irradiação capazes de simular a luz solar.

O trabalho iniciou-se com a utlização de diferentes tipos de TiO_2 nomeadamente de origem comercial como o Aeroxide® P25 (EP) e o TiO_2 anatase (SA), além de um TiO_2 preparado pelo método sol-gel (SG). Estes materiais foram imobilizados em anéis de vidro (anéis Raschig) e testados na degradação do fenol. Utilizou-se um sistema reacional em regime de recirculação, com luz solar simulada.

Os resultados mostraram que a degradação do fenol aumenta com o número de camadas de TiO_2 depositadas sobre os anéis de vidro. Os filmes preparados com SA revelaram-se mais eficientes na degradação do fenol, tendo-se observado contudo que após reutilização a respetiva atividade fotocatalítica é reduzida devido à desagregação das partículas de TiO_2 dos anéis de vidro. Se considerar-mos um conjunto de 3 reutilizações, os filmes EP são os que revelam maior estabilidade.

Tendo em conta estes resultados, mediu-se o efeito de várias condições operacionais na velocidade de reação (*r*) assumindo uma cinética de primeira ordem. Verificou-se que *r* é influenciada pela variação na concentração inicial de fenol, pela intensidade de radiação, pelo número de anéis com TiO_2 imobilizado, pela presença de peróxido de hidrogénio, e é pouco afectada pelo caudal utilizado. Foi também desenvolvido um modelo cinético com o objetivo de determinar uma equação empírica de *r* em função dos vários parâmetros operacionais.

Os filmes EP foram aplicados no tratamento de uma mistura sintética contendo 7 compostos fenólicos (ácido 3,4-diidroxibenzóico, 4-metoxifenol, álcool 4-hidroxifenetílico, ácido benzóico, ácido gálico e fenol). Foi proposta uma relação entre a degradação dos compostos e a natureza dos grupos substituintes (ativantes/desativantes) do anel aromático dos poluentes orgânicos.

Com vista a aumentar a fotoeficiência dos materiais à base de TiO_2, sintetizaram-se compósitos fotocatalisadores (TiO_2/nanotubos de carbono de parede múltipla) pelos métodos de hidratação-dehidratação e sol-gel (SG), utilizando nanotubos de carbono funcionalizados (CNT_f) e não funcionalizados (CNT).

Os diferentes compósitos foram imobilizados em lamelas de vidro e a respetiva atividade fotocatalítica foi testada na degradação do azul de metileno sob irradiação no UV-visível. Distintas propriedades espectroscópicas, morfológicas e texturais foram registadas dependendo da natureza do TiO_2, e da quantidade de CNT presente nos compósitos. Adicionalmente foi demostrado que a presença de grupos oxigenados na superfície dos CNT era essencial para obter compósitos com elevada fotoatividade. Estes grupos promovem a dispersão das partículas de TiO_2 e induzem a actuação dos CNT como fotossensibilizadores.

O TiO_2 e o compósito SG/CNT_f-20 preparados pelo método SG, foram então testados na degradação de 4 compostos fenólicos *para*-substituídos: 4-aminofenol, 4-metoxifenol, 4-clorofenol e 4-nitrofenol. Foi encontrada uma relação entre as constantes de Hammett de cada composto e a sua degradabilidade, verificando-se em particular, que a degradação dos compostos 4-aminofenol e 4-metoxifenol é afetada beneficamente pela presença de CNT nos compósitos.

A eficiência promovida pela presença dos CNT no TiO_2 conduziu ao desenvolvimento de compósitos utilizando outros materiais de carbono, tais como: óxido de grafeno (GO) e nanodiamantes (ND). Estes compósitos foram testados na degradação da cianotoxina microcistina-LA (MC-LA) sob luz solar simulada e visível. Os resultados obtidos mostraram que a atividade fotocatalítica dos compósitos é dependente da natureza da fase de carbono, seguindo a ordem: GO-TiO_2-4 > ND-TiO_2-15 > CNT-TiO_2- 4. A elevada atividade do compósito GO-TiO_2-4 foi atribuída à ótima organização e acoplamento interfacial entre as nanopartículas de TiO_2 e as folhas de grafeno, inibindo deste modo a recombinação e^-/h^+. Os intermediários resultantes da degradação fotocatalítica da MC-LA utilizando o compósito GO-TiO_2-4 foram identificados por espectroscopia de massa LC/Q-TOF e LC/MS/MS. Na

generalidade os intermediários identificados resultam do ataque de radicais hidroxilo à molécula MC-LA.

Numa fase posterior foram preparados compósitos contendo ZnO sintetizado por deposição química em fase de vapor (CVD) e materiais de carbono: nanotubos (CNT), nanofibras (CNF), nanodiamantes (ND), fulereno (C_{60}) e grafeno (FLG). A eficiência fotocatalítica dos compósitos carbono/ZnO foi testada na degradação do fenol sob luz solar simulada. Globalmente, a presença de materiais de carbono aumentou a atividade do fotocatalisador. O compósito contendo nanotubos de carbono dopados com nitrogénio (N-CNT/ZnO) apresentou a maior eficiência fotocatalítica. Análises de fotoluminescência confirmaram a eficiente capacidade de transferência de eletrões entre a fase de carbono e o ZnO. Tanto o ZnO como o compósito N-CNT/ZnO mostraram elevada estabilidade após 4 utilizações.

Ao depositar metais nobres (ouro e prata) sobre o ZnO com diferentes morfologias observou-se uma melhoria na atividade fotocatalítica. Entre os materiais testados, o ZnO sintetizado por CVD (Au/ZnO-cvd) e o ZnO preparado por decomposição térmica do acetato de zinco (Au/ZnO-t) apresentaram maior atividade na oxidação fotocatalítica do fenol. Verificou-se que a eficiência dos catalisadores é influenciada pela dimensão das partículas de ouro assim como pela fonte de irradiação utilizada.

Relativamente aos materiais dopados com prata (Ag/ZnO) a maior eficiência resulta do tipo de ZnO utilizado e essencialente da quantidade de Ag presente nos materiais. Dos Ag/ZnO testados o ZnO sintetizado por deposição térmica do acetato de zinco e com 0.25 *at*% de Ag (0.25%Ag/ZnO) apresentou melhor eficiência fotocatalítica. A utilização de reagentes capturadores de buracos (h^+) e radicais ($HO^\bullet$) fotogerados revelou que ambos participam na reação, no entanto os buracos assumem o papel crucial na fotodegradação do fenol.

Por fim, os materiais ZnO-t e 0.25%Ag/ZnO-t foram testados numa mistura contendo 4 compostos fenólicos (4-metoxifenol, 4-clorofenol, fenol and resorcinol). As reações fotocatalíticas foram realizadas em dois sistemas de reação, um a actuar em regime descontínuo e outro em recirculação. Os materiais foram testados em suspensão e imobilizados em anéis de vidro com 3 camadas de catalisador. Os resultados mostraram uma maior eficiência quando nanopartículas de Ag foram depositadas no ZnO-t.

Résumé

La photocatalyse hétérogène est une discipline à part entière, très active dans le domaine de la conversion et de la minéralisation d'une grande variété de polluants organiques, présents dans les eaux usées. Le processus est basé sur la formation de paire électron-trou (e^-/h^+), quand des photocatalyseurs (matériaux semi-conducteurs) dérivés d'oxydes métalliques (comme le TiO_2 et ZnO) sont activés par une radiation d'énergie égale ou supérieure à leurs énergies de gap. Ces paires e^-/h^+ se diffusent jusqu'à la superficie du semi-conducteur et réagissent avec des substances adsorbées, permettant la dégradation des molécules organiques polluantes.

Les désavantages de ce processus sont la recombinaison non désiré des paires e^-/h^+ formées, la difficile récupération du semi-conducteur à la fin de la réaction et la nécessité de sources de radiation artificielle. Dans le but de répondre à ces limitations, ce travail d'investigation s'est focalisé sur le développement de photocatalyseurs hautement efficients. La stratégie visait á augmenter l'absorption dans la zone du visible, á immobiliser les catalyseurs en superficie et á utiliser des sources de radiation capables de simuler la lumière du soleil.

Au début, différents types de TiO_2 ont été utilisés, notamment l'Aeroxide® P25 (EP) et un TiO_2 anatase (SA), tous deux d'origine commercial, et un TiO_2 préparé par procédé sol-gel (SG). Ces matériaux ont été immobilisés sur anneaux de verre (anneaux de Raschig), puis testé pour la dégradation du phénol, à l'aide d'un système réactionnel de recirculation, sous lumière solaire simulée.

Les résultats ont montré que la dégradation du phénol augmente au fur et à mesure du nombre de couches de TiO_2 déposées sur les anneaux. Les films préparé avec SA se montrèrent plus efficients pour la dégradation du phénol; cependant, après réutilisation, l'activité photocatalytique est diminuée due à la désagrégation des particules de TiO_2 de la surface des anneaux de verre. Considérant une série de 3 réutilisations, les films EP montrèrent une meilleure stabilité.

Tenant compte de ces résultats, l'effet de plusieurs variables influençant la vitesse de la réaction (*r*) a été mesurée, supposant une cinétique de premier ordre. Il a été vérifié que *r* est influencée par la variation de la concentration initial de phénol, par l'intensité de la radiation, par le nombre d'anneaux avec du TiO_2 immobilisé, par la présence de peroxyde d'hydrogène; par contre, *r* est peu affectée par le débit utilisé. Un modèle cinétique a été développé, dans le but de déterminer une équation empirique de *r* en fonction des différents paramètres opérationnels.

Les films EP ont été appliqués pour le traitement d'une mixture synthétique de 7 composés phénoliques (acide 3,4-dihydrobenzoïque, 4-methoxyphénol, alcool 4-hydroxiphénétilique, acide benzoïque, acide gallique et phénol). Une relation entre la dégradation des composés et la nature des groupes substituants de l'anneau aromatique des polluants organiques a été proposée.

Dans le but d'augmenter l'efficience photocatalytique des matériaux à base de TiO_2, des photocatalyseurs TiO_2 composite ont été synthétisés (TiO_2/nanotubes de carbone multi-parois), via la méthode d'hydratation/déshydratation et sol-gel (SG), en utilisant des nanotubes de carbone fonctionnalisés (CNT_f) et non-fonctionnalisés (CNT).

Les différents composites ont étés fixés sur lamelle de verre et leur activité photocatalytique a été testé pour la dégradation du bleu de méthylène, sous irradiation UV-visible. Les différentes propriétés spectroscopiques, morphologiques et de textures ont été identifiées, par rapport à la nature du TiO_2 et de la quantité de CNT présente dans les composites. L'importance de la présence de groupes oxygénés à la superficie des CNT a aussi été démontrée, pour obtenir des composites à activité élevée. Ces groupes permettent la dispersion des particules de TiO_2 et induisent l'activation des CNT comme agents de photosensibilisations.

Le TiO_2 et le composite SG/CNT_f-20 ont été testés dans la dégradation de quatre composés phénoliques *para* substitués: 4-aminophénol, 4-metoxiphénol, 4-chlorophénol et 4-nitrophénol. Une corrélation entre les constantes de Hammett de chaque composé et leur dégradabilité a été trouvée. Une interaction positive entre la dégradation des composés 4-aminophénol et 4-metoxiphénol et la présence de CNT avec les composites a aussi été constatée.

L'efficience résultant de la présence des CNT avec les composites de TiO_2 a conduit au développement de composites avec d'autres matériaux de carbone, notamment, l'oxyde de graphène (GO) et des nanodiamants (ND). Ces composites ont été testés dans la dégradation de la cyanotoxine microcystine-LA (MC-LA), sous lumière solaire simulée.

Les résultats ont montré que l'activité photocatalytique des composites est dépendante de la nature de la phase de carbone, suivant cet ordre: GO-TiO_2-4 > ND-TiO_2-15 > CNT-TiO_2-4. La haute activité du composite GO-TiO_2 a été attribuée à l'organisation optimale des couches interfaciales entre les nanoparticules de TiO_2 et les feuilles de graphène, inhibant ainsi la recombinaison e^-/h^+. Les produits intermédiaires résultants de la dégradation photocatalytique de la MC-LA par

le composite GO-TiO_2-4 ont été identifiés par spectroscopie de masse LC/Q-TOF et LC/MS/MS. Globalement, les intermédiaires identifiés résultent de l'attaque des radicaux hydroxyles sur la molécule de MC-LA.

Ultérieurement, des composites à base d'oxyde de zinc (ZnO), synthétisé par déposition chimique en phase de vapeur (CVD), et des matériaux de carbone ont été préparés: nanotubes (CNT), nanofibres (CNF), nanodiamants (ND), fullerène (C_{60}) et graphène (FLG). L'efficacité photocatalytique des composites de carbone/ZnO a été testé dans la dégradation du phénol sous lumière solaire simulée. Globalement, la présence des matériaux de carbone a augmenté l'activité du photocatalyseur.

Les composites avec des nanotubes de carbone dopés avec du nitrogène (N-CNT/ZnO) ont présenté la meilleure efficience photocatalytique. L'analyse par photoluminescence a confirmé une grande capacité de transfert des électrons entre la phase de carbone et le ZnO. Autant le ZnO comme le composite N-CNT/ZnO ont montré une haute stabilité, même après quatre utilisations.

La déposition de matériaux nobles (or ou argent) sur du ZnO de différente morphologie a révélé une meilleure activité photocatalytique. De tous les matériaux testés, le ZnO synthétisé par CVD (Au/ZnO-CVD) et le ZnO préparé par déposition thermique de l'acétate de zinc (Au/ZnO-t) ont présenté une plus grande activité d'oxydation photocatalytique du phénol. Il a été vérifié que l'efficience des catalyseurs est influencée par la dimension des particules d'or, ainsi que par la source de radiation utilisée.

Par rapport aux matériaux dopés à l'argent (Ag/ZnO), la plus grande efficience résulte du type de ZnO utilisé et, essentiellement, de la quantité d'argent présente dans les matériaux. Des Ag/ZnO testés, le ZnO, synthétisé par déposition thermique d'acétate de zinc avec 0.25% d'Ag (0.25%Ag/ZnO), a présenté la meilleure efficience photocatalytique. L'utilisation d'additif sacrificiel pour les trous positifs (h^+) ou les radicaux ($HO^\bullet$) photogérés a montré que tous deux sont actifs dans la photodégradation du phénol, tout particulièrement les trous positifs.

Pour terminer, les matériaux ZnO-t et 0.25%Ag/ZnO-t ont été testés dans une mixture contenant 4 composés phénoliques (4-méthoxyphénol, 4-chlorophénol, phénol et résorcinol). Les réactions photocatalytiques ont été réalisées dans deux systèmes de réaction: l'un dans un régime discontinu et l'autre en recirculation. Les matériaux ont été testés en suspension et fixés sur anneaux de verre, avec trois couches de catalyseur. Les résultats montrèrent une meilleure efficacité, tout particulièrement dans le cas de nanoparticules d'Ag déposées sur ZnO-t.

Agradecimentos

Desejo expressar os meus sinceros agradecimentos, em primeiro lugar, ao meu orientador Professor Doutor Joaquim Faria e aos meus coorientadores, Doutor Adrián Silva e Doutora Cláudia Silva, pelo acompanhamento incondicional durante este trabalho, pela disponibilidade e dedicação demonstrada ao longo destes 4 anos. Agradeço-lhes as correções, sugestões e críticas que me enriqueceram tanto a nível científico como pessoal. Acima de tudo, agradeço-lhes a amizade e a confiança em mim depositada.

Ao Laboratório Associado LSRE-LCM, em especial ao Diretor do LCM, Professor Doutor José Luís Figueiredo, por disponibilizar os recursos técnicos para a realização deste trabalho.

Aos Professores Doutores José Órfão e Fernando Pereira pelo apoio na interpretação de técnicas de caracterização de materiais.

Sem citar nomes, quero agradecer a todos os meus colegas de laboratório, que demostraram sempre vontade em ajudar e amizade durante estes anos.

Ao Doutor Carlos Sá, diretor do CEMUP, e ao Doutor Pedro Tavares (UTAD), por disponibilizar as instalações para a caraterização de materiais.

Ao Doutor Dionysios Dionysiou, Professor na Universidade de Cincinnati (EUA) e, igualmente, ao Professor Doutor Philippe Serp da Universidade de Toulouse (França), pela oportunidade de integrar nos seus respetivos grupos de trabalho, durante três meses. Esses dois estágios proporcionaram-me um contato multicultural, que me permitiu crescer quer científica, quer pessoalmente.

Agradeço à Fundação para a Ciência e Tecnologia (FCT) pelo financiamento da bolsa de doutoramento com referência SFRH/BD/79878/2011.

Aos meus amigos, em especial ao Nuno e à Cláudia, agradeço a sua amizade e os conselhos dados durante este percurso.

Por fim, quero agradecer aos meus pais e irmãos, aos meus sogros e aos meus dois amores, Helder e Tomás, pelo amor e pela infinita paciência.

Mais uma vez, a todos, os meus sinceros agradecimentos.

List of contents

Part II – Chapter 2

Part II – Chapter 3

Part II – Chapter 4

List of figures

Part I – Chapter 1

Part II – Chapter 2

Part II – Chapter 3

Part II – Chapter 4

Part III – Chapter 5

Part III – Chapter 6

Part IV – Chapter 7

List of tables

List of schemes

List of abbreviations

AAS	Atomic absorption spectrometry
Ads	Adsorbed
AFM	Atomic force microscopy
AK-CNT	Carbon nanotubes from Arkema
AOPs	Advanced oxidation processes
AP	4-aminophenol
ATR	Attenuated total reflectance
BA	Benzoic acid
BJH	Barrett-Joyner-Halenda pore size distribution
BQ	Benzoquinone
C	Concentration
C_0	Initial concentration
C_{60}	Fullerene
CB	Conduction band
CNF	Carbon nanofibers
CNT	Carbon nanotubes
CNT_f	Functionalized carbon nanotubes
CP	4-chlorophenol
CT	Catechol
C_t	Concentration at time t
CVD	Chemical vapor deposition
CWAO	Catalytic wet air oxidation
CWPO	Catalytic wet peroxide oxidation
DHBA	Protocatechuic acid
DRIFT	Diffuse reflectance infrared Fourier transform
DRUV-Vis	Diffuse reflectance ultraviolet - visible
e^-_{CB}	Conduction band electron
e^- / h^+	Electron-hole pairs

E_g	Bandgap energy
EP	Aeroxide® titanium dioxide from Evonik
eV	Electron-Volt
FLG	Few layer graphene
GA	Gallic acid
GO	Graphene oxide
h^+_{VB}	Valence band hole
HABs	Harmful algal blooms
HBA	4-hydroxybenzoic acid
HD	Hydration-dehydration method or titanium dioxide prepared by hydration-dehydration method
HME	4-Methoxyphenol
HO^-	Hydroxide ion
$HO^\bullet$	Hydroxyl radical
HOMO	Highest occupied molecular orbital
$HOO^\bullet$	Hydroperoxide radical
HPA	4-hydroxyphenethyl alcohol
HPLC	High performance liquid chromatography
HQ	Hydroquinone
HR-TEM	High resolution transmission electron microscopy
ICP-OES	Inductively Coupled Plasma Optical Emission Spectroscopy
I	Light intensity
K	Kelvin [T]
k_{app}	Apparent first order kinetic constant
K_i	Langmuir–Hinshelwood reaction intermediates adsorption constant
k_{LH}	Langmuir–Hinshelwood reaction rate constant
K_{LH}	Langmuir–Hinshelwood adsorption constant
λ	Wavelength
L	Layer

LED	Light emitting diode
LC/MS/MS	Liquid chromatography coupled to mass spectrometry
LPD	Liquid phase deposition
LUMO	Lowest unoccupied molecular orbital
MB	Methylene blue
MB_{deg}	Methylene blue degradation
MC-LA	Microcystin-LA
MP	4-methoxyphenol
m/z	mass-to-charge ratio
N	Number of glass raschig rings
N-CNT	Nitrogen-doped carbon nanotubes
NC-CNT	Carbon nanotubes from Nanocyl
ND	Nanodiamond
NHE	Normal hydrogen electrode
NP	4-nitrophenol
$^1O_2$	Singlet oxygen
$O_2^{\bullet-}$	Superoxide anion radical
ºC	Degree Celsius
OS	Organic species
P25	Aeroxide® titanium dioxide from Evonik (the same as EP)
PH	Phenol
PL	Photoluminescence
PYG-CNT	Pyrograph III carbon nanotubes
Q	Flow rate
r	First order reaction rate
r_b	Reaction rate for batch system
RC	Resorcinol
r_{calc}	Calculated reaction rate
r_{exp}	Experimental reaction rate

R	Synergy factor
r_r	Reaction rate for recirculation system
R_t	Retention time
SA	Titanium dioxide from Sigma-Aldrich
S_{BET}	Brunauer–Emmett–Teller specific surface area
SC	Semiconductor
SEM	Scanning electron microscopy
SG	Sol-gel method or titanium dioxide prepared by sol-gel method
T	Temperature
t	Time
t_b	Reaction time in the batch system
TEM	Transmission electron microscopy
TG	Thermogravimetry
TPD	Temperature programmed desorption
TPh	Total phenolic content
TPR	Temperature programmed reduction
t_r	Reaction time in the recirculation system
UV	Ultraviolet
VB	Valence band
Vis	Visible
VOC	Volatile organic compound
V_P	Total volume of pores
V_R	Volume inside of the reactor
V_T	Total volume
WPO	Wet peroxide oxidation
WAO	Wet air oxidation
X	Conversion [%]
XPS	X-ray photoelectron spectroscopy
XRD	X-ray diffraction crystallography

Y	Carbon nanotubes mass fraction
y_{TiO2}	Mass fraction of TiO_2
[Int.]	Concentration of intermediate products
[PhOH]	Phenol concentration
$[PhOH]_0$	Phenol concentration for time = 0

Part I

Chapter 1

General Introduction

This chapter provides the research background, which emphasizes the water quality issues. It begins with a general overview of water pollution sources and a brief description of effective processes capable to remove persistent contaminants in water. This is followed by the introduction of heterogeneous photocatalysis as a promising process for water remediation.

The main semiconductors used in photocatalytic reactions and methods to improve their photoactivity under solar light and ultimately visible light irradiation are discussed. Additionally, the identification of operating parameters which may influence the photocatalytic reactions is presented.

The aim and the scope of research are included at the end of this chapter.

1.1. Introduction

Water is one of the most essentials natural resources in the world for both human life and environment, thus the protection of water resources is a key environmental issue of the XXI century. Over the last decades natural variations in freshwaters related to the rapid growth of population, the intensification of agricultural and industrial activities affected the values of global water resources and water quality. The agricultural sector is the biggest user of freshwater (Figure 1.1). According to estimates for the year 2025, agriculture is expected to increase its water requirements by 1.3 times, industry 1.5 and the domestic consumption by 1.8 times [1, 2]. The environmental problems associated with the effluents resulting from these activities provide the driving force for sustained fundamental and applied research in water remediation. Besides all that, there is a special concern for global water scarcity that affects more than 40 % of the world population, mostly concentrated in underdeveloped countries of Africa, Asia and Latin America. More than 25 % suffers from health and hygienic problems related to lack of access to improved water supplies and sanitation [1, 2].

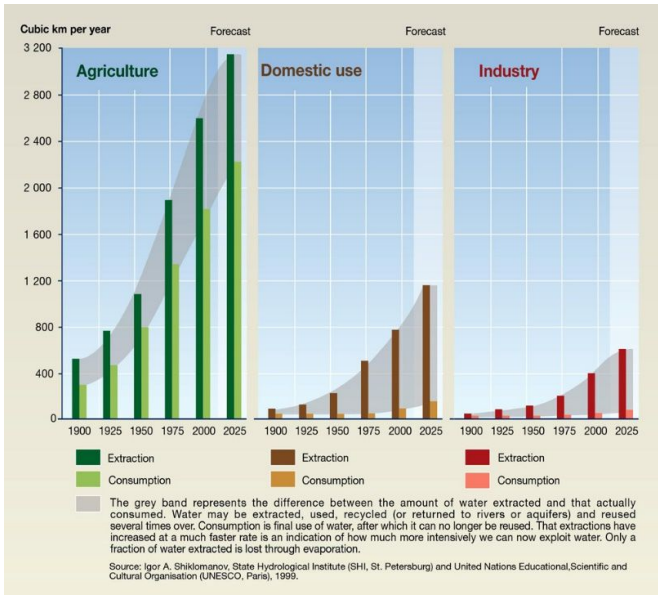

Figure 1.1 – Estimative of water extraction and consumption in different fields (Copyright© 2008, United Nations Environment Programme UNEP [1])

Some of the substances found in freshwater and wastewaters are suspected of interfering with the endocrine system leading to cancer, behavior alteration, and disruption of the reproductive system [3-5]. These pollutants of emerging concern

include compounds resulting from agricultural and industrial activity, domestic use and hospital effluents (*e.g.*, pesticides, pharmaceuticals and personal care products, steroid hormones, medical drugs and others). Some of the compounds are considered emerging pollutants due to the lack of regulations and their pesistence in the environment causing negative effects for both human and ecosystem [6-8]. Recently a directive (Directive 2013/39/EU [9]) was launched for hazardous priority substances. The main concern of this directive is the overall reduction of human exposure to chemical pollutants and the simultaneous minimization of human impact in biodiversity and sensitive eco-systems.

The wide range and complexity of water contaminants derived from the global development are rendering the conventional physicochemical and biological treatment processes of water and wastewater rather ineffective. Therefore, the implementation of adapted technologies to eliminate specific pollutants from waste waters and water sources is required.

1.2. Advanced Oxidation Process (AOPs)

AOPs have been considered highly competitive for treating water and wastewater (*i.e.*, removal of organic and inorganic pollutants, and pathogens), in particular organic pollutants that are not treatable by conventional techniques, due to the high chemical stability and low biodegradability of the pollutants [10-13]. Many different chemicals are discharged into the aquatic environment, where some of them are not only toxic but also non-biodegradable either partly or barely. The need to restore water for reutilization makes wastewater treatment essential to achieve a desired degree of quality.

AOPs feature the capability of using unselectivity and high reactivity of hydroxyl radicals ($HO^{\bullet}$) to drive oxidation processes [14]. Generaly the reactions between $HO^{\bullet}$ and the organic species are extremely fast and often controlled by difusion control, which are suitable for achieving the complete elimination and full mineralization of various contaminants present in water [6, 13, 15, 16]. The routes that influence the generation of these radicals include the presence of ultraviolet (UV) radiation, hydrogen peroxide (H_2O_2), oxygen (O_2) and ozone (O_3).

The possibilities offered by AOPs can be exploited by an integrated approach with a pre or post biological treatment for the oxidative degradation of toxic or refractory species [17]. For wastewater treatment, the main AOPs include: photolysis (UV and/or visible light), heterogeneous photocatalysis (semiconductor + UV and/or visible light),

Fenton processes (*e.g.*, Fenton's reagent, $H_2O_2 + Fe^{2+}$; Fenton-like, $H_2O_2 + Fe^{3+}$; and photo-Fenton, $H_2O_2 + Fe^{2+}$ + UV and/or visible light), wet peroxide oxidation (WPO) and catalytic wet peroxide oxidation (CWPO), wet air oxidation (WAO) and catalytic wet air oxidation (CWAO), and ozonation. However, some of the above mentioned processes promote a partial oxidation of the pollutants requiring the combination with other AOPs to achieve complete mineralization of the pollutants [18].

Among the aforementioned techniques, heterogeneous photocatalysis has a wide application in the mineralization of organic compounds to H_2O and CO_2 [19, 20]. Within the major advantages of this technology is the possibility of using solar energy, which is an inexhaustible source of energy.

1.3. Heterogeneous photocatalysis

Heterogeneous photocatalysis has been widely studied as an effective technology for water and wastewater treatment [21, 22]. Semiconductors can act as sensitizers for light-induced redox processes due to their electronic structure. By hitting a semiconductor (SC) surface with electromagnetic radiation of energy ($h\nu$) greater or equal to the bandgap energy (E_g), the electrons are excited from the valence band (VB, HOMO) to the conduction band (CB, LUMO) creating an electronic vacancy at the valence edge, generating electron-hole (e^-/h^+) pairs (Figure 1.2). As a result of light irradiation, the semiconductor particle can behave either as an electron acceptor or donor for organic molecules in contact with its surface.

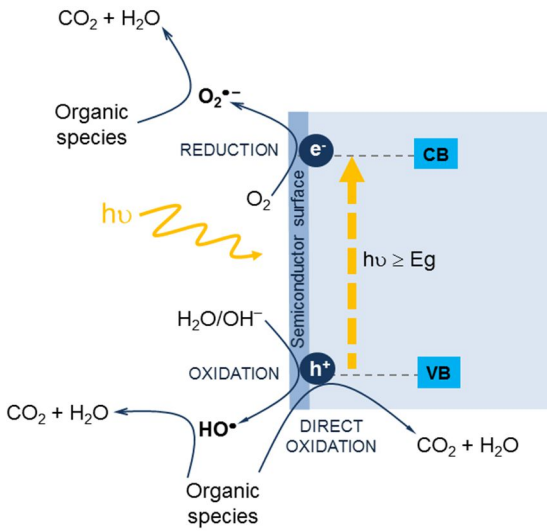

Figure 1.2 – Main processes occurring on a semiconductor particle (adapted from [24]).

The photocatalytic process can proceed by e^-/h^+ pairs recombination releasing light energy as heat, with no chemical reaction taking place or the e^-/h^+ pairs can participate in redox reactions with adsorbed species due to the strongly oxidizing VB hole and strongly reducing CB electron. At the surface of the semiconductor the excited electrons and holes can participate in redox reaction with hydroxide ions (HO^-), water, organic compounds or oxygen. If the photoexcitation occurs directly in the adsorbate organic molecules, which then interacts with the ground state of the semiconductor, the process is called catalyzed photoreaction. When the photoexcitation begins in the semiconductor substrate and the photoexcited semiconductor then interacts with the ground state of the adsorbate molecule, the process is referred as a sensitized photoreaction, where the sensitizer is the semiconductor [23].

In a classical heterogeneous photocatalytic reaction, the overall process can be decomposed into five independent steps [24, 25]:

1. Diffusion of the reactants from the bulk phase to the surface of the catalyst.
2. Adsorption of at least one of the reactants.
3. Reaction in the adsorbed phase.
4. Desorption of the product(s).
5. Diffusion of the product(s) from the interface region to the bulk phase.

In heterogeneous photocatalysis either the semiconductor, or the adsorbed molecule, or both, are in the excited state during the catalytic step 3. The heterogeneous photocatalytic reaction can be represented as a number of mechanistic steps [24-26]. In aerated conditions, the oxygen is omnipresent at the particle surface acting as an electron acceptor (Eq. 1.2) with formation of superoxide radicals. On the other hand, adsorbed water molecules and anions act as electron donors leading to the formation of hydroxyl radicals ($HO^\bullet$) (Eq. 1.3 and 1.4).

$$h\nu + SC \rightarrow SC^\bullet(e^-_{CB}) + SC^\bullet(h^+_{VB}) \quad (1.1)$$

$$SC^\bullet(e^-_{CB}) + [O_2]_{ads} \rightarrow SC + O_2^{\bullet -} \quad (1.2)$$

$$SC^\bullet(h^+_{VB}) + [H_2O]_{ads} \rightarrow SC + [HO^\bullet]_{ads} + [H^+]_{ads} \quad (1.3)$$

$$SC^\bullet(h^+_{VB}) + [HO^-]_{ads} \rightarrow SC + [HO^\bullet]_{ads} \quad (1.4)$$

Once generated the highly oxidizing $HO^\bullet$ radicals react with the organic species (OS) adsorbed in the catalyst surface or they will diffuse away and react in the bulk

solution. In either case the structure will breakdown into intermediate compounds that can be totally mineralized to CO_2 and H_2O (Eq. 1.5).

$$[OS]_{ads} + [HO^{\bullet}]_{ads} \rightarrow \text{intermediates} \rightarrow H_2O + CO_2 \quad (1.5)$$

Due to the high oxidation potencial of the photogenerated holes, direct oxidation of the organic species can also occur. Peroxide radical ($HOO^{\bullet}$) is generated from the protonation of the $O_2^{\bullet-}$ radical to form hydrogen peroxide (H_2O_2) (Eq. 1.7 and 1.8). Then, H_2O_2 can undergo by thermal desorption from the semiconductor surface under light irradiation leading to the formation of $HO^{\bullet}$ (Eq. 1.9).

$$[OS]_{ads} + SC^{\bullet}(h^{+}_{VB}) \rightarrow OS^{\bullet+} \rightarrow OS^{\bullet} + [H^{+}]_{ads} \quad (1.6)$$

$$[H^{+}]_{ads} + O_2^{\bullet-} \rightarrow HOO^{\bullet} \quad (1.7)$$

$$HOO^{\bullet} + O_2^{\bullet-} + [H^{+}]_{ads} \rightarrow H_2O_2 + O_2 \quad (1.8)$$

$$H_2O_2 + h\nu \rightarrow 2HO^{\bullet} \quad (1.9)$$

Nevertheless, Eq. 1.3 and Eq. 1.4 are the main reactions that often occurs in heterogeneous photocatalysis. In the presence of highly oxidative radicals the degradation of organic species may occur through the generation of oxygenated intermediates followed by the decomposition to lower molecular species and ideally achieve total mineralization.

1.4. Semiconductors for heterogeneous photocatalysis

An ideal semiconductor for photocatalytic oxidation of organic species should be a substance that, after being irradiated by a light source induces a chemical reaction in such a way that the substance itself will not be consumed. Also, an efficient photocatalyst must satisfy the following characteristics: i) chemically and biologically inert in nature; ii) capable to adsorb reactants under photonic activation ($h\nu \geq E_g$); iii) holds photo-stability; iv) availability and low cost; v) insoluble in water, and iv) non-toxic or low toxicity.

Several semiconductors have been studied and tested as photocatalysts for the oxidation of organic compounds, which includes TiO_2, ZnO, CdSe, Cds, SnO_2, Fe_2O_3, WO_3 and others [27-30]. Figure 1.3 shows the most common semiconductors used in photocatalytic applications.

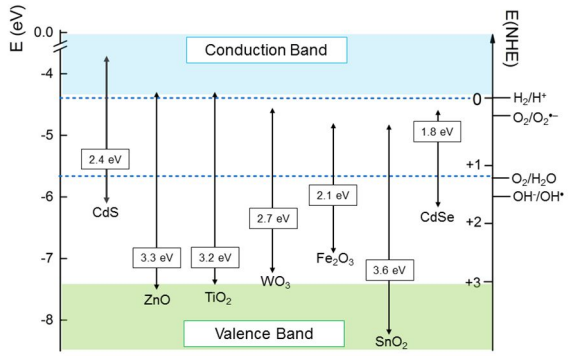

Figure 1.3 – Schematic representation of the position of selected semiconductors CB and VB and the redox potentials vs. NHE at pH 0.(adapted from [28]).

These semiconductor materials have been studied as promising photocatalysts for the decomposition of a wide range of refractory organic species either into readily biodegradable compounds or eventually mineralized into CO_2 and H_2O. However, despite their efficiency in aqueous media some semiconductors exhibit limitations.

For instance, CdS and CdSe are slightly stable undergoing photocorrosion [31, 32]. To avoid this phenomenon the addition of specific anions is needed, thus increasing the number of species in the final solution. These semiconductors are also very toxic materials [32].

Semiconductor oxides with one-dimension (1D) nanostructures such as SnO_2 have also actracted attention due to their excellent photoelectronic properties, gas sensitivity, and superior chemical stability [33, 34]. However, due to the high bandgap (E_g = 3.6 eV) [34] they require higher energy to be photo-excited.

Hematite (α-Fe_2O_3) is another semiconductor that has been reported as a photoactive material showing response to light of wavelengths $\leq$ 500 nm. Yet, it also suffers from limitations that affects its efficiency, such as relative low absorptivity in the visible range leading to the formation of short-lived metal-to-ligand or ligand-to-metal charge transfer states [35]. Among the above mentioned semiconductor catalysts, TiO_2 has received the greatest attention for heterogeneous photocatalysts technology, with the Aeroxide® TiO_2 P25 from Evonik Industries being the benchmark for photocatalytic oxidation reactions [36-39].

1.4.1. Titanium dioxide

In the 1970s, A. Fujishima and K. Honda's published a work that would change the use of TiO_2 as a catalyst for photocatalytic applications, including hydrogen

production, effuents detoxification and organic synthesis [27, 40]. Since then the extensive use and the interest in TiO_2 for both academy and industry has been in exponential growth. The attention given to this material is due its chemical stability, non-toxicity and photoactivity under UV irradiation. The two main TiO_2 production methods used by industry are the sulfate process and the chloride process [41]. In the sulfate process, the α-Fe_2TiO_3 mineral found in metamorphic rocks, is treated with concentrated sulfuric acid to selectively extract the titanium oxygen sulfate and converte it into titanium dioxide. Alternatively, in the chloride process the α-$FeTiO_3$ dry ore is firstly reduced with a carbon source (often carbon monoxide) in the presence of chlorine, generating titanium tetrachloride and carbon dioxide. Then the titanium tetrachloride is further oxidized yielding pure TiO_2

Titanium dioxide can be mainly found in different polymorph forms (Figure 1.4) anatase, rutile, brookite and TiO_2–B. Anatase and rutile are the most abundant phases of TiO_2, having crystalline structures that correspond to the tetragonal system (dipyramidal and prismatic habit, respectively). Brookite type TiO_2 has an orthorhombic cristalline structure, yet the difficult preparation method and rareness of the brookite structure limites its usage [42]. Finally, TiO_2-B, which has a monoclinic crystal structure, can be synthesized by hydrolysis of $K_2Ti_4O_9$ followed by thermal treatment [43], however its pure form is difficult to obtain.

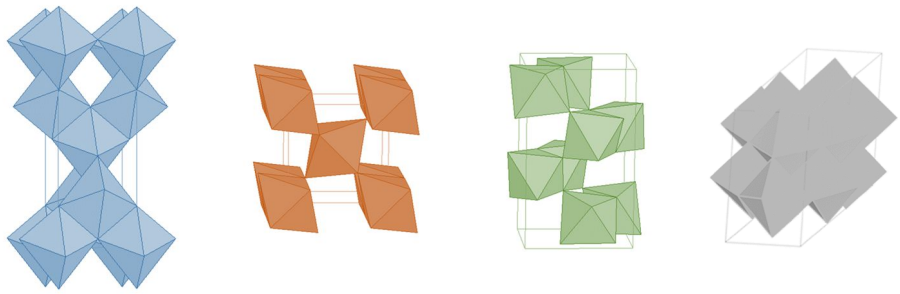

Figure 1.4 – Representation of crystal structures of TiO_2 [44].

As previously referred, Aeroxide® TiO_2 P25 is the most used semiconductor catalyst in photocatalytic applications, and is considered a standard photocatalyst in several research works [44, 45]. This material is a fine white powder composed by a mixture of 80% of anatase and 20% of rutile and with hydrophilic character, thus leading to a good interacton with water due to the presence of hydroxyl groups in its surface, creating hydrogen bonds with water molecules. This feature and its relatively

high surface area (*ca.*, 50 $m^2 g^{-1}$) leads to a good dispersion in water, which is an advantage for photocatalytic water treatment.

Different methods at lab-scale have been reported for the production of TiO_2 nanopowders, such as co-precipitation [46], solvothermal and hydrothermal methods [47], combustion [48] and electrochemical synthesis [49], microemulsion [48] and the most popular technique the sol-gel method [50-52].

The sol-gel method has many advantages in the preparation of new hybrid organic-inorganic materials. Consequently, pure anatase phase can be easily obtained by calcination at low temperature (below 400 ºC), while rutile requires moderate temperature (400-600ºC) becoming the predominant phase after annealing at higher temperatures [53]. Furthermore, the sol-gel method allows the introduction, during the synthesis procedure, of other solid phases into the TiO_2 matrix, this being an advantage if the goal is the preparation of composite materials [54, 55].

The widespread use of systems based on this material for water treatment is occasionally a constraint due to some technological drawbacks such as: (i) small amount of photons absorbed in the visible region, with the consequent need to irradiate with UV light; (ii) low photonic yield of the degradation process; (iii) the need of a final step to separate the photocatalyst from the treated water when suspensions are used; and (iv) the difficulty of immobilizing powdered TiO_2 on some supports.

Over the last years, a great effort has been made to overcome some of these issues. Doping with metal and nonmetal ions, dye photosensitization, deposition of noble metals, coupling with other semiconductors, and addition of inert supports are some of the options to increase TiO_2 absorption in the visible light range [56-60]. The implementation of immobilized TiO_2 for water treatement meeting the requirements of technological applications has been also extremely worked [44, 45, 56, 61]. The application of TiO_2 suspensions to treat water or wastewater ensures a shorter time for pollutant degradation compared to the use of immobilized TiO_2, due to the larger amount of catalyst per unit of volume. Yet, several practical problems arise from the use of a catalyst in powder form, such as difficult separation from the slurry and particle aggregation at higher catalyst loads. Additionally, the utilization of TiO_2 powder is normally technologically impracticable in continuous processes. Besides this, it is difficult to illuminate all the catalyst particles in slurry systems, since the particles further away from the light source are shaded from radiation by those near to it [42, 57]. On the other hand, the use of immobilized TiO_2 can decrease the efficiency of the process, however in terms of technological applications and process costs it could be

considered a good alternative. There are numereous works in the literature describing the use of TiO_2 immobilized into surfaces, such as stainless steel [58], polypropylene fabrics [59], glass slides [60], beads [62] and Raschig rings [63]. Glass is the most commonly used supporting substrate since it allows calcination up to 400 ºC and is highly transparent. TiO_2 films can be prepared following distinct techniques like spin coating [64], dip coating [44] and doctor blade [65] starting from Ti precursor sols [44] or using TiO_2 suspensions [63].

Moreover, heterogeneous photocatalytic technology using TiO_2 films has been applied not only in water and wastewater treatement but also in other areas including self-cleaning surfaces (*e.g.*, exterior tiles, coated glass covers for highway tunnel lamps, paper window blinds, etc.), air-cleaning surfaces (*e.g.,* room air cleaner, air cleaner for factories, building walls, concrete for highways, etc.) and self-sterilizing devices (*e.g.*, silicone rubber for medical catheters, hospital garments and uniforms, and others) [66, 67].

The widespread use of TiO_2, led to massive consumption of this commodity and triggered the interest on alternative materials capable of efficiencies similar, or even higher, than TiO_2 for specific applications. Zinc oxide (ZnO) has a bandgap and a redox potential level similar to that of TiO_2 (Figure 1.3) being a potential alternative in photocatalytic applications.

1.4.2. Zinc oxide

ZnO is not a novelty in the semiconductor field, the pioneering work was published in 1935 by *C.W. Bunn* [68] who reported the characterization of the lattice-dimensions of ZnO. Several studies followed and nanostructured ZnO materials received a broad attention in the 1960s due to their performance in electronics, optics and photonic devices. Since then, ZnO has gained substantial interest in the photocatalysis field for wastewater treatment.

Considered as a multifunctional material, ZnO has unique physical and chemical properties, such as high chemical stability, broad range of UV absorption, morphological versatily and lower cost comparing with TiO_2 [69]. The hardness, rigidity, low toxicity, biocompatibility and biodegradability makes ZnO a widespread used material in several fields of nanotechnology, including biomedicine, ceramics industry, photocatalytic applications for water and air decontamination, or as an antibacterial agent controling the spread and infection of bacterial strains under irradiation [70, 71].

The control of the shape, size and spatial confinement of the ZnO crystals are the key to obtain materials with good performance in catalytic applications. In term of crystal structures, ZnO can be found as zincblende, rocksalt and wurtzite

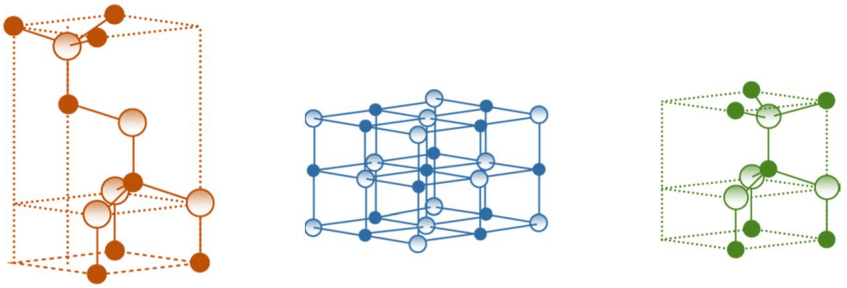

Zincblende Rocksalt Wurtzite

Figure 1.5 – Representation of ZnO crystal structures. Open and filled spheres denote Zn and O atoms, respectively [72].

The zincblende and rocksalt structures are thermodynamically unstable: the zincblende structure growths naturally only in cubic substracts (*e.g.*, ZnS, GaAs/ZnS or Pt/Ti/SiO_2/Si); the rocksalt growth requires pressure conditions [72]. Thus, the research and applications are mainly focused in the wurtzite structure, which is the most stable at ambient temperature and presure conditions.

Depending on the synthesis method and preparation conditions, ZnO provides one of the greateast assortments of varied shapes and offers a wide range of properties. Some of the synthesis routes to obtain distinct shape and size of ZnO structures include, solvothermal [73] and hydrothermal [74] techniques, sol-gel process [75], precipitation from microemulsions [76], mechanochemical processes [77], and chemical vapor deposition (CVD) [78]. Different shapes at the micro- and nanoscale with 1-2-3 dimensions can be obtained, such as rods, needles, spheres, flowers, rings, ribbons, tubes, belts, wires and tetrapods [79, 80]. Some selected structures of ZnO materials obtained during the present work are shown in Figure 1.6.

In photocatalytic applications the activity of these structures can vary. For instance, during this research was found that a ZnO material (with deposition of a nominal loading of 1 *wt.* % Au) composed by spherical and 1D needle-like structures exhibited high efficiency for the photocatalytic oxidation of aqueous solutions of phenol under simulated solar light irradiation [80]. However, when the same material was tested for the photocatalytic performance for hydrogen production [81] its activity was very low compared with a ZnO material with a nanoflower structure. These observations

indicate that ZnO performance is influenced by its strucure, morphology and also depend on the applications.

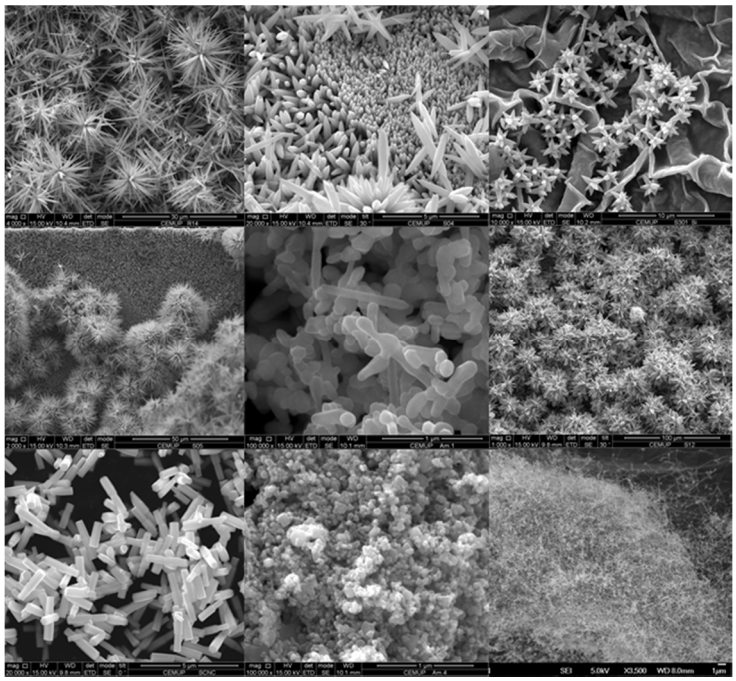

Figure 1.6 – Examples of zinc oxide morphologies.

As TiO_2, the major drawback of ZnO is its bandgap (3.1–3.3 eV) accounting only for 5% of the total solar spectrum reaching Earth's surface. Also, some problems can arise when ZnO materials are used at extreme pH conditions: photocorrosion and dissolution of inert $Zn(OH)_2$ or Zn ions. Numerous attempts have been drawn to study possible pathways to improve the performance of ZnO (and TiO_2): heterostructuring with other semiconductors; noble metal deposition; and modification with carbon nanostructures [80, 82, 83]

1.5. Improving the photocatalytic activity of metal oxides

The enhancement of photocatalyst activity in the visible range is one of the most important challenges of heterogeneous photocatalysis. Therefore, the design of active photocatalysts for heterogeneous water remediation must take in consideration three fundamental factors: (i) light flux into the system; (ii) ability of the material to absorb light; and (iii) capability of electron-hole utilization. These factors can be combined in a way that they are directly proportional to the rate of a photocatalytic reaction [84, 85]. Solar technologies need to take into account all these factors, but still suffer from

several different complications and challenges that include inefficient photon capture, slow conversion kinetics, unpredictable and unsolved reaction mechanisms [86, 87]. Therefore, the quest to find new photocatalysts with better overlap with the solar spectrum remains open.

As mentioned above, TiO_2 and ZnO materials hold physical and chemical characteristics favorable to be used in photocatalysis applications, in particular for the decontamination of water containing organic pollutants. As consequence, research in heterogeneous photocatalysis addresses issues such as to modify TiO_2 and ZnO materials in order to enhance their photoefficiency. In this sense, in the next section, some techniques such as coupling the metal oxides (TiO_2 and ZnO) with carbon materials or deposition of noble metals (to increase their stability and efficiency in the visible range) will be presented.

1.5.1. Coupling semiconductors with carbon materials

The interest in carbon materials has been well documented in the last decades by the scientific community and represents an important topic in materials science [88-91]. Carbon-based structures are recognized as one of the most versatile materials in the field of catalyst science. The ability of carbon atoms to bond each other allows the formation of different structures (linear, planar and tetrahedral bonding arrangements). Some of these structures include carbon nanotubes (single-wall, double-wall, and multi-wall carbon nanotubes), carbon nanofibers, graphene, graphene oxide, carbon nanohorns (graphene sheets wrapped to form cone shapes), fullerene, diamonds, foams, charcoal and activated carbon. These materials may be prepared using several carbon sources (*i.e.*, fossil-derived percursors) and using different methods depending which carbon structure is required. CVD is a well known technique to prepare carbon nanotubes and nanofibers, and also graphene [91-93]. When the goal is preparing graphene oxide, the Hummer's method is the most used [94]. On the other hand, nanodiamonds are generaly synthesized by detonation processes of carbon-containing explosives [95].

The high mechanical strength, the chemical, mechanical, electrical and field emission properties of carbon materials, and the possibility to control these properties make these materials good candidates for the preparation of composites for photocatalytic applications. In addition, it has been demonstrated that surface modification of the carbon material influences the performance of the composite photocatalyst. Due to the graphitic structure of carbon materials, their surface

chemistry is easily modified by the reaction between the deffects of the graphene layers with chemical species such as adsorbed water, oxygen, or nitrogen compounds.

The so formed covalent bonds originate, in case of oxygen surface groups, carboxylic acids, anhydrides, lactones, phenols, carbonyl and ether groups [96, 97]. The presence of these groups in the carbon phase allows the easy functionalization and consequently the anchoring of the catalyst or catalyst percursors, creating in this way active sites that may be relevant for the efficiency of the catalysts.

The introduction of nitrogen groups (pyridine, pyrrole or pyridone, oxidized nitrogen, and quaternary nitrogen) on carbon materials has been also explored as an important route to improve their catalytic performance by providing additional electrons [96, 98, 99]. When these carbon-nitrogen containing groups are used to prepare composites for photocatalyst applications the presence of additional electrons may prevent the recombination of photoexcited electron-hole pairs improving the photoactivity of the resulting materials.

Additionaly, reports exist showing that carbon materials produce beneficial effects on the photocatalytic activity of metal oxides, such as, TiO_2 and ZnO by inducing synergies or cooperative effects between the metal oxide and the carbon phases [83, 100, 101]. The separation of the photo-generated electron-hole pairs by formation of heterojunctions at the carbon/metal oxide interface, may promote faster photocatalytic reaction rates.

According to these reports, the development of sustainable materials for environmental applications in particular for water and wastewater remediation make carbon structures special materials.

A wide range of methods to synthesize TiO_2 (or ZnO)-based carbon composite materials are discussed in the literature, such as impregnation [102], CVD [103], hydrothermal [104] and sol-gel [100] methods, liquid phase deposition method (LPD) [101], hydration/dehydration process [105] or by simply mixing of the two phases [106].

1.5.2. Deposition of noble metals on semiconductors

The enhancement of the photocatalyst activity induced by the incorporation of metal nanoparticles at the surface of semiconductor materials is generally attributed to: (i) improvement of the electron-hole separation by trapping the electrons; (ii) modification of the surface adsorption properties of the photocatalyst; and (iii) shift of the absorption into the visible-light range due to plasmon formation.

Several studies have reported that an improvement in the performance of TiO_2 (or ZnO) by loading them with noble metals (*e.g.*, Ag, Pt, Au and Pd), as metal nanoparticles leading to an increase in the yield and lifetime of the charge separation state [80, 107, 108]. Moreover, metal nanoparticles, such as Ag and Au have strong absorption in the visible light due to the surface plasmon resonance as consequence of collective electron oscillation in response to electromagnetic field radiation. The schematic representation of the action of noble metals deposited on metal oxide semiconductor is shown in Figure 1.7.

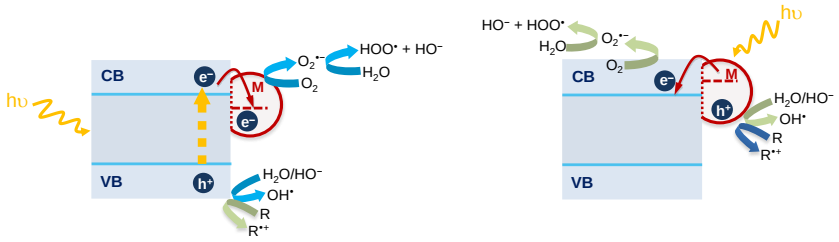

a) Electron sink b) Photosensitization

Figure 1.7 – Schematic representation of noble metals acting as electron sink (a) and photosensitizer (b). “R” and “M” correspond to reactive species and noble metal, respectively.

These plasmonic photocatalysts are characterized by the creation of an electrical junction between the noble metal and the semiconductor, known as Schottky barrier [109]. An electric field is built in the noble metal/semiconductor interface that forces the electrons and holes to move in different directions once they are created inside or near the Schottky barrier suppressing this way the electron-hole recombination.

The recombination of photogenerated charge carriers is the major limitation in photocatalytic reactions. If recombination occurs, the excited electrons return to the valence band without reacting with the adsorbed species thus dissipating the energy non-radiatively or radiatively as light or heat. Deposition of noble metal can be a good approach to enhance the efficency of semiconductors, in a way to avoid such mechanism.

It has been also described in the literature that there is an optimum amount of metal above which the efficiency of the photocatalytic process actually decreases. When the metal content is high, metal clusters are numerous and large, creating some drawbacks: (i) the negatively charged metal particles can act as recombination centers trapping holes; (ii) metal deposits can inhabit the semiconductor surface active sites; and (iii) the semiconductor surface is covered with deposits decreasing the light that

reaches its surface leading to a decrease of photogenerated electron-hole pairs. Typical metal loads found in the literature vary between 0.25 and 1 *wt*% [80, 110], for optimal content.

Gold and silver are noble metals with particular interest in heterogeneous photocatalysis because they exhibit resonant behavior when interacting with light. By manipulating the composition, shape and size of plasmonic nanoparticles, it is possible to prepare nanostructures that interact with the entire solar spectrum enhancing the efficiency of the photocatalytic process.

1.6. Photocatalytic reaction system for water treatment

The development of systems for water and wastewater remediation based on heterogeneous photocatalysis is an area of major technical importance. Thus, the scientific community is long lasting focused on the research for new technologies. As seen before, the advances in the preparation of high efficient semiconductors is one important goal to be achieved. However, at lab-scale other approaches to enhance the photocatalytic process must also be explored such as, the type and geometry of the photoreactor, the irradiation source (natural or artificial), and the study of operating parameters. In addition, the choice of the target pollutant is another important issue to be considered.

In terms of photocatalytic reactors, the most used for heterogeneous photocatalysis are slurry systems. As described before, these systems require separation of the powders from the treated milk-like water suspensions. The immobilization of the photocatalysts on a support can increase the feasibility of the process; however, other problems arise such as, the limited exposure of active area of the semiconductor.

Additionally, the type of radiation source used can also influence the efficiency and the viability of the process. At lab-scale the most common artificial light sources are mercury arc lamps (low, medium and high pressure), incandescent and fluorescent lamps, lasers and Xenon lamps. This latter one produces a bright white light that simulates natural sunlight, which from the technological point of view is an advantage if the final goal is the application in the real field under natural sunlight. More recently LEDs (Light Emitting Diodes) have been used due their variety of advantages over other light sources (high-levels of brightness, intensity and efficiency, low-voltage and current requirments, low heat dispersion, long source life and can be easily controlled and programmed).

Overall, it is imperative to consider all these factors when we are planning the experiments at lab-scale so meaningful information can be obtainded and used for upscaling the process.

1.6.1. Operation parameters in photocatalytic processes

Most of the reports found in the literature studying the effect of operating conditions on the photocatalytic degradation of organic pollutants in water, use very simple equations such as pseudo-first order or Langmuir-Hinshelwood kinetic models. Nevertheless, these kinetic models only take into account the concentration of the target pollutant [111, 112]. The effect of other parameters such as the catalyst load and radiation absorption are then included in the apparent kinetic constant determined from the fitting of the model to the experimental data, which will render this way the validity of the kinetic expressions to the experimental conditions tested and to the experimental setup being used. Therefore, additional operation parameters should be also controlled in heterogeneous photocatalysis, which include: (i) mass of catalyst; (ii) initial concentration of the reactant; (iii) photon flux; (iv) oxygen pressure; (v) additional oxidant agents; and (vi) pH of the medium. Taking into account these parameters, the development of a kinetic model that can predict the overall efficiency of the process is facilitated and if the main goal is the application to real field conditions this information can be of major relevance.

1.6.2. Target pollutants

Research into semiconductor photocatalysts has been focused on the removal of a wide range of model pollutants that can be found in wastewaters (Table 1.1). Some of these target molecules are considered emerging pollutants, which may cause a global concern related to their eventual impact in human health and in the ecosystem.

As mentioned before, the rapid growing of population and the consequent intensification of industrial and agricultural activities promote the appearance of contaminants that can be persistent or hard to remove from water.

For instance, phenolic compounds are often found in real effluents (*e.g.*, from olive oil mills, cork, pulp and paper industries) in high concentrations. Thus biological treatments are strongly affected and can be rather ineffective. In particular, olive oil mill wastes constitute a environmental problem in the Mediterranean region, Portugal standing as a representative olive oil producer [119].

Table 1.1– Selected examples of target molecules used in photocatalytic reactions.

Class	Examples	References
Aliphatic carboxylic acids	formic, acetic, propanoic, oxalic acids	[113-115]
Aromatics	benzene, naphthalene	[116, 117]
Aromatics carboxylic acids	Benzoic, 4-aminobenzoic, 3-, 4- hydroxybenzoic, gallic, protocatechuic acids	[118, 119]
Phenols	phenol, hydroquinone, benzoquinone, cathecol resorcinol, o-, m-, p-cresol	[119-122]
Halophenols	2-, 3-, 4-chlorophenol, phentachlorophenol	[118, 120]
Pesticides	atriazine, diuron, hexachlorobenzene,	[6, 121]
Dyes	methylene blue, methyl orange, rhodamine B, reactive black 5	[123-126]
Pharmaceuticals and personal care products (PPCPs)	caffeine, clofibric acid, diphenhydramine, diclofenac, ibuprofen	[123, 127, 128]

Industrial dyes are other targeted contaminants with special interest because of their toxicity and significant nondegradability, thus difficult to remove using conventional methods. In addition, removing color from wastes is often more important than other colorless organic substances, because even at low concentrations (< 1 ppm) dyes could negatively influence the aquatic environment.

Furthermore, the presence of organic pollutants can lead to eutrophication, which is the ecosystem's response to the addition of natural or artificial substances in the superficial freshwater bodies (used for recreation purposes) and drinking water supplies. Environmental conditions such as higher temperature and pH values, as well high nutrient inputs increase the natural algae growth, leading to the formation of "blooms" produced by photo-autotrophic organisms such as cyanobacteria (aka, blue-green algae) [129, 130]. These harmful algal blooms (HABs) can release toxins that produce adverse effects in both humans and animals. The common toxins found in freshwaters are microcystins, cylindrospermopsin, anatoxins and saxitoxins [131], where microcystins (MCs) are among the most common cyanobacterial toxins found in freshwaters. Some procedures that have been proposed for the removal of these toxins from freshwaters, include adsorption on active carbon, oxidation using hydrogen peroxide or permanganate, ozonation and photolysis [132]. These methods have some limitations such as transfer of the pollutant from one to another phase (in the case of adsorption) or the formation of refractory (or even toxic) intermediates.

Therefore, attention has been paid in heterogeneous photocatalysis as a process to mineralize pollutants and reduce the incidence of HABs in freshwaters. Efficient heterogeneous photocatalytic processes using titanium dioxide (TiO_2) have been amply confirmed in literature [61, 133].

The above facts have in common a general goal, which is the research intensificaton to find an effective method for water/freshwater treatment in order to reduce the incidence of target pollutants, where semiconductor photocatalysis has proved to be a promising solution.

1.7. Aim of the work and thesis outline

Water quality and availability has become a collective society concern leading to a growing conscientiousness on the issues related with treatment and reuse of this natural resource of finite quantity and increasing limited access. Heterogeneous photocatalysis is an efficient method for the removal of a wide variety of recalcitrant organic water pollutants, meeting the very important requirement of sustainability for process development when solar energy is used.

Although the benchmark TiO_2 material has gained special attention in the field of photocatalysis, some limitations may affect its applicability. The low photonic yield and negligible efficiency under visible light due to the wide band gap lead to an intensive research to overcome these issues.

The present research work seeks to use TiO_2 as well as ZnO due to its similar wide band gap (3.1-3.3 eV) in the development of semiconductor photocatalysts. The optimization of the preparation conditions and the exploitation of new trends (such as, photocatalyst immobilization, modification with carbon materials and the deposition of noble metals) to produce highly efficient photocatalysts are the main goals of the present research work.

Phenolic compounds, methylene blue dye and cyanotoxin microcystin-LA are chosen in this study as model compounds since they are actual pollutants found in contaminated water sources.

The dissertation is organized in seven chapters divided by four parts. This introductory chapter is included in Part I, wherein the environmental water issues and implementation of potential technologies that can be used for water remediation are discussed. In Part II are included chapters 2, 3 and 4 that report trends to improve the efficiency of TiO_2 materials in different photocatalytic applications for water/freshwater

decontamination. The development of different ZnO-based materials is described in Part III (chapters 5 and 6). Finally, Part IV includes chapter 7 which deals with the final remarks from this work and suggestions for future work. A detailed description of each chapter is given in the following.

Chapter 2 describes the immobilization of different TiO_2 materials on Raschig rings. The reactivity and robustness of the TiO_2-coated rings is tested for phenol degradation in a recirculation reactor under simulated solar light irradiation. A kinetic model is developed for the determination of the first order reaction rate as function of the operating parameters. Subsequently the study is extended to the treatment of a synthetic effluent containing phenolic derivatives.

Chapter 3 reports the introduction of carbon nanotubes as a way to improve the photocatalytic activity of TiO_2 (commercial and lab synthetized). The preparation methods of the composites and the functionalization of the carbon material are discussed. The composites are coated on glass slides and tested in the photocatalytic degradation of methylene blue and *para*-substituted phenol compounds in a batch reactor with near-UV to visible light irradiation.

Chapter 4 deals with the introduction of carbon nanotubes, graphene oxide and nanodiamonds in the TiO_2 matrix. The TiO_2-carbon materials are fully characterized and tested in a batch reaction system under both solar and visible light irradiation for the photocatalytic oxidation of a cyanotoxin often found in superficial freshwaters. Insights in the identification of cyanotoxin intermediates produced during the oxidation process are given.

In Part III, where are included chapters 5 and 6, are presented new trends to improve ZnO photocatalytic activity.

In chapter 5 a wide range of carbon materials are combined with a ZnO material prepared by chemical vapour deposition. Detailed characterization of the carbon materials and ZnO-carbon materials is discussed. The carbon materials functionalization is also described. The efficiency and stability of the powder composites are evaluated using phenol as a model compound under simulated solar light irradiation.

In chapter 6 a different approach is used with the deposition of noble metals (Ag or Au) on ZnO materials with distinct morphologies. The characterization of the ZnO materials is fully described using a variety of techniques. The Au/ZnO powder materials are tested on phenol oxidation under simulated solar light. The reaction

mechanism is investigated using radical and hole scavengers. In the case of Ag-loaded ZnO, the study is extended to the degradation of different phenolic compounds using the photocatalyst as powder and immobilized on glass Raschig rings.

Finally, Part IV which inclued chapter 7, is dedicated to the final remarks and suggestions for future work.

References

[1] Trends in global water use by sector, in, United Nations Environment Programme (UNEP), Accessed on October 2015.

[2] United Nations Educational, Scientific and Cultural Organization, International Hydrological Programme, (Accessed on October 2015).

[3] M. Petrović, E. Eljarrat, M.J. López de Alda, D. Barceló, Analysis and environmental levels of endocrine-disrupting compounds in freshwater sediments, TrAC Trends in Analytical Chemistry, 20 (2001) 637-648.

[4] C. Bicchi, T. Schilirò, C. Pignata, E. Fea, C. Cordero, F. Canale, G. Gilli, Analysis of environmental endocrine disrupting chemicals using the E-screen method and stir bar sorptive extraction in wastewater treatment plant effluents, Sci. Total Environ., 407 (2009) 1842-1851.

[5] L.J. Mills, C. Chichester, Review of evidence: Are endocrine-disrupting chemicals in the aquatic environment impacting fish populations?, Sci. Total Environ., 343 (2005) 1-34.

[6] A.R. Ribeiro, O.C. Nunes, M.F.R. Pereira, A.M.T. Silva, An overview on the advanced oxidation processes applied for the treatment of water pollutants defined in the recently launched Directive 2013/39/EU, Environ. Int., 75 (2015) 33-51.

[7] Y. Luo, W. Guo, H.H. Ngo, L.D. Nghiem, F.I. Hai, J. Zhang, S. Liang, X.C. Wang, A review on the occurrence of micropollutants in the aquatic environment and their fate and removal during wastewater treatment, Sci. Total Environ., 473-474 (2014) 619-641.

[8] A. Jurado, E. Vàzquez-Suñé, J. Carrera, M. López de Alda, E. Pujades, D. Barceló, Emerging organic contaminants in groundwater in Spain: A review of sources, recent occurrence and fate in a European context, Sci. Total Environ., 440 (2012) 82-94.

[9] Directive 2013/39/EU of the European Parliament and of the Council of 12 August 2013 amending Directives 2000/60/EC and 2008/105/EC as regards priority substances in the field of water policy Off. J. Eur. Union, L226 (2013) 1-17.

[10] I. Oller, S. Malato, J.A. Sánchez-Pérez, Combination of Advanced Oxidation Processes and biological treatments for wastewater decontamination-A review, Sci. Total Environ, 409 (2011) 4141-4166.

[11] A. Matilainen, M. Sillanpää, Removal of natural organic matter from drinking water by advanced oxidation processes, Chemosphere, 80 (2010) 351-365.

[12] D.P. Mohapatra, S.K. Brar, R.D. Tyagi, P. Picard, R.Y. Surampalli, Analysis and advanced oxidation treatment of a persistent pharmaceutical compound in wastewater and wastewater sludge-carbamazepine, Sci. Total Environ, 470-471 (2014) 58-75.

[13] M. Cheng, G. Zeng, D. Huang, C. Lai, P. Xu, C. Zhang, Y. Liu, Hydroxyl radicals based advanced oxidation processes (AOPs) for remediation of soils contaminated with organic compounds: A review, Chem. Eng. J., 284 (2016) 582-598.

[14] J.L. Wang, L.J. Xu, Advanced oxidation processes for wastewater treatment: Formation of hydroxyl radical and application, Crit. Rev. Env. Sci. Tec., 42 (2012) 251-325.

[15] M. Antonopoulou, E. Evgenidou, D. Lambropoulou, I. Konstantinou, A review on advanced oxidation processes for the removal of taste and odor compounds from aqueous media, Water Res., 53 (2014) 215-234.

[16] M.A. Oturan, J.-J. Aaron, Advanced Oxidation Processes in Water/Wastewater Treatment: Principles and Applications. A Review, Crit. Rev. Env. Sci. Tec., 44 (2014) 2577-2641.

[17] U.I. Gaya, A.H. Abdullah, Heterogeneous photocatalytic degradation of organic contaminants over titanium dioxide: A review of fundamentals, progress and problems, J. Photochem. Photobio. C: Photochem. Rev., 9 (2008) 1-12.

[18] R. Andreozzi, V. Caprio, A. Insola, R. Marotta, Advanced oxidation processes (AOP) for water purification and recovery, Catal. Today, 53 (1999) 51-59.

[19] S. Dong, J. Feng, M. Fan, Y. Pi, L. Hu, X. Han, M. Liu, J. Sun, J. Sun, Recent developments in heterogeneous photocatalytic water treatment using visible light responsive photocatalysts: a review, RSC Adv., 5 (2015) 14610-14630.

[20] D.F. Ollis, C. Turchi, Heterogeneous photocatalysis for water purification: Contaminant mineralization kinetics and elementary reactor analysis, Environ. Prog., 9 (1990) 229-234.

[21] M. Pelaez, N.T. Nolan, S.C. Pillai, M.K. Seery, P. Falaras, A.G. Kontos, P.S.M. Dunlop, J.W.J. Hamilton, J.A. Byrne, K. O'Shea, M.H. Entezari, D.D. Dionysiou, A review on the visible light active titanium dioxide photocatalysts for environmental applications, Appl. Catal. B: Environ., 125 (2012) 331-349.

[22] V. Likodimos, D.D. Dionysiou, P. Falaras, Clean Water: Water detoxification using innovative photocatalysts, Rev. Environ. Sci. Biotechnol., 9 (2010) 87-94.

[23] A. Mills, S. Le Hunte, An overview of semiconductor photocatalysis, J. Photochem. Photobio A: Chem., 108 (1997) 1-35.

[24] J.-M. Herrmann, Fundamentals and misconceptions in photocatalysis, J. Photochem. Photobio. A: Chem., 216 (2010) 85-93.

[25] M.N. Chong, B. Jin, C.W.K. Chow, C. Saint, Recent developments in photocatalytic water treatment technology: A review, Water Res., 44 (2010) 2997-3027.

[26] J. Schneider, M. Matsuoka, M. Takeuchi, J. Zhang, Y. Horiuchi, M. Anpo, D.W. Bahnemann, Understanding TiO_2 Photocatalysis: Mech. Mat., Chem. Rev., 114 (2014) 9919-9986.

[27] M.D. Hernandez-Alonso, F. Fresno, S. Suarez, J.M. Coronado, Development of alternative photocatalysts to TiO_2: Challenges and opportunities, Energy Environ. Sci., 2 (2009) 1231-1257.

[28] M. Gao, L. Zhu, W.L. Ong, J. Wang, G.W. Ho, Structural design of TiO_2-based photocatalyst for H_2 production and degradation applications, Catal. Sci. Technol., 5 (2015) 4703-4726.

[29] M. Faisal, A.A. Ibrahim, F.A. Harraz, H. Bouzid, M.S. Al-Assiri, A.A. Ismail, SnO_2 doped ZnO nanostructures for highly efficient photocatalyst, J. Mol. Catal. A: Chem., 397 (2015) 19-25.

[30] H. Bouzid, M. Faisal, F.A. Harraz, S.A. Al-Sayari, A.A. Ismail, Synthesis of mesoporous Ag/ZnO nanocrystals with enhanced photocatalytic activity, Catal. Today, 252 (2015) 20-26.

[31] C.C. Nascimento, G.R.S. Andrade, E.C. Neves, C.D.A.E.S. Barbosa, L.P. Costa, L.S. Barreto, I.F. Gimenez, Nanocomposites of CdS Nanocrystals with Montmorillonite Functionalized with Thiourea Derivatives and Their Use in Photocatalysis, J. Phys. Chem. C, 116 (2012) 21992-22000.

[32] A. Hermández-Ramírez, I. Medina-Ramírez, Photocatalytic Semiconductors-Synthesis, characterization and environmental applications, Springer, 2015.

[33] J. Pan, H. Shen, S. Mathur, One-Dimensional SnO_2 Nanostructures: Synthesis and Applications, J. Nanotechnol.., 2012 (2012) 12.

[34] N. Chiodini, A. Paleari, D. DiMartino, G. Spinolo, SnO_2 nanocrystals in SiO_2: A wide-band-gap quantum-dot system, Applied Physics Letters, 81 (2002) 1702-1704.

[35] X. Zhang, H. Li, S. Wang, F.-R.F. Fan, A.J. Bard, Improvement of Hematite as Photocatalyst by Doping with Tantalum, J. Phys. Chem. C, 118 (2014) 16842-16850.

[36] K. Nakata, A. Fujishima, TiO_2 photocatalysis: Design and applications, Journal of Photochemistry and Photobiology C: Photochemistry Reviews, 13 (2012) 169-189.

[37] A. Fujishima, T.N. Rao, D.A. Tryk, Titanium dioxide photocatalysis, J. Photochem. Photobio. C: Photochem. Rev., 1 (2000) 1-21.

[38] J. Coronado, M. Hernández-Alonso, The Keys of Success: TiO2 as a Benchmark Photocatalyst, in: J.M. Coronado, F. Fresno, M.D. Hernández-Alonso, R. Portela (Eds.) Design of Advanced Photocatalytic Materials for Energy and Environmental Applications, Springer London, 2013, pp. 85-101.

[38] J. Coronado, M. Hernández-Alonso, The Keys of Success: TiO_2 as a Benchmark Photocatalyst, in: J.M. Coronado, F. Fresno, M.D. Hernández-Alonso, R. Portela (Eds.) Design of Advanced Photocatalytic Materials for Energy and Environmental Applications, Springer London, 2013, pp. 85-101.

[39] S.G. Kumar, L.G. Devi, Review on Modified TiO_2 Photocatalysis under UV/Visible Light: Selected Results and Related Mechanisms on Interfacial Charge Carrier Transfer Dynamics, J. Phys. Chem. A, 115 (2011) 13211-13241.

[40] A. Fujishima, K. Honda, Electrochemical Photolysis of Water at a Semiconductor Electrode, Nature, 238 (1972) 37-38.

[41] E. Reck, M. Richards, TiO_2 manufacture and life cycle analysis, Pigment & Resin Technol., 28 (1999) 149-157.

[42] O. Carp, C.L. Huisman, A. Reller, Photoinduced reactivity of titanium dioxide, Prog. Solid State Chem., 32 (2004) 33-177.

[43] Z. Liu, Y.G. Andreev, A. Robert Armstrong, S. Brutti, Y. Ren, P.G. Bruce, Nanostructured TiO2(B): the effect of size and shape on anode properties for Li-ion batteries, Prog. Nat. Sci.: Mater. Inter., 23 (2013) 235-244.

[44] Y. Chen, D.D. Dionysiou, Bimodal mesoporous TiO_2-P25 composite thick films with high photocatalytic activity and improved structural integrity, Appl. Catal. B: Environ., 80 (2008) 147-155.

[45] Y. Chen, D.D. Dionysiou, TiO_2 photocatalytic films on stainless steel: The role of Degussa P-25 in modified sol-gel methods, Appl. Catal. B: Environ., 62 (2006) 255-264.

[46] D. Dambournet, I. Belharouak, K. Amine, Tailored Preparation Methods of TiO_2 Anatase, Rutile, Brookite: Mechanism of Formation and Electrochemical Properties, Chem. Materials, 22 (2010) 1173-1179.

[47] H. Kominami, Y. Ishii, M. Kohno, S. Konishi, Y. Kera, B. Ohtani, Nanocrystalline Brookite-Type Titanium(IV) Oxide Photocatalysts Prepared by a Solvothermal Method: Correlation Between Their Physical Properties and Photocatalytic Activities, Catal. Letters, 91 (2003) 41-47.

[48] S.-S. Hong, M.S. Lee, S.S. Park, G.-D. Lee, Synthesis of nanosized TiO_2/SiO_2 particles in the microemulsion and their photocatalytic activity on the decomposition of p-nitrophenol, Catal. Today, 87 (2003) 99-105.

[49] P. Anandgaonker, G. Kulkarni, S. Gaikwad, A. Rajbhoj, Synthesis of TiO_2 nanoparticles by electrochemical method and their antibacterial application, Arabian J. Chem., in press.

[50] G. Li, L. Li, J. Boerio-Goates, B.F. Woodfield, High Purity Anatase TiO_2 Nanocrystals: Near Room-Temperature Synthesis, Grain Growth Kinetics, and Surface Hydration Chemistry, J. Am. Chem. Soc., 127 (2005) 8659-8666.

[51] C.G. Silva, J.L. Faria, Anatase vs.rutile efficiency on the photocatalytic degradation of clofibric acid under near UV to visible irradiation, Photochem. Photobiol. Sci., 8 (2009) 705-711.

[52] N. Nasralla, M. Yeganeh, Y. Astuti, S. Piticharoenphun, N. Shahtahmasebi, A. Kompany, M. Karimipour, B.G. Mendis, N.R.J. Poolton, L. Šiller, Structural and spectroscopic study of Fe-doped TiO_2 nanoparticles prepared by sol–gel method, Scientia Iranica, 20 (2013) 1018-1022.

[53] N. Wetchakun, B. Incessungvorn, K. Wetchakun, S. Phanichphant, Influence of calcination temperature on anatase to rutile phase transformation in TiO_2 nanoparticles synthesized by the modified sol–gel method, Mater. Letters, 82 (2012) 195-198.

[54] B. Gao, C. Peng, G.Z. Chen, G. Li Puma, Photo-electro-catalysis enhancement on carbon nanotubes/titanium dioxide (CNTs/TiO_2) composite prepared by a novel surfactant wrapping sol–gel method, Appl. Catal. B: Environ., 85 (2008) 17-23.

[55] C.G. Silva, W. Wang, J.L. Faria, Nanocrystalline CNT-TiO_2 Composites Produced by an Acid Catalyzed Sol-Gel Method, Mater. Sci. Forum 587-588 (2008) 849-853

[56] H. Choi, E. Stathatos, D.D. Dionysiou, Photocatalytic TiO_2 films and membranes for the development of efficient wastewater treatment and reuse systems, Desalination, 202 (2007) 199-206.

[57] S. Mozia, Photocatalytic membrane reactors (PMRs) in water and wastewater treatment. A review, Sep. Purific. Technol., 73 (2010) 71-91.

[58] M.G. Antoniou, D.D. Dionysiou, Application of immobilized titanium dioxide photocatalysts for the degradation of creatinine and phenol, model organic contaminants found in NASA's spacecrafts wastewater streams, Catal. Today, 124 (2007) 215-223.

[59] H. Han, R. Bai, Effect of Thickness of Photocatalyst Film Immobilized on a Buoyant Substrate on the Degradation of Methyl Orange Dye in Aqueous Solutions under Different Light Irradiations, Ind. Eng. Chem. Res., 50 (2011) 11922-11929.

[60] J. Krýsa, P. Novotná, Š. Kment, A. Mills, Effect of glass substrate and deposition technique on the properties of sol gel TiO_2 thin films, J Photochem. Photobio. A: Chem., 222 (2011) 81-86.

[61] C. Han, M. Pelaez, V. Likodimos, A.G. Kontos, P. Falaras, K. O'Shea, D.D. Dionysiou, Innovative visible light-activated sulfur doped TiO_2 films for water treatment, Appl. Catal. B: Environ., 107 (2011) 77-87.

[62] S. Yurdakal, V. Loddo, G. Palmisano, V. Augugliaro, H. Berber, L. Palmisano, Kinetics of 4-Methoxybenzyl Alcohol Oxidation in Aqueous Solution in a Fixed Bed Photocatalytic Reactor, Ind. Eng. Chem. Res. 49 (2010) 6699-6708.

[63] N. Quici, M.L. Vera, H. Choi, G.L. Puma, D.D. Dionysiou, M.I. Litter, H. Destaillats, Effect of key parameters on the photocatalytic oxidation of toluene at low concentrations in air under 254 + 185 nm UV irradiation, Appl. Catal. B: Environ., 95 (2010) 312-319.

[64] Z.M. Seeley, A. Bandyopadhyay, S. Bose, Titanium dioxide thin films for high temperature gas sensors, Thin Solid Films, 519 (2010) 434-438.

[65] A.I. Kontos, A.G. Kontos, D.S. Tsoukleris, M.-C. Bernard, N. Spyrellis, P. Falaras, Nanostructured TiO_2 films for DSSCS prepared by combining doctor-blade and sol-gel techniques, J. Mater. Process. Technol., 196 (2008) 243-248.

[66] L. Zhang, R. Dillert, D. Bahnemann, M. Vormoor, Photo-induced hydrophilicity and self-cleaning: models and reality, Energ. Environ. Sci., 5 (2012) 7491-7507.

[67] K. Hashimoto, H. Irie, A. Fujishima, TiO_2 Photocatalysis: A Historical Overview and Future Prospects, Jpn. J. Appl. Phys., 44 (2005) 8269-8285.

[68] C.W. Bunn, The lattice-dimensions of zinc oxide, Proceedings of the Physical Society, 47 (1935) 835.

[69] C. Tian, Q. Zhang, A. Wu, M. Jiang, Z. Liang, B. Jiang, H. Fu, Cost-effective large-scale synthesis of ZnO photocatalyst with excellent performance for dye photodegradation, Chem. Commun., 48 (2012) 2858-2860.

[70] Ü. Özgür, Y.I. Alivov, C. Liu, A. Teke, M.A. Reshchikov, S. Doğan, V. Avrutin, S.-J. Cho, H. Morkoç, A comprehensive review of ZnO materials and devices, J. Appl. Phys., 98 (2005) 041301.

[71] C. Klingshirn, ZnO: Material, Physics and Applications, ChemPhysChem, 8 (2007) 782-803.

[72] H. Morkoç, Ü. Özgür, General Properties of ZnO, in: Zinc Oxide, Wiley-VCH Verlag GmbH & Co. KGaA, 2009, pp. 1-76.

[73] Y. Chen, C. Zhang, W. Huang, Y. Situ, H. Huang, Multimorphologies nano-ZnO preparing through a simple solvothermal method for photocatalytic application, Mater. Letters, 141 (2015) 294-297.

[74] M. Guo, P. Diao, S. Cai, Hydrothermal growth of well-aligned ZnO nanorod arrays: Dependence of morphology and alignment ordering upon preparing conditions, J. Solid State Chem., 178 (2005) 1864-1873.

[75] M. Ristić, S. Musić, M. Ivanda, S. Popović, Sol–gel synthesis and characterization of nanocrystalline ZnO powders, J. Alloys Compd., 397 (2005) L1-L4.

[76] X. Li, G. He, G. Xiao, H. Liu, M. Wang, Synthesis and morphology control of ZnO nanostructures in microemulsions, J. Colloid Interface Sci., 333 (2009) 465-473.

[77] A. Moballegh, H.R. Shahverdi, R. Aghababazadeh, A.R. Mirhabibi, ZnO nanoparticles obtained by mechanochemical technique and the optical properties, Surf. Sci., 601 (2007) 2850-2854.

[78] R. Bacsa, Y. Kihn, M. Verelst, J. Dexpert, W. Bacsa, P. Serp, Large scale synthesis of zinc oxide nanorods by homogeneous chemical vapour deposition and their characterisation, Surf. Coat. Technol., 201 (2007) 9200-9204.

[79] W. Zhong Lin, Zinc oxide nanostructures: growth, properties and applications, J. Phys.: Condens. Matter., 16 (2004) R829.

[80] C.G. Silva, M.J. Sampaio, S.A.C. Carabineiro, J.W.L. Oliveira, D.L. Baptista, R. Bacsa, B.F. Machado, P. Serp, J.L. Figueiredo, A.M.T. Silva, J.L. Faria, Developing highly active photocatalysts: Gold-loaded ZnO for solar phenol oxidation, J. Catal., 316 (2014) 182-190.

[81] M.J. Sampaio, J.W.L. Oliveira, C.I.L. Sombrio, D.L. Baptista, S.R. Teixeira, S.A.C. Carabineiro, C.G. Silva, J.L. Faria, Photocatalytic performance of Au/ZnO nanocatalysts for hydrogen production from ethanol, Appl. Catal. A: General.

[82] C. Cheng, A. Amini, C. Zhu, Z. Xu, H. Song, N. Wang, Enhanced photocatalytic performance of TiO_2-ZnO hybrid nanostructures, Sci. Reports, 4 (2014) 4181.

[83] C. Han, M.-Q. Yang, B. Weng, Y.-J. Xu, Improving the photocatalytic activity and anti-photocorrosion of semiconductor ZnO by coupling with versatile carbon, Phys. Chem. Chem. Phys., 16 (2014) 16891-16903.

[84] J.M. Herrmann, Heterogeneous photocatalysis: fundamentals and applications to the removal of various types of aqueous pollutants, Catal. Today, 53 (1999) 115-129.

[85] J.M. Herrmann, Heterogeneous photocatalysis: state of the art and present applications In honor of Pr. R.L. Burwell Jr. (1912–2003), Former Head of Ipatieff Laboratories, Northwestern University, Evanston (Ill), Top Catal, 34 (2005) 49-65.

[86] B. Ohtani, Design and Development of Active Titania and Related Photocatalysts, in: Photocatalysis and Water Purification, Wiley-VCH Verlag GmbH & Co. KGaA (2013) 73-102.

[87] Z. Wang, C. Chen, W. Ma, J. Zhao, Sensitization of Titania Semiconductor: A Promising Strategy to Utilize Visible Light, in: Photocatalysis and Water Purification, Wiley-VCH Verlag GmbH & Co. KGaA (2013) 199-240.

[88] M.M. Titirici, R.J. White, N. Brun, V.L. Budarin, D.S. Su, F. del Monte, J.H. Clark, M.J. MacLachlan, Sustainable carbon materials, Chem. Soc. Rev., 44 (2015) 250-290.

[89] P. Serp, Carbon, in: Comprehensive Inorganic Chemistry II (Second Edition): From Elements to Applications, (2013) 323-369.

[90] J.L. Faria, W. Wang, Carbon Materials in Photocatalysis, in: Carbon Materials for Catalysis, John Wiley & Sons, Inc., (2008) 481-506.

[91] R.R. Bacsa, I. Cameán, A. Ramos, A.B. Garcia, V. Tishkova, W.S. Bacsa, J.R. Gallagher, J.T. Miller, H. Navas, V. Jourdain, M. Girleanu, O. Ersen, P. Serp, Few layer graphene synthesis on transition metal ferrite catalysts, Carbon, 89 (2015) 350-360.

[92] M. Corrias, B. Caussat, A. Ayral, J. Durand, Y. Kihn, P. Kalck, P. Serp, Carbon nanotubes produced by fluidized bed catalytic CVD: first approach of the process, Chem. Eng. Sci., 58 (2003) 4475-4482.

[93] R. Bacsa, P. Serp, Graphene production method and graphene obtained by said method, in: WO2013093350 A1, France, 2013.

[94] W.S. Hummers, R.E. Offeman, Preparation of Graphitic Oxide, J. Am. Chem. Soc., 80 (1958) 1339-1339.

[95] O. Shenderova, A.M. Panich, S. Moseenkov, S.C. Hens, V. Kuznetsov, H.M. Vieth, Hydroxylated Detonation Nanodiamond: FTIR, XPS, and NMR Studies, The J. Phys. Chem. C, 115 (2011) 19005-19011.

[96] J.L. Figueiredo, Functionalization of porous carbons for catalytic applications, J. Mater. Chem. A, 1 (2013) 9351-9364.

[97] J.L. Figueiredo, M.F.R. Pereira, M.M.A. Freitas, J.J.M. Órfão, Modification of the surface chemistry of activated carbons, Carbon, 37 (1999) 1379-1389.

[98] A. Benyounes, M. Kacimi, M. Ziyad, P. Serp, Conversion of isopropyl alcohol over Ru and Pd loaded N-doped carbon nanotubes, Chin. J. Catal., 35 (2014) 970-978.

[99] R.P. Rocha, J. Restivo, J.P.S. Sousa, J.J.M. Órfão, M.F.R. Pereira, J.L. Figueiredo, Nitrogen-doped carbon xerogels as catalysts for advanced oxidation processes, Catal. Today, 241, Part A (2015) 73-79.

[100] C.G. Silva, J.L. Faria, Photocatalytic oxidation of benzene derivatives in aqueous suspensions: Synergic effect induced by the introduction of carbon nanotubes in a TiO_2 matrix, Appl. Catal. B: Environ., 101 (2010) 81-89.

[101] L.M. Pastrana-Martínez, S. Morales-Torres, S.K. Papageorgiou, F.K. Katsaros, G.E. Romanos, J.L. Figueiredo, J.L. Faria, P. Falaras, A.M.T. Silva, Photocatalytic behaviour of nanocarbon–TiO_2 composites and immobilization into hollow fibres, Appl. Catal. B: Environ., 142–143 (2013) 101-111.

[102] P. Berki, B. Reti, K. Terzi, I. Bountas, E. Horvath, D. Fejes, A. Magrez, C. Tsakiroglu, L. Forró, K. Hernadi, The effect of titania precursor on the morphology of prepared TiO_2/MWCNT nanocomposite materials, Phys. Status Solidi (b), 251 (2014) 2384-2388.

[103] H. Yu, X. Quan, S. Chen, H. Zhao, Y. Zhang, TiO_2–carbon nanotube heterojunction arrays with a controllable thickness of TiO_2 layer and their first application in photocatalysis, J. Photochem. Photobio. A: Chem., 200 (2008) 301-306.

[104] Z. Chen, N. Zhang, Y.-J. Xu, Synthesis of graphene-ZnO nanorod nanocomposites with improved photoactivity and anti-photocorrosion, CrystEngComm, 15 (2013) 3022-3030.

[105] R.R.N. Marques, M.J. Sampaio, P.M. Carrapiço, C.G. Silva, S. Morales-Torres, G. Dražić, J.L. Faria, A.M.T. Silva, Photocatalytic degradation of caffeine: Developing solutions for emerging pollutants, Catal. Today, 209 (2013) 108-115.

[106] S. Morales-Torres, L.M. Pastrana-Martínez, J.L. Figueiredo, J.L. Faria, A.M.T. Silva, Graphene oxide-P25 photocatalysts for degradation of diphenhydramine pharmaceutical and methyl orange dye, Appl. Surf. Sci., 275 (2013) 361-368.

[107] Z. Zheng, B. Huang, X. Qin, X. Zhang, Y. Dai, M.-H. Whangbo, Facile in situ synthesis of visible-light plasmonic photocatalysts M@TiO_2 (M = Au, Pt, Ag) and evaluation of their photocatalytic oxidation of benzene to phenol, J. Mater. Chem., 21 (2011) 9079-9087.

[108] H. Choi, W.T. Chen, P.V. Kamat, Know Thy Nano Neighbor. Plasmonic versus Electron Charging Effects of Metal Nanoparticles in Dye-Sensitized Solar Cells, ACS Nano, 6 (2012) 4418-4427.

[109] M.R. Khan, T.W. Chuan, A. Yousuf, M.N.K. Chowdhury, C.K. Cheng, Schottky barrier and surface plasmonic resonance phenomena towards the photocatalytic reaction: study of their mechanisms to enhance photocatalytic activity, Catal. Sci. Technol., 5 (2015) 2522-2531.

[110] E. Pulido Melián, O. González Díaz, J.M. Doña Rodríguez, G. Colón, J.A. Navío, M. Macías, J. Pérez Peña, Effect of deposition of silver on structural characteristics and photoactivity of TiO_2-based photocatalysts, Appl. Catal. B: Environ., 127 (2012) 112-120.

[111] H.T. Chang, N.-M. Wu, F. Zhu, A kinetic model for photocatalytic degradation of organic contaminants in a thin-film TiO_2 catalyst, Water Res., 34 (2000) 407-416.

[112] J. Marugán, R. van Grieken, C. Pablos, M.L. Satuf, A.E. Cassano, O.M. Alfano, Modeling of a bench-scale photocatalytic reactor for water disinfection from laboratory-scale kinetic data, Chem. Eng. J., 224 (2013) 39-45.

[113] T. Sakata, T. Kawai, K. Hashimoto, Heterogeneous photocatalytic reactions of organic acids and water. New reaction paths besides the photo-Kolbe reaction, J. Phys. Chem., 88 (1984) 2344-2350.

[114] J. Araña, O. González Díaz, M. Miranda Saracho, J.M. Doña Rodríguez, J.A. Herrera Melián, J. Pérez Peña, Photocatalytic degradation of formic acid using Fe/TiO_2 catalysts: the role of Fe3+/Fe2+ ions in the degradation mechanism, Appl. Catal. B: Environ., 32 (2001) 49-61.

[115] N. Barka, M. Abdennouri, A. Boussaoud, A. Galadi, M. Baâlala, M. Bensitel, A. Sahibed-Dine, K. Nohair, M. Sadiq, Full factorial experimental design applied to oxalic acid photocatalytic degradation in TiO_2 aqueous suspension, Arabian J. Chem., 7 (2014) 752-757.

[116] B. Long, J. Huang, X. Wang, Photocatalytic degradation of benzene in gas phase by nanostructured $BiPO_4$ catalysts, Prog. Nat. Sci.: Mater. Inter., 22 (2012) 644-653.

[117] K. Mondal, S. Bhattacharyya, A. Sharma, Photocatalytic Degradation of Naphthalene by Electrospun Mesoporous Carbon-Doped Anatase TiO_2 Nanofiber Mats, Ind. Eng. Chem. Res., 53 (2014) 18900-18909.

[118] A.M.T. Silva, E. Nouli, Â.C. Carmo-Apolinário, N.P. Xekoukoulotakis, D. Mantzavinos, Sonophotocatalytic/H_2O_2 degradation of phenolic compounds in agro-industrial effluents, Catal. Today, 124 (2007) 232-239.

[119] A.M.T. Silva, E. Nouli, N.P. Xekoukoulotakis, D. Mantzavinos, Effect of key operating parameters on phenols degradation during H_2O_2-assisted TiO_2 photocatalytic treatment of simulated and actual olive mill wastewaters, Appl. Catal. B: Environ., 73 (2007) 11-22.

[120] C.G. Silva, J.L. Faria, Photocatalytic oxidation of phenolic compounds by using a carbon nanotube-titanium dioxide composite catalyst, ChemSusChem, 3 (2010) 609-618.

[121] S. Ahmed, M.G. Rasul, R. Brown, M.A. Hashib, Influence of parameters on the heterogeneous photocatalytic degradation of pesticides and phenolic contaminants in wastewater: A short review, J. Environ. Man., 92 (2011) 311-330.

[122] E.P. Melián, O.G. Díaz, J. Araña, J.M.D. Rodríguez, E.T. Rendón, J.A.H. Melián, Kinetics and adsorption comparative study on the photocatalytic degradation of o-, m- and p-cresol, Catal. Today, 129 (2007) 256-262.

[123] L.M. Pastrana-Martínez, S. Morales-Torres, V. Likodimos, J.L. Figueiredo, J.L. Faria, P. Falaras, A.M.T. Silva, Advanced nanostructured photocatalysts based on reduced graphene oxide-TiO_2 composites for degradation of diphenhydramine

pharmaceutical and methyl orange dye, Appl. Catal. B: Environ., 123-124 (2012) 241-256.

[124] A.R. Khataee, M.B. Kasiri, Photocatalytic degradation of organic dyes in the presence of nanostructured titanium dioxide: Influence of the chemical structure of dyes, J. Mol. Catal. A: Chem., 328 (2010) 8-26.

[125] C. Tang, V. Chen, The photocatalytic degradation of reactive black 5 using TiO2/UV in an annular photoreactor, Water Res., 38 (2004) 2775-2781.

[126] Q.I. Rahman, M. Ahmad, S.K. Misra, M. Lohani, Effective photocatalytic degradation of rhodamine B dye by ZnO nanoparticles, Mater. Letters, 91 (2013) 170-174.

[127] R.R.N. Marques, M.J. Sampaio, P.M. Carrapiço, C.G. Silva, S. Morales-Torres, G. Dražić, J.L. Faria, A.M.T. Silva, Photocatalytic degradation of caffeine: Developing solutions for emerging pollutants, Catal. Today, 209 (2013) 108-115.

[128] T.E. Doll, F.H. Frimmel, Kinetic study of photocatalytic degradation of carbamazepine, clofibric acid, iomeprol and iopromide assisted by different TiO_2 materials – determination of intermediates and reaction pathways, Water Res., 38 (2004) 955-964.

[129] D.R. de Figueiredo, U.M. Azeiteiro, S.M. Esteves, F.J.M. Gonçalves, M.J. Pereira, Microcystin-producing blooms—a serious global public health issue, Ecotox. Environ. Saf., 59 (2004) 151-163.

[130] P. Rao, N. Gupta, A. Bhaskar, R. Jayaraj, Toxins and bioactive compounds from cyanobacteria and their implications on human health, J. Environ. Biol., 23 (2002) 215-224.

[131] J. Westrick, D. Szlag, B. Southwell, J. Sinclair, A review of cyanobacteria and cyanotoxins removal/inactivation in drinking water treatment, Anal. Bioanal. Chem., 397 (2010) 1705-1714.

[132] L. A. Lawton, P. K. J. Robertson, Physico-chemical treatment methods for the removal of microcystins (cyanobacterial hepatotoxins) from potable waters, Chem. Soc. Rev., 28 (1999) 217-224.

[133] H. Choi, M.G. Antoniou, M. Pelaez, A.A. de la Cruz, J.A. Shoemaker, D.D. Dionysiou, Mesoporous Nitrogen-Doped TiO_2 for the Photocatalytic Destruction of the Cyanobacterial Toxin Microcystin-LR under Visible Light Irradiation, Environ. Sci. Technol., 41 (2007) 7530-7535.

Part II

Chapter 2

Photocatalytic TiO_2 films for water treatment

Glass Raschig rings are coated with different types of TiO_2, namely Aeroxide® TiO_2 P25 (EP), anatase TiO_2 from Sigma-Aldrich (SA), and TiO_2 obtained from a sol-gel procedure. The efficiency, stability and the number of TiO_2 layers deposited on the Raschig rings is analyzed using degradation of phenol as model reaction, in a recirculation reactor operating under simulated solar light irradiation.

The efficiency of the photocatalytic process using glass Raschig rings coated with TiO_2–EP is evaluated by comparing the first order reaction rate (*r*) as a function of several operation parameters. A kinetic model is developed for the determination of *r* as a function of the various operation parameters.

The study is extended to the treatment of a synthetic effluent consisting of a solution with a mixture of seven phenolic derivatives. A relationship between the extent of photocatalytic degradation and the activating/deactivating nature of the aromatic ring substituents is proposed.

This chapter is based on the following articles:

M.J. Sampaio, C.G. Silva, A.M.T. Silva, V.J.P. Vilar, R.A.R. Boaventura, J.L. Faria, Photocatalytic activity of TiO_2-coated glass Raschig rings on the degradation of phenolic derivatives under simulated solar light irradiation. Chem. Eng. J. 224 (2013) 32-38, reproduced by permission of Elsevier.

M.J. Sampaio, C.G. Silva, A.M.T. Silva, J.L. Faria, Kinetic modeling for the photocatalytic degradation of phenol using TiO_2-coated glass Raschig rings under simulated solar light. J. Chem. Technol. Biotechnol. 91 (2016) 346-352, reproduced by permission of Wiley.

2.1. Introduction

Heterogeneous photocatalysis is considered as a very important tool in the development of sustainable technologies for environmental protection including clean energy production, water and air treatment [1-3]. The photocatalytic water purification process has earned increasing attention due to its effectiveness in degrading and mineralizing a wide variety of organic and inorganic pollutants [4-6], and because it meets the requirements of sustainable process development when combined with solar energy.

Titanium dioxide (TiO_2) has been found to be capable of decomposing a wide variety of contaminants in wastewater. In most of the photocatalytic applications, TiO_2 is used as a suspended powder in slurry reactors, which implies a post-separation step, hindering the application of the process in continuous flow systems. A technological approach to overcome this limitation is to immobilize TiO_2 particles as films on solid substrates, such as stainless steel, glass, plastic or fabrics [7-9].

In the present chapter, the use of TiO_2–coated glass Raschig rings for photocatalytic water treatment is explored. The effect of several parameters on the photoefficiency of the process, such as the type of TiO_2, the number of catalyst layers and film robustness, are evaluated under simulated solar light. The objective is the optimization of operation conditions for maximizing the efficiency of the photocatalytic process. The effect of other operation parameters such as the catalyst load, initial concentration of phenol, irradiance intensity and concentration of hydrogen peroxide (which is used as oxidant agent) is also evaluated with the aim of develop a kinetic model that could accurately predict the efficiency of the process in a wide range of conditions. In addition, the study was extended to the photocatalytic treatment of a synthetic solution containing seven aromatic compounds, which are typically found in actual phenolic effluents (*e.g.*, olive oil mills [10, 11], cork [12], pulp and paper industries [13]).

2.2. Experimental

2.2.1. Reagents and methods

Aeroxide® TiO_2 P25 (~ 80% anatase:20% rutile) powder was supplied by Evonik. Ethanol (C_2H_5OH, 99.5%) was obtained from Panreac. Titanium (IV) butoxide ($Ti[O(CH_2)_3CH_3]_4$, 97%), nitric acid ($HNO_3 \geq 65\%$), hydrofluoric acid ($HF \geq 40\%$) and phenol ($C_6H_5OH \geq 99$ %), protocatechuic acid ($C_7H_6O_4 \geq 98\%$), benzoic acid

($C_7H_6O_2 \geq 99\%$), 4-hydroxyphenethyl alcohol ($HOC_6H_5CH_2CH_2OH \geq 99\%$) and titanium dioxide anatase were purchased from Sigma-Aldrich. Gallic acid monohydrate ($C_7H_6O_5.H_2O \geq 98\%$), 4-hydroxybenzoic acid ($C_7H_6O_3 \geq 99\%$) and 4-methoxyphenol ($CH_3OC_6H_4OH \geq 98\%$) were purchased from Fluka. The chemical formulae of the phenolic derivatives are shown in Scheme 2.1. The Folin–Ciocalteu's phenolic reagent and sodium carbonate ($Na_2CO_3 \geq 99.0\%$), were used for the determination of total phenolic content, sodium phosphate (NaH_2PO_4), phosphoric acid ($H_3PO_4 \geq 85\%$) and acetonitrile ($C_2H_3N \geq 99.8\%$) for high performance liquid chromatography, were supplied by Sigma-Aldrich. Ultrapure water was produced in a Direct-Q Millipore system.

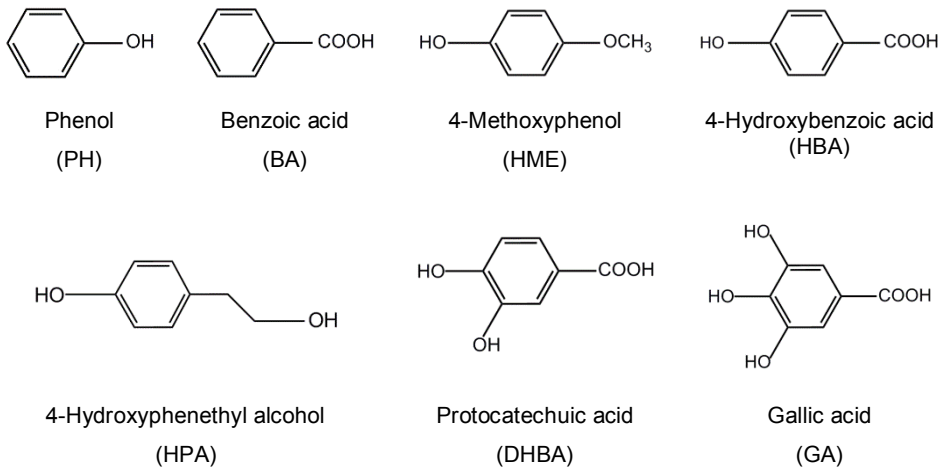

Phenol (PH) | Benzoic acid (BA) | 4-Methoxyphenol (HME) | 4-Hydroxybenzoic acid (HBA)

4-Hydroxyphenethyl alcohol (HPA) | Protocatechuic acid (DHBA) | Gallic acid (GA)

Scheme 2.1 – Chemical formulae of phenolic derivatives.

2.2.2. Preparation and characterization of the films

Glass rings (diameter = 7 mm, length = 8 mm) were cleaned with distilled water containing an anionic detergent and subsequently washed exhaustively with milli-Q water and sonicated for 15 min. Then, they were immersed in acetone and sonicated for another 15 min. The procedure was repeated using isopropanol. Finally, the rings were heated up to 100 ºC to dryness.

Three different types of TiO_2-coated glass rings were used in this study, *i.e.*, prepared with three different TiO_2 materials: Aeroxide®TiO_2 P25 from Evonik (EP); anatase TiO_2 obtained from Sigma-Aldrich (SA); and anatase TiO_2 obtained by a sol-gel method (SG). For the sol-gel procedure, an ethanol:titanium-butoxide 50:35 molar ratio solution was added drop wise to a water:ethanol:citric acid 50.0:60.8:0.36 molar ratio solution and mixed for 30 min [14]. The glass rings were immersed by

dip-coating in this sol at a rate of 50 mm min^{-1} and withdrawn at the same rate. Finally, the films were calcined at 450 ºC for 2 h. This procedure was repeated several times to obtain samples with increasing thickness. The calcination treatment was performed after each deposition.

Glass rings coated with commercial TiO_2 were prepared by immersion in a 5% w/V titanium dioxide-ethanol suspension after 30 min ultrasound treatment of the TiO_2 powder [15]. Each layer was dried at 100 ºC for 1 h and the whole films were calcined at 450 ºC for 2 h.

The different TiO_2–coated glass rings were labelled as XX-YL, where XX = EP, SA or SG stands for the type of TiO_2 and Y is the number of TiO_2 layers (L).

A Quantachrome NOVA 4200e multi-station apparatus was used for the determination of the Brunauer–Emmett–Teller specific surface area (S_{BET}), Barrett-Joyner-Halenda (BJH) pore size distribution, and pore volume and porosity of the TiO_2 materials scraped from the films. All samples were first degassed in vacuum for 3 h at 150 ºC before analysis. The S_{BET} was calculated from the nitrogen adsorption data in the relative pressure range from 0.05 to 0.15.

Observations of the surface morphology and roughness of the films were performed using scanning electron microscopy (SEM) FEI Quanta 400FEG ESEM/EDAX Genesis X4M instrument. The SEM apparatus was equipped with a special multiple sample holder, in which the broken glass slides were vertically positioned to observe and measure the cross-section of the catalyst films by using SEM instrument software. X-ray diffraction (XRD) analysis was carried out in a PANalytical X'Pert MPD equipped with a X'Celerator detector and secondary monochromator (Cu *K*α λ = 0.154 nm, 50 kV, 40 mA; data recorded at a 0.017° step size, 100 s/step). Rietveld refinement with Powder Cell software (CCP14, UK) was used to identify the crystallographic phases present and to calculate the crystallite size from the XRD diffraction patterns. The DR UV–Vis spectra of the powder solids were measured on a Jasco V-560 UV–Vis spectrophotometer, equipped with an integrating sphere attachment (JASCO ISV-469). The spectra were recorded in diffuse reflectance mode and transformed by the instrument software (JASCO) to equivalent absorption Kubelka–Munk units.

2.2.3. Photocatalytic experiments

The photocatalytic degradation of phenol in aqueous solutions was performed under simulated solar light using a Solarbox 1500e (CO.FO.MEGRA, Milano). The

irradiation source consisted in a 1500 W xenon lamp equipped with a cut-off soda-lime glass UV filter (λ > 290 nm) with infrared reflection coating, to simulate outdoor exposure. The nominal irradiation power was allowed to vary between 250 and 1000 W m^{-2} by the apparatus control system, corresponding to light intensities between 18.5 - 58.6 mW cm^{-2}, respectively. Light intensity (*I*) reaching the photocatalytic reactor was determined by using a UV-Vis spectroradiometer (USB2000+, OceanOptics, USA). The reactions took place under natural pH ($pH_{nat.,phenol}$ = 6.1). A glass cylindrical reactor (19 mm of internal diameter and 33 mm length) with 8.2 mL of useful volume was packed with nine glass Raschig rings. The volume of solution introduced in the reactor packed with the glass rings was of 7.2 mL.

The reactor (a) was placed inside of the solar simulator (b) in a fixed position at the center of the irradiation system (Scheme 2.2). In a typical experiment the phenol solution was loaded in a 50 mL reservoir (c) and continuously circulated in the reactor using a peristaltic pump (d) at constant flow rate (*Q*). The solution was magnetically stirred and continuously saturated with air.

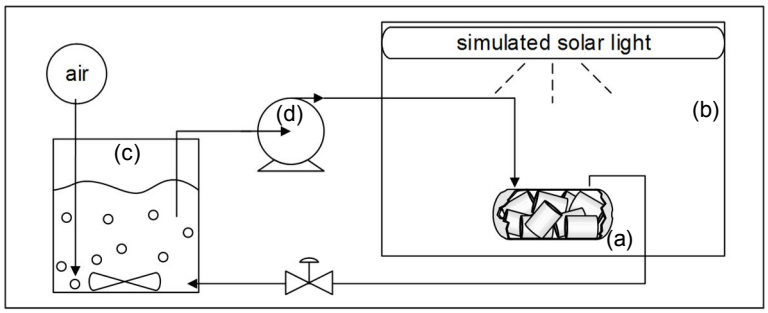

Scheme 2.2 – Experimental set-up used in the photocatalytic experiments.

Before switching on the illumination, the phenol solution was passed through the reactor to establish an adsorption-desorption equilibrium. The first sample was taken from the reservoir at the end of the dark adsorption period (30 min), just before switched on the light, to determine the concentration of the compound in bulk solution, which was thereafter considered as the initial concentration ($[C_6H_5OH]_0$). Then, the solution was irradiated with simulated solar light typically for 4 hours and samples were then withdrawn regularly from the reservoir. Triplicate points were used and mean values were quoted as results. The standard deviation of the experiments never exceeded 4%. The same procedure was used in the experiments performed with the solution containing a mixture of the seven aromatic compounds with a concentration of 20 mg L^{-1} each, but the irradiation was carried out for 8 hours.

2.2.4. Analytic techniques

The concentration of phenol was analyzed by high performance liquid chromatography (HPLC) using a Hitachi Elite LaChrom apparatus equipped with a L-2450 diode array detector. The stationary phase consisted in a Purospher Star RP-18 endcapped column (250 mm×4.6 mm, 5 μm particles) working at room temperature. The method starts with an equilibrated mixture of water (A):methanol (B) (70:30) at a flow rate of 1 mL min^{-1} followed by a linear gradient step to A:B (37:63) in 20 min; finally the initial conditions were re-established in a 1 min gradient step and the A:B (70:30) mixture was isocratically eluted for 7 min. The concentration of the individual compounds in the mixture of phenolic derivatives was followed using an optimized gradient elution method at a flow rate of 1 mL min^{-1}. Firstly, the column was equilibrated with an A:B (10:90) mixture of 1% acetic acid and 0.5% acetonitrile in methanol (A) and 1% acetic acid in water (B). Then the following program was used: isocratic elution for 15 min followed by a linear gradient run to A:B (60:40) in 27 min and finally to A:B (10:90) in 5 min.

The synthetic solution samples were also analyzed colorimetrically in terms of their total phenolic (TPh) content using the Folin–Ciocalteu method [16], as adapted by *Silva et al.* [11]. Briefly, 20 μL of a sample were introduced in a cuvette and 100 mL of the Folin–Ciocalteu reagent were added together with 1.58 mL of water. After 5 min, 300 mL of a saturated sodium carbonate solution were added and the resulting solution was left in the dark for 2 h. The absorbance was measured at 750 nm using a UV-Vis Jasco V-560 spectrophotometer. A calibration curve was prepared using gallic acid at different concentrations; therefore, the TPh values are reported as gallic acid equivalent.

Total organic carbon (TOC) analysis was performed in a Shimadzu TOC-5000A apparatus at the end of each reaction.

2.3. Influence of TiO_2 nature and stability of the films

2.3.1. Characterization of the TiO_2 films

XRD analysis of the TiO_2 films (Figure 2.1) revealed that, as expected, SA and SG films are constituted by anatase crystallites while EP is formed by 83% of anatase and 17% rutile. The crystallite dimensions were obtained from the XRD patterns, varying from 20 nm in the case of SG and 51 nm or 30 nm (average size) for SA or EP, respectively (Table 2.1).

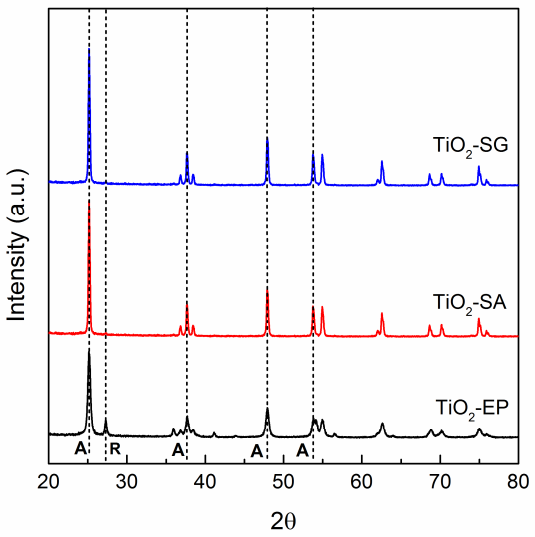

Figure 2.1 – XRD analysis of the TiO_2 materials.

Table 2.1 – Crystalline and textural properties and thickness of the films prepared with 3 layers of TiO_2.

	EP-3L	SA-3L	SG-3L
Crystalline phase (% vol.)	A(83%) / R(17%)	A(100%)	A(100%)
Crystal size (nm)	27(A) / 38(R)	51	20
S_{BET} (m^2/g)	53	12	46
Pore volume[a] (cm^3/g)	0.3534	0.0485	0.26
Porosity[b] (%)	57.39	15.94	49.63
Film weight (mg)	0.70	0.55	0.48
Film thickness[c] (nm)	1420	570	834

A: anatase; R: rutile.
[a] BJH desorption cumulative volume of pores.
[b] Based on pore volume and 3.79 g/cm^3 and 4.13 g/cm^3 of anatase and rutile average densities, respectively. Porosity (%) = pore volume (cm^3/g)/[(pore volume (cm^3/g) + solid catalyst volume without pore (cm^3/g)] × 100%; solid catalyst volume without pore (cm^3/g)=1/density of the solid catalyst volume without pore.
[c] Calculation based on pore volume and average film weight with average density of 3.79 g/cm^3 for anatase and 4.13 g/cm^3 for rutile. Film thickness = film weight (g) × [pore volume (cm^3/g) + solid catalyst volume without pore (cm^3/g)]/area of the coated support (cm^2).

SEM images show continuous EP and SA films with rough surface morphology (Figures 2.2a and 2.2d, respectively), while the presence of TiO_2 aggregates was observed for SG films (Figure 2.2f). A granular texture was observed at the surface of the films, being attributed to the spheroidal shape of the TiO_2 particles. The thickness of the 3L films was calculated based on the porosity and the density of anatase/rutile

phases [17, 18] (Table 2.1). EP films were the thicker with 1.420 μm, while TiO_2-3L films of 570 nm and 834 nm were obtained for SA and SG, respectively.

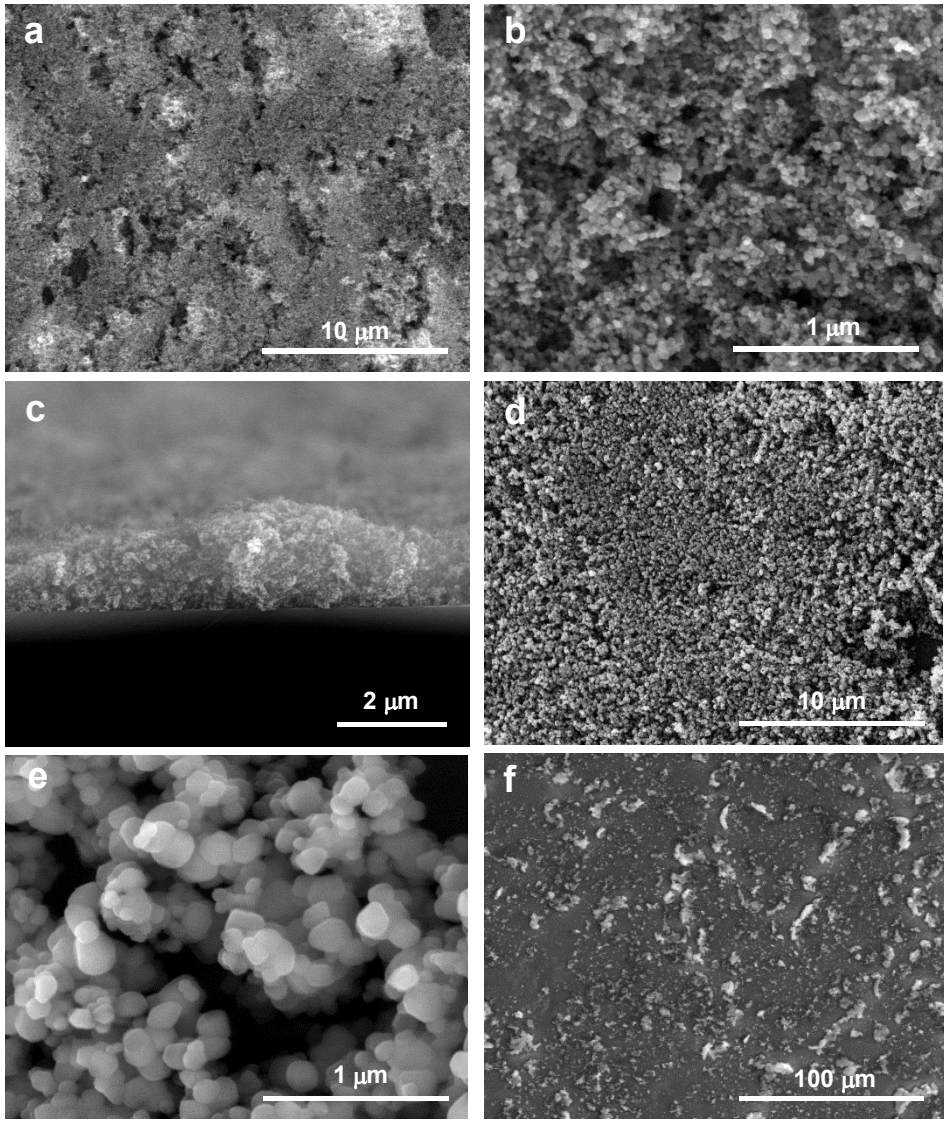

Figure 2.2 – SEM micrographs of EP-3L surface (a and b) and cross-section (c), SA-3L surface (d and e) and SG-3L (f).

The calculated thickness of EP-3L is in good agreement to the determined by cross-section SEM image (Figure 2.2c). In the case of SA-3L and SG-3L, thickness determination by SEM may be affected by larger error because of the higher roughness of the films and also to the order of magnitude in the nanometer range. This difference in the thickness of the films produced with the same number of TiO_2 layers can be attributed to the different viscosity of the solutions used in the dip-coating

preparation process. It was also observed by SEM analysis that, as expected, the thickness of the films increased with the number of layers. Nevertheless, for the films prepared with 4 and 5 layers it was observed an increase in the roughness of the films due to particle aggregation. The strength of adhesion of the TiO_2 films was loosely assessed following an adaptation of the crosshatch adhesion test [19].

In the case of EP films up to 3L, good adhesion and resistance to scratch was observed. In the case of the rings coated with 4L and 5L it was noticeable that some particles were easily released from the films. In the case of SA and SG films, adhesion problems were detected and, in some cases it was noticed that some particles detached from the films.

2.3.2. Efficiency of 3-layer films in phenol degradation

The photochemical degradation of phenol was carried out at first, in the absence of catalyst using simulated solar light. Under these conditions, phenol concentration decreased 22% after 4 h irradiation (Figure 2.3).

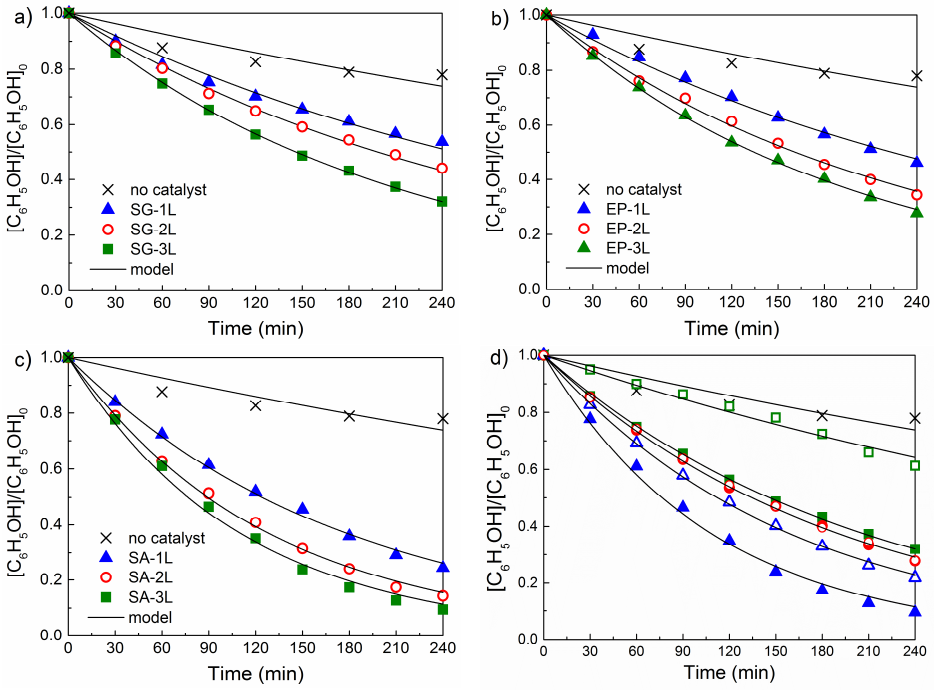

Figure 2.3 – Effect of the number of TiO_2 layers on the degradation of phenol using SG (a), EP (b) and SA (c) films, respectively; phenol degradation during photolytic (-×-) and photocatalytic reactions using glass Raschig rings coated with 3 layers of SG (-■-), EP (-●-) and SA (-▲-) with open symbols corresponding to reutilization tests using SG-3L, EP-3L and SA-3L, (-□-), (-○-) and (-△-), respectively (d).

The efficiency in the photocatalytic removal of phenol by TiO_2 films prepared with different types of TiO_2 and a variable number of layers (up to 3) was measured. Experiments using SG (Figure 2.3a), EP (Figure 2.3b) and SA (Figure 2.3c) with 1, 2 or 3 layers, show that phenol degradation increases with the number of layers, regardless the kind of TiO_2 tested. Final phenol conversions after 240 min of 46, 56 and 68 % for SG, 53, 65 and 72% for EP or 75, 86 and 90 % for SA, were achieved using one, two or three layers, respectively. Among all materials tested, the best photocatalytic efficiency was obtained when using three layers of SA.

2.3.3. Robustness of 3-layer films

In order to assess the robustness of the TiO_2 films, reutilization tests were performed using glass rings coated with the three layers (Figure 2.3d). The activity of SG–coated rings markedly decreases, resulting in a final phenol degradation of 68% with the fresh film and 39 % after reuse (total decrease of 43%). A loss in the photocatalytic activity was also observed for SA–coated rings, the final phenol degradation decreasing from 90 to 78 % (total decrease of 13%), and reaching that observed for EP–coated rings which were the only rings whose maintained their activity in reutilization tests (variance of ± 0.3 %).

The results clearly show that the highest efficiency with fresh TiO_2–coated glass rings was obtained for SA films after reutilization; a decrease in the activity of these films was observed. This can be explained by loss of the catalyst powder from the glass rings. Simple visualization and subsequent UV-Vis spectroscopic analysis of the samples before and after the reaction (Figure 2.4), confirmed this.

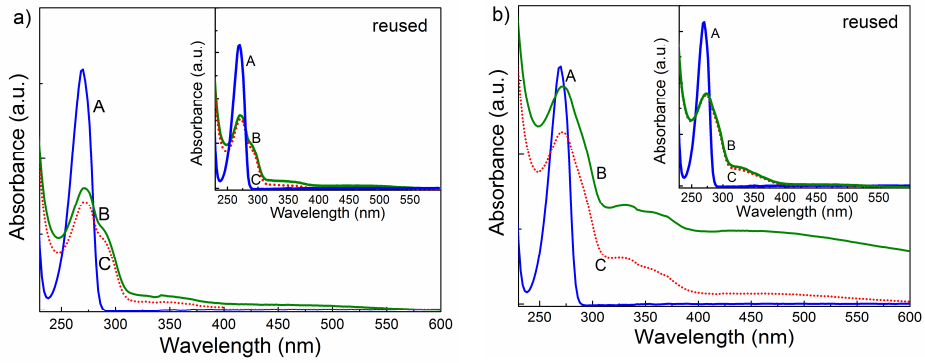

Figure 2.4 – UV-Vis spectra of the initial phenol solution (A), final solution after 4 h of irradiation (B) and final solution after centrifugation (C) for photocatalytic experiments using fresh EP-3L (a) and SA-3L (b) materials. Inset: UV-Vis spectra of samples obtained with reused films.

As expected, phenol is efficiently converted by EP-3L from the initial solution (Figure 2.4a A) after 240 min of irradiation (Figure 2.4a B). The spectrum of the final solution obtained with fresh EP-3L (Figure 2.4a B), is practically coincident with the one recorded after centrifugation of that sample (Figure 2.4a C) indicating that TiO_2 particles were not suspended. If this was the case a decrease in the absorption for $\lambda < 400$ nm (TiO_2 absorption edge) would be expected.

The stability of the photocatalytic film is confirmed by the spectra taken in reutilization experiments (inset Figure 2.4a). These stability results are in agreement with the matching of the photocatalytic activity obtained with fresh and reused films.

When using fresh SA-3L, the spectrum of the sample taken at the end of the photocatalytic reaction Figure 2.4b B shows a broad absorption in the 225-600 nm spectral range. After centrifugation, a significant decrease in the absorption was observed (Figure 2.4b C). These results suggest the presence of a considerable amount of catalyst particles in the final solution that may result from disaggregation of the film. The broad absorbance observed at wavelength higher than 400 nm, could be due to either the presence of reaction by products or intermediates and, most probably, to very fine particles released in the initial cycles, which contribute to light dispersion.

By contrast, no particle disaggregation seems to occur with the reused film, as confirmed by the similar spectra obtained before (Figure 2.4b B inset) and after (Figure 2.4b C inset) the centrifugation of the final sample.

It should be noticed that when preparing the films by dip-coating, the suspension of EP in ethanol was more homogeneous than the suspension of SA, *i.e.* EP seems to disperse uniformly into the solution, while for SA sedimentation of SA particles was observed after the first coating, which may lead to a non-homogeneous TiO_2 layer and ultimately to particle disaggregation during the photocatalytic experiments.

2.3.4. Effect of photocatalytic immobilization

For comparison purposes, reactions using the same volume, phenol concentration, aeration and illumination conditions, in the presence 1 g L^{-1} of TiO_2 in powder form (in place of TiO_2–coated Raschig rings) were performed in a stirred reactor. Total phenol removal was achieved after 1 h irradiation using both EP and SA photocatalysts. Nevertheless, faster degradation was observed for EP (80% phenol removal at 30 min of reaction contrasting with 60% removal obtained with SA at the same period of time).

Regarding SG, merely 30% of the initial phenol content was eliminated after 1 h of reaction.

It is recognized that anatase crystal phase show, in most cases, better activity than rutile phase. Nevertheless, EP (the benchmark catalyst for photocatalytic reactions), consisting of a mixture of anatase and rutile (Table 2.1), is for many reactions more active than the pure crystalline anatase phase. This enhanced activity is normally attributed to the increased efficiency of the electron–hole separation due to the multiphase nature of the particles [20, 21]. In the case of the reactions using immobilized catalysts it was observed that, even maintaining the number of TiO_2 layers, different porosity, film weight and thickness were obtained for SA, EP and SG (Table 2.1). EP-3L presents higher surface area, porosity and thickness and was mechanically more stable than SA-3L film, all these factors accounting for the good performance of the film.

2.3.5. Phenol photocatalytic degradation

Using the different TiO_2 films with 3 layers, the HPLC analysis performed during the photocatalytic runs revealed that hydroquinone (HQ; 4-hydroxyphenol), catechol (CT; 2-hydroxyphenol) and benzoquinone (BQ; 1,4-benzoquinone) are the main products of phenol degradation (Figure 2.5), but in particular the concentration of catechol significantly change depending on the type of TiO_2 tested.

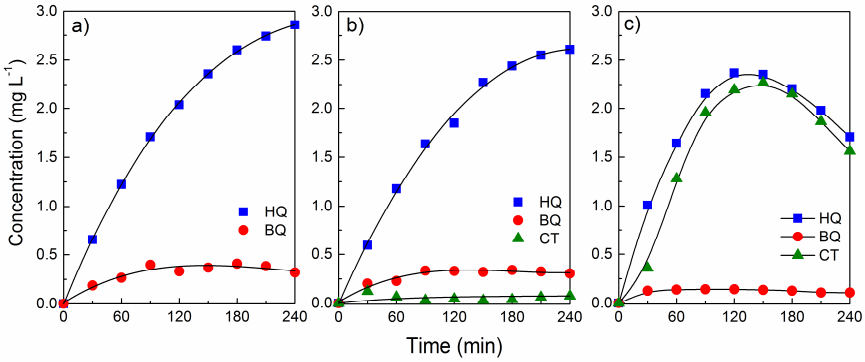

Figure 2.5 – Concentration profiles for hydroquinone (HQ), benzoquinone (BQ and catechol (CT) for the photocatalytic degradation of phenol using SG-3L (a), EP-3L (b) and SA-3L (c).

In general, these results are in agreement with the activation/deactivation properties of benzene substituent groups. Photocatalytic oxidation of aromatics containing electron donor groups, which is the case of –OH group in phenol molecule, generates *para* (HQ) and *ortho* (CT) mono-hydroxy derivatives as primary intermediates, by $HO^{\bullet}$ attack of the phenol molecule. BQ is formed by oxidation of

hydroquinone (redox equilibrium). Independently from the type of TiO_2 present in the film, HQ was always found as the intermediate with the highest concentration, while low amounts of BQ were detected in all the reactions. In the particular case of CT, a distinct behavior was observed for the reactions performed using the different films: it was detected at negligible concentrations for SG-3L, at very low concentrations (even lower than BQ) for EP-3L and at concentrations similar to those of HQ for SA-3L film. These results indicate that CT was formed and accumulated in the solution when the SA-3L film was used. In fact, lower total organic carbon (TOC) removal was achieved for SA-3L (22%) at the end of the photocatalytic experiments, when comparing to SG-3L (29%) and EP-3L (28%), which indicate that in the case of SA-3L, phenol is being more efficiently converted, however the intermediate's degradation being slower.

2.3.6. Increasing the number of layers

The effect of increasing the number of EP layers (from one to five) on the photocatalytic degradation of phenol in reutilization tests is shown in Figure 2.6 for fresh and reused EP–coated Raschig rings.

The photocatalytic activity increased with the number of TiO_2 layers, even when the number of layers was higher than three. However, when reutilization tests were performed on glass rings coated with more than three layers, a significant loss in photocatalytic activity was observed. As the thickness of the overall TiO_2 coating increases, particle disaggregation is more likely to occur. This disaggregation was confirmed by UV-Vis analysis of the samples taken before and after centrifugation. Even after reused for 2 times, the same phenol removal was obtained in experiments with the EP-3L film (Appendix, Figure A.1) and the respective stability confirmed.

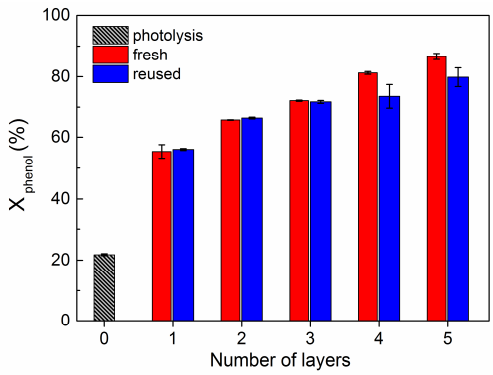

Figure 2.6 – Effect of the number of EP layers on the phenol removal using fresh and reused films and during photolytic reaction as reference.

This chapter continues with a kinetic study of the photocatalytic process. The effect of several key operational parameters, such as initial concentration, pH solution, flow rate, light intensity, number of coated glass Raschig rings and the effect of an extra oxidant to increase the generation of hydroxyl radicals on phenol's degradation efficiency will be discussed in the following. The ultimate objective was the development of a kinetic model that could accurately predict the conversion for the process in a wide range of operating conditions.

2.4. Influence of operation parameters on the photocatalytic degradation of phenol

Heterogeneous photocatalytic reactions are influenced by several parameters, such as catalyst load, concentration of the substrate, presence of oxidants and irradiation intensity. The effect of different operation parameters in the photocatalytic efficiency of phenol was studied in order to optimize the performance and to fully characterize the reaction system. The previous results revealed that TiO_2–coated glass Raschig rings are photocatalytic active for phenol degradation in aqueous solution. The degradation of phenol follows a pseudo-first order kinetic rate model described by:

$$r = \frac{-\mathrm{d[PhOH]}}{\mathrm{dt}} = k_{app}[\mathrm{PhOH}] \tag{2.1}$$

where [PhOH] corresponds to phenol concentration in the course of reaction, k_{app} is the apparent first order kinetic constant and t is the reaction time. The integrated form of Eq. (2.1) gives:

$$\frac{[\mathrm{PhOH}]}{[\mathrm{PhOH}]_0} = \mathrm{e}^{-k_{app}\mathrm{t}} \tag{2.2}$$

where $[\mathrm{PhOH}]_0$ is the phenol concentration for t = 0. The values of $k_{app,}$ for the photocatalytic reactions were obtained by non-linear fitting of Eq. (2.2) to the experimental data. The influence of operational parameters in the kinetics of the photocatalytic degradation reactions was evaluated by comparing the respective reaction rate (r) calculated from Eq. (2.1) using phenol concentration at the moment the irradiation is started ($[\mathrm{PhOH}]_0$).

The stability of the aqueous phenol in the dark and under simulated solar light irradiation was checked. No degradation of phenol under dark conditions was

observed. For the direct photochemical reaction, a 22% phenol removal after 4h of irradiation and a reaction rate of 2.52×10^{-2} mg L^{-1} min^{-1} were obtained. In this case, the abatement of phenol concentration is attributed to residual absorption of this compound in the wavelength range 290-340 nm.

2.4.1. Catalyst load

The optimization of the amount of catalyst used in a photocatalytic reaction is very important to avoid using a useless excess of catalyst and to ensure a total absorption of efficient photons. It has been extensively demonstrated in previous studies that the rate of the photocatalytic reaction is strongly influenced by the amount of catalyst in the reaction media. Normally, the reaction rate increases proportionally to the mass of catalyst as this behavior indicates a true heterogeneous catalytic regime. However, above a certain mass of catalyst, the reaction rate levels off and becomes independent of the catalyst load. This limit corresponds to the maximum amount of catalyst at which all particles are totally illuminated and depends on the geometry and on the working conditions of the photoreactor. Furthermore, excessive catalyst charge may produce a screening effect resulting in a decrease on the efficiency of the process.

In the present study, since the catalyst was immobilized in Raschig rings, the mass of catalyst was varied by changing the number of TiO_2–coated rings (*N*) inside of the reactor, between 3 and 9 (the maximum number the reactor can hold). A total of 9 rings was maintained for all the reactions by using uncoated rings, so the hydrodynamic behavior and light diffusion conditions on the reactor can be maintained. As shown in Figure 2.7, the reaction rate increased proportionally with the number of coated rings, confirming the heterogeneous nature of the photocatalytic process.

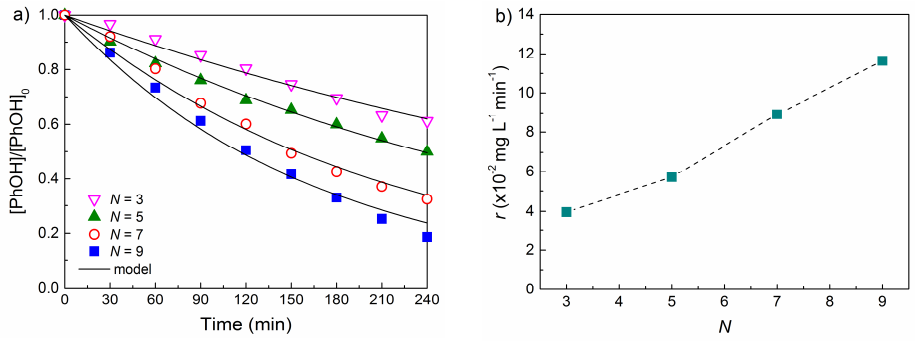

Figure 2.7 – Effect of the number of TiO_2 coated Raschig rings (*N*) on the kinetics of the photocatalytic degradation of phenol (a); rate of phenol degradation (*r*) as a function of the number of TiO_2 coated Raschig rings (b). (Q = 17 mL min^{-1}; $[PhOH]_0$ = 20 mg L^{-1}; I = 30.9 mW cm^{-2}; $[H_2O_2]$ = 0 mmol L^{-1}).

It can be desirable to further increase the catalyst load for determining the optimal conditions. Though, photocatalytic runs using higher amounts of catalyst would be only possible by increasing (i) the number of TiO_2–coated rings or (ii) the number of catalyst layers in the TiO_2 coatings. The first approach is not possible to accomplish in the present system since 9 is the maximum number of rings that can be allocated in the reactor. Yet, it was previously found that catalyst disaggregation problems occur when more than 3 TiO_2 layers are used in Raschig ring coatings. Thus, the work was proceeded using 9 TiO_2–coated Raschig rings.

2.4.2. Phenol concentration

A comparative effect of initial phenol concentration ($[PhOH]_0$) on its degradation rate was studied in the range 10 - 50 mg L^{-1} (Figure 2.8a). The reaction rate obtained for $[PhOH]_0$ = 10 mg L^{-1} was 7.87×10^{-2} mg L^{-1} min^{-1} while for the higher $[PhOH]_0$ tested (50 mg L^{-1}), a reaction rate of 12.10×10^{-2} mg L^{-1} min^{-1} was achieved. Nevertheless, above a phenol concentration of 30 mg L^{-1} (r = 11.98×10^{-2} mg L^{-1} min^{-1}), r reached a plateau, which indicates that all catalytic sites are occupied and the reaction rate becomes independent of the phenol concentration (Figure 2.8b).

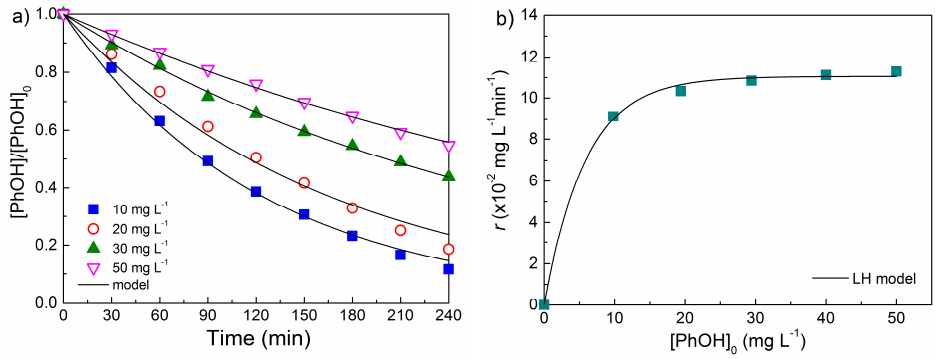

Figure 2.8 – Effect of initial phenol concentration ($[PhOH]_0$) on the kinetics of the photocatalytic degradation of phenol (a); rate of phenol degradation (r) as a function of $[PhOH]_0$ (b). (Q=17 $mLmin^{-1}$; N = 9; I = 30.9 mW cm^{-2}; $[H_2O_2]$ = 0 mmol L^{-1}).

For photocatalytic reactions using powder catalysts in slurry reactors, the dependency of the reaction rate on the concentration of the target molecule is generally described by the Langmuir–Hinshelwood (LH) kinetic model [22], expressed by:

$$r = k_{LH}\frac{K_{LH}[\mathrm{PhOH}]}{1+K_{LH}[\mathrm{PhOH}]+\sum_i K_i[Int.]} \qquad (2.3)$$

where k_{LH} is the reaction rate constant, K_{LH} and K_i are the Langmuir adsorption constants for PhOH (K_{LH}) and reactions intermediates (K_i), respectively, and [*Int.*] refers to the concentration of the various intermediate products of phenol degradation. If it is assumed that the adsorption coefficients for all organic molecules present in the reacting mixture are effectively equal and the concentrations of by-products are much lower than the concentration of phenol during the reaction (at least one order of magnitude, as happens in the present case), the following assumption can be made:

$$K_{LH}[\text{PhOH}] + \sum_i K_i[\text{Int.}] \approx K_{LH}[\text{PhOH}] \tag{2.4}$$

The final aspect of the Langmuir-Hinshelwood equation will then be:

$$r = k_{LH}\ \frac{K_{LH}[\text{PhOH}]}{1 + K_{LH}[\text{PhOH}]} = k_{app}[\text{PhOH}] \tag{2.5}$$

It has been reported that k_{LH} and K_{LH} are light intensity dependent [23, 24]. In a photocatalytic reaction, K_{LH} has a different meaning than the dark adsorption constant, since the number of active sites in the catalyst is in fact much fewer than the total surface adsorption sites. It should be noted that the active sites exist only under illumination and the species involved do not exist appreciably in the dark. Additionally, the amount of hydroxyl radicals generated is a function of absorbed light intensity, which in turn will be proportional to the incident light intensity (I), and therefore k_{LH} will also be a function of the absorbed light intensity. The k_{LH} and K_{LH} parameters, obtained by fitting the LH model Eq. (2.5) to the experimental data (as shown in Figure 2.8b), were 1.44×10^{-1} mg L^{-1} min^{-1} and 1.47×10^{-1} mg^{-1} L, respectively, for a light intensity of 30.9 mW cm^{-2}.

2.4.3. Irradiation intensity

For the range of irradiation intensities studied (18.5 – 58.6 mW cm^{-2}), it was observed that the variation of the reaction rate followed two distinct regimes (Figure 2.9). At lower intensities (for I up to 30.9 mW cm^{-2}), r varied linearly with I confirming the photoinduced nature of the catalytic process. This linear variation of r with light intensity indicates that e^-/h^+ pairs are consumed more rapidly by redox reactions at the surface of the photocatalyst than by undesired recombination [22].

However, a further increase in light intensity up to 58.6 mW cm^{-2} didn't produce any effect on r. At these conditions, the rate of e^-/h^+ pairs formation becomes greater than

the phenol degradation rate, which favors charge recombination. The optimal light power utilization corresponds to the domain where *r* is proportional to *I* [25], *i.e.* for radiation intensities between 18.5 and 30.9 mW cm^{-2}.

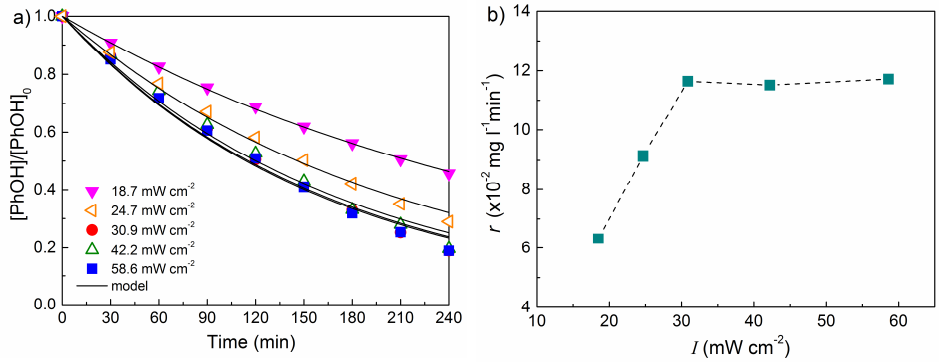

Figure 2.9 – Effect of irradiation intensity (*I*) on the kinetics of the photocatalytic degradation of phenol (a); rate of phenol degradation (*r*) as a function of the irradiation intensity (b). (Q = 17 mL min^{-1}; $[PhOH]_0$ = 20 mg L^{-1}; N = 9; $[H_2O_2]$ = 0 mmol L^{-1}).

2.4.4. Hydrogen peroxide concentration

The presence of H_2O_2 in photocatalytic processes is considered advantageous since it may act as both hydroxyl radical source and electron–hole recombination inhibitor, the latter being the major cause of the low TiO_2 photocatalytic quantum yield [26]. The effect of the addition of H_2O_2 on the degradation of phenol was studied by varying the concentration of H_2O_2 from 0 to 30 mmol L^{-1} (Figure 2.10a). No further addition of this agent has been performed during the irradiation experiment.

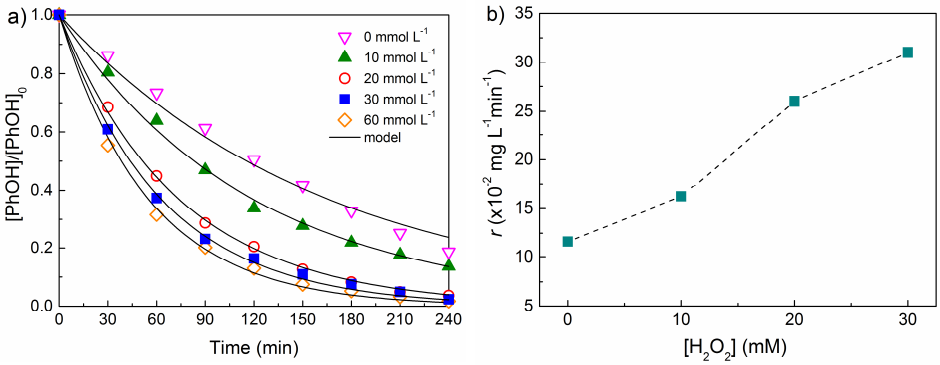

Figure 2.10 – Effect of the concentration of H_2O_2 on the kinetics of the photocatalytic degradation of phenol (a); rate of phenol degradation (*r*) as a function of the $[H_2O_2]$ (b). (Q = 17 mL min^{-1}; $[PhOH]_0$ = 20 mg L^{-1}; N = 9; I = 30.9 mW cm^{-2}; $[H_2O_2]$ = 0-30 mmol L^{-1}).

As expected, the introduction of H_2O_2 leads to an increase in the efficiency of phenol photodegradation (Figure 2.10b). At lower intensities (for *I* up to 30.9 mW cm^{-2}),

r varied linearly with *I* confirming the photoinduced nature of the catalytic process. This linear variation of *r* with light intensity indicates that e^-/h^+ pairs are consumed more rapidly by redox reactions at the surface of the photocatalyst than by undesired recombination [22-24].

It was observed that even for the lowest concentration of H_2O_2 used (10 mmol L^{-1}), a significant enhancement in the photocatalytic efficiency was observed with respect to the photocatalytic reaction in the absence of this oxidant, with an increase of 56% in the value of *r* being obtained (10.4×10^{-2} mg L^{-1} min^{-1} and 16.2×10^{-2} mg L^{-1} min^{-1} for the photocatalytic reactions in the absence and in the presence of 10 mmol L^{-1} H_2O_2, respectively). Increasing amounts of added H_2O_2 lead to a fairly linear increase on the *r* value up to 30 mmol L^{-1}. For this H_2O_2 concentration a reaction rate of 31.0×10^{-2} mg L^{-1} min^{-1} was obtained. However, a further increase in the H_2O_2 concentration up to 60 mmol L^{-1} only produced a 15% increase in the reaction rate ($r = 35.6\times10^{-2}$ mg L^{-1} min^{-1}). This behaviour can be attributed to the presence of an excessive amount of H_2O_2 which may act as hydroxyl radical scavenger [27].

2.4.5. Residence time

The flow rate of the phenol solution (*Q*) was varied between 10 and 25 mL min^{-1}, corresponding to a variation of the residence time in the photoreactor between 43.2 and 17.3 s, respectively. As can be observed in Figure 2.11a, very little effect in the kinetics of the photocatalytic degradation of phenol was observed by varying phenol solution's flow rate.

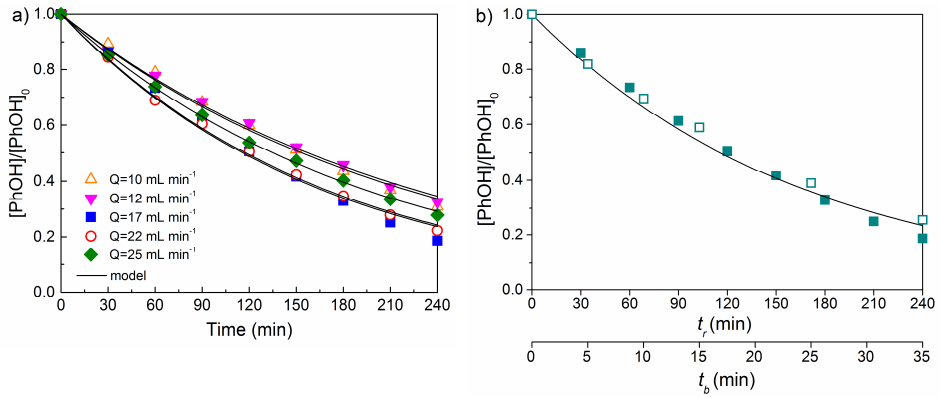

Figure 2.11 – Effect of the flow rate (*Q*) in the kinetics of the photocatalytic degradation of phenol (a); (*Q* = 10 – 25 mL min^{-1}; *I* = 30.9 mW cm^{-2}; $[PhOH]_0$ = 20 mg L^{-1}; N = 9; $[H_2O_2]$ = 0 mmol L^{-1}); photocatalytic degradation of phenol in recirculation (-■-) and batch (-□-) operation mode as function of time, t_r and t_b, respectively.

The values for *r* varied between 8.54×10^{-2} mg L^{-1} min^{-1} and 11.4×10^{-2} mg L^{-1} for a residence time of 36.0 s (*Q* = 12 mL min^{-1}) and 19.6 s min^{-1} (*Q* = 22 mL min^{-1}), respectively. Therefore, for the range of *Q* tested in the present system, the expected *r* can be estimated as 9.97×10^{-2} mg L^{-1} min^{-1} ($\pm$ 16.7%).

These results suggest a minor influence of the residence time in the kinetics of the process, which indicates that an approximation to a system of batch reactors working in parallel can be assumed. The reaction time in the batch system can be then calculated by:

$$t_b = t_r \frac{V_R}{V_T} \tag{2.6}$$

where t_b corresponds to the reaction time in the batch system, t_r to the reaction time in the recirculation system, V_R to the solution's volume inside of the reactor (7.2 mL), and V_T to the total solution's volume (50 mL). In order to validate this assumption, a batch reaction was performed in the same cylindrical reactor filled with 9 TiO_2-coated Raschig rings using 7.2 mL of a 20 mg L^{-1} phenol solution. An air stream was continuously introduced in the reactor for maintaining the aeration conditions. As expected, the kinetics of the photocatalytic degradation of phenol were very similar when comparing both batch and recirculation operation mode (Figure 2.11b).

The k_{app} for the parallel batch system can be therefore estimated as:

$$r_b = r_r \frac{t_r}{t_b} \tag{2.7}$$

where r_b and r_r correspond to the reaction rate obtained for the batch and for the recirculation systems, respectively. In the conditions tested, corresponding to the results shown in Figure 2.11b, the r_b estimated by Eq. (2.7) is 8.11×10^{-1} mg L^{-1} min^{-1}, while the r_b obtained by adjusting a pseudo first order kinetic model to the experimental data was 7.29×10^{-1} mg L^{-1} min^{-1}, which represents a 11% deviation to the value estimated by Eq. (2.7) and therefore, validating the parallel batch assumption.

2.4.6. Kinetic modelling

The results reported in the previous sections showed that in most cases there is a correlation between each operation parameter and the kinetic behavior of the photocatalytic system, quantified in terms of the first order reaction rate. *r* was found

to vary linearly with some parameters in a determined operation range: i) with the irradiation intensity in the range 18.5 – 30.9 mW cm^{-2}; ii) with the concentration of H_2O_2 when varied between 0 – 30 mmol L^{-1}; and iii) with the number of TiO_2–coated Raschig rings between 3 and 9. In addition, the Langmuir-Hinshelwood model was successfully used to correlate the initial concentration of phenol ($[PhOH]_0$) with the reaction rate in the range 10 – 50 mg L^{-1}. These correlations are summarized in Figure 2.12.

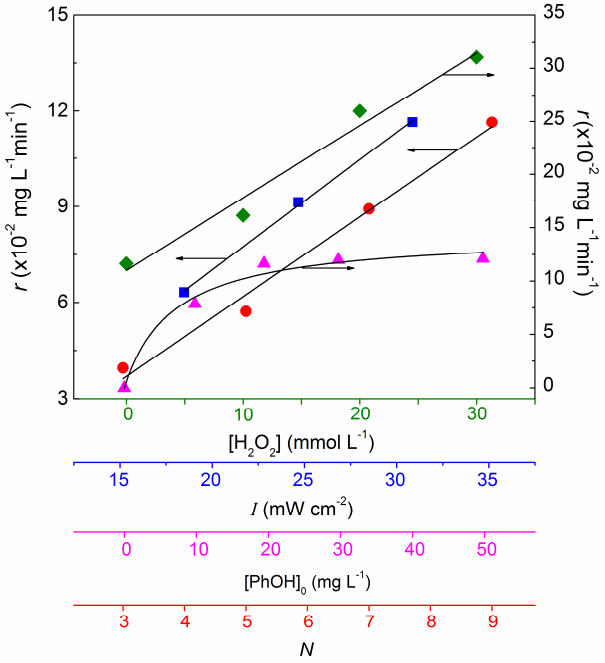

Figure 2.12 – Modelization of the reaction rate (*r*) as a function of several operation conditions. Experimental points and analytical fit given for individual parameter: $[H_2O_2]$ (-◆-, R^2 = 0.98), *I* (-■-), R^2 = 0.9989), $[PhOH]_0$ (-▲-, R^2 = 0.9768) and *N* (-●-, R^2 = 0.988).

An empirical rate law was determined from the results above as a function of the studied operation parameters as follows:

$$r = 737 \times (1.31\times10^{-2}N - 3.16\times10^{-3}) \times (4.30\times10^{-3}I - 1.59\times10^{-2}) \times (6.81\times10^{-3}[H_2O_2] + 1.10\times10^{-1}) \times \left[\frac{1.44\times10^{-1}\times1.47\times10^{-1}[PhOH]}{(1+1.47\times10^{-1}[PhOH]}\right] \quad (2.8)$$

A comparison between experimental (r_{exp}) and calculated (r_{calc}) by Eq. (2.8) at different operation conditions is shown in Figure 2.13. The plot illustrates the good agreement between the results obtained from the model and the experimental data, indicating that *r* can be accurately predicted at different operation conditions by using the developed model.

As described above, this kinetic model was developed by varying only one parameter at a time. In order to better validate the correlation that was found (Eq. 8), four experiments were performed by randomly combining the operation parameters, namely **E1** : $[PhOH]_0$ = 10 mg L^{-1}; I = 18.5 mW cm^{-2}; N = 7 and $[H_2O_2]$ = 0 mmol L^{-1}; **E2** : $[PhOH]_0$ = 10 mg L^{-1}; I = 18.5 mW cm^{-2}; N = 7 and $[H_2O_2]$ = 30 mmol L^{-1}; **E3** : $[PhOH]_0$ = 10 mg L^{-1}; I = 30.9 mW cm^{-2}; N = 5 and $[H_2O_2]$ = 30 mmol L^{-1}; **E4** : $[PhOH]_0$ = 10 mg L^{-1}; I = 24.7 mW cm^{-2}; N = 6 and $[H_2O_2]$ = 10 mmol L^{-1}.

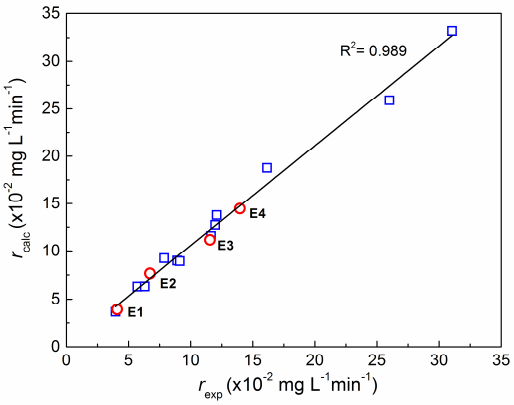

Figure 2.13 – Comparison between experimental and calculated rate (r) for the photocatalytic degradation of phenol using TiO_2–coated glass Raschig rings under simulated solar light at different operation parameters: (□) corresponds to the variation of each parameter separately and (○) to the combination of four random parameters. Correlation as given in figure.

As can be observed in Figure 2.13, the experimental (□) and calculated values (○) match satisfactorily the linear relationship, which indicates that the developed kinetic model can be considered an important tool to predict any combination of operation conditions within the studied ranges, *i.e.* I = 18.5 – 30.9 mW cm^{-2}, $[H_2O_2]$ = 0 – 3 mmol L^{-1}, N = 3 – 9 and $[PhOH]_0$ = 10 – 50 mg L^{-1}.

2.5. Photocatalytic degradation of a mixture of phenolic derivatives

Taking into account the photocatalytic performance observed for glass Raschig rings coated with three layers of EP (EP-3L) in the degradation of phenol, the photocatalytic treatment of a synthetic effluent constituted by a mixture of seven phenolic derivatives was studied under similar conditions and using the same photocatalytic material, *i.e.* EP-3L. Phenol (PH), 4-hydroxybenzoic acid (HBA), 4-methoxyphenol (HME), 4-hydroxyphenylethyl alcohol (HPA), benzoic acid (BA), protocatechuic acid (DHBA) and gallic acid (GA) were selected as model compounds generate a possible mixture of compounds that may be encountered in real

wastewater. Direct photochemical degradation under non-catalytic conditions revealed that the mixture is quite stable in the absence of a catalyst.

Figure 2.14 shows the concentration histories of the seven pollutants contained in the synthetic effluent during the photocatalytic treatment using EP-3L coated glass Raschig rings. In opposition to what occurs in the photolytic reaction, most of the aromatic compounds are degraded by heterogeneous photocatalysis and a decrease in the total phenolic content of around 50% was obtained after 8 h irradiation (Appendix, Figure A.2).

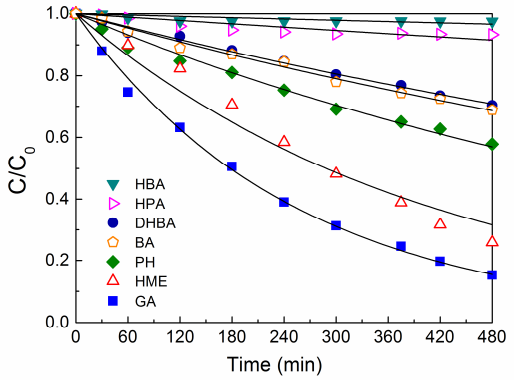

Figure 2.14 – Concentration histories of the individual compounds in the synthetic effluent during photocatalytic experiments using EP-3L.

It can be noticed that the photocatalytic degradation efficiency was different depending on the organic compound, in terms of long term conversion (after 480 min irradiation), following the order GA (85%) > HME (74%) > PH (42 %) > BA (30 %) ~ DHBA (29%) > HPA (7 %) ~ HBA (3 %).

It is known that the photocatalytic reactivity of benzene derivatives can be affected by the number of substituents, their electronic nature and their position on the aromatic ring [28]. Indeed, the photocatalytic degradability of phenolic compounds has been correlated with the nature of the different substituents in the aromatic system [29]. Photocatalytic reactions are recognized to be electrophilic processes, being accelerated by the presence of electron-donating (activating) groups in aromatic molecules and retarded when electron-withdrawing (deactivating) substituents are present. Additionally, when an aromatic ring has more than one functional group, the effects of the substituents are combined and their total effect is generally the result of the sum of these different contributions. Qualitatively it was attempted to correlate the observed reactivity with the number and type of functional groups attached to the aromatic ring. GA has three hydroxyl groups (very strongly activating groups) and a

strongly deactivating group (–COOH). The combination of the effect of those substituents has resulted in the prevalence of the highly activating nature of the three –OH groups, which makes GA the most easily degraded compound.

HME, with a very strong –OH and a less strong $-OCH_3$ activating group, was the second most easily degraded compound. In opposition, HPA and HBA were very refractory to the photocatalytic treatment. In the case of HBA, the presence of an electron-withdrawing group (–COOH) may explain the almost negligible degradation observed for this compound. The resistance of HPA to degradation by using advanced oxidation processes has been already reported [30-32]. Azabou et al. [30] have reported the low degradation (31% abatement at the end of 24 h) of HPA (C_0 = 0.5 g L^{-1}) in a mixture of several phenolic compounds by a wet peroxide photo-oxidation process catalyzed by aluminium–iron pillared montmorillonite. The same authors reported complete conversion of HPA under the same conditions when individually tested [31]. These results indicate that the photo-oxidation of HPA is inhibited by the presence of other aromatic compounds. In the present work, the weak activating nature of the $-CH_2CH_2OH$ substituent and the simultaneous presence of several other aromatic derivatives that compete for the same active sites of the photocatalyst may explain the low photocatalytic degradation observed for this compound.

2.6. Conclusions

TiO_2–coated glass Raschig rings prepared by dip-coating are photocatalytic active for phenol degradation in aqueous solution, under simulated solar irradiation and are feasible candidates to be used as photoactive fillings in photocatalytic reactors.

The photoefficiency of the degradation process depends on the type of TiO_2 used, on the number of TiO_2 layers and on the robustness of the catalyst films.

Fresh SA–coated rings, mainly anatase, show the highest initial activity for phenol degradation. However, due to particle disaggregation, activity decreases with reutilization. EP-3L Raschig rings show the best compromise between photocatalytic activity and film stability.

The process efficiency using EP-3L films, quantified in terms of the reaction rate, is influenced by several operating parameters such as the number of coated-TiO_2 Raschig rings, H_2O_2 concentration, irradiation intensity and initial phenol concentration.

The flowrate of the recirculating solution, *i.e.* the residence time, marginally affects the rate of the degradation process and an approximation to a system of batch reactors working in parallel has been demonstrated.

The *r* values revealed to vary linearly with *N*, *I* and with H_2O_2 concentration in the ranges 3 – 9, 18.5 – 30.9 mW cm^{-2} and 0 – 30 mmol L^{-1}, respectively.

The relationship between the reaction rate and $[PhOH]_0$ is well described by the Langmuir-Hinshelwood model. A kinetic model has been successfully developed, allowing the prediction of the photocatalytic phenol degradation rate over a wide combination of operation conditions when using TiO_2–coated glass Raschig rings.

When used in the photocatalytic treatment of a mixture of seven phenolic derivatives, EP-3L led to a 50% reduction of the total phenolic content. The degradation extent observed for the different compounds is in a first approximation dependent on the nature of the substituents on the aromatic ring. GA, with 3 very strong activating groups (–OH) and a strong deactivating group (–COOH) was the easiest degraded compound. In contrast, almost negligible degradation of HBA was observed. In this case, the resistance to degradation is attributed to the presence of an electron-withdrawing group (–COOH) that prevails over the effect of the –OH substituent. Also some synergetic interactions between the compounds cannot be ruled out.

References

[1] A. Di Paola, E. García-López, G. Marcì, L. Palmisano, A survey of photocatalytic materials for environmental remediation, J. Hazard. Mater., 211–212 (2012) 3-29.

[2] M.D. Hernandez-Alonso, F. Fresno, S. Suarez, J.M. Coronado, Development of alternative photocatalysts to TiO_2: Challenges and opportunities, Energy Environ. Sci., 2 (2009) 1231-1257.

[3] K. Shimura, H. Yoshida, Heterogeneous photocatalytic hydrogen production from water and biomass derivatives, Energy Environ. Sci., 4 (2011) 2467-2481.

[4] N. Miranda-García, S. Suárez, B. Sánchez, J.M. Coronado, S. Malato, M.I. Maldonado, Photocatalytic degradation of emerging contaminants in municipal wastewater treatment plant effluents using immobilized TiO_2 in a solar pilot plant, Appl. Catal. B: Environ., 103 (2011) 294-301.

[5] V. Augugliaro, M. Bellardita, V. Loddo, G. Palmisano, L. Palmisano, S. Yurdakal, Overview on oxidation mechanisms of organic compounds by TiO_2 in heterogeneous photocatalysis, Journal of Photochemistry and Photobiology C: Photochemistry Reviews, 13 (2012) 224-245.

[6] Y. Haldorai, A. Rengaraj, C.H. Kwak, Y.S. Huh, Y.-K. Han, Fabrication of nano TiO_2@graphene composite: Reusable photocatalyst for hydrogen production, degradation of organic and inorganic pollutants, Synthetic Metals, 198 (2014) 10-18.

[7] H. Guo, M. Kemell, M. Heikkilä, M. Leskelä, Noble metal-modified TiO_2 thin film photocatalyst on porous steel fiber support, Appl. Catal. B: Environ., 95 (2010) 358-364.

[8] J. Krýsa, P. Novotná, Š. Kment, A. Mills, Effect of glass substrate and deposition technique on the properties of sol gel TiO_2 thin films, J. Photochem. Photobiol. A: Chem., 222 (2011) 81-86.

[9] R.S. Sonawane, M.K. Dongare, Sol–gel synthesis of Au/TiO_2 thin films for photocatalytic degradation of phenol in sunlight, J. Mol. Catal. A: Chem., 243 (2006) 68-76.

[10] E. Chatzisymeon, S. Foteinis, D. Mantzavinos, T. Tsoutsos, Life cycle assessment of advanced oxidation processes for olive mill wastewater treatment, J. Cleaner Prod., 54 (2013) 229-234.

[11] A.M.T. Silva, E. Nouli, N.P. Xekoukoulotakis, D. Mantzavinos, Effect of key operating parameters on phenols degradation during H_2O_2-assisted TiO_2

photocatalytic treatment of simulated and actual olive mill wastewaters, Appl. Catal. B: Environ., 73 (2007) 11-22.

[12] A.M.A. Pintor, V.J.P. Vilar, R.A.R. Boaventura, Decontamination of cork wastewaters by solar-photo-Fenton process using cork bleaching wastewater as H_2O_2 source, Sol. Energy, 85 (2011) 579-587.

[13] M.Y. Ghaly, T.S. Jamil, I.E. El-Seesy, E.R. Souaya, R.A. Nasr, Treatment of highly polluted paper mill wastewater by solar photocatalytic oxidation with synthesized nano TiO_2, Chem. Eng. J., 168 (2011) 446-454.

[14] J. Araña, J.M. Doña-Rodríguez, D. Portillo-Carrizo, C. Fernández-Rodríguez, J. Pérez-Peña, O. González Díaz, J.A. Navío, M. Macías, Photocatalytic degradation of phenolic compounds with new TiO_2 catalysts, Appl. Catal. B: Environ., 100 (2010) 346-354.

[15] N. Quici, M.L. Vera, H. Choi, G.L. Puma, D.D. Dionysiou, M.I. Litter, H. Destaillats, Effect of key parameters on the photocatalytic oxidation of toluene at low concentrations in air under 254 + 185 nm UV irradiation, Appl. Catal. B: Environ., 95 (2010) 312-319.

[16] O. Folin, V. Ciocalteu, On Tyrosine and Tryptophane Determinations in Proteins, J. Biol. Chem., 73 (1927) 627-650.

[17] Y. Chen, D.D. Dionysiou, Bimodal mesoporous TiO_2–P25 composite thick films with high photocatalytic activity and improved structural integrity, Appl. Catal. B: Environ., 80 (2008) 147-155.

[18] M. Pelaez, P. Falaras, A.G. Kontos, A.A. de la Cruz, K. O'Shea, P.S.M. Dunlop, J.A. Byrne, D.D. Dionysiou, A comparative study on the removal of cylindrospermopsin and microcystins from water with NF-TiO_2-P25 composite films with visible and UV-vis light photocatalytic activity, Appl. Catal. B: Environ., 121-122 (2012) 30-39.

[19] W.C. American Society for Testing and Materials, PA, D-3359-02 cross-cut tape test for adhesion.

[20] O. Carp, C.L. Huisman, A. Reller, Photoinduced reactivity of titanium dioxide, Prog. Solid State Chem., 32 (2004) 33-177.

[21] T. Ohno, K. Sarukawa, K. Tokieda, M. Matsumura, Morphology of a TiO_2 Photocatalyst (Degussa, P-25) Consisting of Anatase and Rutile Crystalline Phases, J. Catal., 203 (2001) 82-86.

[22] J.M. Herrmann, Titania-based true heterogeneous photocatalysis, Environ. Sci. Pollut. Res., 19 (2012) 3655-3665.

[23] A. Mills, J. Wang, D.F. Ollis, Dependence of the kinetics of liquid-phase photocatalyzed reactions on oxygen concentration and light intensity, J. Catal., 243 (2006) 1-6.

[24] C.G. Silva, J.L. Faria, Effect of key operational parameters on the photocatalytic oxidation of phenol by nanocrystalline sol-gel TiO_2 under UV irradiation, J. Mol. Catal. A, 305 (2009) 147-154.

[25] J.M. Herrmann, Heterogeneous photocatalysis: State of the art and present applications, Top. Catal., 34 (2005) 49-65.

[26] L. Prieto-Rodriguez, S. Miralles-Cuevas, I. Oller, P. Fernández-Ibañez, A. Aguera, J. Blanco, S. Malato, Optimization of mild solar TiO_2 photocatalysis as a tertiary treatment for municipal wastewater treatment plant effluents, Appl. Catal. B: Environ., 128 (2012) 119-125.

[27] W. Chu, C.C. Wong, The photocatalytic degradation of dicamba in TiO_2 suspensions with the help of hydrogen peroxide by different near UV irradiations, Water Res., 38 (2004) 1037-1043.

[28] M.H. Priya, G. Madras, Kinetics of photocatalytic degradation of phenols with multiple substituent groups, J. Photochem. Photobiol. A: Chem., 179 (2006) 256-262.

[29] C.G. Silva, J.L. Faria, Photocatalytic Oxidation of Phenolic Compounds by Using a Carbon Nanotube-Titanium Dioxide Composite Catalyst, ChemSusChem, 3 (2010) 609-618.

[30] S. Azabou, W. Najjar, A. Gargoubi, A. Ghorbel, S. Sayadi, Catalytic wet peroxide photo-oxidation of phenolic olive oil mill wastewater contaminants: Part II. Degradation and detoxification of low-molecular mass phenolic compounds in model and real effluent, Appl. Catal. B: Environ., 77 (2007) 166-174.

[31] W. Najjar, S. Azabou, S. Sayadi, A. Ghorbel, Catalytic wet peroxide photo-oxidation of phenolic olive oil mill wastewater contaminants: Part I. Reactivity of tyrosol over (Al–Fe)PILC, Appl. Catal. B: Environ., 74 (2007) 11-18.

[32] S. Khoufi, F. Aloui, S. Sayadi, Treatment of olive oil mill wastewater by combined process electro-Fenton reaction and anaerobic digestion, Water Res., 40 (2006) 2007-2016.

Chapter 3

TiO_2/carbon nanotubes thin films for photocatalytic applications

TiO_2/carbon nanotubes composites using different types of TiO_2 materials are prepared by hydration-dehydration technique using functionalized carbon nanotubes (CNT). Then the influence of the synthesis route and the effect of using functionalized and non-functionalized CNT is evaluated.

The TiO_2/CNT powder materials are immobilized on glass slides by using the doctor blade technique. The photoefficiency of the TiO_2/CNT films is tested on the photocatalytic degradation of methylene blue

Aiming at technological application the study is followed by the photocatalytic treatment of aqueous solutions of four *para*-substituted phenols. The relationship between the Hammett constant of each para-substituted phenol compound and its degradability by photocatalysis is proposed.

This chapter is based on the following articles:

M.J. Sampaio, C.G. Silva, R.R.N. Marques, A.M.T. Silva, J.L. Faria, Carbon nanotube-TiO_2 thin films for photocatalytic applications. Catal. Today 161 (2011) 91-96, reproduced by permission of Elsevier.

M.J. Sampaio, C.G. Silva, R.R.N. Marques, P.B. Tavares, A.M.T. Silva, J.L. Faria, Tailoring the properties of immobilized titanium dioxide/carbon nanotube composites for photocatalytic water treatment. J. Environ. Chem. Eng. 1 (2013) 945–953, reproduced by permission of Elsevier.

3.1. Introduction

Since they were discovered by Iijima [1], carbon nanotubes (CNT) have been extensively employed in a wide range of applications, from energy storage to electronics and catalysis [2-4]. Particularly in the field of photocatalysis, CNT have been used in the preparation of hybrid materials, based on its combination with metal oxides [5-7]. Although TiO_2 is considered the catalyst of excellence in photocatalysis applications, it requires excitation in the near UV region (bandgap energy of 3.2 eV), accounting for its low solar efficiency.

Therefore, efforts have been made to extend the light absorption of TiO_2 into the visible region, which include the use of composite materials based on CNT and TiO_2 [5, 8, 9]. The conductive nature of the CNT is believed to favor the separation of the photo-generated electron–hole pairs by formation of heterojunctions at the TiO_2/CNT interface [10]. Moreover CNT can provide spatial confinement of TiO_2 and large supporting surface areas, leading to faster observed rates of redox reactions [11].

Several factors including the synthesis route, the presence of oxygenated groups at CNT's surface, CNT content, TiO_2 crystal nature and particle size play a crucial role in the efficiency of TiO_2/CNT composites. The adequate combination of all these factors would lead to the production of materials with enhanced photocatalytic properties [9, 10, 12]. Another important aspect concerns the practical problems arising from the use of a photocatalyst as powder such as, the difficulty/cost of the post-separation step, particle aggregation, and difficulty of applying the method for continuous flow systems. One way of circumventing these drawbacks is by using coatings or films on support surfaces where the catalyst particles are immobilized [8, 13, 14].

In this chapter, the main objective is to show how to control the film photoefficiency of TiO_2/CNT films according to the TiO_2 nature in the composite. The influence of the synthetic route and the use of functionalized and non-functionalized CNT is also evaluated. The resulting films are used for the photocatalytic degradation of methylene blue (MB), chosen as probe molecule because it is a commonly tested model compound for photocatalyst screening reactions using TiO_2-based films. The study is extended to the photocatalytic treatment of aqueous solutions of four *para*-substituted phenols (4-aminophenol, 4-chlorophenol, 4-nitrophenol, and 4-methoxyphenol), which are commonly in industrial wastewaters [15, 16].

3.2. Experimental

3.2.1. Reagents

Titanium (IV) isopropoxide ($Ti[OCH(CH_3)_2]_4$, 97%), titanium (IV) oxide powder anatase (TiO_2, 99.8% metal basis), nitric acid (HNO_3, ≥ 65%), methylene blue hydrate (MB, 95+%), 4-aminophenol (AP, 98+%), 4-chlorophenol (CP, 99+%), 4-nitrophenol (NP, 98%), 4-methoxyphenol (MP, 99%), α-terpineol (90%), acetone (99.5+%) and ethylcellulose were purchased from Sigma–Aldrich. Ethanol (99.5%) was obtained from Panreac. Ultrapure water was produced in a Direct-Q millipore system. Aeroxide® TiO_2 P25 was obtained from Evonik. Multi-walled carbon nanotubes were purchased from Shenzen Nanoport Co. Ltd (manufacturer data: purity > 95%, diameter < 10 nm, length = 5-15 μm; ash content ≤ 0.2 *wt.*%, surface area = 40-300 $m^2\ g^{-1}$, amorphous carbon < 3%). The measured BET surface area of the original carbon nanotubes was 100 m^2/g.

3.2.2. Catalyst preparation

Bare TiO_2 was prepared by means of an acid-catalyzed sol-gel method from an alkoxide precursor. The synthesis was performed at room temperature as follows. Briefly, a 0.5 M $Ti[OCH(CH_3)_2]_4$ solution in ethanol was magnetically stirred for 30 min and then acidified with 0.8% v/v HNO_3. The solution was loosely covered and kept stirring until a homogeneous gel formed. The obtained gel was aged in air for one week, ground into fine powder, and calcined at 400 ºC under a flow of N_2 for 2 h.

To prepare functionalized CNT (hereafter referred as CNT_f), pristine carbon nanotubes were treated in liquid phase with 10 M HNO_3 at boiling temperature for 3 h. After cooling, the suspension was washed up to neutral pH of the rising waters and the recovered powders were stored after being dried overnight at 110 ºC.

TiO_2/CNT composite catalysts were prepared by two different approaches, sol-gel and hydration-dehydration methods, using functionalized and non-functionalized CNT. The sol-gel method used to prepare the TiO_2/CNT and TiO_2/CNT_f composites was similar to the one used to synthesize bare TiO_2, but in this case a certain amount of CNT (or CNT_f) was directly introduced into the $Ti[OCH(CH_3)_2]_4$ ethanol solution.

In a first approach, the effect of TiO_2 nature on the resulting composites was assessed and the TiO_2/CNT_f composites were prepared by the hydration-dehydration technique. Briefly, the CNT_f were dispersed in water under ultrasonication for 30 min, and then TiO_2 powder was added to the suspension. The mixture was heated and

magnetically stirred until the water was completely evaporated. The obtained composites were dried overnight at 110 ºC to eliminate the remaining humidity before being stored. The catalysts were labeled as WW/CNT_f-Y, where "WW" corresponds to the type of TiO_2 ("EP" for Aeroxide® TiO_2 P25, "SA" for TiO_2 obtained from Sigma-Aldrich and "HD" for TiO_2 produced by sol-gel method with a post-treatment by the hydration-dehydration technique, and "Y" corresponds to the weight ratio of CNT_f (5, 10 and 20).

Subsequently, a study on the effect of catalyst preparation method and carbon nanotube surface chemistry in the photoefficiency of immobilized CNT-TiO_2 composites was performed. The catalysts were labeled as XX/CNT-Y, where "XX" corresponds to the method used to prepare the respective composite material: "SG" prepared by sol-gel and "HD" prepared by hydration-dehydration. Pure TiO_2 prepared by sol-gel was labeled as TiO_2-SG. For comparison purposes this TiO_2 material was also treated by the hydration-dehydration technique (TiO_2-HD).

3.2.3. Films preparation

Glass slides of 1.5 cm diameter coated on one side with different pastes of each material were used to prepare thin films. To remove contaminants, glass slides were cleaned with distilled water containing an anionic detergent and subsequently washed exhaustively with milli-Q water and sonicated for 15 min. Then the slides were immersed in acetone and sonicated for 15 min. The same procedure was repeated using isopropanol.

A paste of each powder material was prepared by mixing 50 mg of the respective solid with 1.5 mL of a solution constituted by acetone (10.0 mL), α-terpineol (5.0 mL) and ethylcellulose (0.3 g). The mixture was left under stirring during 24 h in a closed vial. After that period, the vial was opened for solvent evaporation under stirring for another 24 h. Each paste was spread on a freshly cleaned transparent glass slide using the doctor blade technique.

The surface to be covered by the semiconductor was defined by two parallel stripes of one layer Scotch® adhesive tape as a spacer to obtain approximately the same film thickness. The area obtained was of 1.0 cm^2. After the tape was removed, the glass plates were calcined at 450 °C for 1 h. The original CNT are stable at this temperature, as confirmed by thermogravimetric analysis.

3.2.4. Catalyst characterization

The analyses performed by DR UV-Vis, SEM, XRD and the BET specific area (S_{BET}) determination were thoroughly described in chapter 2, section 2.2.2.

Diffuse reflectance infrared Fourier transform (DRIFT) spectroscopic analysis of the materials was performed on a Nicolet 510P FTIR Spectrometer. The equipment was also equipped with a Pike ATR (attenuated total reflection) accessory with a high-pressure clamp and a ZnSe crystal plate. The interferograms were converted to equivalent absorption units in the Kubelka–Munk scale.

Temperature programmed desorption (TPD) analysis was carried out using an AMI-200 Catalyst Characterization Instrument (Altamira Instruments) equipped with a quadrupole mass spectrometer (Ametek, Mod. Dymaxion). The sample (0.1 g) was placed in a U-shaped quartz tube and heated until 1050 ºC at 5 ºC min^{-1} in an electrical furnace under a constant flow of 25 cm^3 min^{-1} (STP) of helium, used as carrier gas.

Elemental analysis of the prepared catalysts was performed by energy-dispersive X-ray spectroscopy (EDXS) using an EDAX Genesis X4M instrument.

Transmission electron microscopy (TEM) was performed in a LEO 906E instrument operating at 120 kV, equipped with a 4 Mpixel 28x28 mm CCD camera from TRS. Atomic force microscopy (AFM) was performed on a Veeco Metrology Nanoscope IVA atomic force microscope, operating in tapping mode.

3.2.5. Photocatalytic experiments

The films were used in the photocatalytic degradation of MB in aqueous solution. The photocatalytic experiments were performed in a glass cylindrical reactor (Scheme 3.1) filled with 6.5 mL of a 10 mg L^{-1} MB aqueous solution. The solution was magnetically stirred and continuously purged with an oxygen flow. The irradiation source consisted in a Heraeus TQ 150 medium-pressure mercury vapor lamp (λ = 254, 313, 365, 436 and 546 nm). A DURAN® glass cooling jacket was used for irradiation in the near-UV to visible light range (λ = 365, 436 and 546 nm). The lamp was located 6 cm from the films, the light irradiance at this position being 33 mW cm^{-2}, determined by integrating the irradiance spectra obtained by using a UV-Vis spectroradiometer USB2000+, OceanOptics, USA) in the range 350-600 nm. The maximum temperature reached during the photocatalytic experiments was of 35 ºC. The illuminated area on the films was kept at 0.79 cm^2 and was delimited by using a Viton® o-ring.

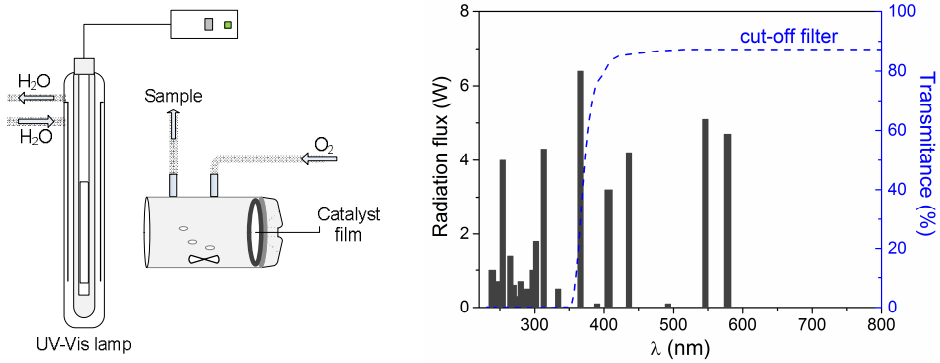

Scheme 3.1 – Experimental set-up used in the photocatalytic experiments (a) and Radiation flux of Heraeus TQ 150 immersion lamp and transmission spectrum of the DURAN 50® filter (b).

Preliminary kinetic experiments of MB adsorption on TiO_2 and on the composite materials were performed previously to the photocatalytic study. The dark adsorption was performed during 120 min. In all cases, at 15 min of adsorption time, the amount of adsorbed MB practically reached the maximum coverage (*i.e.*, plateau). The adsorption capacity of TiO_2 films was around 4% of the initial amount of MB and less than 10% for all the composites. Then, the solution was irradiated with near-UV to visible light at constant stirring speed. The first sample was taken out at the end of the dark adsorption period, just before the light was turned on, in order to determine the MB concentration in solution, which was hereafter considered as the initial concentration (C_0) after dark adsorption. Samples were analyzed by UV-Vis spectrophotometry in a Jasco V-560 spectrophotometer.

The same procedure was used in the experiments performed for the photocatalytic treatment of 10 mg L^{-1} solutions of four *para*-substituted phenols: 4-aminophenol (AP), 4-chlorophenol (CP), 4-nitrophenol (NP) and 4-methoxyphenol (MP). The analysis of the *para*-substituted phenols concentration was performed in the same HPLC apparatus used for phenol concentration evaluation, described in chapter 2, section 2.2.4.

The reactions took place at natural pH conditions and a variation of only ±0.5% was observed at the end of the photocatalytic reactions. Reactions in the absence of catalyst were also performed as blank experiments in order to characterize the pure photochemical regime.

3.3. Photocatalytic activity of TiO_2/CNT_f composite: effect of TiO_2 nature

3.3.1. Films characterization

In a first approach the different types of TiO_2 powders (TiO_2-EP, TiO_2-SA and TiO_2-HD) were combined with CNT_f and immobilized on glass slides using the doctor blade technique. The so prepared films were than tested in the degradation of MB.

Figure 3.1 shows representative SEM micrographs of the films obtained using the CNT_f-TiO_2 composites with higher percentages of functionalized CNT (Y = 20).

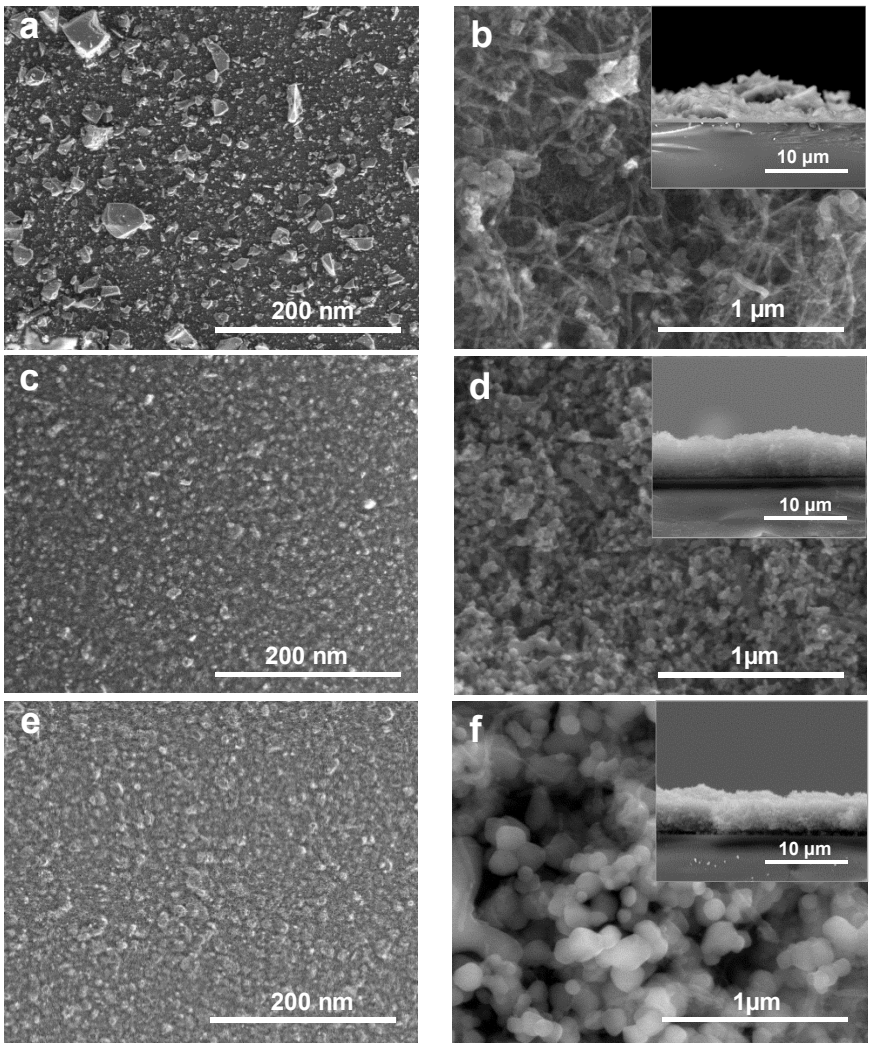

Figure 3.1– SEM images of HD/CNT_f-20 (a) and (b), EP/CNT_f-20 (c) and (d), and SA/CNT_f-20 (e) and (f). Inset figures (b), (d) and (f) are sectional cuts of the HD/CNT_f-20, EP/CNT_f-20 and SA/CNT_f-20 films, respectively.

These images clearly reveal the differences in the size, uniformity and shape of the particles of the composite materials. SEM images show that relatively homogeneous films at the microscale were obtained when EP (Figures 3.1c and 3.1d) and SA (Figures 3.1e and 3.1f) were used as titanium dioxide phase. However, for TiO_2-HD composites it was observed the presence of particles of relatively large dimensions settled at the surface of the substrate (Figures 3.1a and 3.1b). Higher magnification micrographs show the typical morphology of CNT-TiO_2 composite materials with TiO_2 particles surrounding carbon nanotubes. From the SEM images it could also be observed the presence of TiO_2 phases with different particle sizes and morphologies.

Typically, the TiO_2 prepared by sol-gel is constituted by very small anatase crystals of around 10 nm aggregated as larger particles [17]. SEM images of the composites prepared with TiO_2-HD reveal that carbon nanotubes are located mainly at the surface of these large TiO_2 particles, as can be observed in Figure 3.1b.

In the case of EP/CNT_f composite films, the TiO_2 phase reveals a more uniform nanoparticle size distribution centered at 30 nm, with the carbon phase (CNT_f) homogeneously distributed into the metal oxide matrix (Figure 3.1d). This uniform morphology was also observed in the case of TiO_2-SA films. In Figure 3.1f a high magnification image of a region on the SA/CNT_f-20 film shows the presence of TiO_2 particles with sizes in the order of hundreds of nanometers, homogeneously embedding carbon nanotubes. This film is in fact the more homogeneous, well-structured and thinner (Figures 3.1e and 3.1f).

The thickness of the films was determined from SEM micrographs by measuring the cross section of sliced films over many samples. As discussed previously, since the films prepared with TiO_2-HD are very heterogeneous and mechanically unstable it is only possible to refer an estimated thickness, which in the case of HD/ CNT_f-20 (Figure 3.1b inset) was about 5.0 μm (with 8.00 μm at the maximum thickness and 3.00 μm at the minimum). For EP/CNT_f-20 and SA/CNT_f-20 the thickness of the films measured from the cross sectional cuts was of 4.50 and 3.75 μm, respectively (Figures 3.1d and 3.1f inset).

Surface roughness of selected films was evaluated by atomic force microscopy (Figure 3.2). For these films, the measured surface roughness was of 151 and 156 nm, respectively. These results indicate that the presence of carbon nanotubes don't affect significantly the film surface which means that carbon nanotubes are well dispersed in the TiO_2 media. In particular for these films, the roughness values are of the same order of the TiO_2-SA particle dimension, confirming the uniformity of the film surface.

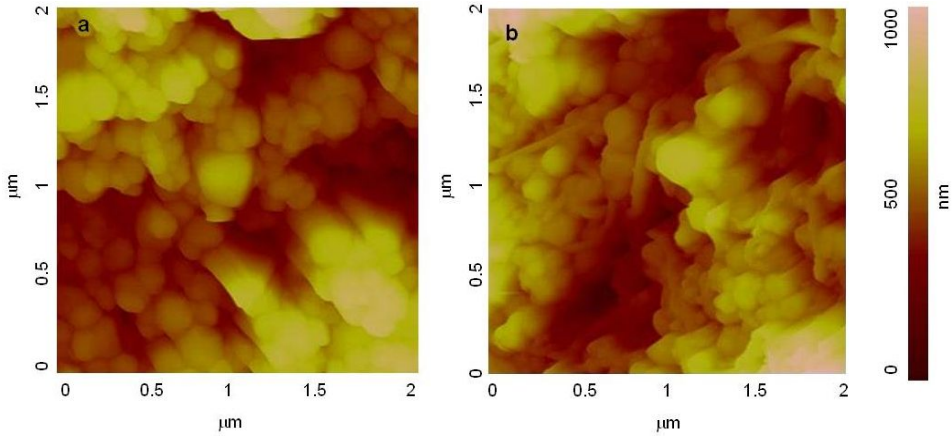

Figure 3.2 – AFM images of TiO_2-SA (a) and SA/CNT_f-20 (b) films.

One of the most important characterization procedures for materials used in photocatalytic applications consists in the determination of the optical absorption spectrum. Figure 3.3 shows the diffuse reflectance UV-Vis spectra of the films prepared on glass substrates. For comparison purposes, the spectra of the three TiO_2 powders (dashed lines) are also shown.

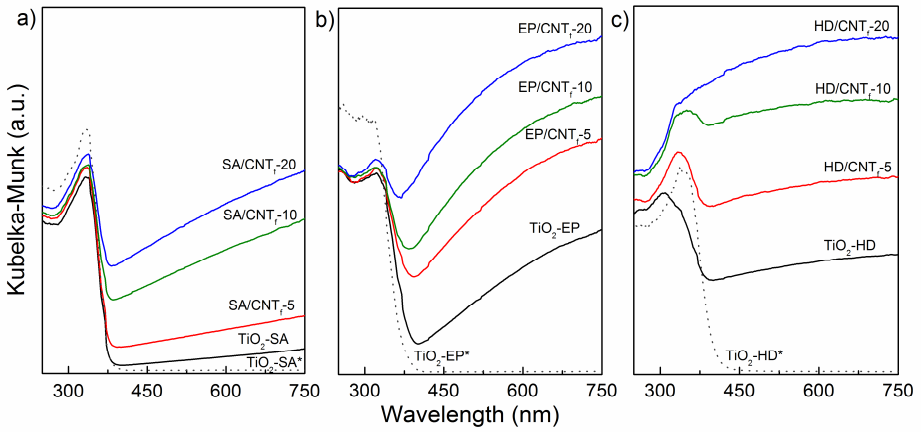

Figure 3.3 – Diffuse reflectance UV-Vis spectra of SA (a), EP (b) and HD (c) TiO_2 films. SA*, EP* and HD* are the spectra of the corresponding TiO_2 powder substrates.

As expected, TiO_2 powders show the characteristic absorption sharp edge located at around 400 nm. However, we could observe that TiO_2 films show optical absorption for wavelengths higher than the typical absorption edge, this absorption increasing following the order HD > EP > SA. Nevertheless, this behavior was already expected since the films show some light transparency, which can be related both to their thickness and homogeneity.

It is noticeable for all cases that the introduction of CNT_f into the TiO_2 matrix leads to an increase in the optical absorption, mainly in the visible spectral range.

The increase in light absorption appears to be proportional to the CNT_f loading. Additionally, as can be observed in Figure 3.3, the introduction of CNT_f leads to an increase in the absorption edge, which indicates a decrease in the bandgap energy for the composite materials. These observations are in agreement with results reported for CNT-TiO_2 composite powders [11, 18, 19], the increase in the absorption being attributed to the creation of an electronic interphase interaction between CNT and TiO_2.

3.3.2. Photocatalytic degradation of methylene blue

The efficiency of the prepared films was evaluated for the photocatalytic degradation of MB under near-UV to visible light irradiation. Since the light irradiation is at $\lambda \geq 365$ nm and MB shows absorption in this wavelength range, a photodegradation reaction, in the absence of catalyst, was performed in order to quantify the amount of dye degraded by the photochemical route. At these conditions, it was observed a decrease in MB concentration of less than 20% at the end of 60 min of irradiation.

Photocatalytic degradation of MB was performed by using films of both pure TiO_2 and TiO_2/CNT composites, obtained with different types of titanium dioxide and different CNT loadings. Since the amount of TiO_2 in each material is different, the MB removal at different reaction times was divided by the mass fraction of the TiO_2 phase (y_{TiO2}) in the composite, as follows:

$$\mathrm{MB_{deg}} / y_{TiO_2} = \frac{(C_0 - C_t) \times \mathrm{V}}{\left(\frac{100}{100 + \mathrm{Y}}\right)} \qquad (3.1)$$

where C_0 is the initial concentration of MB, C_t is the concentration at time t, V is the volume of the solution used for the photocatalytic reaction and Y is the CNT_f mass fraction in the composite. The results were therefore quantified in terms of the amount of MB degraded per mass fraction of TiO_2 (y_{TiO2}) in each catalyst. Figure 3.4 summarizes the results obtained using HD, EP and SA TiO_2-containing films.

Results show that in most cases there is an increase in the photoefficiency when CNT_f are present in the films. For TiO_2-EP and TiO_2-SA containing films, this increase in the activity for MB removal was proportional to the CNT_f loading. In the case of

TiO_2-HD films, no effect was observed when low amounts of CNT_f were used. Nevertheless, for HD/CNT_f-20, an increase in the efficiency of about 20% was obtained when comparing with the analogous TiO_2 film. However, among the tested films, those containing TiO_2-HD presented the lowest efficiencies than the ones produced using TiO_2-SA and TiO_2-EP, which can be attributed to the lower homogeneity of the resulting films.

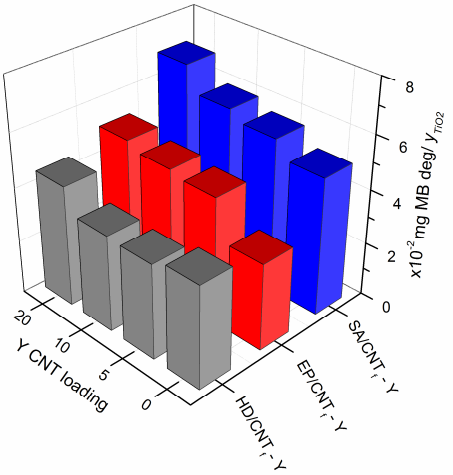

Figure 3.4 – MB conversion after 60 min of irradiation using HD, EP and SA TiO_2-based materials.

TiO_2-SA films have shown the highest efficiencies, with the SA/CNT_f-20 being the most efficient material. These good results obtained for TiO_2-SA containing materials can be attributed to both the homogeneity of the obtained films and to the photocatalytic properties of the composite materials. The interaction between CNT and TiO_2 phases in the composite materials also depends on key aspects such as TiO_2 particle size, TiO_2 crystal phase composition and surface chemistry of both CNT and TiO_2. TiO_2-SA and TiO_2-HD consist only of anatase crystalline phase. The lower activity found for TiO_2-HD composites should be related with the very small particles that form big aggregates, therefore leading to a weak interaction with the CNT phase. TiO_2-EP is composed by anatase and also rutile crystallites, which is expected to account for the photocatalytic activity of TiO_2-EP composites. Figure 3.5 shows the time conversion plots of MB degradation in the presence of TiO_2-SA, SA/CNT_f-5, SA/CNT_f-10 and SA/CNT_f-20 catalyst films. For comparison purposes the data obtained for the photolytic reaction are also presented. From Figure 3.5 it can be seen that the kinetics of MB removal increase when the composite catalyst films are used.

In Figure 3.5 inset is shown the evolution of the spectra of the aqueous solution during the photocatalytic reaction using SA/CNT_f-20 film. After 60 min of irradiation, a

decrease in MB concentration of 89% was observed using this catalyst, which is considerably higher than the 79% of MB removal obtained with the film prepared with pure TiO_2-SA. It can also be observed in Figure 3.5 that even without normalizing the data for MB removal using SA/CNT_f-20 per mass fraction of TiO_2, the observed MB removal was higher than the obtained with TiO_2-SA.

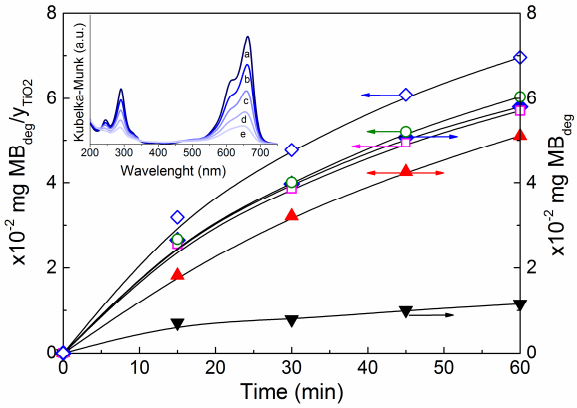

Figure 3.5 – MB degraded during photolytic (-▼-) and photocatalytic reactions using TiO_2-SA (-▲-), SA/CNT_f-5 (-□-), SA/CNT_f-10 (-○-), SA/CNT_f-20 (-◇- and -◆-). Open and filled symbols correspond to normalized (per y_{TiO2}) and non-normalized results, respectively. Inset: UV-Vis spectra of MB at 0 min (a), 15 min (b), 30 min (c), 45 min (d) and 60 min (e) of irradiation using SA/CNT_f-20 as photocatalyst.

Globally, the results obtained indicate that a synergy effect exists between CNT_f and TiO_2 phases, leading to an increase in the efficiency for MB removal. Results obtained in the degradation of MB using suspensions of the same catalysts revealed a similar tendency as when films were used, *i.e.*, the highest efficiencies were obtained for TiO_2-SA containing catalysts. However, the optimal CNT_f load when using CNT_f-TiO_2 composites in suspension were in some cases different that those obtained for films. In the case of TiO_2-EP materials, the maximum efficiency was obtained for EP/CNT_f-10. At the end of 60 min of irradiation the conversion of MB using TiO_2-EP and EP/CNT_f-10 were of 6.4×10^{-2} and 7.5×10^{-2} mg MB/$_{yTiO2}$, respectively. For TiO_2-SA and TiO_2-HD materials, the composite catalysts with the highest CNT_f loading were the most efficient, with MB removals of 6.5×10^{-2} and 7.8×10^{-2} mg MB/$_{yTiO2}$ obtained for TiO_2-SA and SA/CNT_f-20 and of 4.9×10^{-2} and 5.3×10^{-2} mg MB/$_{yTiO2}$ for TiO_2-SG and SG/CNT_f-20, respectively. In another study, photocatalytic experiments for degradation of caffeine using the same powder materials were also performed [9]. A glass immersion reactor charged with 250 mL of caffeine solution (50 mg L^{-1}) and the amount of suspended catalyst of 1 g L^{-1} was used. For these reactions the irradiation source was maintained. It was found a negligible effect when CNT_f were combined

with TiO_2-SG (here labeled as TiO_2-HD). The weak interaction between the TiO_2 particles and the CNT_f observed by the SEM images was the main factor that affected the interfacial charge transfer process that effectively inhibits electron-hole recombination. For TiO_2-P25 (here labeled as TiO_2-EP), when combined with CNT_f a better distribution of the TiO_2 particles on the CNT_f was observed, however in terms of caffeine photocatalytic removal a markedly decrease was obtained. In contrast, in case of TiO_2-SA a positive effect was observed when CNT_f were introduced. These results were attributed to the larger TiO_2 crystallite size leading to the good contact between both phases. The presence of the oxygenated surface groups in the CNT_f also revealed as a crucial step on the high activity of the SA/CNT_f composites.

Regarding these results using photocatalyst suspensions the optimal CNT loading corresponds to the amount of CNT_f in the composite that leads to the higher catalyst activity, *i.e.*, to the maximum of synergy effect between CNT and TiO_2 phases. For higher CNT loadings, the increasing amount of carbon nanotubes may cause light scattering, leading to a decrease of the photoefficiency of the process. In the case of TiO_2/CNT_f films, this occurrence is avoided by the immobilization of the catalysts on the glass slides. Therefore the photoefficiency of the composite catalysts cannot only be attributed to the intrinsic properties of the materials, but also to the characteristics of the films.

Studies using TiO_2/CNT slurries have suggested that the role of the CNT phase in the composite catalyst can be ascribed to three distinct mechanisms: i) CNT may act as a dispersing media for TiO_2 nanoparticles; ii) CNT can act as a co-adsorbent; or iii) CNT can act as a photosensitizer [5, 11, 20]. The first mechanism is more significant when TiO_2 particles are generated simultaneously during the synthesis of the composite catalyst. In this case, chemical groups at the surface of the CNT may act as anchoring points to TiO_2 nanoparticles.

The introduction of high amounts of CNT in the composite catalysts lead to an increase of the S_{BET} of the materials, which can be attributed to a better dispersion of TiO_2 particles avoiding the formation of aggregates. The specific surface areas of TiO_2-EP, TiO_2-SA and TiO_2-HD were of 56, 13 and 99 $m^2\ g^{-1}$, while for the corresponding composite materials with the highest CNT load (TiO_2/CNT_f-20) these values increased to 73, 25 and 108 $m^2\ g^{-1}$, respectively.

In the photocatalytic reactions using TiO_2/CNT_f films, it was observed for all cases a maximum decrease of 10% in the concentration of MB after the dark adsorption period. Being so, it is not reasonable to ascribe the beneficial effect promoted by CNT_f

to its action as a co-adsorbent. Therefore, it is more reasonable to attribute the positive effect resulting from the presence of CNT_f in the composite material to its action as a photosensitizer, promoting electric charge transfer between the two phases, reducing the bandgap of the resulting composite catalyst and thus increasing the efficiency of the photocatalytic process. For the composite films the synergy effect was in general proportional to the increase in the absorbance observed for these materials mainly in the visible spectral range, which supports the creation of an electronic interphase interaction between CNT and the semiconductor.

It is known that the efficiency of photocatalyst materials depends on structural and optical properties such as particle size, surface area, presence of surface hydroxyl groups and bandgap energy, which are in turn related to the synthesis route [21, 22]. Moreover, as shown before, when photocatalysts are immobilized as films, characteristics such as thickness, homogeneity and roughness have to be taken into account. Globally it was found that the properties of the films were intimately related to the characteristics of the different types of TiO_2 powders used in the production of the TiO_2/CNT composites such as particle size and morphology.

In the next section, since the TiO_2 phase is obtained from a common sol-gel route, the differences observed in the behavior of the different films is not expected to be related particularly to the morphology of the films but to the intrinsic properties of the photocatalyst materials, such as S_{BET}, particle size and optical spectrum.

3.4. Photocatalytic activity of TiO_2/CNT composite films: effect of preparation method and CNT functionalization

3.4.1. Catalyst characterization

Representative SEM micrographs of the films obtained using the TiO_2/CNT composites with highest percentage of CNT are shown in Figure 3.6. Figures 3.6a and 3.6c show the morphology of the materials prepared with non-functionalized CNT by HD and SG methods, respectively, where some particle agglomeration can be observed. Materials prepared with CNT_f (Figures 3.6b and 3.6d) show a more homogeneous morphology with TiO_2 particles of smaller dimensions surrounding carbon nanotubes.

Typical TEM image of HD/CNT_f-20 (Figure 3.6b inset) shows the existence of phase segregation while a more homogeneous distribution of the TiO_2 particles around the CNT_f phase was observed for SG/CNT_f -20 composite (Figure 3.6d inset).

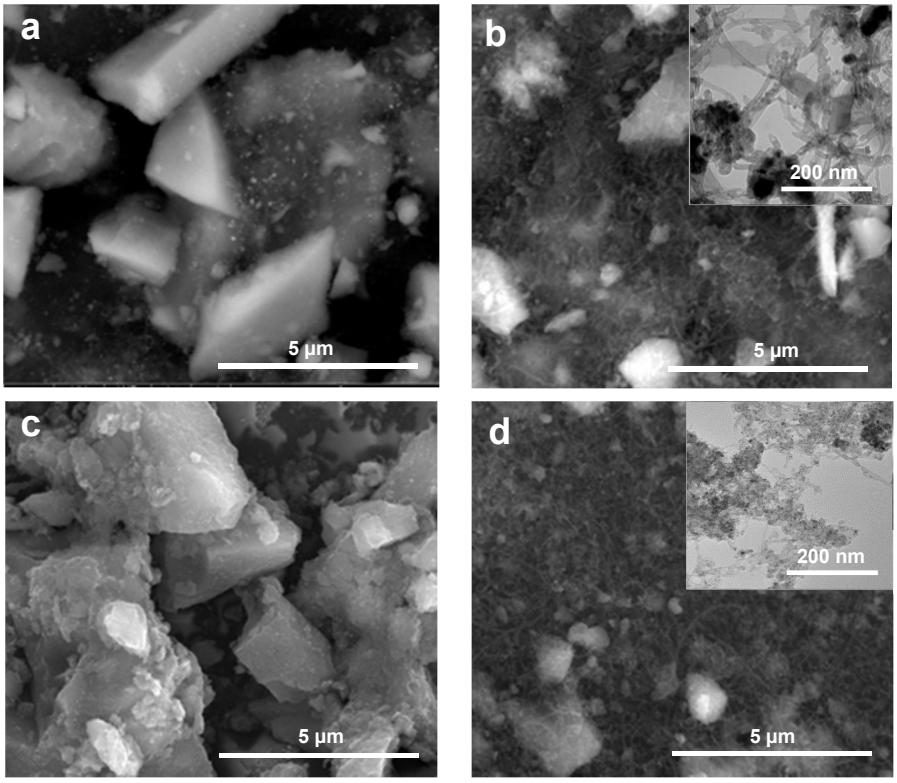

Figure 3.6 – SEM images of HD/CNT-20 (a), HD/CNT_f-20 (b), SG/CNT-20 (c) and SG/CNT_f-20 (d) and TEM images of HD/CNT_f-20 and SG/CNT_f-20 (inset b and d, respectively).

The S_{BET} of pure TiO_2, CNT, TiO_2/CNT and respective hydrated powder materials, obtained from the N_2 adsorption isotherms at -196 ºC are given in Table 3.1. It has to be noticed that the surface area of CNT_f is around 1.6 times higher than that of pristine CNT. This occurs because oxidative treatment with HNO_3 creates sidewall defects and can open up the endcaps of CNTs, therefore increasing the porosity [23]. The theoretical S_{BET} value, *i.e.*, the weighted average of the S_{BET} of CNT and TiO_2 phases in the composite materials taking into account its relative weight fraction, is also presented. The existence of a strong interaction between the metal oxide and the carbon phases can be inferred by comparing the determined S_{BET} with the theoretical values. A low amount of CNT (Y=5) leads to a marked decrease in S_{BET} with relation to both phases. This may happen because TiO_2 particles agglomerate on the surface of CNT resulting in a decrease in an overall S_{BET} of the composite catalysts. The introduction of progressively higher amounts of CNT leads to an increase of the S_{BET} of the composite materials. For HD/CNT materials the S_{BET} are lower than for the materials prepared by SG method with the same CNT loadings. This difference can

be associated to the aggregation of particles that may occur during the hydration-dehydration process. It was also observed that CNT functionalization promote the increase of S_{BET} of the resulting composites.

Table 3.1 – Surface area (S_{BET}) of the composite TiO_2/CNT powder materials.

	S_{BET} (± 3 m^2 g^{-1})			
CNT loading	HD/CNT	HD/CNT$_f$	SG/CNT	SG/CNT$_f$
0[a]	90	90	91	91
5	79 (90)[b]	85 (93)[b]	70 (91)[b]	73 (94)[b]
10	80 (90)[b]	93 (96)[b]	94 (91)[b]	111 (97)[b]
20	102 (91)[b]	106 (101)[b]	131 (91)[b]	141 (102)[b]
100[c]	94	155	94	155

[a] Pure TiO_2-SG or TiO_2-HD; [b] S_{BET} estimate from the mass compositions; [c] Pure CNT or CNT$_f$.

TPD analysis was used for determination and quantification of chemical oxygen species present at the surface of the functionalized CNT Figure 3.7. Oxygen surface groups on carbon materials are thermally decomposed into CO and CO_2, being possible to identify and quantify particular functional groups from TPD spectra [24-26].

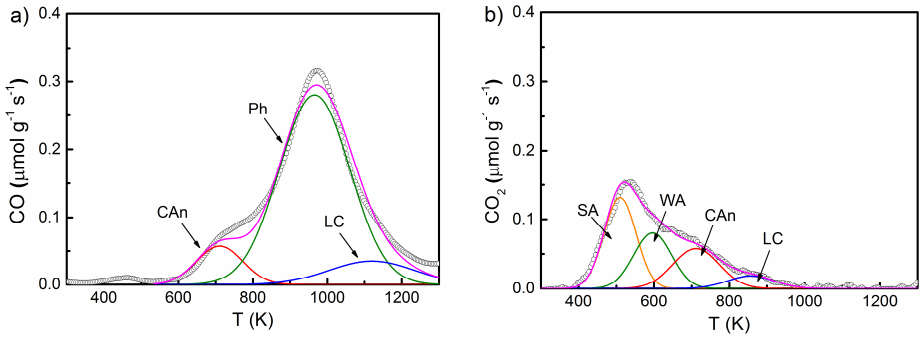

Figure 3.7 – Deconvolution of TPD spectra using a multiple Gaussian function: CO evolution (a); CO_2 evolution (b). CAn: Carboxylic anhydrides; Ph: Phenols; CQ: Carbonyl/Quinones; SA: string acids; WA: weak acids; LC: lactones.

The CO_2 is released from the decomposition of carboxylic acid groups at low temperatures or from lactones at high temperatures, while phenols and carbonyl/quinone basic groups decompose into CO at high temperatures. Anhydrides are released as both CO and CO_2 at intermediate temperatures. The total amount of oxygen containing groups released as CO and CO_2, was of 1066 µmol g^{-1} and 434 µmol g^{-1}, respectively. Deconvolution procedures for the evolved CO and CO_2 peaks provide reliable estimates for the amounts of individual oxygen groups [24]. A multiple Gaussian function was used for fitting each spectrum (Figure 3.7). The

amount of phenols (released as CO) is 803 μmol g^{-1} and the amount of carboxylic acids (released as CO_2) is 289 μmol g^{-1}, which represent 55 and 20% of the total groups at the CNT surface, respectively. The remaining 25% correspond to the contribution of carbonyl anhydrides, carbonyl/quinones and lactones.

Chemical groups present at the surface of carbon nanotubes can act as anchoring points for the TiO_2 precursors when the composites are prepared by sol-gel method [27, 28]. In the condensation step of the sol-gel synthesis, the polymeric Ti–OH chains, which are precursors of the TiO_2 crystallites, compete for the carboxylic acid and phenol groups at the surface of functionalized CNT and undergo esterification and/or oxolation reactions, respectively [27, 29]. The functional groups present at the surface of CNT_f promote the anchoring of the TiO_2 particles as well as their dispersion, avoiding agglomeration and subsequently increasing the surface area of the resulting materials.

Functionalization also contributes to a better dispersion of CNT in water, which is considered a key aspect when producing TiO_2/CNT composites by the HD technique. In fact, agglomeration of CNT was observed for suspensions of the non-functionalized material, attributed to the hydrophobic properties of pristine CNT. The introduction of hydrophilic surface chemical groups, such as hydroxyl and carboxylic groups, promotes the dispersion of functionalized CNT in water enhancing particle deagglomeration therefore increasing the surface area of the composites.

XRD analysis of TiO_2-SG, TiO_2-HD and of composite catalysts produced with the higher CNT load revealed that all samples are mainly constituted by anatase crystallites with only a very small fraction of rutile phase being identified (Figure 3.8).

The anatase crystallite dimensions were found to be around 9.0 nm except in the case of SG/CNT_f-20, which present anatase crystallites of 8.0 nm. These results indicate that the HD procedure do not induce any effect on TiO_2 crystallite dimensions. Nevertheless, as mentioned before, for materials produced by SG method, functionalization of CNT favors less extended crystallized TiO_2 domains on CNT surface thus avoiding TiO_2 particle agglomeration [27].

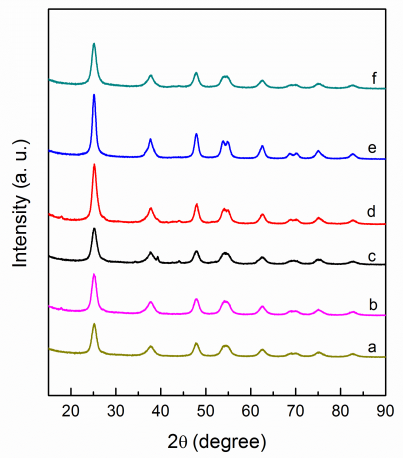

Figure 3.8 – XRD patterns of TiO_2-SG (a), TiO_2-HD (b), HD/CNT-20 (c), HD/CNT_f-20 (d), SG/CNT-20 (e), SG/CNT_f-20 (f) powders.

The diffuse reflectance UV-Vis spectra of the different films expressed in terms of Kubelka-Munk equivalent absorption units are shown in Figure 3.9. For comparison purposes, the spectra of the TiO_2-SG and TiO_2-HD powders are also shown (dashed lines).

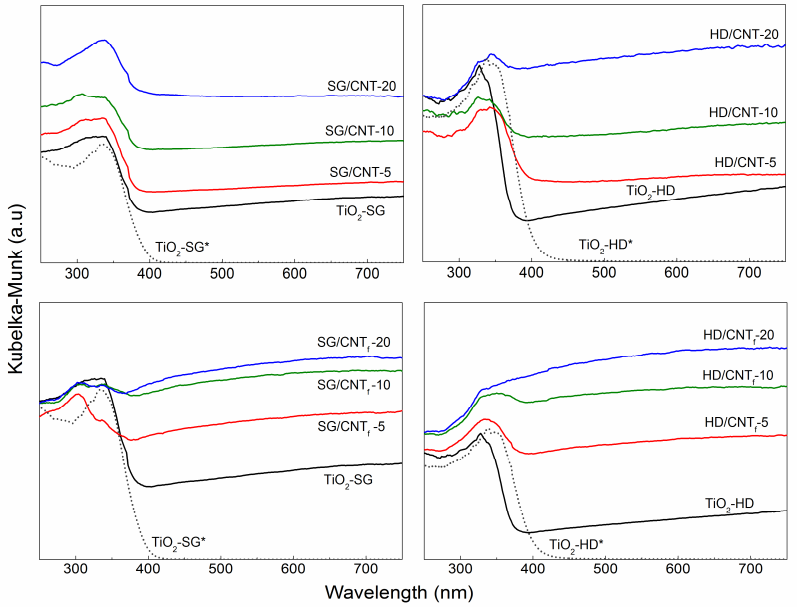

Figure 3.9 – Diffuse reflectance UV-Vis spectra of the different films. TiO_2-SG* and TiO_2-HD* refer to the spectra of the corresponding TiO_2 powders.

As already observed in previous chapters, bare TiO_2 powder (TiO_2-HD*) show the characteristic spectrum with its fundamental absorption sharp edge rising at 400 nm. Also, for TiO_2-SG* the same adsorption sharp is observed. Additionally, is noticeable

for all cases that the introduction of CNT into the TiO_2 matrix leads to an increase in the optical absorption mainly in the visible spectral range.

The DRIFT spectra of TiO_2 prepared by sol-gel before (SG) and after the hydration-dehydration (HD) treatment are shown in Figure 3.10. An increase in the intensity of the broad band located between 2600 and 3800 cm^{-1} can be observed, which is attributed to stretching vibration of hydrogen-bonded surface water molecules and hydroxyl groups [22, 30, 31].

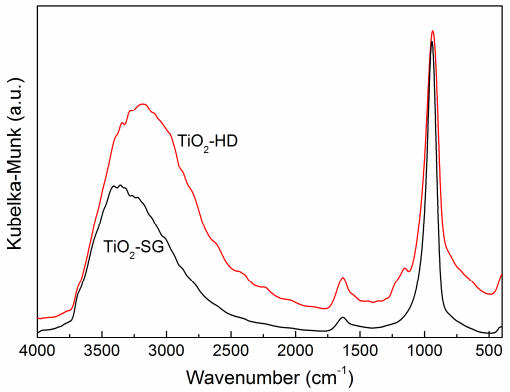

Figure 3.10 – DRIFT spectra of TiO_2-HD and TiO_2-SG.

Moreover, there is an increase in the intensity of the weak band at around 1640 cm^{-1} caused by bending vibration of coordinated water as well as from Ti-OH groups [20, 32].

3.4.2. Photocatalytic degradation of methylene blue

In the previous section the degradation of MB was described in terms of the amount of TiO_2 in each material. Now the photoefficiency of the immobilized materials was evaluated in terms of the pseudo-first-order apparent rate constant (k_{app}), since the photocatalytic experiments revealed good agreement to the model, described by the following equation:

$$C = C_0 e^{-k_{app} \cdot t} \qquad (3.2)$$

where C is the MB concentration, k_{app} is the apparent first order kinetic constant, t is the reaction time, and C_0 is the MB concentration at $t = 0$ (*i.e.*, when the illumination is switched on). Figure 3.11 shows the results obtained using the different catalysts. It can be noticed that the film produced only with TiO_2 (CNT load = 0) and treated by hydration-dehydration (HD) show higher efficiency than that produced by SG. Both TiO_2 materials were obtained by sol-gel method, but a hydration-dehydration

post-treatment was applied to the TiO_2-HD sample. This difference in the photocatalytic behavior can then be explained by the introduction of hydroxyl surface groups during the HD procedure that are known to play an important role in the photocatalytic oxidation reaction [33, 34]. This increase in the amount of hydroxyl surface groups was confirmed by DRIFT analysis of both TiO_2 materials (Figure 3.10) In photocatalytic reactions, the surface OH groups and adsorbed water react with photogenerated holes to produce the hydroxyl radical (HO•), a strong oxidant.

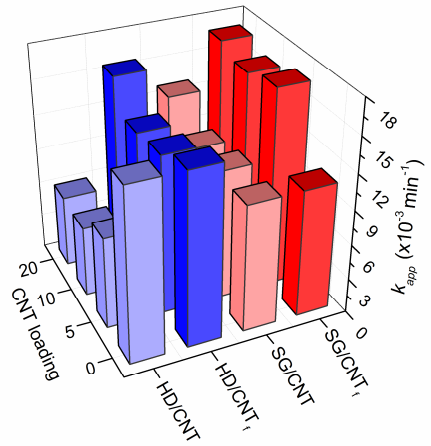

Figure 3.11 – First order apparent rate constant (k_{app}) for the photocatalytic degradation of MB using TiO_2 and XX/CNT-Y materials.

For the composites prepared by SG method, the introduction of CNT leads to a slight increase in the photocatalytic efficiency of the films, more than expected based in the amount of CNT in the composites (Figure 3.11). This behavior has already been observed in previous works where similar materials were used in suspensions, the synergy effect being attributed to the creation of an electronic interphase interaction between CNT and TiO_2 phases [11, 20, 27]. In addition, a marked increase of the films photocatalytic activity was observed when CNT_f were used to prepare the composites as compared to CNT.

Materials prepared by HD technique show different behavior than those prepared by SG. For HD composites produced with non-functionalized CNT the introduction of carbon nanotubes produced a negative effect in the efficiency of the photocatalytic process. These results indicate that the efficiency of the composite catalysts cannot be only related to its light absorption properties. It is worth noticing that HD materials have lower surface areas, therefore there is a decrease in the number of active sites for adsorption and reaction, which may explain the poor efficiency of these catalysts. A typical method to evaluate the effect of the surface area on the overall efficiency of

the catalysts consists in comparing the kinetic rate constant per unit surface area (Figure 3.12) of each material.

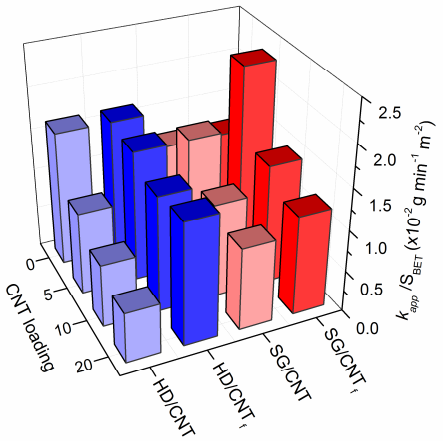

Figure 3.12 – Apparent rate constant normalized per unit surface area (k_{app}/S_{BET}) after 60 min of irradiation using TiO_2 and XX/CNT-Y materials.

As expected, an increase in the value of this parameter was observed for composites prepared by SG. The low surface area obtained for the composites prepared by HD may result from the agglomeration of catalyst particles and segregation of TiO_2 and CNT phases due to the reduced capability of non-functionalized CNT to disperse in water during the HD synthesis procedure. The increase in the dimensions of the photocatalyst particles promotes bulk electron-hole recombination, decreasing the quantum yield of the photocatalytic degradation process. For composites produced by HD using functionalized CNT, the introduction of low amounts of the carbon phase has no effect in the photocatalytic efficiency for MB degradation, while for HD/CNT_f-20 a 7% increase in k_{app} was observed comparing to TiO_2-HD (Figure 3.11).

The time-conversion plots of MB degradation are given in Figure 3.13 for TiO_2-SG, TiO_2-HD and for the respective TiO_2/CNT composite catalysts with the highest CNT load (Y = 20). For comparison purposes results obtained for the photolytic reaction are also presented and in that case, after 60 min of irradiation, only 17% of the initial MB content is converted. In comparison with bare TiO_2, it can be seen that MB removal increases when the composite catalysts produced by SG are used. In fact, among the films tested, the highest efficiency was obtained for SG/CNT_f-20. As discussed in the previous section, the MB conversion obtained with films of TiO_2-EP and the respective EP/CNT_f-20 composite was 53% and 66%, respectively. Although, TiO_2-EP and corresponding composite show higher efficiency,

the effect of CNT introduction was more pronounced in the case of the materials prepared by SG, the increase in MB conversion being of 25% and 34%, respectively Figure 3.13a. However, for the film produced with HD/CNT_f-20, the difference in activity is roughly negligible when comparing to neat TiO_2-HD (Figure 3.13b). This result indicates that from a technological standpoint there is no significant benefit on using HD/CNT_f-20 catalyst when compared to bare TiO_2-HD.

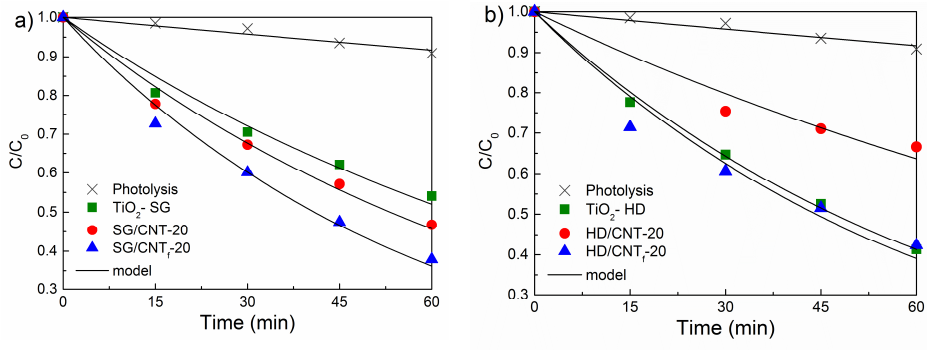

Figure 3.13 – Evolution of the normalized concentration (C/C_0) of MB during photolysis and photocatalytic reactions using: (a) TiO_2-SG, SG/CNT-20 and SG/CNT_f-20; (b) TiO_2-HD, HD/CNT-20 and HD/CNT_f-20.

As mentioned before, CNT may promote the dispersion of TiO_2 particles and this is more significant when TiO_2 particles are generated simultaneously during the synthesis of the composite catalyst, which is the case of the materials produced by SG method. Additionally, when functionalized CNT are used, chemical groups at the surface of the CNT may act as anchoring points to TiO_2 nanoparticles, therefore avoiding particle agglomeration promoting the TiO_2 dispersion. In the case of HD/CNT materials the poor efficiency observed in the degradation of MB can be probably attributed to the formation of particle aggregates and to the segregation of the two solid phases.

A maximum decrease of 10% in the concentration of MB after the dark adsorption period was observed for all cases, thus it is not reasonable to ascribe the beneficial effect promoted by CNT to its action as a co-adsorbent. Therefore, the results indicate that CNT acts as photosensitizer, by absorbing light and transferring electrons to the conduction band of TiO_2, hence increasing the efficiency of the photocatalytic process. For the composite films the synergy effect was in general proportional (exception observed for HD/CNT) to the increase in the absorbance observed for these materials mainly in the visible spectral range (Figure 3.9), which supports the creation of an electronic interphase interaction between CNT and the semiconductor [11, 20, 27].

3.4.3. Photocatalytic degradation of *para*-substituted phenolic compounds

The influence that a substituent has on the electronic character of a particular aromatic system is represented by the Hammett constant (σ). By definition, hydrogen *para*-substituted phenol is taken as reference, with $\sigma_p = 0$. Generally, for reactions involving phenols, a modified Hammett constant (σ_p^-) is used since the substituent may enter into some resonance with the reaction center in as electron-rich transition state [5, 35, 36]. A positive value of σ_p^- indicates the presence of an electron-withdrawing (deactivating) group, and a negative value an electron-donating (activating) group. The Hammett constants for $–NH_2$, $–OCH_3$, –Cl and $–NO_2$ groups are -0.66, -0.27, 0.23 and 1.25, respectively [37].

The influence of the substituent nature on the photodegradation of four *para*-substituted phenols (AP, CP, NP and MP) was investigated by comparing their initial rates of degradation (r_0) and correlating it with the corresponding σ_p^- value. For this purpose only the most active catalysts of the preceding section were used, namely SG/CNT_f-20 and TiO_2-SG.

For all compounds, the photodegradation reactions fit well a pseudo-first-order reaction rate kinetic model. The concentration after the dark adsorption period was determined in the presence of the TiO_2-SG and SG/CNT_f-20 catalyst films, which was considered as the initial concentration for the calculation of the respective r_0 value. In all cases adsorption at the end of the dark period was less than 10% of the initial concentration (10 mg L^{-1}).

Results, represented as $log(r_0)$ *vs.* σ_p^-, revealed that the photocatalytic degradation rates depend in a good degree on the nature of the substituent, reactions being accelerated in the presence of electron-donating groups and retarded by electron-withdrawing groups (Figure 3.14). A linear correlation was observed between σ_p^- and $log(r_0)$. The negative slope indicates the electrophilic nature of the photocatalytic reactions, which suggest that the rate determining elementary step may undergo by the attack of the organic molecules by an electrophilic species such as hydroxyl radicals or photogenerated holes. The SG/CNT_f-20 film is more efficient than TiO_2-SG for AP, MP and CP photodegradation, the beneficial effect promoted by the composite catalyst being higher as σ_p^- decreases. In the case of AP, the particularly high r_0 values obtained with both TiO_2-SG and SG/CNT_f-20 films can be in a good extent attributed to a large percentage of this molecule that is degraded by photolysis. The r_0 value for the photochemical degradation reaction, normalized per mass fraction

of TiO_2 (y_{TiO2}), was of 0.296 mg L^{-1} y_{TiO2}^{-1} min^{-1} being of 0.599 mg L^{-1} y_{TiO2}^{-1} min^{-1} and 1.263 mg L^{-1} y_{TiO2}^{-1} min^{-1}, for the photocatalytic reactions using TiO_2-SG and SG/CNT_f-20, respectively.

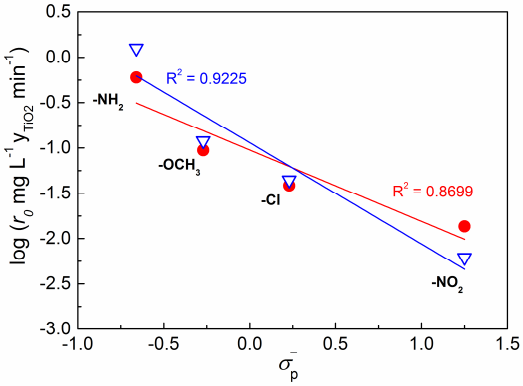

Figure 3.14 – Hammett plot for the different *para*-substituted phenols using TiO_2-SG (●) and SG/CNT_f-20 (▽) films; y_{TiO2} corresponds to the mass fraction of TiO_2 in each catalyst.

The effect of the presence of CNT in TiO_2/CNT catalysts can be quantified in terms of a synergy factor (*R*), which has been described in the literature as the ratio between k_{app}(TiO_2/CNT) and k_{app}(TiO_2), where k_{app} are the respective pseudo-first order apparent rate constants [38]. The highest synergy factor was obtained for AP, *R*=2.0, followed by MP and CP, with synergy factors R=1.2 and 1.1, respectively. For NP, the photocatalytic degradation reactions were very slow with little degradation being observed for this compound. In this case TiO_2-SG showed even slightly higher photocatalytic activity than SG/CNT_f-20 (*R*=0.5), which can be attributed to the highly deactivating nature of the –NO_2 group.

The relationship found between the Hammett constant of the four *para*-substituted phenols and the respective initial reaction rates using both catalysts constitutes a useful tool to predict the behavior of these materials when used for the photocatalytic degradation of other phenolic molecules. There is little or even no benefit from using SG/CNT_f-20 film for the photocatalytic degradation of *para*-substituted phenols with Hammett constant higher than 0.2.

3.5. Conclusions

TiO_2 and TiO_2/CNT composites immobilized in glass slides by the doctor blade technique show photocatalytic activity for the degradation of MB in aqueous media under irradiation in the near-UV to visible spectral range.

The photoefficiency of the degradation process depends on the type of TiO_2, the synthesis route and the presence of oxygenated groups on the surface of CNT.

In the films prepared with different types of TiO_2 materials (TiO_2-HD, TiO_2-EP and TiO_2-SA) the efficiency appears to be related to the inherent properties of the materials and to the characteristics of the resulting films. TiO_2-SA containing films show higher efficiency for the photocatalytic degradation of MB than TiO_2-HD and TiO_2-EP based ones, which is attributed to the physical-chemical and optical properties of these materials, as well as, to the higher homogeneity of these films.

In terms of the influence of the synthesis route and the presence of oxygenated groups, the photoefficiency of the immobilized catalysts depends on morphologic and optical properties such as surface area, anatase crystallite dimensions and light absorption spectrum. TiO_2/CNT composites prepared with functionalized CNT (CNT_f) show higher efficiency for the photocatalytic degradation of MB than those synthesized with pristine CNT. The composite prepared by sol-gel method (SG/CNT_f-20) is the most efficient film. This is attributed to the enhanced TiO_2 particle dispersion, thereby enhancing electronic interphase interaction between CNT and TiO_2 phases.

A relationship between the Hammett constant of AP, MP, CP and NP the initial degradation reaction rate of those compounds was found using TiO_2-SG and SG/CNT_f-20 composite films. The effect of the presence of CNT in the photocatalytic behavior of SG/CNT_f-20 catalyst varies inversely with the Hammett constant of *para*-substituted phenols.

References

[1] S. Iijima, Helical microtubules of graphitic carbon, Nature, 354 (1991) 56-58.

[2] C.G. Silva, M.J. Sampaio, R.R.N. Marques, L.A. Ferreira, P.B. Tavares, A.M.T. Silva, J.L. Faria, Photocatalytic production of hydrogen from methanol and saccharides using carbon nanotube-TiO_2 catalysts, Appl. Catal. B: Environ., 178 (2015) 82-90.

[3] W.-J. Lin, C.-T. Hsu, Y.-C. Tsai, Dye-sensitized solar cells based on multiwalled carbon nanotube–titania/titania bilayer structure photoelectrode, J. Colloid Interf. Sci., 358 (2011) 562-566.

[4] R.P. Rocha, A.M.T. Silva, S.M.M. Romero, M.F.R. Pereira, J.L. Figueiredo, The role of O- and S-containing surface groups on carbon nanotubes for the elimination of organic pollutants by catalytic wet air oxidation, Appl. Catal. B: Environ., 147 (2014) 314-321.

[5] C.G. Silva, J.L. Faria, Photocatalytic Oxidation of Phenolic Compounds by Using a Carbon Nanotube-Titanium Dioxide Composite Catalyst, ChemSusChem, 3 (2010) 609-618.

[6] B. Czech, W. Buda, S. Pasieczna-Patkowska, P. Oleszczuk, MWCNT-TiO_2-SiO_2 nanocomposites possessing the photocatalytic activity in UVA and UVC, Appl. Catal. B: Environ., 162 (2015) 564-572.

[7] M. Ahmad, E. Ahmed, Z.L. Hong, W. Ahmed, A. Elhissi, N.R. Khalid, Photocatalytic, sonocatalytic and sonophotocatalytic degradation of Rhodamine B using ZnO/CNTs composites photocatalysts, Ultrason. Sonochem., 21 (2014) 761-773.

[8] Z. Li, B. Gao, G.Z. Chen, R. Mokaya, S. Sotiropoulos, G. Li Puma, Carbon nanotube/titanium dioxide (CNT/TiO_2) core–shell nanocomposites with tailored shell thickness, CNT content and photocatalytic/photoelectrocatalytic properties, Appl. Catal. B: Environ., 110 (2011) 50-57.

[9] R.R.N. Marques, M.J. Sampaio, P.M. Carrapiço, C.G. Silva, S. Morales-Torres, G. Dražić, J.L. Faria, A.M.T. Silva, Photocatalytic degradation of caffeine: Developing solutions for emerging pollutants, Catal. Today, 209 (2013) 108-115.

[10] H. Yu, X. Quan, S. Chen, H. Zhao, TiO_2-Multiwalled Carbon Nanotube Heterojunction Arrays and Their Charge Separation Capability, J. Phys. Chem. C, 111 (2007) 12987-12991.

[11] B. Gao, G.Z. Chen, G. Li Puma, Carbon nanotubes/titanium dioxide (CNTs/TiO_2) nanocomposites prepared by conventional and novel surfactant wrapping sol–gel methods exhibiting enhanced photocatalytic activity, Appl. Catal. B: Environ., 89 (2009) 503-509.

[12] Y. Chuan-Yu, L. Yu-Feng, H. Chih-Hung, T. Yao-Hsuan, M.M. Chen-Chi, C. Min-Chao, S. Hsin, The effects of synthesis procedures on the morphology and photocatalytic activity of multi-walled carbon nanotubes/TiO_2 nanocomposites, Nanotechno., 19 (2008) 045604.

[13] B. Gao, C. Peng, G.Z. Chen, G. Li Puma, Photo-electro-catalysis enhancement on carbon nanotubes/titanium dioxide (CNTs/TiO_2) composite prepared by a novel surfactant wrapping sol–gel method, Appl. Catal. B: Environ., 85 (2008) 17-23.

[14] Q. Wang, J. Shang, H. Song, T. Zhu, J. Ye, F. Zhao, J. Li, S. He, Visible-light photoelectrocatalytic degradation of rhodamine B over planar devices using a multi-walled carbon Nanotube-TiO_2 composite, Mater. Sci. Semiconductor Process., 16 (2013) 480-484.

[15] D. Mantzavinos, N. Kalogerakis, Treatment of olive mill effluents: Part I. Organic matter degradation by chemical and biological processes - an overview, Environ. Inter., 31 (2005) 289-295.

[16] A.M.T. Silva, E. Nouli, N.P. Xekoukoulotakis, D. Mantzavinos, Effect of key operating parameters on phenols degradation during H_2O_2-assisted TiO_2 photocatalytic treatment of simulated and actual olive mill wastewaters, Appl. Catal. B: Environ., 73 (2007) 11-22.

[17] W. Wang, C.G. Silva, J.L. Faria, Photocatalytic degradation of Chromotrope 2R using nanocrystalline TiO_2/activated-carbon composite catalysts, Appl. Catal. B: Environ., 70 (2007) 470-478.

[18] W. Wang, P. Serp, P. Kalck, J.L. Faria, Visible light photodegradation of phenol on MWNT-TiO_2 composite catalysts prepared by a modified sol–gel method, J. Mol. Catal. A: Chem., 235 (2005) 194-199.

[19] L.M. Pastrana-Martínez, S. Morales-Torres, S.K. Papageorgiou, F.K. Katsaros, G.E. Romanos, J.L. Figueiredo, J.L. Faria, P. Falaras, A.M.T. Silva, Photocatalytic behaviour of nanocarbon–TiO_2 composites and immobilization into hollow fibres, Appl. Catal. B: Environ., 142–143 (2013) 101-111.

[20] W. Wang, P. Serp, P. Kalck, J.L. Faria, Photocatalytic degradation of phenol on MWNT and titania composite catalysts prepared by a modified sol–gel method, Appl. Catal. B: Environ., 56 (2005) 305-312.

[21] R.-C. Xie, J. Shang, Morphological control in solvothermal synthesis of titanium oxide, J. Mater. Sci., 42 (2007) 6583-6589.

[22] C.G. Silva, J.L. Faria, Anatase vs.rutile efficiency on the photocatalytic degradation of clofibric acid under near UV to visible irradiation, Photochem. Photobiol. Sci., 8 (2009) 705-711.

[23] M. Monthioux, B.W. Smith, B. Burteaux, A. Claye, J.E. Fischer, D.E. Luzzi, Sensitivity of single-wall carbon nanotubes to chemical processing: an electron microscopy investigation, Carbon, 39 (2001) 1251-1272.

[24] J.L. Figueiredo, M.F.R. Pereira, M.M.A. Freitas, J.J.M. Órfão, Modification of the surface chemistry of activated carbons, Carbon, 37 (1999) 1379-1389.

[25] J.L. Figueiredo, M.F.R. Pereira, M.M.A. Freitas, J.J.M. Órfão, Characterization of Active Sites on Carbon Catalysts, Ind. Eng. Chem. Res., 46 (2007) 4110-4115.

[26] J.L. Figueiredo, M.F.R. Pereira, The role of surface chemistry in catalysis with carbons, Catal. Today, 150 (2010) 2-7.

[27] C.G. Silva, J.L. Faria, Photocatalytic oxidation of benzene derivatives in aqueous suspensions: Synergic effect induced by the introduction of carbon nanotubes in a TiO_2 matrix, Appl. Catal. B: Environ., 101 (2010) 81-89.

[28] L. Chen, B.-L. Zhang, M.-Z. Qu, Z.-L. Yu, Preparation and characterization of CNTs–TiO_2 composites, Powder Technol., 154 (2005) 70-72.

[29] C.G. Silva, W. Wang, J.L. Faria, Nanocrystalline CNT-TiO_2 Composites Produced by an Acid Catalyzed Sol-Gel Method, Mater. Sci. Forum 587-588 (2008) 849-853.

[30] J.R.S. Brownson, M.I. Tejedor-Tejedor, M.A. Anderson, Photoreactive Anatase Consolidation Characterized by FTIR Spectroscopy, Chem. Mater., 17 (2005) 6304-6310.

[31] J.-Y. Zhang, I.W. Boyd, B.J. O'Sullivan, P.K. Hurley, P.V. Kelly, J.P. Sénateur, Nanocrystalline TiO2 films studied by optical, XRD and FTIR spectroscopy, J. Non-Crystalline Sol., 303 (2002) 134-138.

[32] Y. Gao, Y. Masuda, W.-S. Seo, H. Ohta, K. Koumoto, TiO_2 nanoparticles prepared using an aqueous peroxotitanate solution, Ceramics Inter., 30 (2004) 1365-1368.

[33] J. Yu, H. Yu, B. Cheng, M. Zhou, X. Zhao, Enhanced photocatalytic activity of TiO_2 powder (P25) by hydrothermal treatment, J. Mol. Catal. A: Chem., 253 (2006) 112-118.

[34] J. Yu, J.C. Yu, W. Ho, Z. Jiang, Effects of calcination temperature on the photocatalytic activity and photo-induced super-hydrophilicity of mesoporous TiO_2 thin films, New J. Chem., 26 (2002) 607-613.

[35] S. Parra, J. Olivero, L. Pacheco, C. Pulgarin, Structural properties and photoreactivity relationships of substituted phenols in TiO_2 suspensions, Appl. Catal. B: Environ., 43 (2003) 293-301.

[36] M.H. Priya, G. Madras, Kinetics of photocatalytic degradation of phenols with multiple substituent groups, J. Photochem. Photobiol. A: Chem., 179 (2006) 256-262.

[37] G.W. Gokel, Dean's Handbook of Organic Chemstry, MacGraw-Hill, 2004.

[38] J. Matos, J. Laine, J.-M. Herrmann, Synergy effect in the photocatalytic degradation of phenol on a suspended mixture of titania and activated carbon, Appl. Catal. B: Environ., 18 (1998) 281-291.

Chapter 4

Carbon-based TiO_2 materials for the degradation of a cyanotoxin

TiO_2 has been under intensive investigation for photocatalytic degradation of cyanobacterial toxins. In order to develop more efficient photocatalysts, TiO_2 is combined with carbon nanotubes, graphene oxide and nanodiamonds to form composite catalysts. Neat TiO_2 and carbon-TiO_2 photocatalysts are prepared by a liquid phase deposition method, and tested for oxidation of microcystin-LA (MC-LA), a cyanotoxin frequently found in freshwaters. The performance of the photocatalysts is studied under both visible and simulated solar light. Insights on the identification of the resulting intermediate products are also given.

The photocatalytic tests presented in this chapter were carried out during a research visit for 3 months at Engineering Research Center, University of Cincinnati, Ohio (USA) under supervision of Professor Dionysios Dionysiou.

This chapter is based on the following articles:

M.J. Sampaio, C.G. Silva, A.M.T. Silva, L.M. Pastrana-Martínez, C. Han, S. Morales-Torres, J.L. Figueiredo, D.D. Dionysiou, J.L. Faria, Carbon-based TiO_2 materials for the degradation of Microcystin-LA, Appl. Catal. B: Environ. 170-171 (2015) 74-82, reproduced by permission of Elsevier.

M.J. Sampaio, L.M. Pastrana-Martínez, A.M.T. Silva, J.G. Buijnsters, C. Han, C.G. Silva, S.A.C. Carabineiro, D.D. Dionysiou, J.L. Faria, Nanodiamond-TiO_2 composites for photocatalytic degradation of microcystin-LA in aqueous solutions under simulated solar light. RSC Adv. 5 (2015) 58363-58370, reproduced by permission of The Royal Society of Chemistry.

4.1. Introduction

The number and complexity of new water contaminants derived from the rapid growth of population and industrial activities are rendering the conventional water and wastewater treatment processes rather ineffective. Cyanobacteria (aka, blue-green algae) are a diverse group of photo-autotrophic organisms which can be found in aquatic systems, such as oceans, freshwater lakes, rivers and reservoirs throughout the world [1, 2]. These organisms are essential to the food chain in many ecosystems; however, some species of cyanobacteria can also produce toxic metabolites, which are harmful to human health and ecosystems [3, 4]. Microcystins (MCs) are among the most common cyanobacterial toxins found in water and freshwater. The variant microcystin-LR (MC-LR) is the most regularly found and investigated [5]. Other frequently detected variants include MC-YR, MC-RR and MC-LA, which are less studied even though their toxicity has been frequently reported [6, 7]. The structure of MC-LA is similar to MC-LR since these toxins only differ in one amino acid group in their chain, *i.e.*, arginine for MC-LR and alanine for MC-LA [8, 9].

Various studies reported that the application of heterogeneous photocatalysis, using titanium dioxide (TiO_2) as a photocatalyst, may improve the removal of MCs from water [10, 11]. In addition, coupling TiO_2 with carbon materials, such as carbon nanotubes (CNT) [12, 13] and graphene oxide (GO) [14, 15] have provided a synergistic effect, which can enhance the overall efficiency of the photocatalytic process in particular under visible light illumination.

Recently, nanodiamond (ND) was used as alternative carbon materials towards the development of efficient photocatalysts upon combination with TiO_2 [16]. Diamonds (carbon with sp^3 hybridization) are potentially applicable candidates for composite synthesis due to their unique chemical, structural, mechanical, biological and optical properties [17, 18].

In previous studies [12, 19, 20] it was found that the efficiency of the photocatalytic process depends on the nature and content of the carbon material used for the preparation of the carbon-based TiO_2 composites. CNT-TiO_2 composites with 20 *wt.*% of the carbon phase revealed to be very efficient for the removal of methylene blue, phenol and caffeine [12, 20]. In chapter 3 it was also shown that the presence of the carbon phase on TiO_2-based materials can increase the efficiency of the resulting composites. In the case of GO-TiO_2 composites, the highest efficiency for the degradation of diphenhydramine was achieved using composites containing 4 *wt.*% of GO [15].

Only a few studies have been focused on the degradation of MCs with carbon-based photocatalysts. For instance, in a recent work, *Fotiou et al.* [21] studied the degradation of MC-LR under both UV-A and solar light irradiation in the presence of graphene-based composites (GO-TiO_2) and proved that the combination of GO with TiO_2 leads to an increase in the efficiency of MC-LR removal when compared with the bare material (TiO_2). *Pastrana-Martinéz et al.* [16] have also described the application of ND-TiO_2 composites for photocatalytic water treatment. In such report a significant improvement in the photocatalytic activity was observed for degradation of an organic pharmaceutical water pollutant (diphenhydramine) when ND were combined with TiO_2, using an optimal content of oxidized NDs (*i.e.*, 15 *wt.*% of ND).

Taking into consideration these previous findings, composites containing 15 *wt.*% of oxidized ND (ND-TiO_2-15) and 4 *wt.*% of GO (GO-TiO_2-4), and others comprising 4 *wt.*% and 20 *wt.*% of oxidized CNT (CNT-TiO_2-4 and CNT-TiO_2-20, respectively) were tested for the photocatalytic degradation of MC-LA under visible and simulated solar light irradiation for the first time in this study.

The study was extended in order to evaluate the reaction intermediates of MC-LA photocatalytic degradation by LC/Q-TOF and LC/MS/MS using the best catalyst.

4.2. Experimental

4.2.1. Carbon materials preparation

Natural graphite (20 μm, purity > 99.9995%, Sigma–Aldrich) was oxidized using the modified Hummers' method, as described elsewhere [15, 22]. Briefly, sulfuric acid (H_2SO_4, 95% > purity > 98%, Sigma–Aldrich) was added with stirring and cooling to a flask containing graphite. Then potassium permanganate ($KMnO_4$, purity > 99%, Sigma–Aldrich) was slowly added to the mixture and the suspension was stirred for 2 h at 35 ºC. Subsequently, the mixture was diluted with deionized water and hydrogen peroxide solution (H_2O_2 30% w/v, Sigma–Aldrich) was added in order to reduce residual permanganate to soluble manganese ions. The oxidized material was purified with hydrochloric acid (HCl, purity = 37%, Sigma–Aldrich), filtered and washed until neutrality of the rinsing waters. Then it was dispersed in water and exfoliated under sonication (ultrasonic processor UP400S, 24 kHz) for 1 h. Finally, the non-exfoliated graphite oxide was removed by centrifugation and a graphene oxide (GO) aqueous dispersion was obtained.

Multi-walled carbon nanotubes (CNTs > 95% purity, purchase from Shenzhen Nanotechnologies Co. Ltd) were oxidized with a 10 M nitric acid solution (HNO_3, purity > 65 %, Fluka) at boiling temperature for 3 h. The suspension was washed several times, until achieve a neutral pH. The CNTs were recovered and dried for 12 h at 110 ºC.

Nanodiamond (ND) produced by detonation of carbon-containing explosives (diameter < 10 nm, purchased from Sigma Aldrich) were oxidized by heating at 430 ºC in an open-air oven for several hours, as described elsewhere [23, 24].

4.2.2. Preparation of carbon-based TiO_2 composites

In several studies [16, 19, 20] was found that the photocatalytic process depends on the nature and content of the carbon material when used for the preparation of carbon-based TiO_2 composites. Therefore, in the present study the composites were prepared and assessed their performance in photocatalytic applications [16, 20].

The different amounts of oxidized CNTs and ND were dispersed in distilled water and sonicated for 30 min. The same procedure was performed for GO suspension. The carbon-TiO_2 composites were prepared by liquid phase deposition method (LPM), as follows: 0.1 M of TiO_2 precursor ($(NH_4)_2TiF_6$, purity > 99.99 %, Sigma-Aldrich) and 0.3 M of boric acid (H_3BO_3, purity > 99.5%, Fluka) were added to the carbon material suspensions and heated at 60 ºC for 2 h under continuous stirring. The resulting materials were washed and dried at 100 ºC for 2 h under vacuum followed by a calcination step under N_2 flow at 200 ºC. The composites were labeled as CNT-TiO_2-Y, GO-TiO_2-Y and ND-TiO_2-Y, where Y corresponds to the carbon load used (4 *wt*.%, 15 *wt*.% and 20 *wt*.%).

Bare TiO_2 was also prepared following the same procedure but without the addition of carbon material.

4.2.3. Catalyst characterization

The thermogravimetric (TG) analysis of the prepared materials were performed by heating the sample from 50 ºC to 1000 ºC at 20 ºC min^{-1} under air flow using a STA 490 PC/4/H Luxx Netzsch thermal instrument. The BET specific area (S_{BET}) was obtained from the N_2 adsorption data in the relative pressure range 0.05-0.20. The total volume of N_2 adsorbed (V_p) was also calculated according to the Gurvitch's rule [25, 26].

The morphology of the materials was analyzed by scanning electron microscopy (SEM) using a Philips XL 30 ESEM-FEG apparatus. Transmission electron microscopy (TEM) was performed in a Philips CM20 equipment.

Temperature programmed desorption (TPD) analysis was performed using an AMI-300 Catalyst Characterization Instrument (Altamira Instruments). The samples were heated to 1050 ºC at 5 ºC min^{-1} under helium flow.

X-ray photoelectron spectroscopy (XPS) was performed in a Kratos AXIS Ultra HSA apparatus using a monochromatic Al Kα X-ray source (1486.7 eV), operating at 15 kV (90 W), in FAT mode (Fixed Analyser Transmission), with a pass energy of 40 eV for regions of interest and 80 eV for survey. Multi-region spectra were recorded at C 1s, O 1s and Ti 2p photoelectron peaks.

The band gap of the photocatalyst was determined using the Kubelka–Munk units as a function of the energy in a UV–Vis spectrophotometer. A better description of the analyses performed namely, DR UV-Vis, XRD and the BET specific area (S_{BET}) equipment are thoroughly described in chapter 2, section 2.2.2, and DRIFT apparatus in chapter 3, section 3.2.4.

4.2.4. Photocatalytic experiments

The photocatalytic degradation MC-LA was evaluated under visible and simulated solar light irradiation. The experiments were carried out under natural pH conditions (pH = 5.7) in a borosilicate glass petri dish (Pyrex, diameter = 60 mm, length = 15 mm) sealed with a cover and air-cooled using appropriate fans to avoid solution evaporation (Scheme 4.1). An initial concentration of 0.2 μM MC-LA (purity > 99.3%, CalBiochem) was prepared using Milli-Q water and the concentration of photocatalyst was kept at 0.5 g L^{-1}. The total volume of the solution was 10 mL. This concentration was selected by taking into consideration the guidance values for the relative probability of acute effects to human health and ecosystems during the exposure to cyanobacteria (~0.02 to 2.2 μM) according to the World Health Organization (WHO) [27].

A Xenon lamp (OF 300W 67005, Newport, Oriel Instrument) was used to simulate solar light irradiation (light irradiance of 47.1 mW cm^{-2}). For the experiments under visible light (Scheme 4.1b), two 15 W fluorescent lamps (Cole-Parmer) with a UV block filter (UV420, Opticology) were applied as irradiation source (irradiance of 0.4 mW cm^{-2}). All the photocatalytic experiments were carried out in triplicate for each catalyst. Experiments in the absence of catalyst were also performed to

determine the contribution from direct photolysis. It was found that the degradation of the MC-LA in presence of photocatalyst follows a pseudo-first order kinetic model:

$$C = C_0 e^{-k_{app} t} \quad (4.1)$$

where C corresponds to MC-LA concentration, k_{app} is the pseudo-first order kinetic constant, t is the reaction time and C_0 is the initial MC-LA concentration at t = 0. The values of k_{app} were obtained by non-linear regression using OriginLab® software.

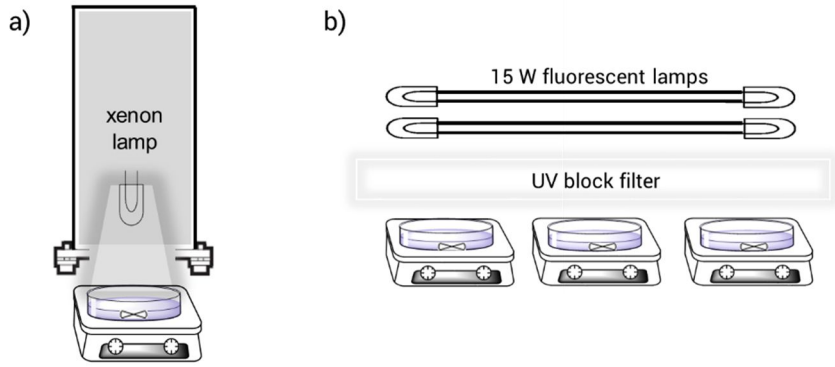

Scheme 4.1 – Experimental set-up used in the photocatalytic experiments using simulated solar light (a) and visible light irradiation (b).

4.2.5. Analytic techniques

Samples were analyzed using a high-performance liquid chromatograph (HPLC, Series 1100, Agilent) with a photodiode-array detector (PDA) set at 238 nm and using a C_{18} Discovery HS (Supelco) column (150 mm × 2.1 mm, 5 µm particle size). The method starts with a mobile phase consisting of 0.05% (v/v) trifluoroacetic (TFA) acid in Milli-Q water (A) and 0.05% TFA in acetonitrile (B) in a ratio of (75:25) followed by a linear gradient step to A:B (30:70) in 6 min; finally the initial conditions were re-established in 1 min gradient step and the A:B (75:25) mixture was isocratically eluted for 5 min. The analysis was performed with a column temperature of 40 ºC, a flow rate of 0.2 mL min^{-1} and an injection volume of 50 µL. Identification of intermediates was performed using a combination of liquid chromatography with a quadrupole time-of-flight (LC/Q-TOF) as well as with mass spectrometry (LC/MS/MS) in an Agilent G6540A apparatus. LC/Q-TOF was used to obtain molecular weight and formula information, and LC/MS/MS was used to determine further structural information. MS/MS data were acquired using the same instrument in targeted MS/MS mode. For

both Q-TOF and MS/MS modes, the same LC method was used, namely an Agilent Eclipse XDB-C18 column (2.1 mm × 50 mm, 3.5 µm), with an isocratic elution mode A:B (95:5) in 5 min (where solvent A is 0.1% formic acid in water and solvent B is 0.1% formic acid in acetonitrile) and a flow rate set at 0.2 mL min^{-1}.

4.3. Effect of graphene oxide and carbon nanotubes on TiO_2 matrix

Based on the degradation ability and extensive material characterization previously reported [19] neat TiO_2, composites CNT-TiO_2 and GO-TiO_2, were selected for preliminary studies. The activity of these materials was tested and compared for the degradation of MC-LA under visible and simulated solar light. Then, in section 4.4 are presented the results using the TiO_2 combined with the nanodiamond as a composite (ND-TiO_2-15). Several physical properties of the photocatalyst were evaluated and its performance tested for MC-LA degradation.

4.3.1. Carbon-TiO_2 based materials characterization

The carbon content (*wt.*%) in the composite materials was determined by thermogravimetric analysis; neat TiO_2, CNT-TiO_2 and GO-TiO_2 composites were submitted to a thermal treatment under air and the weight loss was monitored. The carbon content in the composite corresponds to the difference between the weight loss observed for the composite and that of neat TiO_2. The obtained results are in a good agreement with the nominal carbon content (*i.e.*, 4 *wt.*% or 20 *wt.*% depending on the composite) which indicate that no appreciable degradation of the carbon phase occurred during the calcination step.

The S_{BET} and the respective total pore volume (V_p) of TiO_2, CNT, GO as well as of the carbon-based TiO_2 composites were obtained from the N_2 adsorption isotherms are shown in Table 4.1. Different tendencies were observed for the composites depending on the type of carbon material used. The results show that V_p and S_{BET} are comparable for GO-TiO_2-4 (0.17 $cm^3\ g^{-1}$ and 110 $m^2\ g^{-1}$, respectively) and neat TiO_2 (0.11 $cm^3\ g^{-1}$ and 118 $m^2\ g^{-1}$, respectively), and higher than for GO (0.003 $cm^3 g^{-1}$ and 21 $m^2\ g^{-1}$, respectively); this is related to agglomeration of GO sheets during the necessary drying process in order to perform N_2 adsorption analysis.

Generally, anchoring and dispersion of the TiO_2 particles on CNT is promoted when functional groups are introduced on CNT by oxidation treatments, avoiding agglomeration of TiO_2 and thus increasing the surface area [12, 28, 29]. However, results show that the presence of a small amount of CNT (4 *wt.*%) in the composite

leads to a marked decrease in S_{BET} with relation to both TiO_2 and CNT phases. A similar behavior was observed previously [12] where the effect of CNT load on CNT-TiO_2 composites was also assessed. The decrease of S_{BET} was attributed to the competitive anchoring and agglomeration of TiO_2 crystallites on the sidewalls of CNTs, leading to the formation of bigger TiO_2 particles than in neat TiO_2. The introduction of a larger amount of CNTs resulted in an increase of the surface area (S_{BET} = 152 m^2 g^{-1} and V_p = 0.48 cm^3 g^{-1} for CNT-TiO_2-20). A higher CNT content, *i.e.* a higher amount of hydrophilic surface chemical groups, enhances the dispersion of the TiO_2 particles thus increasing the surface area.

Table 4.1 – BET specific area and total pore volume of the materials.

Sample	S_{BET} (m^2 g^{-1})	V_p (cm^3 g^{-1})
GO	21	0.003
CNT	155	0.61
TiO_2	118	0.11
GO-TiO_2-4	110	0.17
CNT-TiO_2-4	59	0.15
CNT-TiO_2-20	152	0.48

SEM analysis was performed for observing of the morphology of the different materials. Representative SEM micrographs of neat TiO_2 (Figure 4.1a), GO-TiO_2-4 (Figure 4.1c), CNT-TiO_2-4 (Figure 4.1e) and CNT-TiO_2-20 (Figure 4.1g) clearly reveal the differences in the morphology of the materials. For neat TiO_2 (Figure 4.1a) spherical-like TiO_2 particles aggregate to form larger particles (Figure 4.1a inset). Images of GO-TiO_2-4 (Figure 4.1c) show a good dispersion of TiO_2 particles on both sides of the GO layers. In the case of CNT-TiO_2 materials (Figures 4.1e and 4.1g), clusters of TiO_2 particles surrounding CNT are observed.

TEM micrographs of the materials are also shown in Figure 4.1. These images corroborate the previous observations by SEM. TEM image of the GO-TiO_2-4 composite (Figure 4.1d) indicates that TiO_2 particles grow around the GO layers, showing a good self-assembly of the TiO_2 nanoparticles on GO. For CNT-TiO_2 composites, some differences are observed between the materials prepared with different carbon load. CNT are hardly seen by TEM analysis in case of CNT-TiO_2-4 (Figure 4.1f), probably because some CNT are embedded into big TiO_2 agglomerates, while TiO_2 particles are dispersed along the sidewalls of CNT in the case of

CNT-TiO_2-20 (Figure 4.1h). These observations are in line with their S_{BET}, the strong agglomeration of the TiO_2 particles in CNT-TiO_2-4 resulting in a lower surface area.

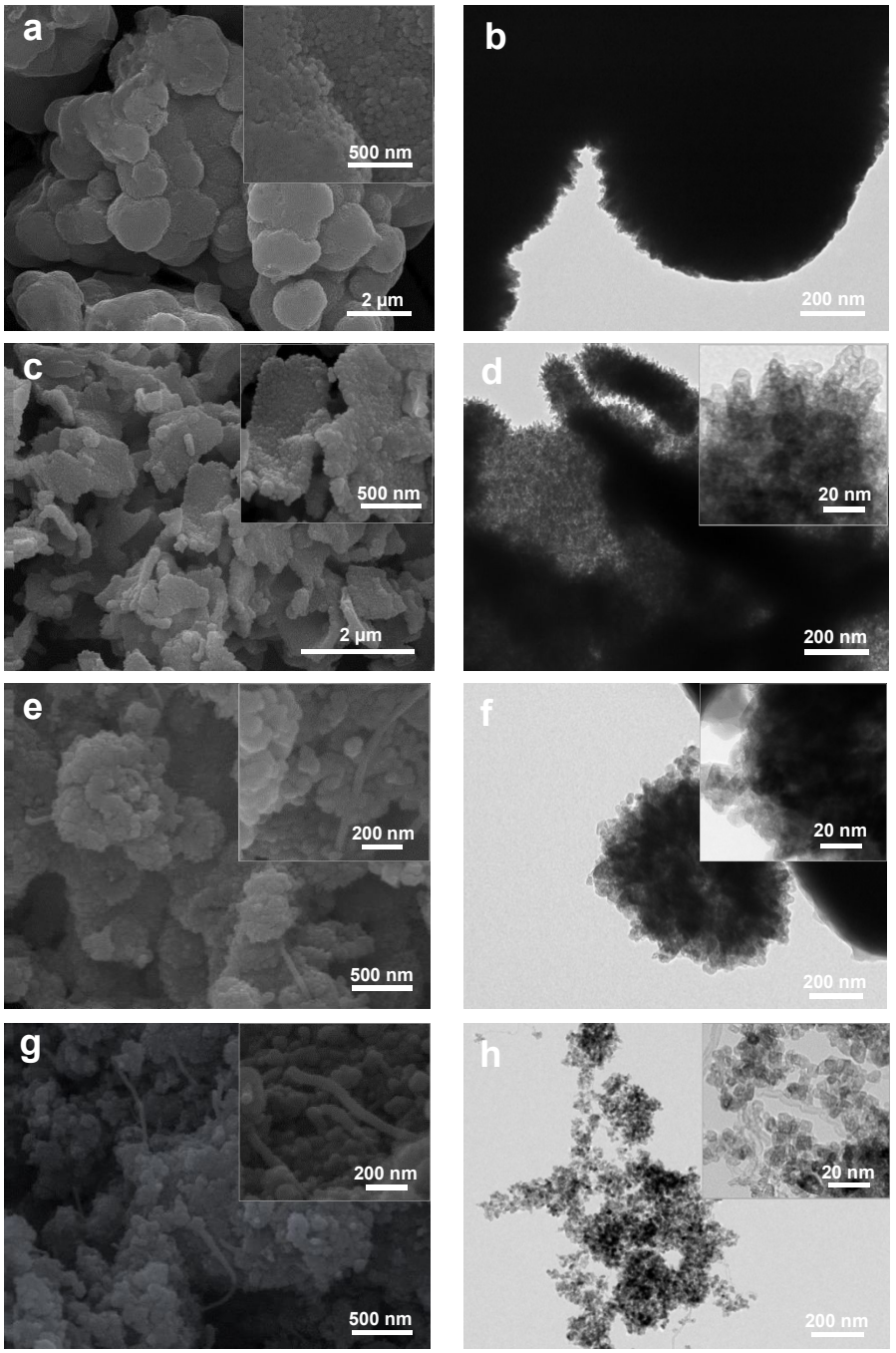

Figure 4.1 – SEM (a, c, e, g) and TEM (b, d, f, h) iages of TiO_2 (a, b), GO-TiO_2-4 (c, d), CNT-TiO_2-4 (e, f) and CNT-TiO_2-20 (g, h).

In terms of optical properties (Figure 4.2), neat TiO_2 shows the characteristic absorption sharp edge rising at 400 nm due to the bandgap transition of the semiconductor, while the carbon-based TiO_2 composites show absorption in the full spectral range.

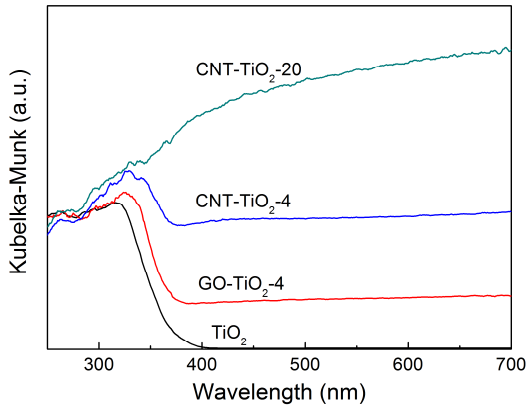

Figure 4.2 – DRUV-Vis spectra of neat TiO_2 and carbon-based TiO_2 materials.

The increase in absorption shown by carbon-TiO_2 composites, mostly in the visible spectral range, has been ascribed in previous studies to the inherent light absorption capacity of carbon materials and also to the possibility of being photoexcited, in this way promoting electronic transitions between carbon and TiO_2 phases [12, 13]. This increase in light absorption is normally proportional to the carbon content, as observed for CNT-TiO_2-4 and CNT-TiO_2-20. For the composites prepared with different carbon sources but with the same carbon content, CNT-TiO_2-4 and GO-TiO_2-4, the higher absorption observed in the visible range for the former can be attributed to some phase segregation, as observed in Figure 4.1e, with the prevalence of visible light absorption by naked CNT. In the case of GO-TiO_2-4, microscopy results (Figures 4.1c and 4.1d) show that GO sheets are uniformly covered by TiO_2. This good assembly between carbon and TiO_2 phases is normally an important requirement for enhanced charge mobility in this type of composite materials upon photoexcitation [12].

ATR-FTIR spectra of neat TiO_2, CNT, GO and the respective carbon-based TiO_2 composites are depicted in Figure 4.3. The ATR spectrum recorded for neat TiO_2 shows mainly a broad band situated between 2500 and 3600 cm^{-1}, associated with stretching vibrations of hydrogen bonded surface water molecules and hydroxyl groups. This is confirmed by the presence of some weak bands around 1630 cm^{-1} caused by bending vibration of coordinated water as well as from the Ti-OH group [30, 31]. The spectra of neat TiO_2 and all the carbon-based TiO_2 composites show a

characteristic band associated to TiO_2 materials (between 800 and 950 cm^{-1}), corresponding to Ti-O-Ti bonds [32].

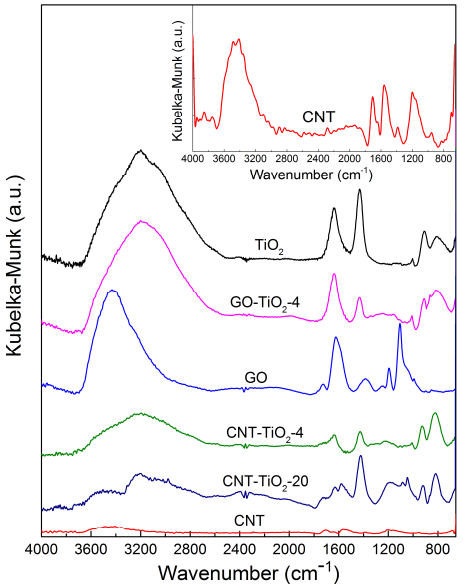

Figure 4.3 – ATR spectra of neat TiO_2, CNT, GO and respective carbon-based TiO_2 composites.

In the case of GO, a broad band situated around 3000-3500 cm^{-1} is assigned to the vibration of C-OH groups. The absorption band at 1720 cm^{-1} is attributed to carbonyl groups, C=O. The band at around 1300-1370 cm^{-1} corresponds to C-OH stretching. The band at 1220 cm^{-1} corresponds to breathing vibrations of epoxy groups (-O-) and the band at 1050 cm^{-1} is attributed to the stretching vibration of C-O groups [32]. The intensity of the peak associated to C-O (hydroxyl and epoxy) decreased significantly in the GO-TiO_2-4 composite, suggesting TiO_2 anchoring to GO preferentially through these sites. The absorption band at around 1600 cm^{-1} can be assigned to the skeletal vibration of graphene sheets. A peak was observed at 1530-1560 cm^{-1} in the CNT spectrum (Figure 4.3 inset), indicating the existence of carbon double bonds (C=C) and confirming the hexagonal-ring structure of the CNT walls. The presence of the peak at 1720 cm^{-1} corresponds to the stretching vibration of carbonyl groups (C=O), generated by the oxidation treatment performed over pristine CNT. The lower peak intensities in the CNT spectrum in comparison with the GO spectrum suggest the presence of larger amounts of oxygen surface groups in GO.

The surface chemistry of GO and CNT was modified by introducing oxygenated surface groups during the oxidation treatments. In general, the presence of oxygenated groups improves the interaction between the carbon phase and TiO_2 particles by the formation of Ti–O–C bonds and promoting TiO_2 dispersion during the synthesis procedure.

TPD analysis was used for the determination and quantification of chemical oxygen species present at the surface of the GO and oxidized CNT. Oxygen surface groups on carbon materials are thermally decomposed into CO and CO_2, being possible to identify and quantify particular functional groups from TPD spectra [33, 34].

The TPD profiles of the groups evolved respectively as CO and CO_2 from the surface of the carbon materials used in this work are shown in Figures 4.4a and 4.4b.

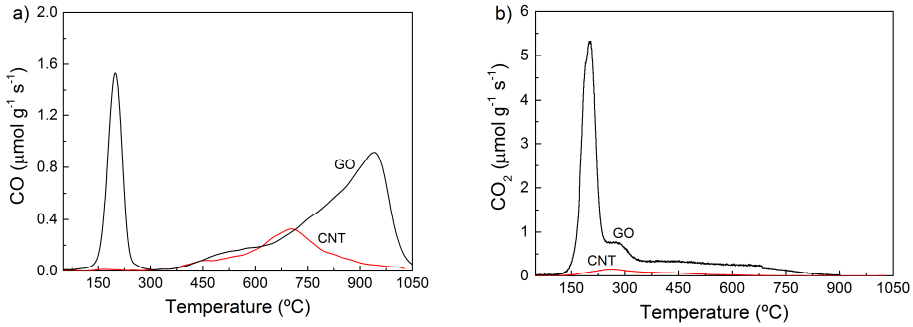

Figure 4.4 – TPD profiles of GO and CNT: (a) CO and (b) CO_2 release.

The oxygen amounts evolved during the TPD experiments are significantly larger for GO (23.6 *wt.*%) than for CNT (ca. 3.1 *wt.*%). These larger amounts of CO and CO_2 detected for GO (4156 and 5305 µmol g^{-1}, respectively), in comparison to CNT (1066 and 434 µmol g^{-1}, respectively), correspond to a larger amount of oxygen surface groups. This can be related with the less severe oxidation treatment performed over CNT in comparison to that used over GO.

Regarding the CO and CO_2 spectra obtained for the GO sample, it is noteworthy the presence of an intense peak at low temperature (~198 ºC) assigned to the epoxy and hydroxyl groups located on basal planes of GO, as previously reported [35, 36]. The CO profile (Figure 4.4a) shows other oxygen surface groups, including carboxylic acids/~237-297 ºC, carboxylic anhydrides/~437-517 ºC, phenols/~627-677 ºC, and carbonyl/quinone groups/~787-1027 ºC. Analyzing the CO_2-TPD spectra (Figure 4.4b), carboxylic acids groups/~227-277 ºC, as well as anhydride groups/~327-487 ºC and lactone groups/~607-707 ºC are also present in the carbon

materials [20, 35]. The high oxygen content on the GO surface can explain its high dispersion in the solution during the preparation of the GO-TiO_2-4 composite, as well as the good assembly of the TiO_2 particles on GO (Figure 4.4c). The TPD analysis is also in agreement with the results of ATR spectroscopy (Figure 4.3), in which more intense peaks were observed for the GO-TiO_2-4 material, in comparison with CNT-TiO_2 composites, due to the higher amount of oxygen groups in GO.

4.3.2. Photocatalytic degradation of MC-LA using GO-TiO_2 and CNT-TiO_2

In order to understand the photo-induced degradation reaction and the role played by the carbon materials in the photocatalytic process, composites were used under simulated solar light and visible light irradiation. Blank experiments under both irradiation conditions and in the absence of any catalyst were also performed for comparison purposes. MC-LA is a very light-stable contaminant, since direct photolysis, *i.e.*, in the absence of a photocatalyst, is negligible under both simulated solar light (Figure 4.5a) and visible light irradiation (Figure 4.5b).

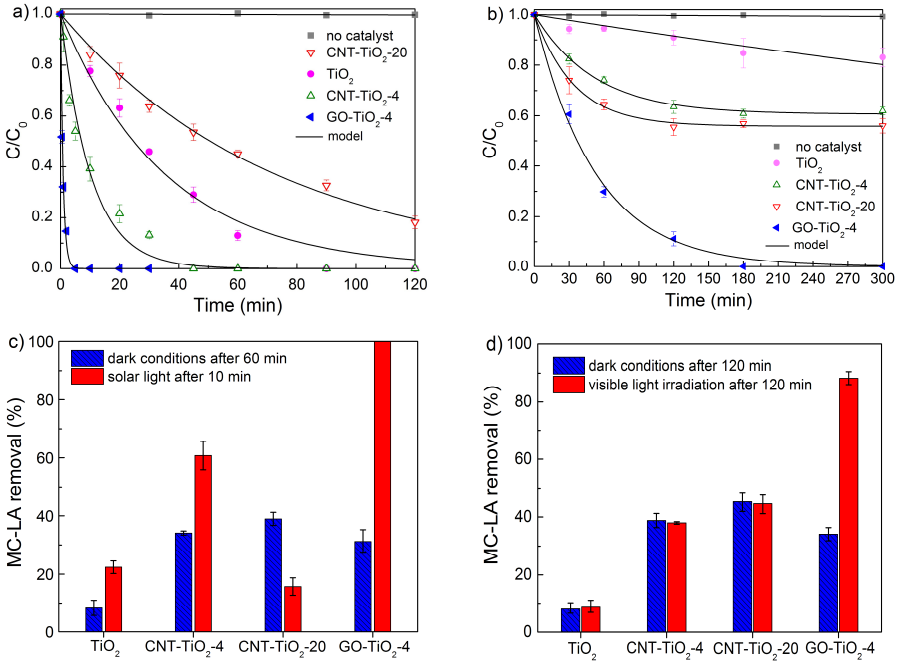

Figure 4.5 – Normalized concentration of MC-LA (C/C_0) using neat TiO_2 and carbon-based TiO_2 composites under simulated solar light (a) and under visible light (b) irradiation. Respective photolysis (no catalyst) is also shown for comparison. MC–LA removal (%) in dark conditions and under simulated solar light (c) and under visible irradiation (d).

Control experiments under dark conditions (absence of light) were also performed to evaluate the extent of adsorption of MC-LA on the tested materials (Figures 4.5c

and 4.5d). All the photocatalytic and adsorption experiments were performed independently. Results show that the adsorption equilibrium is established after 60 min for all the photocatalysts tested, as previously confirmed by performing dark adsorption runs for 5 h (Appendix, Figure A.3).

A synergistic effect between the carbon phase and TiO_2 particles is shown in Figures 4.5a and 4.5c. The magnitude of this effect depends on the nature and content of the carbon material. Among the photocatalysts containing 4 *wt.%* of carbon phase, the highest photocatalytic performance under simulated solar light was found for the GO-TiO_2-4 composite (k_{app} = 116$\times 10^{-2}$ min^{-1}). The results revealed that after 5 min of solar light irradiation, the GO-TiO2-4 composite produced the complete removal of MC-LA, while this was achieved only after 90 min with neat TiO_2.

The synergistic effect could be attributed to the interfacial charge transfer process that can effectively inhibit electron−hole recombination, allowing GO-TiO_2-4 to generate a higher amount of reactive radicals when compared with neat TiO_2 [19, 21]. Also, the good assembly and interfacial coupling between GO and TiO_2 particles, as observed by SEM and TEM (Figures 4.1c and 4.1d, respectively), could explain the high efficiency of the GO-TiO_2-4 composite.

Recalling the results showed in chapter 3, it was found that 20 *wt.*% of CNT is the optimal load for the degradation of different organic compounds (methylene blue and phenolic compounds), yet using different preparation methods for the synthesis of the CNT-TiO_2 composites. In fact, CNT-TiO_2 composites with different carbon loads have been investigated in a number of studies [12, 28]. In most cases TiO_2 nanoparticles were loaded onto or randomly mixed with CNTs, and the photocatalytic activity of the resulting materials increased with the CNT content up to optimal value and then decrease.

In the present study, results show an increase in k_{app} (9.87$\times 10^{-2}$ min^{-1}) for the CNT-TiO_2 composites containing 4 *wt.*% of CNT, when compared with neat TiO_2 (2.77$\times 10^{-2}$ min^{-1}) under simulated solar light. However, the increase of the CNT load to 20 *wt.*% (CNT-TiO_2-20) led to a decrease in the efficiency of MC-LA removal compared with neat TiO_2. This different behavior can be attributed to the different physical-chemical, morphological and optical properties of the composites resulting from different synthesis procedures, which will influence the photoefficiency of the resulting materials. The weak interaction between the CNT and TiO_2 particles would clearly affect the interfacial charge transfer process that can effectively inhibit electron-hole recombination. These results underline the importance of controlling the

carbon load and the preparation method of the composites in order to achieve an optimal synergistic interaction between the carbon material and TiO_2.

The photocatalytic activity of the carbon-based TiO_2 composites for the degradation of MC-LA under visible light irradiation was also evaluated (Figure 4.5d). Once again, the results show that the GO-TiO_2-4 composite exhibited the highest photocatalytic activity, with 88% removal of MC-LA after 120 min and complete conversion after 180 min (k_{app} = 1.87$\times 10^{-2}$ min^{-1}). These results can be attributed to the role of GO as photosensitizer, enabling electron transfer to TiO_2 upon visible excitation. The activity of neat TiO_2 was negligible at such conditions due to its low absorption in the visible spectral range (λ > 400 nm). For CNT-TiO_2-4 and CNT-TiO_2-20 composites, results reveal that the removal of MC-LA under visible light was mostly due to the adsorption of MC-LA on these materials. CNTs normally enhance the activity of TiO_2 due to their structural and electronic properties [12, 37]. However, a different behavior was found in the degradation of MC-LA under visible light. The negligible photocatalytic activity observed can be attributed to the very low amount of oxygen surface groups as observed by TPD analysis that leads to a weak interaction between TiO_2 and CNT.

Overall, the above results showed that the carbon phase improve significantly the photocatalytic activity of TiO_2 for MC-LA degradation. In addition, nanodiamonds due to their unique features are being increasingly used in a wide variety of applications ranging from nanomedicine, biotechnology, catalysis, etc. [38], thus an alternative carbon materials towards the development of efficient photocatalysts upon combination with TiO_2. As mentioned before, *Pastrana-Martinez et al.* [16] reported a significant improvement in the photocatalytic activity when NDs were combined with TiO_2, using an optimal content of oxidized NDs (*i.e.*, 15 *wt.* % of ND) for degradation of diphenhydramine. Therefore, the present study was extended using nanodiamond as carbon phase for preparation of a composite with 15 *wt.*% oxidized ND content (ND-TiO_2-15) and its application on the degradation of MC-LA under both visible and simulated solar light.

4.4. Effect of nanodiamond on TiO_2 matrix

4.4.1. Characterization of nanodiamond-TiO_2 based materials

The carbon content was determined by thermogravimetric analysis. The catalysts (TiO_2 and ND-TiO_2-15) were submitted to a thermal treatment under air flow and the

weight loss was monitored. The obtained results were in agreement with the nominal carbon content (*i.e.*, 15 *wt.%*). As already seen before the S_{BET} for TiO_2 was 118 $m^2\ g^{-1}$ (Table 4.1). For the ND and ND-TiO_2-15 the S_{BET} were 253 and 81 $m^2\ g^{-1}$, respectively [16]. The S_{BET} of the ND-TiO_2-15 composite (81 $m^2\ g^{-1}$) was lower than the nominal value (138 $m^2\ g^{-1}$) obtained by the weighted average of the S_{BET} of ND and TiO_2 phases in the composite material (*i.e.*, taking into account their relative weight contents), evidencing the contact between the surface of both phases or the formation of larger TiO_2 particles when the composite is prepared.

The X-ray powder diffractograms of TiO_2, ND and ND-TiO_2-15 composite are shown in Figure 4.6.

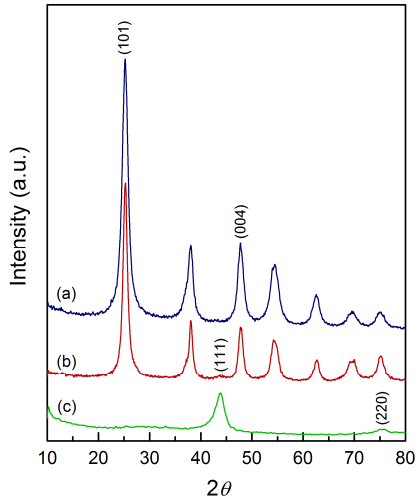

Figure 4.6 – XRD diffractograms of TiO_2 (a), ND-TiO_2-15 (b) and ND (c) materials.

The presence of crystalline anatase TiO_2 is confirmed by XRD measurements, where the peaks at 25.1º and 47.6º correspond to the lattice plane of (101) and (004), respectively. The anatase crystallite size, determined by Rietveld refinement from the XRD data is around 8 nm. The XRD analysis of ND shows two signals at 44.0º and 75.3º, resulting from the diamond reflection (111) and (220) planes, respectively [39]. The crystallite dimension found for ND was 5 nm. The diffractogram of ND-TiO_2-15 composite was similar to that obtained in the case of TiO_2 (Figure 4.6) with a small contribution of (111) reflection of ND. No significant change on the crystallite size of ND was observed for ND-TiO_2-15 composite. Nevertheless, the crystallite dimension of TiO_2 slightly increases to 11 nm, which could be related with the lower S_{BET} of the composite in comparison with the respective nominal value. This increase in the crystallite TiO_2 dimensions has been previously reported for oxidized carbon

nanotube-TiO_2 composites, being attributed to the competition of the TiO_2 precursor species to the oxidized sites at the surface of the carbon material during the synthesis process, affecting the size of the TiO_2 crystallites [12].

DRIFT analysis was performed for investigating possible interactions between TiO_2 and ND, and the results are depicted in Figure 4.7. The DRIFT spectrum recorded for TiO_2 shows a broad band located between 2500 and 3800 cm^{-1} ascribed to the stretching vibrations of hydrogen-bonded surface water molecules and hydroxyl groups. These observations are confirmed by the presence of a weak band centered at 1640 cm^{-1} associated to the bending vibration of water molecules as well as the presence of Ti-OH bonds [40, 41]. A typical band of TiO_2 materials around 970 cm^{-1} due to the Ti-O vibration was also observed [40] while the sharp peak at 1420 cm^{-1} can be assigned to the lattice vibrations of TiO_2 [42, 43].

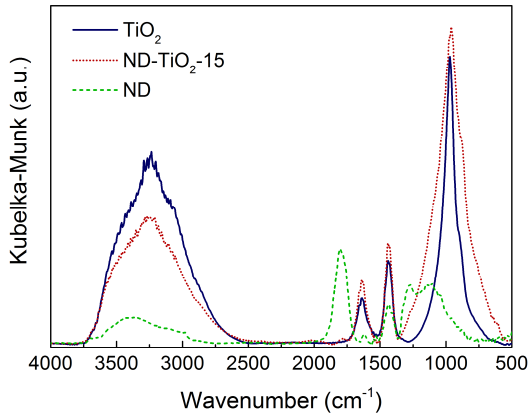

Figure 4.7 – DRIFT spectra of ND, TiO_2 and ND-TiO_2-15 materials.

The DRIFT spectrum of ND shows characteristic bands of surface oxidized carbon materials, with a broad band around 3400 cm^{-1} that can be usually attributed to vibration of C-OH groups of carboxylic acids and phenols, and to adsorbed water as confirmed by the presence of a OH bending mode at 1640 cm^{-1}. A small shoulder at *c.a.* 3000 cm^{-1} attributed to C-H stretching is also observed. The band at 1800 cm^{-1} can be assigned to the vibration of C=O bonds in carboxylic acids, carboxylic anhydrides, quinones and lactones, while the band peaking at 1470 cm^{-1} corresponds to C=C aromatic bending [24]. The bands in the range 1000 to 1300 cm^{-1} are characteristic of C-O stretching vibrations from anhydrides and lactones.

As previously reported [16] the temperature programmed desorption (TPD) analysis of ND revealed that carboxylic acid groups are not present at the surface of ND since the oxidation treatment was carried out at a temperature (430 ºC) higher

than the decomposition temperature of these functional groups (around 230-376 ºC) [16, 33, 34]. Therefore, carboxylic anhydrides, lactones, phenols and carbonyl/quinone are the main oxygen groups present on the surface of ND.

Regarding the DRIFT spectrum of the ND-TiO_2-15 composite, the broadening of the intense band centered at 970 cm^{-1} (characteristic of Ti-O) can be assigned to Ti-O-C bonds [44], thus suggesting the creation of an heterojunction at the interface between ND and TiO_2. The bands at *c.a.* 1640 and 1470 cm^{-1} became more intense in the spectrum of the composite, resulting from the additive contribution of the vibration bands observed for both TiO_2 and ND phases. Yet, the ND band at 1800 cm^{-1} corresponding to carbonyl group vibration practically disappeared, while the broad band at 3400 cm^{-1} became less intense, indicating the existence of an interphase interaction between ND and TiO_2.

XPS deconvolution spectra of the of Ti 2p, C 1s and O 1s binding regions of TiO_2 and the ND-TiO_2-15 composite were performed in order to identify possible chemical interactions between the elements in the near surface range. The XPS spectrum of Ti 2p region for ND-TiO_2-15 composite (Figure 4.8a) shows two peaks at binding energies of 458.8 and 464.5 eV, corresponding respectively to Ti $2p_{3/2}$ and Ti $2p_{1/2}$ spin-orbital splitting photoelectrons (5.7 eV) in the Ti^{4+} chemical state [15, 45] as also observed for neat TiO_2. In contrast, the spectra of O 1s core level for TiO_2 (Figure 4.8b) and ND-TiO_2-15 (Figure 4.8c) were slightly different (insight of Figure 4.8c is shown for better comparison).

While neat TiO_2 exhibits two peaks centered at 529.9 eV and 531.1 eV in the O 1s spectrum (Figure 4.8b), which are due to the lattice of Ti-O bond and –OH groups, respectively, the deconvolution fitting for the ND-TiO_2-15 composite shows three constituents centered at 529.9, 531.1 and 532.7 eV (Figure 4.8c), that could be attributed to the presence of Ti-O, -OH and carbon phase (C-O) bonds, respectively [46, 47].

In the case of the C 1s core level spectra, carbon bonds were identified for neat TiO_2, probably resulting from some organic species that were not removed by the thermal treatment (N_2, 473 K). Even so, it was possible to conclude that C-O (287.0 eV) [48, 49] is the main bond in the composite (as expected due to the known carbon sp^3 hybridization in diamonds), followed by C-C/C-H (285.0 eV) and C=O (288.9 eV) [38,39], while other type of chemical bonds cannot be confirmed by this characterization technique. These results are in agreement with TPD analysis [12], where phenol or ether (C-OH, C-O-C; 286.3 eV [47]) and quinone (C=O) groups were

detected, while carboxylic acids (-COOH), carboxylic anhydrides (-C(O)$_2$O) and lactones (-COO) were not identified in the composite.

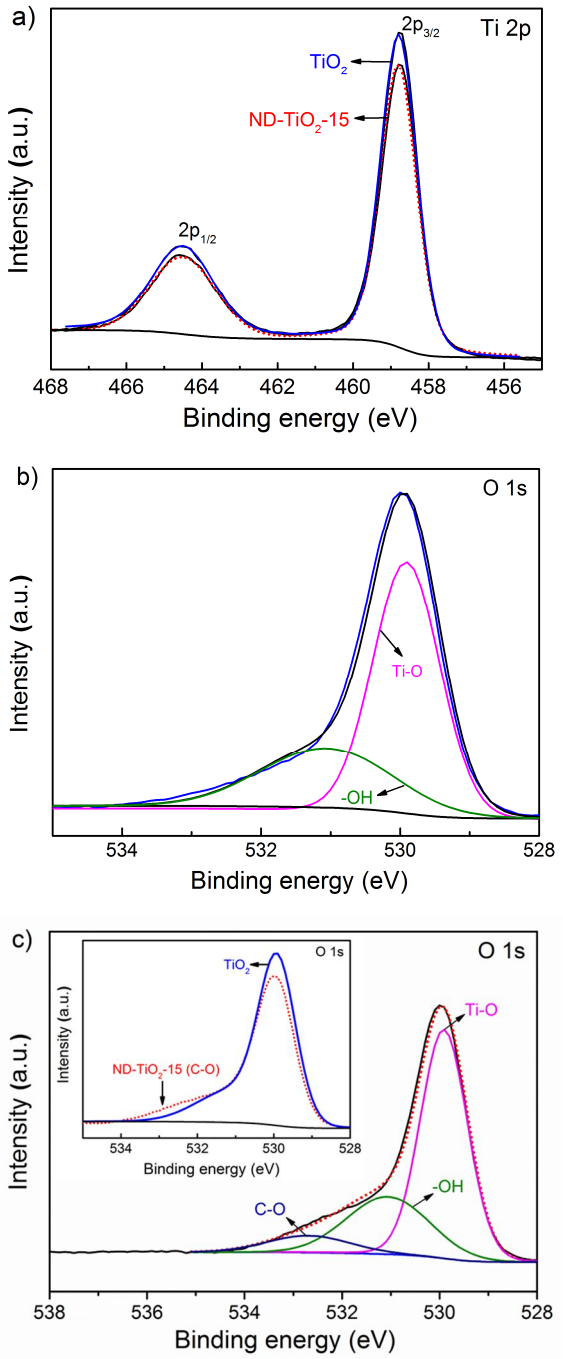

Figure 4.8 – XPS peak deconvolution of the binding energy regions: (a) Ti 2p for TiO_2 and ND-TiO_2-15, (b) O 1s for TiO_2, (c) O 1s for ND-TiO_2-15 (inset: comparison of O 1s spectra).

Several authors [38, 50] have reported that detonated NDs when dispersed in liquid medium induce strong particle aggregation, attributing the phenomenon to the harsh conditions in the detonation chamber that leads to the creation of dandling bonds on the ND surface. The free electron surfaces can cooperate via intermolecular surface forces such as van der Waals and hydrogen bonding creating covalent bonds between the primary particles [38]. This finding combined with the air oxidation treatment of NDs, which has been proved to increase the functional groups at the surface of NDs [16], can promote the interphase interaction between ND and TiO_2.

Figure 4.9 shows the DR UV-Vis spectra of the photocatalysts. A characteristic absorption sharp edge rising at 400 nm was observed for TiO_2.

For this material, the valence band (VB) is composed of O 2p states and the conduction band (CB) is composed of Ti 3d states. The 330 nm absorption band is attributed to the charge transfer from O 2p to Ti 3d [51]. In case of the ND-TiO_2-15 spectrum it was notice that the TiO_2 band is blue-shifted by the incorporation of ND and a decrease in the shoulder tail in the UV range being also observed. These observations can be attributed to the creation of site defects at the TiO_2 crystalline structure, which can be linked with the carbon phase.

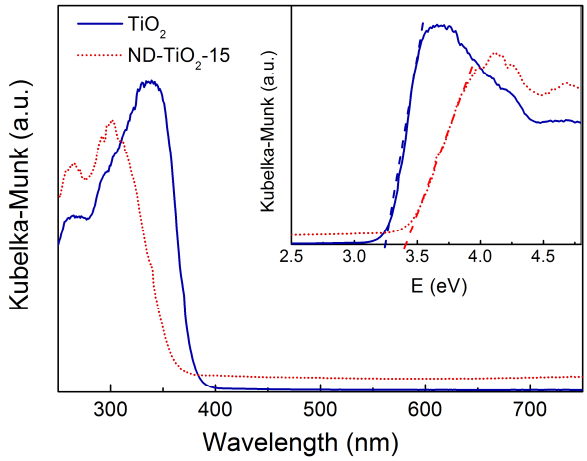

Figure 4.9 – DR UV-Vis spectra of TiO_2 and ND-TiO_2-15, and plot of Kubelka–Munk units as a function of the light energy (inset).

The transformed Kubelka-Munk function was plotted as a function of the energy of light (inset Figure 4.9) for the determination of the bandgap of the semiconductor materials. The band gaps for TiO_2 and ND-TiO_2-15 were estimated as 3.26 and 3.41 eV, respectively. Quantum size and electronic interphase effects may constitute the major contributions for the increase of the bandgap energy of the composite

material. Also, the high band gap of ND (5.0 eV [52, 53]) when mixed with TiO_2 may contribute to the increase of the band gap energy of the resulting composite material.

The representative SEM micrographs of ND, and ND-TiO_2-15 are shown in Figures 4.10a and 4.10c, respectively (higher magnifications are shown as insets). As already seen in Figure 4.1a neat TiO_2 shows spherical-like particles aggregated to form larger (micron-size) particles and consisting of small anatase crystallites as determined by XRD analysis.

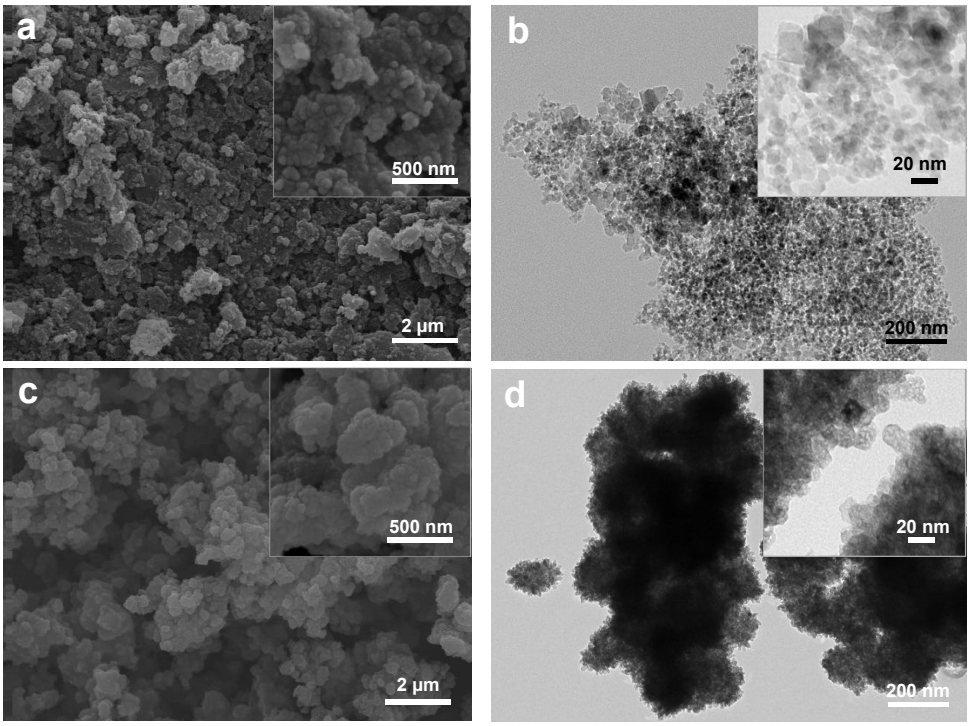

Figure 4.10 – SEM (a, c) and TEM (b, d) images of neat ND, and ND-TiO_2-15, respectively.

It is known that when NDs are functionalized with oxygen-containing functional groups, the microscale morphology consists of small nanoparticles forming porous aggregates (as observed in Figure 4.10a) due to hydrogen bonding and van der Waals forces between the particles [52]. ND-TiO_2-15 shows a convoluted morphology, where particles of very small dimensions are grouped forming composite clusters (Figure 4.10c).

The TEM micrographs of ND (Figure 4.10b) reveal that the aggregates are formed by small (~5 nm) nanoparticles of NDs confirming the value obtained by XRD analysis. The TEM micrograph of the ND-TiO_2-15 composite reveals a homogeneous

distribution of TiO_2 and ND particles forming small clusters (Figure 4.10d) of okenite-like structures.

4.4.2. Photocatalytic degradation of MC-LA using nanodiamond-TiO_2 composite

The photocatalytic activity of ND and ND-TiO_2-15 materials was assessed in the degradation of MC-LA under simulated solar and visible light irradiation and compared with neat TiO_2. As discussed before, MC-LA is resistant under such conditions, while the photocatalytic degradation of MC-LA under simulated solar light follows a pseudo-first order rate law (Figure 4.11).

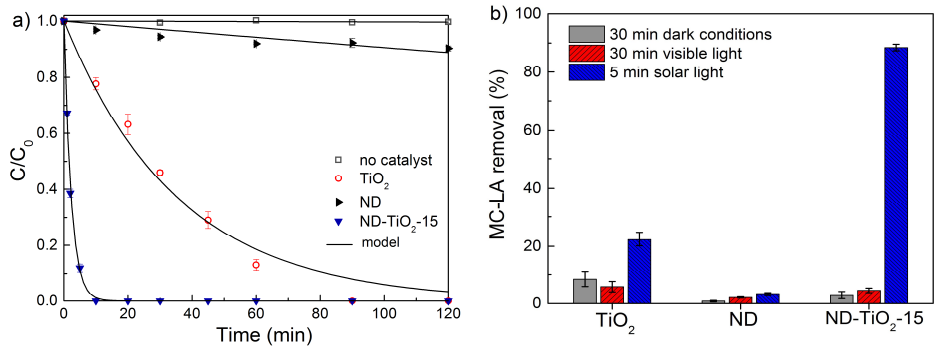

Figure 4.11 – (a) Normalized concentration of MC-LA (C/C_0) using the different materials under simulated solar light. (b) MC-LA removal under dark conditions and both visible and solar light irradiation.

The k_{app} determined by non-linear curve fitting to the experimental data, indicate that no appreciable MC-LA degradation when the pristine ND sample was used (k_{app}= 9.8×10^{-4} min^{-1}), while the introduction of ND to the TiO_2 matrix produced a notorious increase in the photocatalytic activity. In fact, ND-TiO_2-15 (k_{app} = 4.42×10^{-1} min^{-1}) exhibits a k_{app} more than fifteen times larger than that for neat TiO_2 (k_{app} = 2.77×10^{-2} min^{-1}).

Superior surface area and narrow band gap are normally required attributes for enhanced efficiency of photocatalysts. However, these factors are not likely to be the main features contributing to the high efficiency observed for the ND-TiO_2-15 composite when compared to the sole ND and TiO_2 phases.

Despite the high band gap of diamond, *Nebel* [54] inferred that this material could be a good candidate for photocatalytic applications due to its inert chemistry and stability in liquids. The functional groups on the surface of air oxidized NDs, such as

oxygen and hydroxyl species, can create a surface dipole layer that could affect their interfacial electron affinity.

In other works, researchers even demonstrated that the presence of hydrogen bonds on H-terminated diamond surfaces could shift the conduction band above the vacuum energy level and the electrons can be directly transferred to the surrounding medium via surface states [55, 56].

In view of the above findings, the good dispersion of ND and TiO_2 phases during the synthesis of the composite material can promote the creation of strong electronic interphase interactions, as inferred from its characterization. Therefore, beneficial synergies and cooperative effects between the semiconductor and the carbon phase are expected, where electrons could be transferred from the ND conduction band to the TiO_2 conduction band as well as the holes transferred from the TiO_2 valence band to the ND valence band under light excitation. Thus, the separation of the photogenerated charges is facilitated, decreasing the occurrence of electron-hole recombination and leading to an increase of the ND-TiO_2-15 photocatalytic activity.

Experiments under dark conditions were also performed to establish the adsorption equilibrium between MC-LA and the photocatalysts. As shown in Figure 4.11b, no significant adsorption was observed after 30 min, with a decrease of only 8%, 1% and 3% of the initial MC-LA concentration being observed using neat TiO_2, ND, and ND-TiO_2-15, respectively. In addition, it is important to refer that 30 min was proved to be sufficient to reach the adsorption equilibrium, as previously confirmed by performing dark adsorption runs for 5 h.

The results also show that the removal of MC-LA using TiO_2 or ND-TiO_2-15 is negligible (Figure 4.11b) under visible light illumination (30 min), which is attributed to the large band gap energies of these materials [54] and thus low light absorption in the visible spectral range. Even after 5 h of reaction it was observed an apparent MC-LA removal of 3.6 % being essentially related to adsorption. The wide band gap of NDs (~5 eV) [52-54] may also explain the inactiveness of ND when irradiated at $\lambda > 400$ nm.

In summary, TiO_2-based composites using GO and CNT as carbon phase (GO-TiO_2-4 and CNT-TiO_2-4, respectively) have revealed efficient under simulated solar light, and in particular the GO-TiO_2-4 composite under visible light radiation. A synergistic effect was found between the carbon and the TiO_2 phase, but low band gap energies were determined for these materials (2.95 eV and 3.04 eV for GO-TiO_2-4 and CNT-TiO_2-4, respectively). In particular, the lower band gap energy of

GO-TiO_2-4 resulted in the best performance under visible light illumination. In contrast, negligible activity was observed when ND-TiO_2-15 was tested under visible light due to the higher band gap of this composite (3.41 eV). Yet, improved efficiency was observed under solar irradiation (which includes UV-photoexcitation). Therefore, the low efficiency of ND-TiO_2-15 under only visible illumination seems to be related with the optical properties of both TiO_2 and ND materials. However, the ND-TiO_2-15 composite it revealed to be highly efficient under real field conditions (*i.e.*, solar light irradiation), thereby of major relevance for solar applications.

4.5. MC-LA reaction intermediates using neat TiO_2 and GO-TiO_2

The above results demonstrated that the presence of carbon materials in a TiO_2 matrix increases the efficiency of the resulting composites. Among the photocatalysts used, GO-TiO_2-4 exhibited the highest efficiency for the degradation of MC-LA. Complete degradation of this pollutant was achieved under both simulated solar light and visible light irradiation.

Identification of intermediate products has been performed for obtaining information about the MC-LA photocatalytic degradation mechanism. An appreciable number of reports have examined the degradation pathway of MC-LR [57, 58], but no reports are found for the degradation of MC-LA. After all the structural similarity between both molecules (they only differ in one amino acid group, arginine for MC-LR and alanine for MC-LA), can be useful for the determination of primary MC-LA intermediates. These intermediates were identified by LC-MS/MS in experiments performed with neat TiO_2 under simulated solar light and with GO-TiO_2-4 under both visible and simulated solar light irradiation. Before identifying the primary intermediates, a scan of the total ion chromatogram (TIC) was performed and distinct peaks were observed.

The products that were detected during the photocatalytic degradation of MC-LA are compiled in Table 4.2 with reference to their molecular formula, mass-to-charge ratio (*m/z*) and retention times (R_t), using the different catalysts. The most intense peaks, corresponding to *m/z* = 926.5 and *m/z* = 944.5, were observed for reactions using either TiO_2 or GO-TiO_2-4 composites with both irradiation systems. Multiple peaks in the TIC were observed for these intermediates, which can represent stereoisomers (differing in the three-dimensional orientation of the bonds) or structural isomers with completely different structures. Two peaks were also observed for the *m/z* = 898.5, 916.5 and 960.5.

Table 4.2 – Reaction intermediates observed for MC-LA degradation using neat TiO_2 and GO-TiO_2-4 photocatalyst under simulated solar (a) and visible light (b) irradiation.

Formula	Peak (*m/z*)	R_t (min)	Catalyst
$C_{46}H_{67}N_7O_{12}$	910.5 (MC-LA)	3.74	-
$C_{35}H_{69}N_5O_{14}$	784.5	2.62	$^{(a)}TiO_2$, $^{(a)}$GO-TiO_2-4
$C_{46}H_{69}N_7O_{15}$	960.5	2.90 3.01	$^{(a)}TiO_2$
$C_{43}H_{67}N_7O_{11}$	858.5	3.16	$^{(a)}TiO_2$, $^{(a)}$GO-TiO_2-4
$C_{45}H_{67}N_7O_{12}$	898.5	3.16 3.27	$^{(b)}$GO-TiO_2-4
$C_{45}H_{67}N_7O_{13}$	914.5	3.16 3.25 3.43	$^{(b)}$GO-TiO_2-4
$C_{42}H_{65}N_7O_{13}$	812.5	3.40	$^{(b)}$GO-TiO_2-4
$C_{45}H_{69}N_7O_9$	916.5	3.14 3.75	$^{(a,b)}$GO-TiO_2-4
$C_{46}H_{69}N_7O_{13}$	926.5	3.23 3.35 3.53	$^{(a)}TiO_2$, $^{(a,b)}$GO-TiO_2-4
$C_{46}H_{69}N_7O_{14}$	944.5	3.21 3.56	$^{(a)}TiO_2$, $^{(a,b)}$GO-TiO_2-4
$C_{43}H_{65}N_7O_{10}$	840.5	3.42	$^{(a)}TiO_2$, $^{(a,b)}$GO-TiO_2-4
$C_{45}H_{65}N_7O_{10}$	864.5	3.75	$^{(a,b)}$GO-TiO_2-4
$C_{44}H_{71}N_3O_{15}$	882.5	3.78	$^{(b)}$GO-TiO_2-4
$C_{44}H_{65}N_4O_9$	836.5	3.82	$^{(b)}$GO-TiO_2-4
$C_{45}H_{69}N_3O_{14}$	876.5	3.83	^{b}GO-TiO_2-4

Under simulated solar light, the majority of the intermediates detected were produced within the first 2 min of irradiation when using the GO-TiO_2-4 composite. A negligible number of intermediates was detected after 10 min, which seems to be attributed to their subsequent and rapid oxidation during the photocatalytic reaction. Nearly the same intermediates were identified when the neat TiO_2 photocatalyst was used under simulated solar light; however, the oxidation of these intermediates was slower in this case. Under visible light illumination, complete conversion of MC-LA was obtained in 180 min when using the GO-TiO_2-4 composite, but the reaction was much

slower than that observed with simulated solar light and, as consequence, more intermediates were detected with visible light illumination.

As mentioned before, MC-LA has a similar structure to MC-LR, consisting of seven amino acid chains, with the Adda (3-amino-9-methoxy-2,6,8-trimethyl-10-phenyl-4,6-decadienoic acid) side chain being largely responsible for the MCs toxicity [59]. Taking into account this information and that already reported in literature [58, 60], a preliminary structural elucidation of the MC-LA degradation pathway is proposed (Scheme 4.2).

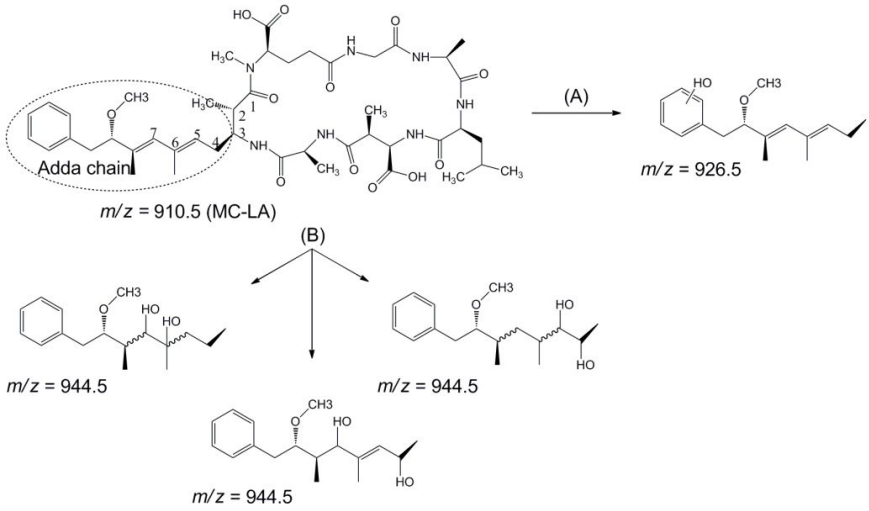

Scheme 4.2 – (A) Attack of hydroxyl radicals on the aromatic ring of MC-LA. (B) Attack of hydroxyl radicals on the conjugated carbon double bonds of MC-LA Adda chain.

Antoniou et al. [58] studied the MC-LR (*m/z* = 995.5) degradation pathway under UV irradiation and observed a peak corresponding to *m/z* = 1011.5, which has been attributed to the addition of a hydroxyl radical (HO•) to one of the aromatic double bonds. Several studies dealing with biomolecules showed that the hydroxylation of aromatic rings is a very common phenomenon [58, 60]. In the case of the photocatalytic degradation of MC-LA (*m/z* = 910.5), using both TiO_2 and GO-TiO_2-4 photocatalysts, an intermediate with a difference of 16 in the *m/z* value was detected, which seems to indicate that the aromatic ring undergoes hydroxyl substitution (HO•) of a hydrogen to form the *m/z* = 926.5 (Scheme 4.2A). The presence of isomers of the intermediate *m/z* = 926.5 seems to indicate that the hydroxylation can occur at different positions of the aromatic ring. Another main intermediate detected corresponds to *m/z* = 944.5 (an *m/z* difference of 34 between MC-LA and the intermediate), which can indicate a HO• radical attack at either bond C_4-C_5 or C_6-C_7 on the Adda chain

(Scheme 4.2B). In studies with MC-LR, this site has been considered as the most prone to be attacked by $HO^{\bullet}$ radicals due to its position [21, 58, 61]. *Antoniou et al.* reported [58] that *m/z* = 1029.5 formation starts with the $HO^{\bullet}$ radical reacting with the diene bonds to produce adducts through the hydroxyl addition and hydroxyl substitution. In our case, the intermediate with *m/z* = 944.5 detected in the degradation of MC-LA seems to correspond to the analogue *m/z* = 1029.5 observed in the degradation of the MC-LR.

Although, the reaction mechanism seems to be mostly driven by $HO^{\bullet}$ radical attack, the formation of reactive species such as radical superoxide anion $O_2^{\bullet-}$ and singlet oxygen ($^1O_2$) may assume a more important role in the photocatalytic mechanism under visible light irradiation [62], which may rationalize the presence of intermediates that were not detected under simulated solar light irradiation. In the present work, the reaction mechanism proposed for the preliminary steps of MC-LA photocatalytic transformation under simulated solar light irradiation seems to follow a similar route to that proposed by Antoniou *et al.* [58] for the photocatalytic degradation of MC-LR when using TiO_2.

Further studies are required, using advanced analytical techniques, for exact identification of all reaction intermediates of MC-LA photocatalytic degradation under different operating conditions.

4.6. Conclusions

The photocatalytic degradation of the cyanotoxin MC-LA under simulated solar light and visible light irradiation was achieved by using carbon-based TiO_2 composites containing 4 *wt.*% of GO, comprising 4 *wt.*% and 20 *wt.*% of oxidized CNT and 15 *wt.*% of oxidized ND. Neat TiO_2 was used as reference.

The efficiency of the photocatalytic process depends on the nature of the carbon material. Among the photocatalysts used, GO-TiO_2-4 exhibited the highest photocatalytic activity under visible and simulated solar light irradiation. The excellent performance of the GO-TiO_2-4 composite can be attributed to the optimal self-assembly between GO and TiO_2 particles. The MC-LA removal observed with CNT-containing composites under visible light irradiation was mostly due to adsorption on the composite material rather than due to photocatalytic degradation.

The ND-TiO_2-15 does not show any activity for the photocatalytic degradation of MC-LA under visible light, which can be explained by the wide band gap of the bare

materials. However, the ND-TiO_2-15 composite shows remarkably enhanced photocatalytic degradation of MC-LA under simulated solar light illumination with a synergistic factor of more than 15 relative to TiO_2, probably due to the good dispersion of both phases in the composite material and the creation of an electronic interphase interaction between the TiO_2 and ND phases.

Preliminary insights to identify MC-LA intermediates are shown for neat TiO_2 and GO-TiO_2-4, under both irradiation conditions. Results suggest that photocatalytic degradation mechanism takes place mostly via hydroxyl radical attack under simulated solar light irradiation.

Overall, this study shows that the GO-TiO_2-4 composite is an efficient photocatalyst for the degradation of MC-LA in water under simulated solar light and also under visible light irradiation, being a promising material for the detoxification of cyanotoxin-contaminated surface water and freshwaters.

References

[1] H.W. Paerl, N.S. Hall, E.S. Calandrino, Controlling harmful cyanobacterial blooms in a world experiencing anthropogenic and climatic-induced change, Sci. Total Environ., 409 (2011) 1739-1745.

[2] P. Rao, N. Gupta, A. Bhaskar, R. Jayaraj, Toxins and bioactive compounds from cyanobacteria and their implications on human health, J. Environ. Biol., 23 (2002) 215-224.

[3] V. Gupta, S.K. Ratha, A. Sood, V. Chaudhary, R. Prasanna, New insights into the biodiversity and applications of cyanobacteria (blue-green algae) – Prospects and challenges, Algal Res., 2 (2013) 79-97.

[4] J.H. Landsberg, The Effects of Harmful Algal Blooms on Aquatic Organisms, Rev. Fisheries Sci., 10 (2002) 113-390.

[5] Y. Lone, R.K. Koiri, M. Bhide, An overview of the toxic effect of potential human carcinogen Microcystin-LR on testis, Toxicol. Rep., 2 (2015) 289-296.

[6] J. Jia, W. Luo, Y. Lu, J.P. Giesy, Bioaccumulation of microcystins (MCs) in four fish species from Lake Taihu, China: Assessment of risks to humans, Sci. Total Environ., 487 (2014) 224-232.

[7] A. Zastepa, F.R. Pick, J.M. Blais, Fate and Persistence of Particulate and Dissolved Microcystin-LA from Microcystis Blooms, Human and Ecological Risk Assessment: Inter. J., 20 (2013) 1670-1686.

[8] S. Merel, D. Walker, R. Chicana, S. Snyder, E. Baurès, O. Thomas, State of knowledge and concerns on cyanobacterial blooms and cyanotoxins, Environ. Inter. 59 (2013) 303-327.

[9] R.M. Dawson, the toxicology of microcystins, Toxicon, 36 (1998) 953-962.

[10] C. Han, M. Pelaez, V. Likodimos, A.G. Kontos, P. Falaras, K. O'Shea, D.D. Dionysiou, Innovative visible light-activated sulfur doped TiO_2 films for water treatment, Appl. Catal. B: Environ., 107 (2011) 77-87.

[11] C. Han, J. Andersen, V. Likodimos, P. Falaras, J. Linkugel, D.D. Dionysiou, The effect of solvent in the sol–gel synthesis of visible light-activated, sulfur-doped TiO_2 nanostructured porous films for water treatment, Catal. Today, 224 (2014) 132-139.

[12] C.G. Silva, J.L. Faria, Photocatalytic oxidation of benzene derivatives in aqueous suspensions: Synergic effect induced by the introduction of carbon nanotubes in a TiO_2 matrix, Appl. Catal. B: Environ., 101 (2010) 81-89.

[13] B. Gao, C. Peng, G.Z. Chen, G. Li Puma, Photo-electro-catalysis enhancement on carbon nanotubes/titanium dioxide (CNTs/TiO_2) composite prepared by a novel surfactant wrapping sol–gel method, Appl. Catal. B: Environ., 85 (2008) 17-23.

[14] S. Morales-Torres, L. Pastrana-Martínez, J. Figueiredo, J. Faria, A.T. Silva, Design of graphene-based TiO_2 photocatalysts – a review, Environ. Sci. Pollut. Res., 19 (2012) 3676-3687.

[15] L.M. Pastrana-Martínez, S. Morales-Torres, V. Likodimos, J.L. Figueiredo, J.L. Faria, P. Falaras, A.M.T. Silva, Advanced nanostructured photocatalysts based on reduced graphene oxide-TiO_2 composites for degradation of diphenhydramine pharmaceutical and methyl orange dye, Appl. Catal. B: Environ., 123-124 (2012) 241-256.

[16] L.M. Pastrana-Martínez, S. Morales-Torres, S.A.C. Carabineiro, J.G. Buijnsters, J.L. Faria, J.L. Figueiredo, A.M.T. Silva, Nanodiamond-TiO_2 composites for heterogeneous photocatalysis, ChemPlusChem, 78 (2013) 801-807.

[17] A.M. Schrand, S.A.C. Hens, O.A. Shenderova, Nanodiamond Particles: Properties and Perspectives for Bioapplications, Crit. Rev. Sol. State Mater. Sci., 34 (2009) 18-74.

[18] O.A. Shenderova, V.V. Zhirnov, D.W. Brenner, Carbon Nanostructures, Crit. Rev. Sol. State Mater. Sci., 27 (2002) 227-356.

[19] L.M. Pastrana-Martínez, S. Morales-Torres, S.K. Papageorgiou, F.K. Katsaros, G.E. Romanos, J.L. Figueiredo, J.L. Faria, P. Falaras, A.M.T. Silva, Photocatalytic behaviour of nanocarbon–TiO_2 composites and immobilization into hollow fibres, Appl. Catal. B: Environ., 142–143 (2013) 101-111.

[20] R.R.N. Marques, M.J. Sampaio, P.M. Carrapiço, C.G. Silva, S. Morales-Torres, G. Dražić, J.L. Faria, A.M.T. Silva, Photocatalytic degradation of caffeine: Developing solutions for emerging pollutants, Catal. Today, 209 (2013) 108-115.

[21] T. Fotiou, T.M. Triantis, T. Kaloudis, L.M. Pastrana-Martínez, V. Likodimos, P. Falaras, A.M.T. Silva, A. Hiskia, Photocatalytic Degradation of Microcystin-LR and Off-Odor Compounds in Water under UV-A and Solar Light with a Nanostructured

Photocatalyst Based on Reduced Graphene Oxide–TiO_2 Composite. Identification of Intermediate Products, Ind. Eng. Chem. Res., 52 (2013) 13991-14000.

[22] W.S. Hummers, R.E. Offeman, Preparation of Graphitic Oxide, J. Am. Chem. Soc., 80 (1958) 1339-1339.

[23] S. Osswald, G. Yushin, V. Mochalin, S.O. Kucheyev, Y. Gogotsi, Control of sp^2/sp^3 Carbon Ratio and Surface Chemistry of Nanodiamond Powders by Selective Oxidation in Air, J. Am. Chem. Soc., 128 (2006) 11635-11642.

[24] O. Shenderova, A.M. Panich, S. Moseenkov, S.C. Hens, V. Kuznetsov, H.M. Vieth, Hydroxylated Detonation Nanodiamond: FTIR, XPS, and NMR Studies, J. Phys. Chem. C, 115 (2011) 19005-19011.

[25] F. Rouquérol, J. Rouquérol, K.S.W. Sing, Adsorption by Powders and Porous Solids. principles, Methodology and Applications, in: A. Press (Ed.), London, 1999.

[26] S.J. Gregg, K.S.W. Sing, Adsorption, surface area, and porosity, Academic Press, London; New York, 1982.

[27] W.H. Organization, Guidelines for safe recreational water environments, Volume 1: Coastal and fresh waters. Accessed on August 2015 at http://www.who.int/water_sanitation_health/bathing/srwe1/en/

[28] B. Gao, G.Z. Chen, G. Li Puma, Carbon nanotubes/titanium dioxide (CNTs/TiO_2) nanocomposites prepared by conventional and novel surfactant wrapping sol-gel methods exhibiting enhanced photocatalytic activity, Appl. Catal. B: Environ., 89 (2009) 503-509.

[29] C.G. Silva, J.L. Faria, Photocatalytic Oxidation of Phenolic Compounds by Using a Carbon Nanotube-Titanium Dioxide Composite Catalyst, ChemSusChem, 3 (2010) 609-618.

[30] A.J. Maira, J.M. Coronado, V. Augugliaro, K.L. Yeung, J.C. Conesa, J. Soria, Fourier Transform Infrared Study of the Performance of Nanostructured TiO_2 Particles for the Photocatalytic Oxidation of Gaseous Toluene, J. Catal., 202 (2001) 413-420.

[31] G. Martra, Lewis acid and base sites at the surface of microcrystalline TiO_2 anatase: relationships between surface morphology and chemical behavior, Appl. Catal. A: General, 200 (2000) 275-285.

[32] R. Yudianti, H. Onggo, Sudirman, Y. Saito, T. Iwata, J. Azuma, Analysis of Functional Group Sited on Multi-Wall Carbon Nanotube Surface, Open Mater. Sci. J., 5 (2011) 242-247.

[33] J.L. Figueiredo, M.F.R. Pereira, M.M.A. Freitas, J.J.M. Órfão, Modification of the surface chemistry of activated carbons, Carbon, 37 (1999) 1379-1389.

[34] J.L. Figueiredo, M.F.R. Pereira, M.M.A. Freitas, J.J.M. Órfão, Characterization of Active Sites on Carbon Catalysts, Ind. Eng. Chem. Res., 46 (2007) 4110-4115.

[35] L.M. Pastrana-Martínez, S. Morales-Torres, V. Likodimos, P. Falaras, J.L. Figueiredo, J.L. Faria, A.M.T. Silva, Role of oxygen functionalities on the synthesis of photocatalytically active graphene-TiO_2 composites, Appl. Catal. B: Environ., 158-159 (2014) 329-340.

[36] P. Solís-Fernández, R. Rozada, J.I. Paredes, S. Villar-Rodil, M.J. Fernández-Merino, L. Guardia, A. Martínez-Alonso, J.M.D. Tascón, Chemical and microscopic analysis of graphene prepared by different reduction degrees of graphene oxide, J. Alloys Compd., 536, Supplement 1 (2012) S532-S537.

[37] R. Leary, A. Westwood, Carbonaceous nanomaterials for the enhancement of TiO2 photocatalysis, Carbon, 49 (2011) 741-772.

[38] R. Kaur, I. Badea, Nanodiamonds as novel nanomaterials for biomedical applications: drug delivery and imaging systems, Inter. J. Nanomed., 8 (2013) 203-220.

[39] A. Nagata, T. Oku, K. Kikuchi, A. Suzuki, Y. Yamasaki, E. Osawa, Fabrication, nanostructures and electronic properties of nanodiamond-based solar cells, Prog. Nat. Sci.: Mater. Inter., 20 (2010) 38-43.

[40] C.G. Silva, J.L. Faria, Anatase vs.rutile efficiency on the photocatalytic degradation of clofibric acid under near UV to visible irradiation, Photochem. Photobiol. Sci., 8 (2009) 705-711.

[41] S. Morales-Torres, L.M. Pastrana-Martínez, J.L. Figueiredo, J.L. Faria, A.M.T. Silva, Graphene oxide-P25 photocatalysts for degradation of diphenhydramine pharmaceutical and methyl orange dye, Appl. Surf. Sci., 275 (2013) 361-368.

[42] S.S. Mali, S.K. Desai, D.S. Dalavi, C.A. Betty, P.N. Bhosale, P.S. Patil, CdS-sensitized TiO_2 nanocorals: hydrothermal synthesis, characterization, application, Photochem. Photobiol. Sci., 10 (2011) 1652-1658.

[43] Y.-d. Wang, C.-l. Ma, X.-d. Sun, H.-d. Li, Synthesis and characterization of amorphous TiO_2 with wormhole-like framework mesostructure, J. Non-Cryst. Sol., 319 (2003) 109-116.

[44] G. Lui, J.-Y. Liao, A. Duan, Z. Zhang, M. Fowler, A. Yu, Graphene-wrapped hierarchical TiO_2 nanoflower composites with enhanced photocatalytic performance, J. Mater. Chem. A, 1 (2013) 12255-12262.

[45] B. Erdem, R.A. Hunsicker, G.W. Simmons, E.D. Sudol, V.L. Dimonie, M.S. El-Aasser, XPS and FTIR Surface Characterization of TiO_2 Particles Used in Polymer Encapsulation, Langmuir, 17 (2001) 2664-2669.

[46] H. Xu, S. Ouyang, L. Liu, P. Reunchan, N. Umezawa, J. Ye, Recent advances in TiO_2-based photocatalysis, J. Mater. Chem. A, 2 (2014) 12642-12661.

[47] C.H. Kim, B.-H. Kim, K.S. Yang, TiO_2 nanoparticles loaded on graphene/carbon composite nanofibers by electrospinning for increased photocatalysis, Carbon, 50 (2012) 2472-2481.

[48] Z. Zhao, Y. Dai, Nanodiamond/carbon nitride hybrid nanoarchitecture as an efficient metal-free catalyst for oxidant- and steam-free dehydrogenation, J. Mater. Chem. A, 2 (2014) 13442-13451.

[49] T. Kondo, I. Neitzel, V.N. Mochalin, J. Urai, M. Yuasa, Y. Gogotsi, Electrical conductivity of thermally hydrogenated nanodiamond powders, J. Appl. Phys., 113 (2013) 214307.

[50] M.V. Korobov, D.S. Volkov, N.V. Avramenko, L.A. Belyaeva, P.I. Semenyuk, M.A. Proskurnin, Improving the dispersity of detonation nanodiamond: differential scanning calorimetry as a new method of controlling the aggregation state of nanodiamond powders, Nanoscale, 5 (2013) 1529-1536.

[51] B. Choudhury, M. Dey, A. Choudhury, Defect generation, d-d transition, and band gap reduction in Cu-doped TiO_2 nanoparticles, Int. Nano. Lett., 3 (2013) 1-8.

[52] K.D. Behler, A. Stravato, V. Mochalin, G. Korneva, G. Yushin, Y. Gogotsi, Nanodiamond-Polymer Composite Fibers and Coatings, ACS Nano, 3 (2009) 363-369.

[53] A.C. Ferrari, J. Robertson, Origin of the 1150 cm−1 Raman mode in nanocrystalline diamond, Phys. Rev., 63 (2001) 121405 (R).

[54] C.E. Nebel, Photocatalysis: A source of energetic electrons, Nat. Mater., 12 (2013) 780-781.

[55] D.M. Jang, Y. Myung, H.S. Im, Y.S. Seo, Y.J. Cho, C.W. Lee, J. Park, A.-Y. Jee, M. Lee, Nanodiamonds as photocatalysts for reduction of water and graphene oxide, Chem. Commun., 48 (2012) 696-698.

[56] D. Zhu, L. Zhang, R.E. Ruther, R.J. Hamers, Photo-illuminated diamond as a solid-state source of solvated electrons in water for nitrogen reduction, Nat. Mater., 12 (2013) 836-841.

[57] M.G. Antoniou, A.A. de la Cruz, D.D. Dionysiou, Intermediates and Reaction Pathways from the Degradation of Microcystin-LR with Sulfate Radicals, Environ. Sci. Technol., 44 (2010) 7238-7244.

[58] M.G. Antoniou, J.A. Shoemaker, A.A.d.l. Cruz, D.D. Dionysiou, Unveiling New Degradation Intermediates/Pathways from the Photocatalytic Degradation of Microcystin-LR, Environ. Sci. Technol., 42 (2008) 8877-8883.

[59] L. Ho, G. Onstad, U.v. Gunten, S. Rinck-Pfeiffer, K. Craig, G. Newcombe, Differences in the chlorine reactivity of four microcystin analogues, Water Res., 40 (2006) 1200-1209.

[60] M. Grootveld, B. Halliwell, Aromatic hydroxylation as a potential measure of hydroxyl-radical formation in vivo. Identification of hydroxylated derivatives of salicylate in human body fluids, Biochem. J., 237 (1986) 499-504.

[61] K. Kaya, T. Sano, A Photodetoxification Mechanism of the Cyanobacterial Hepatotoxin Microcystin-LR by Ultraviolet Irradiation, Chem. Res. Toxicol., 11 (1998) 159-163.

[62] S. Banerjee, S.C. Pillai, P. Falaras, K.E. O'Shea, J.A. Byrne, D.D. Dionysiou, New Insights into the Mechanism of Visible Light Photocatalysis, J. Phys. Chem. Lett., 5 (2014) 2543-2554.

Part III

Chapter 5

ZnO/carbon nanomaterials for photocatalytic water decontamination

In the previous chapters was found that TiO_2-based materials show good efficiency for photocatalytic degradation of different pollutants. Nevertheless, the quest to find new efficient photocatalysts that overlap significantly with the solar spectrum is still open. The massive use of TiO_2 as photocatalyst has triggered the interest on alternative materials with similar or even higher efficiencies, such as zinc oxide (ZnO). Additionally, as already seen in previous chapters, carbon materials can provide beneficial effects in the photocatalytic activity of metal oxide semiconductors by inducing positive synergies between the two phases in composite photocatalysts. The effect of coupling carbon nanotubes (CNT), carbon nanofibers (CNF), graphene (FLG), fullerene (C_{60}) and nanodiamonds (ND) with ZnO nanotetrapods prepared by chemical vapour deposition (CVD) is now evaluated for the photocatalytic degradation of phenol under simulated solar light irradiation.

The materials used on the photocatalytic experiments were prepared at Laboratoire de Chimie de Coordination, INP-ENSIACET, Université de Toulouse (France), during a 3 months research visit under supervision of Professor Philippe Serp.

This chapter is based on the following article:

M.J. Sampaio, R. Bacsa, A. Benyounes, R. Axet, P. Serp, C.G. Silva, A.M.T. Silva, J.L. Faria, Synergistic effect between carbon nanomaterials and ZnO for photocatalytic water decontamination, J. Catal. 331 (2015) 172–180, reproduced by permission of Elsevier.

5.1. Introduction

ZnO is an alternative to TiO_2 in photocatalytic applications due to its similar bandgap (3.3 eV), its morphologic versatility and lower cost [1, 2]. Althouh ZnO is considered as highly efficient in photocatalytic applications, it also requires excitation in the near UV region. Therefore, efforts have been devoted to design ZnO-based composite materials with increased absorption in the visible spectrum range. These attempts involve catalyst modification by metal doping [3], dye photosensitization [4], deposition of noble metals [5], combining ZnO with other semiconductors [6], or addition of nanoscale carbon materials [7-9]. The unique structure, chemical and electronic properties, and the good stability of carbon materials make the latter a very promising technique. Various studies have reported that carbon materials, such as carbon nanotubes (CNT) [7, 9], few layer graphene (FLG) [10, 11], fullerene (C_{60}) [12], and nanodiamonds (ND) [13] can provide beneficial effects on the photocatalytic activity of metal oxide semiconductors by inducing positive synergies between the two phases in the composite photocatalyst. The introduction of carbon materials favors the separation of the photo-generated electron-hole pairs by formation of heterojunctions at the carbon/metal oxide interface, promoting faster photocatalytic reaction rates [9, 14].

It has been demonstrated that surface modification of the nanocarbon material influences the performance of the composite photocatalyst [9, 15, 16]. In the previous chapters it was shown that the presence of oxygen species on carbon materials' surface, such as carboxylic acid and phenol groups, can enhance the dispersion of the metal oxide, thus increasing the performance of the resulting composite materials. In addition, the acid treatment removes residual impurities, such as amorphous carbon or metal catalyst that may be present in the carbon material [17]. The introduction of nitrogen groups on carbon materials has been also explored as an important route to improve their catalytic performance [18]. Nitrogen doping can induce the generation of free electrons on the carbon materials surface that can be transferred from its surface to adsorbed oxygen [19].

In the present chapter, the effect of coupling carbon nanotubes, nanofibers, graphene, fullerene and nanodiamonds with ZnO tetrapods in the photocatalytic degradation of phenol under simulated solar light irradiation was evaluated. The effect of surface oxidation and N-doping of the nanocarbon has also been assessed for selected carbon materials.

5.2. Experimental

5.2.1. Materials

Pristine CNT sample was purchased from Nanocyl Belgium (NC-CNT, purity > 95%; diameter = 5-50 nm). Graphistrength® CNTs (AK-CNT, purity > 90%; diameter = 5-50 nm) were supplied by Arkema, France. Large-diameter CNTs (PYG-CNT, Pyrograph III; diameter = 60-150 nm) were supplied by Applied Sciences. Carbon nanofibers (CNF) and few layer graphene with different average thicknesses (FLGtk and FLGtn) were synthetized by catalytic chemical vapour deposition (CVD) in cooperation with Laboratoire de Chimie de Coordination UPR CNRS 8241, composante ENSIACET, Université de Toulouse UPS-INP-LCC. The details of the preparation samples are described elsewhere [20, 21]. Before being used the CNT samples were purified with 50 % *v/v* sulfuric acid (99.9 *wt.*%, H_2SO_4, Sigma-Aldrich, 120 °C, 3 h), while nanofibers and FLG samples were purified with hydrochloric acid (37 *wt.*%, HCl, Sigma-Aldrich, 12 h). The CNT (NC-CNT, AK-CNT and PYG-CNT), CNF and few layer graphene (FLGtk and FLGtn) samples were oxidized with nitric acid (65 *wt.*% HNO_3, Sigma-Aldrich) at 120 ºC temperature for 3 h under reflux. After cooling, the suspensions were washed with distilled water and dried at 130 ºC for 12 h.

Nanodiamonds (ND) were obtained by diamond (Carbodeon) and disaggregation was performend as follows: 1 g of the diamond sample was added to a sodium chloride aqueous solution and the suspension was sonicated for 6 h in a cooled bath. The suspension was centrifuged to recover the ND powder. The collected powders were then oxidized by boiling with nitric/sulfuric acid mixture (1:3, HNO_3:H_2SO_4) for 24 h. After cooling, the suspension was then washed up to neutral pH and dried overnight at 130 ºC.

Nitrogen doped carbon nanotubes (N-CNT) were synthesized by catalytic-CVD in a fluidized bed reactor using ethylene as carbon source and acetonitrile/N_2 as carbon/nitrogen source, as described elsewhere [18]. The fullerene (C_{60}) carbon sample was purchased from Sigma-Aldrich and used as received.

5.2.2. Synthesis of ZnO and carbon/ZnO composites

ZnO tetrapods were synthesised by CVD according to a previously described procedure [22]. Briefly, Zn metal powder (Alfa Aesar) was allowed to melt under argon flow atmosphere at 900°C and oxidized by maintaining a controlled flow of air in the

opposite direction. Nanoparticles of ZnO produced in the mixing zone were collected using cold traps and used without further purification.

The carbon/ZnO materials were prepared by adding the required amount of ZnO to a suspension of the carbon material in tetrahydrofuran (THF, purity > 99.9%, Sigma-Aldrich) under vigorous stirring followed by sonication for 30 min and stirring of the resultant suspension for 1h. The composite material was filtered, washed with water and dried at 130 ºC for 12h. The photocatalysts are denoted as X/ZnO, where X corresponds to the carbon material used. In the present work the carbon phase was fixed at 16.7 *wt.*% for all materials take into account previous results using CNT as a carbon phase [23], as well the performance obtained in the degradation of organic compounds with the TiO_2/CNT composite films presented in chapter 3.

5.2.3. Catalyst characterization

The photocatalysts were investigated by thermogravimetry, physical adsorption of nitrogen, DR UV-Vis and photoluminescence spectroscopies, transmission electron microscopy and temperature programmed desorption. A description on the procedure used for DR UV-Vis, TG and S_{BET} analysis is carefully given in chapter 2, section 2.2.2.

Temperature programmed desorption (TPD) analysis was carried out by heating the samples to 1100 ºC at 5 ºC min^{-1} under helium flow using an AMI-300 Catalyst Characterization Instrument (Altamira Instruments).

Photoluminescene (PL) measurements were carried out at room temperature on a Hitachi 4500 Flourescence spectrometer with a 150W Xenon lamp as light source. Excitation spectra were taken in the synchronous mode with the simultaneous variation of the excitation and emission wavelengths.

Transmission electronic microscopy (TEM) images were taken using a TEM-FEI Tecnai-G2-20-FEI 2006 microscope. X-ray photoelectron spectroscopic analysis (XPS) was performed using a VG Escalab MKII spectrophotometer operating with a non-monochromatized Mg K_α source (1253.6 eV).

5.2.4. Photocatalytic experiments

The photocatalytic efficiency of the carbon/ZnO materials was evaluated in the degradation of an aqueous solution of phenol under natural pH conditions (pH = 6.1) and using simulated solar light irradiation. In a typical experiment, a pyrex cylindrical reactor was filled with 50 mL of a 20 mg L^{-1} phenol solution. The suspension was

magnetically stirred and continuously purged with air. The irradiation source consisted of a 1500 W xenon lamp equipped with a cut-off soda-lime glass UV filter with infrared reflection coating, to simulate outdoor exposure (30.9 $mW.cm^{-2}$ irradiance, determined with an Ocean Optics USB2000+ spectroradiometer). A dark period of 30 min before switching on the lamp was maintained to allow the system to attain the adsorption-desorption equilibrium condition.

The evolution of phenol concentration was performed in the HPLC apparatus described in chapter 2, section 2.2.4.

To identify the concentration of some organic acids resulting from phenol degradation, a Hitachi Elite Lachrom apparatus equipped with a diode array detector was used. The stationary phase consisted in an Aminex HPX-87H column (300 mm × 7.8 mm) working under isocratic elution (H_2SO_4 4 mM).

Total organic carbon (TOC) was also evaluated at the end of each experiment in the equipment described in chapter 2, section 2.2.4.

Atomic absorption spectrometry (AAS) analyses for dissolved Zn determination were performed using and AAS UNICAM spectrophotometer model 939/959.

To avoid an excess of catalyst and to ensure a total absorption of efficient photons, a preliminary study on the effect of ZnO load was performed. The optimum load found was 0.83 g L^{-1} of ZnO (Appendix, Figure A.4).

Thereby, the load of neat ZnO was maintained on 0.83 g L^{-1} and for carbon/ZnO composites the catalyst load was kept at 1 g L^{-1} (0.83 g L^{-1} and 0.17 g L^{-1} of metal oxide and carbon phase, respectively), which correspond to the nominal content of each phase of the composites

5.3. Effect of carbon materials on ZnO

5.3.1. Photocatalytic characterization

The carbon content in the composite materials was determined by TG analysis. Neat ZnO and carbon materials, as well as the respective composites, were submitted to a thermal treatment under air flow and the weight loss was determined. In general the results indicate a mass loss in the range 16-17 %*wt.* for all the X/ZnO samples (Figure 5.1), which is in agreement with the nominal carbon content (16.7 %*wt.*), *i.e.* the difference between the weight losses obtained for the X/ZnO sample and that observed for neat ZnO.

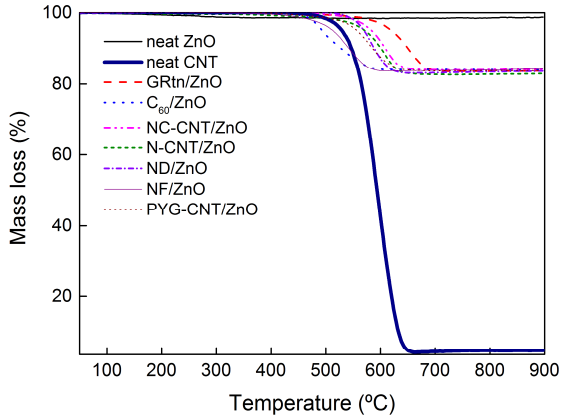

Figure 5.1 – TG analysis of both neat ZnO and CNT, and selected X/ZnO composites.

The S_{BET} of the bare carbon materials and composites is given in Table 5.1. The S_{BET} found for neat ZnO was 17 $m^2 g^{-1}$. In general, the introduction of carbon materials lead to an increase of the S_{BET}, which in most cases is in agreement with the calculated value (in brackets) *i.e.*, the weighted average of the S_{BET} of ZnO and carbon phases in the composites taking into account their relative weight fraction (*c.a.* 17 *wt. %* of carbon phase, as confirmed by thermogravimetric analysis). It was noticed that the S_{BET} of C_{60}/ZnO is lower than that of ZnO, which may be attributed to a high contact surface between ZnO and very small (~0.5 nm) C_{60} nanoparticles [24]. Also a slight decrease on S_{BET} for AK-CNT/ZnO and ND/ZnO materials compared with the theoretical value can be due to an the agglomeration of ZnO hindering the carbon surface, resulting in a lower contribution of the respective carbon material in the overall surface area of the composite.

Table 5.1 – Specific surface area (S_{BET}) determined from the N_2 adsorption isotherms and values calculated (in brackets) from mass composition of ZnO and carbon phase (% CP).

	S_{BET} ($m^2 g^{-1}$)[a]								
%CP	NC-CNT	PYG-CNT	AK-CNT	ND	C_{60}	CNF	FLG_{tk}	FLG_{tn}	N-CNT
100	306	27	257	240	n.d.[b]	103	50	46	228
16.7	64(65)	19(19)	47(57)	48(54)	10	28(31)	20(23)	20(21)	49(52)

[a]within the determination error (± 5 $m^2 g^{-1}$); [b]not determined.

The N_2 adsorption-desorption isotherms of the ZnO and X/ZnO composite materials is shown in Figure 5.2. It can be classified as type-II, characteristic of non-porous solids, according to the IUPAC classification [25]. In addition, a larger N_2

uptake at higher relative pressures (P/P_0) and a clear hysteresis loop characteristic of type H3 is observed, indicating a very wide pore size distribution. However, the porosity could mainly refer to interparticle channels on the powder materials.

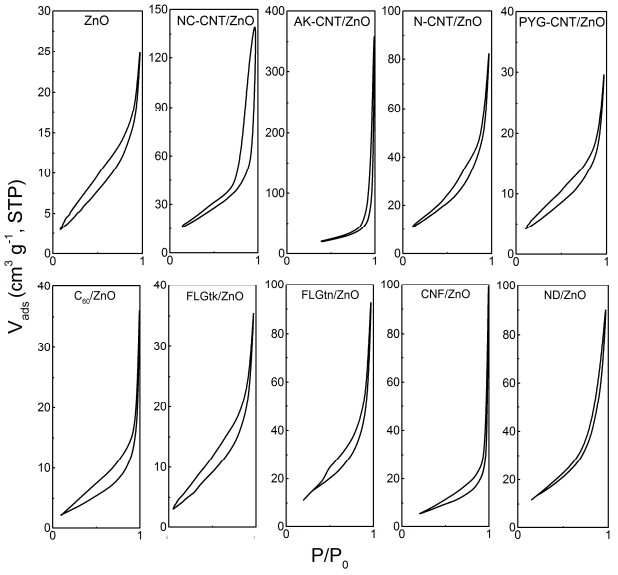

Figure 5.2 – N_2 adsorption-desorption isotherms at -196 ºC for ZnO and carbon/ZnO composite materials.

The optical properties of the photocatalysts were analyzed by DR UV-Vis (Figure 5.3).

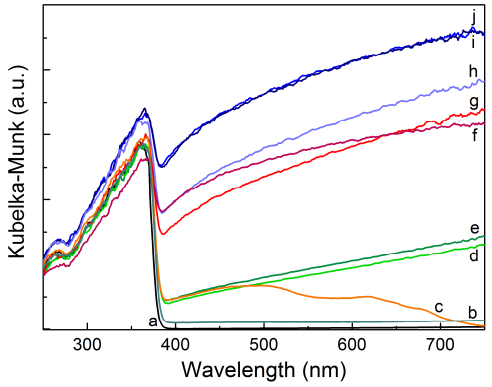

Figure 5.3 – DR UV-Vis spectra of ZnO and carbon-ZnO materials. (a) ZnO, (b) ND/ZnO, (c) C_{60}/ZnO, (d) FLGtn/ZnO, (e) FLGtk/ZnO, (f) PYG-CNT/ZnO, (g) CNF/ZnO, (h) N-CNT/ZnO, (i) NC-CNT/ZnO and (j) AK-CNT/ZnO.

The spectrum of neat ZnO shows a characteristic intense absorption band in the UV spectral range (λ < 400 nm). In the presence of carbon, an increased adsorption

in the visible region was observed. The increase in the absorption capacity of carbon containing composites has been attributed, in literature, both to the ability of carbon to absorb light and to the creation of an electronic interaction between the carbon and metal oxide phases [11, 23, 26]. This increase depends on the nature of the carbon material used, higher absorption being found for composites containing CNT, followed by FLG, fullerene and nanodiamonds.

Images of bare ZnO and X/ZnO composites by TEM are show in Figure 5.4. For ZnO (Figure 5.4a) the micrograph reveals the presence of tetrapod-like structures, where needles grow from a faceted seed particle [22, 27]. The needles have diameters varying between 8 and 50 nm and over 1 μm in length, producing an aspect ratio of around 20-100. The TEM images of the composite materials show different structures depending on the carbon phase that was used. The commercial carbon nanotubes NC-CNT and AK-CNT have diameters of 10-20 nm (Figures 5.4b and 5.4d), while PYG-CNT have diameters around 100 nm (Figure 5.4c). The TEM micrograph of the composite prepared with the nitrogen doped-carbon nanotubes (N-CNT/ZnO) reveal a particular bamboo-like structure [18] typical of N-doped CNTs (Figure 5.4j inset) with diameters around 20 nm. A different structure was noticed for composites prepared with nanodiamonds (Figure 5.4e), where aggregates of small nanodiamond particles being observed. In fact it was already reported that when nanodiamonds are oxidized, they could form nanoparticle clusters due to hydrogen bonding and interparticle van der Wall forces [13, 28]. Due to its small size (~ 0.5 nm) [24], the presence of fullerene is hardly detected in the TEM images of C_{60}/ZnO composites (Figure 5.4f). Yet, as already mentioned, as the surface area of the composite is lower than that of ZnO, it is expected that C_{60} nanoparticles are partially covering the ZnO surface.

The TEM images in Figure 5.4g show the typical morphology of CNF/ZnO composites, where CNF with diameter of *c.a.* 70 nm can be observed. In the samples using FLG as the carbon phase, the TEM images show a similar structure for both FLGtk/ZnO and FLGtn/ZnO materials, where the presence of aggregated sheet-like structures can be observed (Figures 5.4h and 5.4i, respectively).

Among all the carbon/ZnO materials, the samples containing FLG and N-doped CNT seem to show a more uniform dispersion of the ZnO and the carbon phase indicating an intimate contact between the two phases (Figures 5.4h, 5.4i and 5.4j).

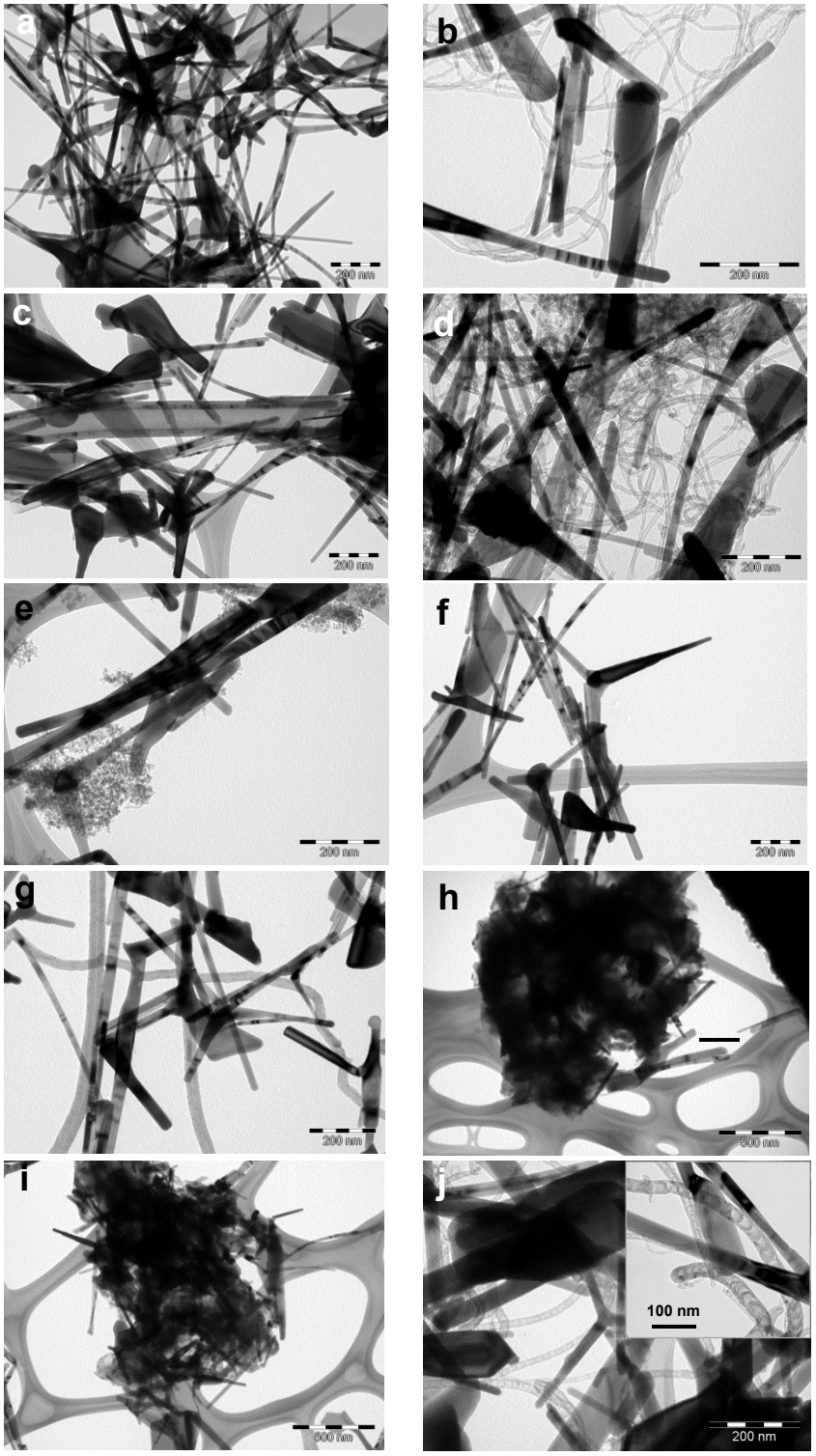

Figure 5.4 – TEM images: (a) ZnO, (b) NC-CNT/ZnO, (c) PYG/ZnO, (d) AK-CNT/ZnO, (e) ND/ZnO, (f) C60/ZnO, (g) CNF/ZnO, (h) FLGtk/ZnO, (i) FLGtn/ZnO and (j) N-CNT/ZnO.

The CO and CO_2 TPD profiles for selected carbon samples are shown in Figures 5.5a and 5.5b, respectively.

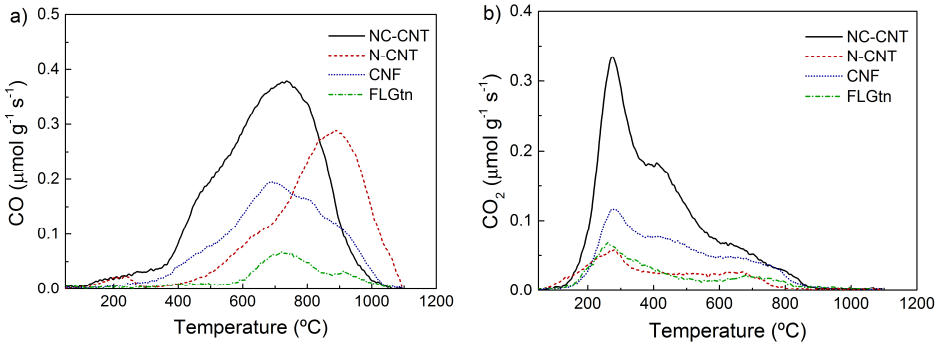

Figure 5.5 – TPD profiles of NC-CNT, N-CNT, CNF and FLGtn: (a) CO and (b) CO_2 release.

The total amount of both CO and CO_2 and the respective oxygen content are given in Table 5.2. Results indicate the presence of different amounts of oxygen species depending on the carbon material. The larger amount of released CO and CO_2 (1966 and 6637 µmol g^{-1}, respectively) was observed for ND (Appendix, Figure A.5), which may be attributed to the severe treatment used for the oxidation of this material. The oxygen amounts evolved during the TPD analysis follow the order: ND (24.4 *wt.*%) > NC-CNT (6.09 *wt.* %) > CNF (3.01 *wt.* %) > N-CNT (2.61 *wt.* %) and FLGtn (0.84 *wt.* %). The amount of oxygen must be related to the number of defects and to the total length of the edges, since oxidation starts preferentially at these sites.

Table 5.2 – Total amounts of CO and CO_2 released by TPD, and corresponding atomic O content, for selected materials.

Sample	CO (µmol g^{-1})	CO_2 (µmol g^{-1})	CO/CO_2	O (%)
ND	1966	6637	0.30	24.4
NC-CNT	1783	1012	1.76	6.09
CNF	923	479	1.93	3.01
FLGtn	204	162	1.26	0.84
N-CNT	1165	232	5.02	2.61

It follows that when ND is made of many small size units, is more easily oxidized. On the other hand, FLGtn made of almost defect free sheets that tend to aggregate and lead to small surface areas, will be less prone to oxidation. Similar TPD profiles were obtained for the samples that were oxidized with HNO_3 (NC-CNT, CNF and FLGtn). The highest CO/CO_2 value was obtained for N-CNT, indicating a highly basic

character [18] presumably due to the presence of N-containing groups. XPS analysis revealed the presence of 31% pyrrolic nitrogen, 29% pyridinic nitrogen, 12% quaternary nitrogen, and 28% nitrogen (Appendix, Figure A.6).

The non-bonded electron pair of the pyridinic nitrogen is mainly responsible for the basic character of N-CNT. The relatively high amount of this nitrogen species in the composite means that this material may act as Lewis base.

Carbon/ZnO materials were characterized using PL spectroscopy to investigate the occurrence of charge separation upon photoexcitation. Due to its high exciton energy and direct band gap (3.3 eV), ZnO shows intense PL emission both in the UV and the visible regions [29, 30]. The UV emission in neat ZnO is due to exciton recombination and the visible luminescence is generally attributed to the presence of defect sites. Figure 5.6a shows the PL spectra taken at room temperature of bare ZnO and ZnO-based composites prepared using C_{60}, NDs, FLGtn and N-CNT as the carbon phase under an excitation energy of 3.64 eV (340 nm).

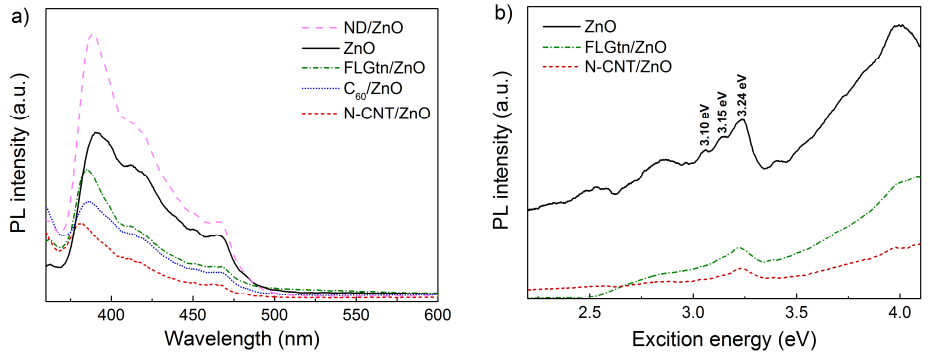

Figure 5.6 – (a) Photoluminescence spectra and (b) the excitation spectra of ZnO and carbon/ZnO materials.

The PL spectrum of ZnO shows a broad and intense UV emission due exciton recombination that can be resolved into two peaks at 3.17 and 3.12 eV and a third lower intensity emission centered at 3.00 eV. The UV emission is accompanied by a low intensity blue band (around 2.8 eV) and the green emission is nearly absent. Changing the excitation energy to 3.4 eV (360 nm) results in a broadening of the emission and the two peaks in the UV region could not be resolved. Except for NDs that increase the luminescence intensity of ND/ZnO compared to bare ZnO, all the other materials showed quenching of the UV luminescence and a blue shift of the highest energy exciton band. The maximum quenching and energy shift (0.8 eV) was observed for N-CNT/ZnO. The presence of the carbon phase also quenches the lower energy peaks at 3.12 eV and 3.0 eV completely, once again this effect being more

pronounced for N-CNT/ZnO. The corresponding excitation spectra (taken in the synchronous derivative mode) are shown in Figure 5.6b.

Excitation peaks at 3.10 and 3.15 eV are absent in the case of FLGtn/ZnO and N-CNT/ZnO, indicating energy transfer from these excited states of ZnO to FLGtn and N-CNT, respectively.

The origin of the UV emission in ZnO is attributed to excitonic recombination processes arising from free excitons or excitons bound to shallow donors [29, 31]. While narrow peaks due to excitons, bound excitons and donors have been resolved at low temperatures, the exciton peak is broad and is shifted (5-8 nm) to lower energies at room temperature. The presence of an intense UV emission and the absence of visible emission is an indication of a low density of point defects and high crystal quality of the ZnO tetrapods used in our experiments. The addition of NDs increased the PL intensity of the ZnO tetrapods but the characteristic emission of the NDs was quenched showing that NDs could act as sensitizers for ZnO. In the case of the other supports (C_{60}, FLGtn and N-CNT), the blue shift of the exciton energy is an important indicator of electronic energy exchange between the ZnO crystal and the carbon phase. Coupling of the photoexcited ZnO and C_{60} has been reported in the literature [32]. For FLGtn/ZnO and N-CNT/ZnO, the absence of PL emission indicates that no sensitizing effect is present between ZnO and the carbon phases. On the other hand, the extensive quenching of exciton luminescence shows that FLGtn and N-CNT act as efficient scavengers of photogenerated hot electrons produced in ZnO tetrapods under UV irradiation.

5.3.2. Photocatalytic degradation of phenol under simulated solar light

The effect of the addition of carbon materials to ZnO was studied in photocatalytic water decontamination under simulated solar light, using phenol as a model compound. In the absence of catalyst a decrease in phenol concentration of 5 % was observed at the end of 1 h of irradiation.

Results show that the kinetics of the photocatalytic phenol degradation follows a pseudo-first order rate law for all the tested photocatalysts. The k_{app} determined by non-linear curve fitting of the experimental data, the k_{app}/S_{BET} ratio and the synergy factor (R_{kapp}) are summarized in Table 5.3.

$$R_{kapp} = \frac{k_{app\,(\text{Carbon material / ZnO})}}{k_{app\,(\text{ZnO})}} \qquad (5.1)$$

Table 5.3 – Apparent first order rate constant (k_{app}), k_{app}/S_{BET} and R_{kapp} obtained for the reactions using the different catalysts.

Catalyst	k_{app} (min^{-1})	$\times 10^2$ k_{app} /S_{BET} (g min^{-1} m^{-2})	R_{kapp}
ZnO	0.131	0.771	1
NC-CNT/ZnO	0.118	0.184	0.90
PYG-CNT/ZnO	0.122	0.643	0.93
AK-CNT/ZnO	0.146	0.310	1.11
ND/ZnO	0.151	0.314	1.15
C60/ZnO	0.160	1.598	1.22
CNF/ZnO	0.185	0.660	1.41
FLGtk/ZnO	0.208	1.039	1.59
FLGtn/ZnO	0.233	1.164	1.79
N-CNT/ZnO	0.260	0.531	1.99

The results in Table 5.3 show that in general, the presence of carbon materials increases the efficiency of the ZnO photocatalyst with the except for materials using NC and PYG as a carbon phase, where a slight decrease is observed compared with bare ZnO.

The effect promoted by the presence of carbon materials in carbon/metal oxide composite photocatalysts has been extensively discussed in the literature [7, 9, 23, 33] and evidenced in the previous chapters for carbon/TiO_2 materials. It was also found that the nature of the carbon phase, the preparation method and the carbon content in the composite materials may also influence the efficiency of the resulting catalysts [7, 23, 33]. As already mentioned some studies have strengthened that the specific surface area can significantly influence the efficiency of carbon/metal oxide photocatalysts [23, 26, 29] with a higher S_{BET} meaning more active sites for contaminant adsorption and degradation. In fact, when carbon materials are combined with ZnO the surface area of the resulting materials is increased. A typical method for evaluating the efficiency of catalysts is to compare the rate constant per unit surface area (k_{app}/S_{BET}, Table 5.3). Nevertheless, no correlation was found between this parameter and the photocatalytic efficiency of the tested catalysts. These results indicate that the efficiency of the carbon/ZnO materials cannot be only related to the surface area of the composites.

The nature of the carbon material seems to play an important role in the photoefficiency of carbon/ZnO catalysts for phenol degradation (Figure 5.7).

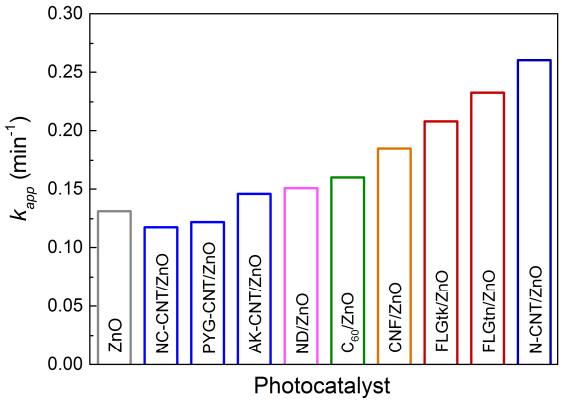

Figure 5.7 – Apparent first order rate constants (k_{app}) for the photocatalytic reactions using ZnO and carbon/ZnO materials.

It was found that the photocatalysts prepared from undoped carbon nanotubes NC-CNT, PYG-CNT and AK-CNT are less active when compared to other photocatalysts containing ND, C_{60}, CNF and FLG. Yet, the highest photocatalytic activity was observed for the composite prepared with N-doped carbon nanotubes (N-CNT), with k_{app} = 0.260 min^{-1} and a total phenol degradation achieved in 20 min. The R_{kapp} = 1.99 (Table 5.3), means that *c.a.* 100 % increase in the k_{app} for phenol degradation when using N-CNT/ZnO in relation with the bare material (ZnO).

For comparison proposes, composites using undoped CNT and oxidized CNT (CNT/ZnO and CNT$_f$/ZnO, respectively) were also prepared and tested in the degradation of phenol. The kinetic constants obtained for the composites followed the order: N-CNT/ZnO (k_{app} = 0.260 min^{-1}) > CNT$_f$/ZnO (k_{app} = 0.132 min^{-1}) > CNT/ZnO (k_{app} = 0.122 min^{-1}). As expected, the results demonstrate that the oxidation of CNT promote an increase in the efficiency of the resulting carbon/ZnO catalysts (around 10 %), much lower than the effect promoted by nitrogen doping.

A photocatalytic experiment using bare N-CNT was also performed (Appendix, Figure A.7). No phenol conversion was observed under these conditions, suggesting that the activity of the composite material results from cooperative interactions between the metal oxide and the carbon phase.

The presence of nitrogen groups in carbon materials' structure has been reported as a way to improve the activity in catalytic applications [18, 31, 32]. The additional electrons provided by nitrogen increases the surface polarity of carbon materials, which leads to a better dispersion in aqueous medium. Additionally, these electrons may be transferred from the carbon material's surface to free adsorbed oxygen,

leading to the formation of highly reactive species. It has been also reported that in the case of semiconductors, doping with nitrogen improves photocatalysis by facilitating charge separation between photogenerated electrons and holes [34-37]. Based on these findings, it can be inferred that the high activity of the N-CNT/ZnO compared with the other composites can be attributed to the presence of nitrogen species that can favor the charge transfer between the ZnO and the carbon phase. More specifically, the significant depression quenching of the PL emission spectrum observed for N-CNT/ZnO (Figure 5.6a) suggests the existence of effective electron transfer from ZnO to N-CNT. After irradiation of the N-CNT/ZnO composite with solar light, N-CNT may act as an electron scavenger for photoexcited ZnO, increasing the efficiency of the charge separation process, by hindering the recombination of electron-hole pairs.

It is also important to refer that the k_{app} obtained for phenol degradation using Aeroxide® TiO_2 P25 from Evonik (0.064 min^{-1}), the benchmark catalyst for photocatalytic applications, was lower than the k_{app} obtained with the ZnO (0.131 min^{-1}) and much lower than the most carbon/ZnO materials used in this study, in particular in the case of N-CNT/ZnO composite. Comparison with commercial ZnO nano powder from Evonik was also performed, a k_{app} of 0.065 min^{-1} being obtained with this material.

5.3.3. Reutilization tests

The photostability of ZnO is often considered as a drawback of this semiconductor for photocatalytic applications, due to the possibility of undergoing photocorrosion [7, 38]. Reutilization tests using ZnO and N-CNT/ZnO were carried out maintaining the conditions used in the previously described reactions. Before each run, the catalysts were thoroughly washed with water and dried overnight at 100 ºC. Figure 5.8 shows the phenol degradation profiles for the reactions using neat ZnO and N-CNT/ZnO composite.

As shown in Figure 5.8, the efficiency for both ZnO and N-CNT/ZnO remains practically constant after four runs, indicating a good stability of the catalysts under the photocatalytic conditions used in this work. For evaluating the degree of mineralization achieved during the photocatalytic reactions, the initial and final total organic carbon (TOC) contents were compared. For the first photocatalytic run, 70% and 87 % of mineralization was found using ZnO and N-CNT/ZnO, respectively. After the fourth utilization, a slight decrease in TOC removal was observed (56 % for ZnO

and 76 % for N-CNT/ZnO), which may be attributed to the presence of some by-products adsorbed at the catalyst's surface.

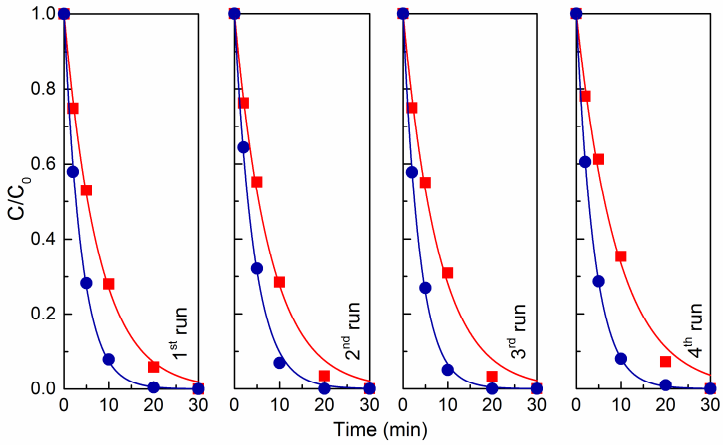

Figure 5.8 – Reusability assessment for ZnO (■) and N-CNT/ZnO (●) as catalysts for the photodegradation of phenol under simulated solar light (pH = 6.1).

Atomic absorption spectrometry analyses were performed to evaluate the presence of Zn dissolved in the solution at the end of the reaction. The results using bare ZnO and N-CNT/ZnO composite revealed the presence of very low amounts of Zn dissolved in the solution (0.73% and 0.48% of the initial Zn amount, respectively), which in terms of the concentration allowed in freshwaters for the production of water for human consumption is within the legal limits. However, the reutilization tests showed that after four cycles the photocatalysts maintain their activity, indicating that this value is only residual.

Despite the good mineralization achieved, there is still a fraction of the initial organic content that remained in solution after 60 min of irradiation. HPLC analysis performed during the photocatalytic runs revealed that hydroquinone, benzoquinone and catechol are the main products of phenol degradation, which is in agreement with previous reports [39-41], and with results obtained in chapter 2, using TiO_2 immobilized on glass rings for phenol degradation. Nevertheless, the concentration of these reaction intermediates initially rise and then decrease until complete disappearance accompanied by the simultaneous total degradation of phenol for both catalysts, being faster when N-CNT/ZnO was used as photocatalyst (Figure 5.9). The remaining organic content is attributed to the presence of aliphatic organic compounds such as oxalic, fumaric, formic and maleic acids, as confirmed by HPLC analysis.

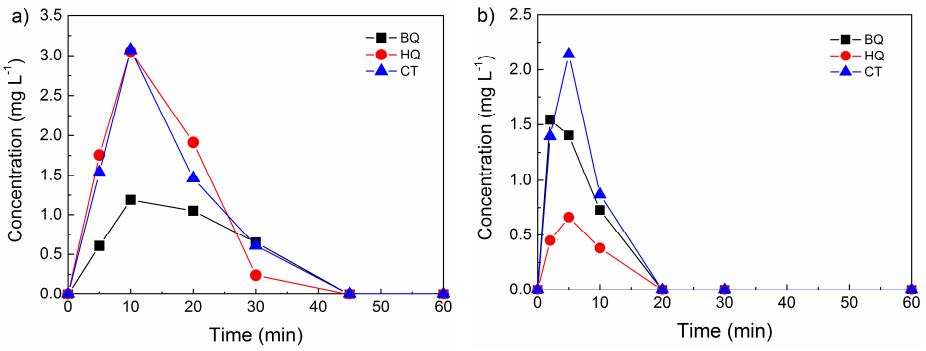

Figure 5.9 – Concentration profiles of benzoquinone (BQ), hydroquinone (HQ) and cathecol (CT) in the photocatalytic degradation of phenol using (a) ZnO and (b) N-CNT/ZnO as catalyst.

A set of experiments using ZnO and N-CNT/ZnO immobilized on glass slides (7.5 cm x 2.6 cm) by doctor blade technique were also carried out (Figure 5.10). The photocatalytic reactions were performed using the same irradiation conditions used for the catalyst in powder form. Yet, a glass cylindrical reactor (9.0 cm x 3.0 cm) was packed with the coated glass slide and 50 mL of phenol solution. In a typical experiment the phenol solution was stored in a reservoir containing 50 mL and introduced into the reactor using a peristaltic pump at constant flow rate. The solution was magnetically stirred and continuously purged with air.

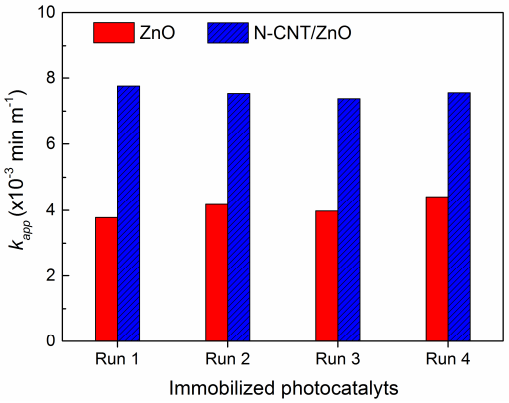

Figure 5.10 – First order apparent rate constants (k_{app}) for the photocatalytic reactions using neat ZnO and N-CNT/ZnO immobilized on glass slides.

Results using the immobilized photocatalysts show that the presence of N-CNT increase the efficiency of the photocatalyst (Figure 5.10), confirming the results obtained using the catalyst in powder form. It is also important to refer that after four runs the efficiency remains which indicate a good stability of the photocatalyst and the

resulting films. Overall, the results show that N-CNT/ZnO is a very effective and stable catalyst for solar photocatalytic applications.

5.4. Conclusions

Photocatalysts of carbon/ZnO prepared by mixing and sonication were successfully prepared and used for phenol degradation under simulated solar light. The efficiency of the photocatalytic process depends on the nature of the carbon material used.

Among the photocatalyst tested, the composite prepared using N-doped CNT as carbon phase (N-CNT/ZnO) showed the highest photocatalytic activity, with total phenol degradation achieved after 20 min under simulated solar light. A TOC removal of 87 % was obtained after 1h of irradiation, with a small fraction of non-mineralized organic acids in the final solution. The reutilization tests proved that both ZnO and N-CNT/ZnO materials have good stability under the reaction conditions tested.

The better performance of N-CNT/ZnO composite was attributed to the presence of electron rich nitrogen groups on the CNT's surface. The PL analysis confirmed that N-CNT acts as an effective electron scavenger for ZnO, inhibiting the recombination of photoexcited electron-hole pairs, thus improving the photoactivity.

References

[1] M.D. Hernandez-Alonso, F. Fresno, S. Suarez, J.M. Coronado, Development of alternative photocatalysts to TiO_2: Challenges and opportunities, Ener. Environ. Sci., 2 (2009) 1231-1257.

[2] S.G. Kumar, K.S.R.K. Rao, Zinc oxide based photocatalysis: tailoring surface-bulk structure and related interfacial charge carrier dynamics for better environmental applications, RSC Advances, 5 (2015) 3306-3351.

[3] R. Saleh, N.F. Djaja, Transition-metal-doped ZnO nanoparticles: Synthesis, characterization and photocatalytic activity under UV light, Spectrochimica Acta Part A: Mol. Biomol. Spectroscopy, 130 (2014) 581-590.

[4] N. Shamim, K. Sharma Virender, Sustainable Nanotechnology and the Environment: Advances and Achievements, in: ACS Symposium Series, Am. Chem. Soc., 2013, pp. 0.

[5] P. Li, Z. Wei, T. Wu, Q. Peng, Y. Li, Au−ZnO Hybrid Nanopyramids and Their Photocatalytic Properties, J. Am. Chem. Soc., 133 (2011) 5660-5663.

[6] C. Cheng, A. Amini, C. Zhu, Z. Xu, H. Song, N. Wang, Enhanced photocatalytic performance of TiO2-ZnO hybrid nanostructures, Sci. Rep., 4 (2014).

[7] C. Han, M.-Q. Yang, B. Weng, Y.-J. Xu, Improving the photocatalytic activity and anti-photocorrosion of semiconductor ZnO by coupling with versatile carbon, Phys. Chem. Chem. Phys., 16 (2014) 16891-16903.

[8] Y. Wang, R. Shi, J. Lin, Y. Zhu, Enhancement of photocurrent and photocatalytic activity of ZnO hybridized with graphite-like C_3N_4, Ener. Environ. Sci., 4 (2011) 2922-2929.

[9] Y.H. Ng, S. Ikeda, M. Matsumura, R. Amal, A perspective on fabricating carbon-based nanomaterials by photocatalysis and their applications, Ener. Environ. Sci., 5 (2012) 9307-9318.

[10] T. Xu, L. Zhang, H. Cheng, Y. Zhu, Significantly enhanced photocatalytic performance of ZnO via graphene hybridization and the mechanism study, Appl. Catal. B: Environ., 101 (2011) 382-387.

[11] L.M. Pastrana-Martínez, S. Morales-Torres, V. Likodimos, J.L. Figueiredo, J.L. Faria, P. Falaras, A.M.T. Silva, Advanced nanostructured photocatalysts based on reduced graphene oxide-TiO_2 composites for degradation of diphenhydramine

pharmaceutical and methyl orange dye, Appl. Catal. B: Environ., 123-124 (2012) 241-256.

[12] H.S. K., L.J.F.-Ko, W. Bae, K.W. B., Synthesis of [60]fullerene-ZnO nanocomposite under electric furnace and photocatalytic degradation of organic dyes, J. Nanosci. Nanotechnol., 11 (2011) 6049-6056.

[13] L.M. Pastrana-Martínez, S. Morales-Torres, S.A.C. Carabineiro, J.G. Buijnsters, J.L. Faria, J.L. Figueiredo, A.M.T. Silva, Nanodiamond-TiO_2 composites for heterogeneous photocatalysis, ChemPlusChem, 78 (2013) 801-807.

[14] A.S. Cherevan, P. Gebhardt, C.J. Shearer, M. Matsukawa, K. Domen, D. Eder, Interface engineering in nanocarbon-Ta_2O_5 hybrid photocatalysts, Ener. Environ. Sci., 7 (2014) 791-796.

[15] R.R.N. Marques, M.J. Sampaio, P.M. Carrapiço, C.G. Silva, S. Morales-Torres, G. Dražić, J.L. Faria, A.M.T. Silva, Photocatalytic degradation of caffeine: Developing solutions for emerging pollutants, Catal. Today, 209 (2013) 108-115.

[16] L.M. Pastrana-Martínez, S. Morales-Torres, V. Likodimos, P. Falaras, J.L. Figueiredo, J.L. Faria, A.M.T. Silva, Role of oxygen functionalities on the synthesis of photocatalytically active graphene-TiO_2 composites, Appl. Catal. B: Environ., 158-159 (2014) 329-340.

[17] C.G. Silva, M.J. Sampaio, R.R.N. Marques, L.A. Ferreira, P.B. Tavares, A.M.T. Silva, J.L. Faria, Photocatalytic production of hydrogen from methanol and saccharides using carbon nanotube-TiO_2 catalysts, Appl. Catal. B: Environ., 178 (2015) 82-90.

[18] A. Benyounes, M. Kacimi, M. Ziyad, P. Serp, Conversion of isopropyl alcohol over Ru and Pd loaded N-doped carbon nanotubes, Chin. J. Catal., 35 (2014) 970-978.

[19] R.P. Rocha, J.P.S. Sousa, A.M.T. Silva, M.F.R. Pereira, J.L. Figueiredo, Catalytic activity and stability of multiwalled carbon nanotubes in catalytic wet air oxidation of oxalic acid: The role of the basic nature induced by the surface chemistry, Appl. Catal. B: Environ., 104 (2011) 330-336.

[20] R. Bacsa, P. Serp, Graphene production method and graphene obtained by said method, in: WO2013093350 A1, France, 2013.

[21] P. Serp, Carbon Materials for Catalysis ed., John Wiley & Sons, Inc., 2008.

[22] R. Bacsa, Y. Kihn, M. Verelst, J. Dexpert, W. Bacsa, P. Serp, Large scale synthesis of zinc oxide nanorods by homogeneous chemical vapour deposition and their characterisation, Surf. Coatings Technol., 201 (2007) 9200-9204.

[23] C.G. Silva, J.L. Faria, Photocatalytic oxidation of benzene derivatives in aqueous suspensions: Synergic effect induced by the introduction of carbon nanotubes in a TiO_2 matrix, Appl. Catal. B: Environ., 101 (2010) 81-89.

[24] A. Goel, J.B. Howard, J.B. Vander Sande, Size analysis of single fullerene molecules by electron microscopy, Carbon, 42 (2004) 1907-1915.

[25] K.S.W. Sing, D.H. Everett, R.A.W. Haul, L. Moscou, R.A. Pierotti, J. Rouquerol, T. Siemieniewska, Reporting Physisorption Data for Gas/Solid Systems, in: Handbook of Heterogeneous Catalysis, Wiley-VCH Verlag GmbH & Co. KGaA, 2008.

[26] B. Gao, G.Z. Chen, G. Li Puma, Carbon nanotubes/titanium dioxide (CNTs/TiO_2) nanocomposites prepared by conventional and novel surfactant wrapping sol–gel methods exhibiting enhanced photocatalytic activity, Appl. Catal. B: Environ., 89 (2009) 503-509.

[27] S.A.C. Carabineiro, B.F. Machado, G. Dražić, R.R. Bacsa, P. Serp, J.L. Figueiredo, J.L. Faria, Photodeposition of Au and Pt on ZnO and TiO_2, in: M.D.S.H.P.A.J.J.A.M. E.M. Gaigneaux, P. Ruiz (Eds.) Studies Surf. Sci. Catal., Elsevier, 2010, pp. 629-633.

[28] K.D. Behler, A. Stravato, V. Mochalin, G. Korneva, G. Yushin, Y. Gogotsi, Nanodiamond-Polymer Composite Fibers and Coatings, ACS Nano, 3 (2009) 363-369.

[29] Y.-C. Chen, K.-i. Katsumata, Y.-H. Chiu, K. Okada, N. Matsushita, Y.-J. Hsu, ZnO–graphene composites as practical photocatalysts for gaseous acetaldehyde degradation and electrolytic water oxidation, Appl. Catal. A: General, 490 (2015) 1-9.

[30] A.D. Purceno, B.F. Machado, A.P.C. Teixeira, T.V. Medeiros, A. Benyounes, J. Beausoleil, H.C. Menezes, Z.L. Cardeal, R.M. Lago, P. Serp, Magnetic amphiphilic hybrid carbon nanotubes containing N-doped and undoped sections: powerful tensioactive nanostructures, Nanoscale, 7 (2015) 294-300.

[31] R.P. Rocha, J. Restivo, J.P.S. Sousa, J.J.M. Órfão, M.F.R. Pereira, J.L. Figueiredo, Nitrogen-doped carbon xerogels as catalysts for advanced oxidation processes, Catal. Today, 241, Part A (2015) 73-79.

[32] W.H. Shin, H.M. Jeong, B.G. Kim, J.K. Kang, J.W. Choi, Nitrogen-Doped Multiwall Carbon Nanotubes for Lithium Storage with Extremely High Capacity, Nano Letters, 12 (2012) 2283-2288.

[33] L.M. Pastrana-Martínez, S. Morales-Torres, S.K. Papageorgiou, F.K. Katsaros, G.E. Romanos, J.L. Figueiredo, J.L. Faria, P. Falaras, A.M.T. Silva, Photocatalytic behaviour of nanocarbon–TiO_2 composites and immobilization into hollow fibres, Appl. Catal. B: Environ., 142–143 (2013) 101-111.

[34] H. Choi, M.G. Antoniou, M. Pelaez, A.A. de la Cruz, J.A. Shoemaker, D.D. Dionysiou, Mesoporous Nitrogen-Doped TiO_2 for the Photocatalytic Destruction of the Cyanobacterial Toxin Microcystin-LR under Visible Light Irradiation, Environ. Sci. Technol., 41 (2007) 7530-7535.

[35] S.S. Shinde, C.H. Bhosale, K.Y. Rajpure, Photocatalytic degradation of toluene using sprayed N-doped ZnO thin films in aqueous suspension, J. Photochem. Photobiol B: Biol,, 113 (2012) 70-77.

[36] R.A.R. Monteiro, S.M. Miranda, V.J.P. Vilar, L.M. Pastrana-Martínez, P.B. Tavares, R.A.R. Boaventura, J.L. Faria, E. Pinto, A.M.T. Silva, N-modified TiO_2 photocatalytic activity towards diphenhydramine degradation and Escherichia coli inactivation in aqueous solutions, Appl. Catal. B: Environ, 162 (2015) 66-74.

[37] S. Kumar, A. Baruah, S. Tonda, B. Kumar, V. Shanker, B. Sreedhar, Cost-effective and eco-friendly synthesis of novel and stable N-doped ZnO/g-C_3N_4 core-shell nanoplates with excellent visible-light responsive photocatalysis, Nanoscale, 6 (2014) 4830-4842.

[38] L. Zhang, H. Cheng, R. Zong, Y. Zhu, Photocorrosion Suppression of ZnO Nanoparticles via Hybridization with Graphite-like Carbon and Enhanced Photocatalytic Activity, The Journal of Physical Chemistry C, 113 (2009) 2368-2374.

[39] E. Grabowska, J. Reszczyńska, A. Zaleska, Mechanism of phenol photodegradation in the presence of pure and modified-TiO_2: A review, Water Res., 46 (2012) 5453-5471.

[40] C.G. Silva, J.L. Faria, Photocatalytic Oxidation of Phenolic Compounds by Using a Carbon Nanotube-Titanium Dioxide Composite Catalyst, ChemSusChem, 3 (2010) 609-618.

[41] A.M. Peiró, J.A. Ayllón, J. Peral, X. Doménech, TiO_2-photocatalyzed degradation of phenol and ortho-substituted phenolic compounds, Appl. Catal. B: Environ., 30 (2001) 359-373.

Chapter 6

Noble metal loaded ZnO materials for photocatalytic water treatment

In chapter 5 it was found that ZnO obtained by CVD is a good candidate as photocatalyst for waste water treatment and that its activity could be enhanced by combination with carbon materials. Another alternative to enhance the photocatalytic activity of semiconductors includes loading with noble metal nanoparticles, seeking for an enhanced charge separation efficiency.

In this sense, the present chapter reports the characterization, and photocatalytic properties of plasmonic composites formed by dispersing gold or silver nanoparticles over ZnO materials synthesized by different routes. The role of the metal nanoparticles in the photocatalytic mechanism is discussed by comparing the kinetic results obtained under different irradiation wavelengths, and in the presence or absence of radical and hole scavengers.

Finally, selected ZnO based materials are immobilized on glass Raschig rings and tested for the degradation of a mixture of phenolic compounds.

This chapter is based on the following article:

C.G. Silva, M.J. Sampaio, S.A.C. Carabineiro, J.W.L. Oliveira, D.L. Baptista, R. Bacsa, B.F. Machado, P. Serp, J.L. Figueiredo, A.M.T. Silva, J.L. Faria, Developing Highly Active Photocatalysts: Gold-loaded ZnO for Solar Phenol Oxidation. Journal of Catalysis, 316 (2014) 182-190, reproduced by permission of Elsevier.

M.J. Sampaio, M.J. Lima, D.L. Baptista, A.M.T. Silva, C.G. Silva, J.L. Faria, Ag-loaded ZnO materials for photocatalytic water treatment, in press (doi: 10.1016/j.cej.2016.05.105).

6.1. Introduction

ZnO materials may show different types of shapes at the micro/nanoscale. Nanospheres, nanowires, nanotubes, nanorings and nanotetrapods can be obtained [1-4], depending on the synthesis route and preparation conditions. Additionally, various attempts have been made to improve the inherently low efficiency of ZnO in harvesting sunlight by shifting the spectral response into the visible and/or by retarding the recombination of electrons and holes [5].

One promising strategy to enhance the photocatalytic activity of semiconductor materials is by introducing noble metal nanoparticles (*e.g.*, Au, Ag, Pt, etc.) onto its surface [6-9]. The first report on the positive effect of adding metal nanoparticles to semiconductor photocatalysts dates back to the 1970s, with the pioneering work of Fujishima and Honda on the photo-assisted generation of hydrogen using a Pt/TiO_2 electrode [10]. Since then, many studies have focused on the role of metal nanoparticles as cocatalyst in semiconductor-based photocatalysts. A variety of explanations have been proposed for rationalizing the observed improvement in photoefficiency, including: i) increased absorption due to surface plasmons and light-trapping effects; ii) improved charge separation as a result of localized electromagnetic field; iii) promotion of electron transfer to adsorbed species; iv) electron storage effects that can drive the Fermi level to more negative potentials [11]. Moreover, different effects are observed depending on the type of metal nanoparticles, its size and shape [12].

Metal nanoparticles such as silver and gold exhibit surface plasmons in the visible spectral range. These metals can absorb visible light via surface plasmon resonance, *i.e.*, through collective oscillations of conduction band electrons in the metal particles driven by the electromagnetic field of incident light [13]. The plasmonic effect is often presented as the main contribute for the enhanced photoactivity of Au-loaded metal oxides upon visible light excitation. However, it has been found that photocharging effects, which would arise from storage of electrons within the metal core, may also play a role [11, 14]. Moreover, the optical properties of Au nanoparticles are influenced by many factors, namely the dielectric constants of both the metal and the surrounding material, the particle size, the particle shape of the metal and the surrounding environment [12].

In this chapter we present an attempt to disclose the main mechanisms involved in the photocatalytic oxidation of phenol using ZnO materials with distinct morphologies, under simulated solar light radiation. In a first approach ZnO materials were loaded

with minute amounts of Au nanoparticles (< 1 *wt.%*). Then, selected ZnO materials were loaded with different amounts of silver particles. In addition, with the aim of studying the reaction mechanism of phenol photocatalytic degradation, reactions using selective radical and hole scavengers were performed using the best performing catalysts. Furthermore, aiming the photocatalytic applications, the study was extended to the oxidation treatment of a solution containing a mixture of phenolic compounds, namely phenol, resorcinol, 4-methoxyphenol and 4-chorophenol using the most efficient materials in powder form and immobilized on glass Raschig rings.

6.2. Experimental

6.2.1. Synthesis of ZnO materials

ZnO materials with different micro/nanoscale morphologies were synthesized by different techniques.

Needle-like ZnO (ZnO-n) was prepared by a hydrothermal procedure [15] as follows: an aqueous solution of 4 M NaOH (Sigma-Aldrich, purity ≥ 97%) was heated to 70 ºC with strong stirring; an aqueous solution of 2 M $Zn(NO_3)_2 \cdot 6H_2O$ (Sigma-Aldrich, purity ≥ 99%) was added dropwise to the previous solution and left stirring for 1 h. The resulting precipitate was collected, thoroughly washed with deionized water in order to remove any residual salt, and allowed to dry at 60 °C in an oven. ZnO rods (ZnO-r) were obtained though a similar procedure, the molar ratio between NaOH and $Zn(NO_3)_2 \cdot 6H_2O$ solutions being of 4:1 instead of 2:1. The reaction temperature was 80ºC and was maintained for 6 h.

Flower-like ZnO material (ZnO-f) was synthesized starting from an equimolar aqueous solution of $Zn(NO_3)_2 \cdot 6H_2O$ and hexamethylenetetramine (Sigma-Aldrich, 99%). Ammonia solution (Sigma-Aldrich, 25%) was used to adjust the pH value to 10.0. The mixture was transferred to a Teflon-lined stainless steel autoclave and maintained at 90 ºC for 1h. Finally, the obtained material was thoroughly washed with deionized water in order to eliminate residual salts, and dried in air.

ZnO-t was prepared by a solid-state thermal process as described elsewhere [16]. Briefly, a porcelain capsule with a certain amount of zinc acetate dihydrate (Sigma-Aldrich, purity ≥ 99.5%) was placed in a horizontal oven, in which the temperature was raised using a 5 ºC min^{-1} rate, until 600 ºC. This temperature was maintained for 2 h followed by natural cooling to room temperature, being the resulting ZnO powder then collected.

Finally, ZnO-cvd was synthesized by chemical vapor deposition, according to the procedure described in chapter 5, section 5.2.2. A commercial ZnO sample from Evonik (ZnO-ev; AdNano VP 20, aggregated nanoparticles of hydrophilic ZnO) was used for comparison purposes.

6.2.2. Synthesis of Au/ZnO materials

Au at 1% nominal *wt.%* was loaded on the supports using $HAuCl_4 \cdot 3H_2O$ (Alfa Aesar) as the gold precursor through a double impregnation method. This procedure is similar to traditional impregnation (the support is impregnated with a solution of $HAuCl_4$ using sonication), but uses also a second impregnation step with a 1 M aqueous solution of Na_2CO_3 (Sigma-Aldrich, purity $\geq$ 99%), under constant ultrasonic stirring [17]. The latter step also allowed chloride removal, which is well known to cause sinterization of gold nanoparticles, thus turning them less active.

6.2.3. Synthesis of Ag/ZnO materials

The liquid impregnation method was used to prepare the Ag/ZnO samples [18]. The amounts of Ag loaded were 0.25, 0.5 and 1.0 *at.%* (atomic percentage). Ag was deposited in the ZnO-n, ZnO-t, ZnO-ev and ZnO-cvd materials. Briefly, 1 g of ZnO material was added to 250 mL of MiliQ water with different amounts of silver precursor ($AgNO_3$, Alfa Aesar, purity > 99.9%). The mixture was stirring for 24 h and then evaporated until dry at boiling temperature. The final catalysts were labeled as xAg/ZnO-y, were x and y corresponds to the percentage of Ag deposit and to the type of ZnO, respectively. The catalysts were then calcined under a 50 mL min^{-1} N_2 flow at 400 ºC for 2 h.

Selected materials were also immobilized on Raschig rings using the dip-coating technique, as described in chapter 2, section 2.2.2. Brifely, the Raschig rings were immersed in 5% *w/V* TiO_2:EtOH (ethanol, Panreac, purity $\geq$ 99.8 %) suspensions containing ZnO based materials. Each layer was dried at 100 ºC for 1 h and the whole films were calcined at 400 ºC for 2 h promoting the adherence of the catalyst on the Raschig rings surface.

6.2.4. Materials characterization

The gold particle distribution and its average size were obtained through high Z-contrast images acquired by scanning transmission electron microscopy (STEM)

and a high-angle annular dark-field (HAADF) detector. High-resolution transmission electron microscopy (HRTEM) of Au/ZnO was also performed. The analyses were carried out in a Cs-corrected FEI Titan 80/300 microscope at INMETRO.

The load of gold deposited on ZnO supports was measured by Inductively Coupled Plasma Optical Emission Spectroscopy (ICP-OES) using a Horiba Jobin Yvon Ultima 2 apparatus. The metal dispersion was calculated as:

$$DM = \frac{6 \times ns \times M}{\rho \times N \times dp} \quad (6.1)$$

where *ns* is the number of atoms at the surface per unit area (1.15×10^{19} m^{-2} for Au), *M* is the molar mass of gold (196.97 g mol^{-1}), ρ is the density of gold (19.5 g cm^{-3}), *N* is Avogadro's number (6.023×10^{23} mol^{-1}) and *dp* is the average particle size (determined by STEM, admitting that particles are spherical).

Temperature programmed reduction (TPR) experiments were carried out using an AMI-200 Catalyst Characterization Instrument (Altamira Instruments) equipped with a quadrupole mass spectrometer (Ametek, Mod. Dymaxion). The sample (150 mg) was placed in a U-shaped quartz tube and heated at 5 ºC min^{-1} up to the desired temperature under a flow of 5% (*v/v*) H_2 diluted in Ar (total flow rate of 30 cm^3 (STP) min^{-1}). The H_2 consumption was followed using a thermal conductivity detector (TCD).

A better description of the analyses performed on the DR UV-Vis, XRD and the BET specific area (S_{BET}) equipment is carefully detailed in chapter 2, section 2.2.2. The description of DRIFT and XPS analyses is given in chapter 3, section 3.2.4 and section 4.3.2, respectively.

6.2.5. Photocatalytic experiments

The photocatalytic efficiency with powders of Au/ZnO and Ag/ZnO materials was evaluated under the same conditions used in the study of carbon-ZnO materials described in chapter 5.

In a typical experiment, a pyrex cylindrical reactor was filled with 50 mL of a 20 mg L^{-1} phenol solution for 60 min. The irradiation source consisted of a 1500 W xenon lamp equipped with a cut-off soda-lime glass UV filter with infrared reflection coating, to simulate outdoor exposure (irradiance equal to 30.9 mW cm^{-2}). The catalyst load was fixed at 1 g L^{-1}. A dark period of 30 min before switching the lamp on was performed in order to establish the adsorption-desorption equilibrium.

The study was extended using selected materials as a powder and immobilized on Raschig ring to the photocatalytic degradation of a mixture containing phenolic compounds: phenol (PH), 4-methoxyphenol (MP; Fluka, purity ≥ 98%), resorcinol (RC; Sigma-Aldrich, purity ≥ 99%) and 4-chlorophenol (CP; Sigma-Aldrich, purity ≥ 99 %) with a concentration of 20 mg L^{-1} each. The irradiation was maintained for 2 h using the catalyst in the powder form. For the reactions with the catalyst immobilized on Raschig rings the irradiation was carried out for 8 h. In the photocatalytic experiments a glass cylindrical reactor (19 mm of internal diameter and 33 mm length) with 8.2 mL of useful volume was packed with nine coated rings. In a typical experiment the mixture of phenolic compounds was introduced in the reactor using a peristaltic pump at constant flow rate (Q = 17 mL min^{-1}) from a reservoir containing 50 mL of solution. Experimental set-up details are shown in chapter 2, section 2.2.3.

The concentration of the phenolic compounds and the TOC was evaluated in the equipment described in chapter 2, section 2.2.4.

The photocatalytic pathway of phenol degradation was studied using 1.0 mM solutions of EDTA and *tert*-butanol (*t*-BuOH) as hole and radical scavengers, respectively [19, 20].

6.3. Effect of gold on the photocatalytic activity of ZnO materials

6.3.1. Characterization of ZnO and Au/ZnO materials

The ZnO materials used in this study have low surface areas (Table 6.1), which is in agreement with several studies reported in the literature for ZnO catalysts [1, 16, 21].

Table 6.1 – BET surface areas and crystallite sizes of ZnO samples, and gold loading, particle size and metal dispersion for the respective Au/ZnO materials.

ZnO material	S_{BET} (m^2 g^{-1})	Crystallite size (nm)	λ_{Au}, max (nm)	Au loading (wt. %)	Au average size (nm)	Au particle dispersion (%)
ZnO-n	2a	39	539	0.38	5.8	19.9
ZnO-r	8a	60	529	0.90	6.2	18.6
ZnO-f	4a	47	525	0.29	5.4	21.4
ZnO-t	6a	54	542	0.35	6.2	18.7
ZnO-ev	26	53	556	0.46	5.0	23.1
ZnO-cvd	17	58	541	0.69	2.9	39.9

[a] within the determination error (± 5 m^2 g^{-1}).

The commercial material (ZnO-ev) had the highest surface area of 26 $m^2 g^{-1}$, whereas the synthesized materials had surface areas smaller than 20 $m^2 g^{-1}$.

The X-ray powder diffractograms of the ZnO supports are shown in Figure 6.1. Several well-defined diffraction reflections characteristic of ZnO were observed in the X-ray diffraction patterns. These peaks appeared at 31.6°, 34.4°, 36.1°, 47.6°, 56.7°, 62.9°, 68.0° and 69.2° corresponding to the lattice planes of (100), (002), (101), (102), (110), (103), (112) and (201), respectively. The observed diffraction peaks can be indexed to the hexagonal wurtzite structure of ZnO (JCPDS 36-1451). The crystallite sizes of the ZnO samples derived from the XRD analysis are displayed in Table 6.1.

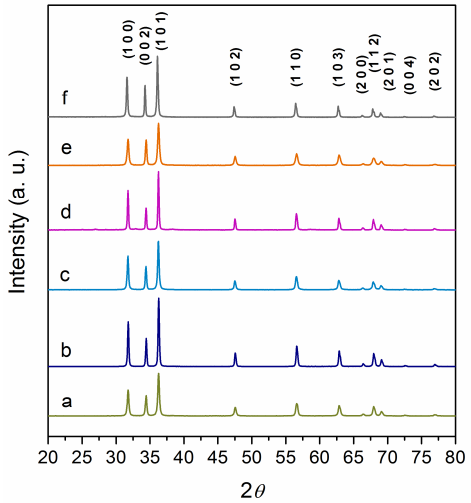

Figure 6.1 – XRD diffractograms of the ZnO materials: ZnO-ev (a), ZnO-t (b), ZnO-f (c), ZnO-r (d), ZnO-n (e) and ZnO-cvd (f).

The DRIFT spectra of selected ZnO materials are shown in Figure 6.2. Common to all spectra there is a high intensity sharp band peaking at around 620 cm^{-1}, attributed to Zn–O stretching vibration [22], and a broad band located between 3000 and 3700 cm^{-1}, attributed to the stretching vibrations of hydrogen bonded surface water molecules and hydroxyl groups [23]. Weak bands in the region 1400–1650 cm^{-1}, caused by bending vibration of coordinated water [23] and at *c.a.* 875 cm^{-1}, attributed to Zn–OH group [24], are also observed, being more pronounced for ZnO-cvd and ZnO-ev materials. For these latter materials, a small shoulder in the 300-3700 cm^{-1} broad band is observed, positioned at 3671 cm^{-1}, attributed to isolated hydroxyl groups present on ZnO crystal faces, characteristic of defects or oxygen vacancies on the catalyst surface [25]. The presence of this band was also observed for ZnO-t.

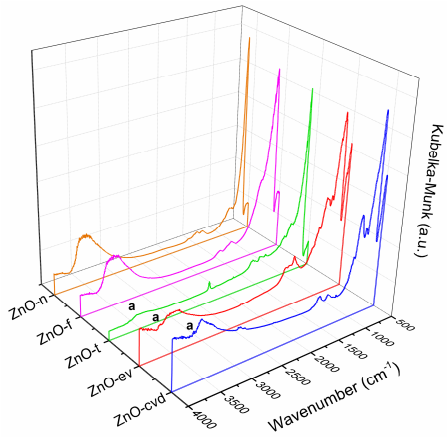

Figure 6.2 – DRIFT spectra of ZnO materials. Hydroxyl isolated groups are marked with "a".

The structural differences between the various ZnO materials are evidenced by the SEM images depicted in Figure 6.3. A notorious change in the morphology was observed for the synthesized materials, depending on the preparation conditions.

ZnO-n and ZnO-r were both obtained by a room pressure hydrothermal procedure, starting from zinc nitrate and sodium hydroxide, the difference being the molar ratio of the reactants of 1:2 and 1:4 and the reaction temperature of 70 ºC and 80 ºC, respectively. In addition, the precursors were left to react only 1 h in the case of ZnO-n and 6 h in the case of ZnO-r. The SEM micrograph of ZnO-n (Figure 6.3a) shows needle-like particles of about 40-50 nm in diameter and 600 nm in length, while for ZnO-r, hexagonal prismatic particles with tops of 200-300 nm of hexagon diagonal and 800-1300 nm length are observed (Figure 6.3c). The distinct morphologies obtained for these materials can be attributed to the different growth rates of the crystalline faces [3]. ZnO is a polar crystal, in which positive planes are rich in Zn and the negative planes are rich in O. During the hydrothermal process, the negatively charged $Zn(OH)_4^{2-}$ growth units of ZnO preferably adsorb on the positive polar plane (0001), which has the highest growth rate [26]. It is known that the higher the growth rate, the quicker is the disappearance of the plane. Therefore, the (0001) plane, which corresponds to the plane of the hexagonal tops observed in ZnO-r (Figure 6.3c inset), disappears in the hydrothermal process at lower concentration of sodium hydroxide, which leads to the needle-like shape observed for the ZnO-n material (Figure 6.3a).

In ZnO-f, ZnO bundle shapes greatly resemble natural flowers (Figure 6.3e). A single "flower" consists of needle-like crystals with diameters of about 250 nm and average length of 2 μm (aspect ratio of 8) radiating from the center. ZnO-t (Figure 6.3g)

is composed by spherical (100-250 nm diameter) and 1D needle-like structures with uneven diameter distribution along their longitudinal directions (500-900 nm).

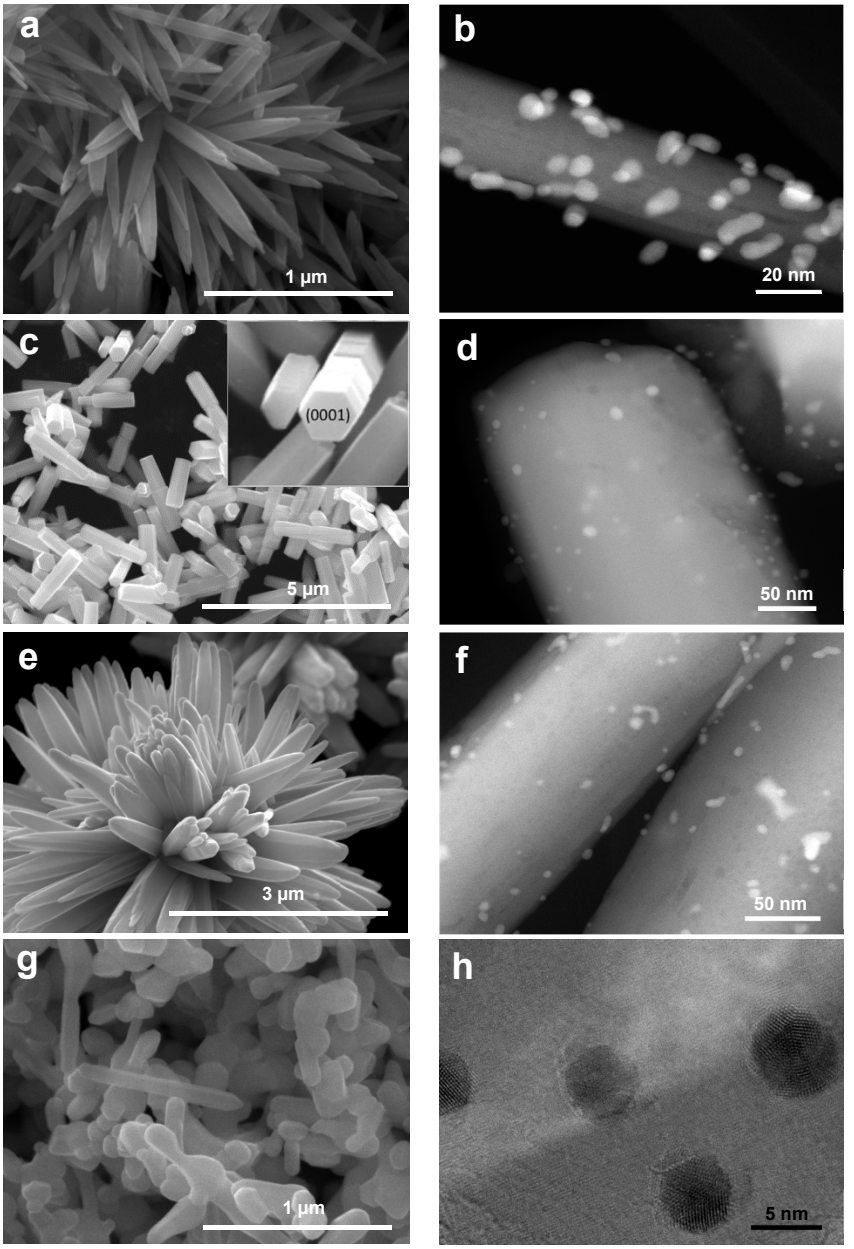

Figure 6.3 – SEM (a, c, e and g), STEM (b, d and f) and HRTEM (h) micrographs of Au/ZnO-n (a and b), Au/ZnO-r (c and d), Au/ZnO-f (e and f), and Au/ZnO-t (g and h), respectively.

Finally, as already described in chapter 5, section 5.3.1, ZnO-cvd material is composed of tetrapod-like structures, where needles grow from a faceted seed

particle. The needles have diameters varying from 8 to 50 nm and grow over 1 μm in length, giving them an aspect ratio of around 20-100.

After gold deposition, the presence of very small Au spheroidal particles was observed for all the materials, as illustrated in the STEM/TEM micrographs displayed in Figure 6.3.

Average gold particle size varied depending on the ZnO support. The smallest particles were observed for Au/ZnO-cvd with an average size of 2.9 nm. For the other materials the average gold particle dimensions varied between 5.0 and 6.2 nm. As reported in a previous work [27], the low dimensions of Au particles deposited on ZnO-cvd can be attributed to the presence of single crystals of ZnO with a high aspect ratio, and to a strong interaction (epitaxy) between Au and the support. It can be also observed that Au particles of very small dimensions can be deposited by DIM even for materials with exceptionally low surface area, which is the case of ZnO-r, ZnO-n, ZnO-f and ZnO-t. Although the nominal gold amount has been set to 1 *wt.*% (by using the adequate amount of gold precursor), lower Au loads were obtained for the different ZnO supports. The low deposition yield obtained by this method has been previously reported for the preparation of Au/ZnO and Au/carbon materials, being attributed to some metal leaching occurring during the preparation of the catalysts [27, 28].

Analysis of the DR UV-Vis spectra of the Au/ZnO samples reveals, as expected, two bands due to the presence of gold nanoparticles: one in the visible region between 450 and 650 nm, characteristic of the gold surface plasmon band [29], and a stronger one, with onset at 400 nm, that is due to the bandgap transition of semiconductor ZnO (Figure 6.4) [30].

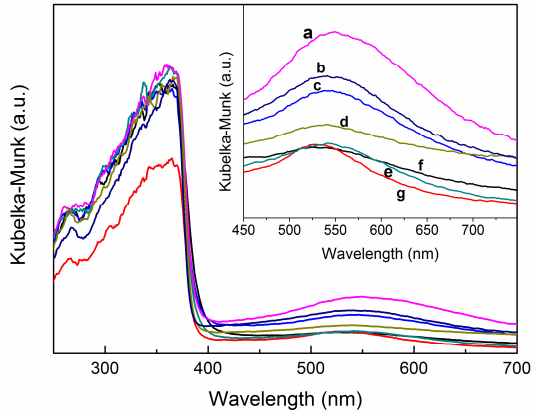

Figure 6.4 – Diffuse reflectance UV-Vis spectra of Au/ZnO-ev (a), Au/ZnO-cvd (b), Au/ZnO-n (c), Au/ZnO-t (d), Au/ZnO-sc (e), Au/ZnO-f (f) and Au/ZnO-r (g).

A careful inspection of the position of the surface plasmon resonance band reveals that Au/ZnO-r and Au/ZnO-f exhibit very similar absorption maxima at around 530 nm, while Au/ZnO-n, Au/ZnO-t and Au/ZnO-cvd at around 540 nm (Figure 6.4 inset). The gold surface plasmon band of Au/ZnO-ev shows a higher relative absorption and is red-shifted from the other set of samples, with a wavelength maximum at 556 nm. The wavelength maximum of the surface plasmon resonance absorption band is determined by the size and shape of gold nanoparticles [31]. The actual wavelength maximum for each sample is given in Table 6.1.

6.3.2. Photocatalytic oxidation of phenol using Au/ZnO materials

Photocatalytic oxidation of phenol in aqueous media was selected as a model reaction for studying the catalytic efficiency of the different ZnO and Au/ZnO materials upon simulated solar light excitation.

A blank experiment, in the absence of any catalyst, was also performed for comparison purposes. As already seen before, only 5% of phenol abatement was achieved after 1 h of irradiation.

Results show that the kinetics of photocatalytic phenol oxidation follows a pseudo-first order rate law, for all the tested catalysts. The magnitudes of the k_{app}, determined by non-linear curve fitting to the experimental data, are represented in Figure 6.5. Distinct kinetic behavior was observed, depending on the ZnO materials used. Among the neat ZnO catalysts, ZnO-f was the least active, while ZnO-cvd was the most efficient, with k_{app} values of 0.26×10^{-2} and 9.26×10^{-2} min^{-1}, respectively.

The presented results show that the synthesis route has a remarkable influence on the structure of ZnO materials at the micro/nanoscale and, consequently, on their photocatalytic activity. The surface areas of the ZnO materials are listed in Table 6.1. ZnO-f, ZnO-r, ZnO-n and ZnO-t show very low surface areas ($S_{BET} \leq 8$ m^2 g^{-1}), indicating that few active sites are available for adsorption and reaction. As already seen before, a typical method to evaluate the effect of the surface area on the overall efficiency of catalysts is to compare the kinetic rate constant per unit surface area (Figure 6.5). By evaluation of this parameter, it can be stated that the relative efficiencies of ZnO-f and ZnO-r remain very low (k_{app}/S_{BET} of 0.64 and 1.2 min^{-1} m^{-2} g, respectively), while the efficiency of ZnO-n increased due to its very low surface area (S_{BET} = 2 m^2 g^{-1}). Although presenting low surface area (S_{BET} = 6 m^2 g^{-1}), ZnO-t shows the highest efficiency in terms of k_{app}/S_{BET}.

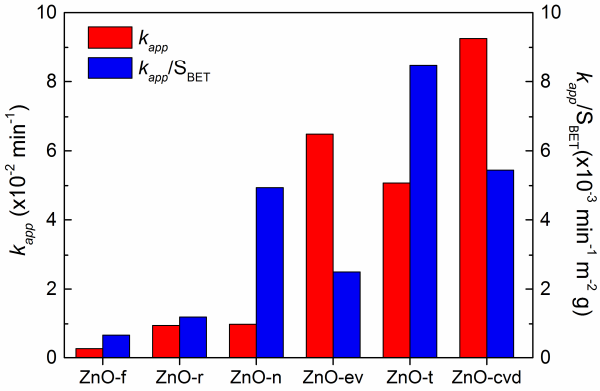

Figure 6.5 – kapp and k_{app}/S_{BET} for the photocatalytic reactions using neat ZnO catalysts.

These results indicate that the surface area is not the only factor accounting for the photoefficiency of the ZnO materials. Surface chemistry, in particular the presence of isolated hydroxyl surface groups, as confirmed by DRIFT analysis (Figure 6.2), is known to play an important role in the performance of metal oxide photocatalysts [25]. The presence of these surface groups also increases the hydrophilicity of the materials, resulting in a better dispersion of the catalysts in the aqueous suspensions, as observed for ZnO-cvd, ZnO-t and ZnO-ev.

In the case of the ZnO materials, an increase in k_{app} upon gold loading was observed in all cases, the highest value being obtained with the Au/ZnO-cvd catalyst (20.0×10^{-2} min^{-1}). The effect of the presence of Au nanoparticles was quantified by means of a synergy factor (R_{kapp}), defined as:

$$R_{kapp} = \frac{k_{app(\mathrm{Au/ZnO})}}{k_{app(\mathrm{ZnO})}} \qquad (6.1)$$

The highest value was obtained with the ZnO-f material (R_{kapp} = 3.6) followed by ZnO-n (R_{kapp} = 2.7). It should be noted that the neat ZnO-f and ZnO-n show very low photocatalytic activity and the introduction of Au produced a significant improvement in the kinetics of the degradation process. With ZnO-r, ZnO-cvd and ZnO-t R_{kapp} of around 2.0 was obtained when the respective Au-loaded catalysts were used. The introduction of Au on ZnO-ev produced only a 20% increase in k_{app}.

Overall, in terms of kinetics, commercial ZnO-ev and synthesized ZnO-cvd and ZnO-t were the most efficient, among neat and Au-loaded catalysts, with practically total phenol removal achieved at 30 min of irradiation (Table 6.2).

Table 6.2 – Phenol conversion (X) after 30 min of irradiation obtained with neat and Au-loaded ZnO materials and synergy factors for k_{app} (R_{kapp}) and TOC removal (R_{TOC}).

Catalyst	$X_{Au/ZnO,30\ min}$ (%)	$X_{ZnO,30\ min}$ (%)	R_{kapp}	R_{TOC}
Au/ZnO-f	24.8	7.46	3.6	7.1
Au/ZnO-r	43.0	25.0	2.0	15
Au/ZnO-n	52.8	27.7	2.7	23
Au/ZnO-ev	96.5	85.9	1.2	1.6
Au/ZnO-t	97.9	75.6	1.9	1.7
Au/ZnO-cvd	100	94.0	2.2	1.1

For better comparison of the results obtained with the different Au-loaded materials, the k_{app} values were normalized by the mass of gold present in each catalyst (Figure 6.6a), since ICP analysis revealed that distinct percentages of gold had been loaded on the ZnO samples. Results show that, even normalizing the kinetic rate constants by the mass of gold, Au/ZnO-ev, Au/ZnO-t and Au/ZnO-cvd remain as the most active photocatalysts. In this case, the relative efficiency of Au/ZnO-t increased significantly (due to the very low amount of gold), the normalized k_{app} being of the same order or magnitude as that obtained with Au/ZnO-cvd (5.6 min^{-1} mg_{Au}^{-1}).

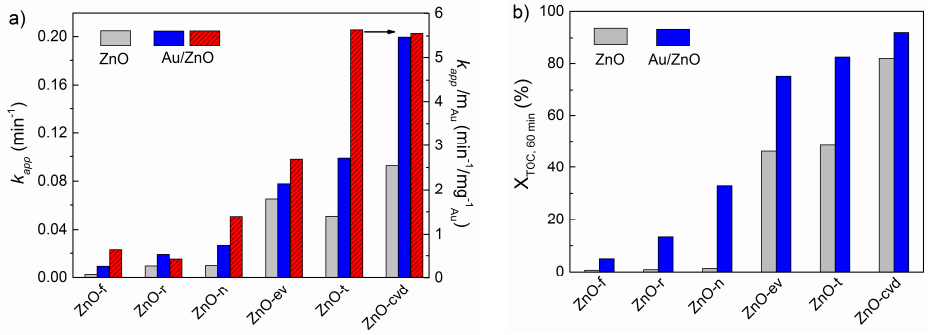

Figure 6.6 – (a) First order apparent rate constants (k_{app} and k_{app}/mg_{Au}) and (b) TOC removal at the end of 60 min of irradiation ($X_{TOC,\ 60\ min}$) for the photocatalytic reactions using neat and Au-loaded ZnO materials.

Although k_{app} is generally accepted as a key parameter to characterize the efficiency of photocatalytic oxidation processes, it has to be taken into account that it mainly provides information about the disappearance rate of the original molecule. The main photo-oxidation intermediates were hydroquinone, benzoquinone and catechol (Figure 6.7). With the neat ZnO-f, ZnO-r and ZnO-n, negligible TOC removal was obtained, while mineralization degrees of 46, 49 and 82% were achieved when using

ZnO-ev, ZnO-t and ZnO-cvd, respectively (Figure 6.6b). It is worth noting that, although phenol and aromatic intermediates are completely removed when using these latter catalysts, there is still a fraction of organic species present in the aqueous phase at the end of the reaction, mostly corresponding to aliphatic compounds resulting from the aromatic ring opening that contribute to the residual TOC content. The photocatalytic reactions using ZnO-f, ZnO-r and ZnO-n based materials were much slower; at the end of 60 min of irradiation there was still an important amount of phenol to be degraded, as well as phenolic intermediates (Figure 6.7), which is reflected in the lower TOC removal efficiencies.

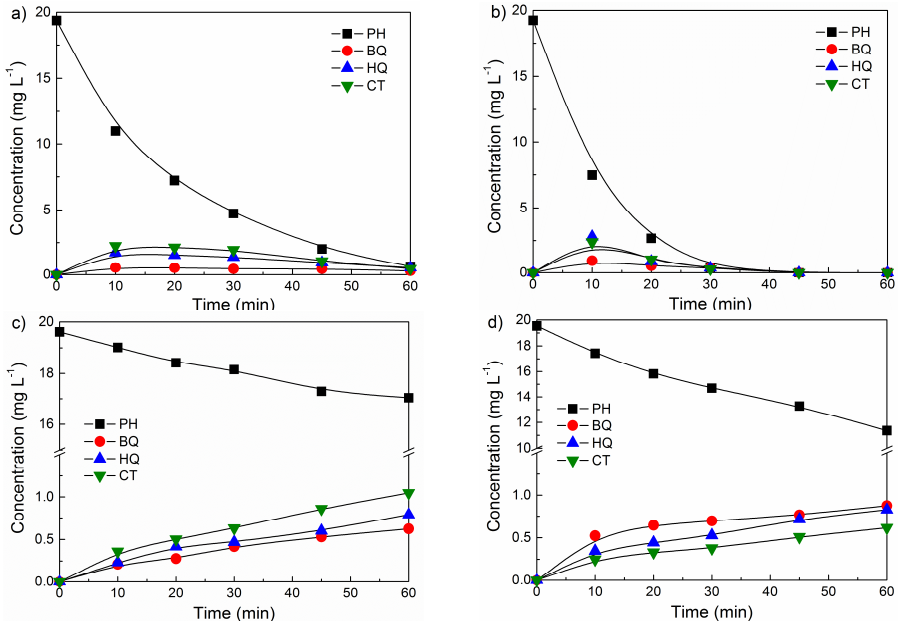

Figure 6.7 – Concentration profiles for phenol (PH), and reaction intermediates benzoquinone (BQ), hydroquinone (HQ) and catechol (CT), using ZnO-t (a), Au/ZnO-t (b), ZnO-f (c) and Au/ZnO-f (d) catalysts.

The introduction of Au produced a notorious increase in the TOC removal capacity of the ZnO materials (Figure 6.6b). Similarly to what was previously described for k_{app}, this effect was quantified by using a synergy factor, R_{TOC}, defined as:

$$R_{TOC} = \frac{X_{TOC(Au/ZnO)}}{X_{TOC(ZnO)}} \quad (6.2)$$

The highest synergy factor value was obtained for Au/ZnO-n (R_{TOC} = 23), followed by Au/ZnO-r (R_{TOC} = 15) and Au/ZnO-f (R_{TOC} = 7.1). These expressive values result from a large increase in the TOC removal capacity of the ZnO materials, promoted by gold nanoparticle incorporation. For Au/ZnO-ev and Au/ZnO-t, R_{TOC} values of 1.6 and

1.7 were obtained, which indicate 60 and 70% increase in the mineralization capacity of the corresponding neat ZnO materials, respectively. Finally, 10% TOC removal improvement was obtained using Au/ZnO-cvd as catalyst.

6.3.3. Photo-activation mechanism of Au/ZnO materials

To better understand the effect of Au on the global efficiency of the ZnO photocatalysts, a set of experiments using the catalysts presenting the best performances, *i.e.*, ZnO-t, ZnO-ev and ZnO-cvd and their respective Au-loaded materials were carried out (Figure 6.8). The irradiation source consisted in a medium-pressure mercury lamp equipped with cut-off filters for emission at $\lambda > 365$ nm or $\lambda > 420$ nm, when near UV to visible or only visible light were required, respectively.

The used photocatalytic reactor was described in detail in chapter 3, section 3.2.5. When the catalysts were irradiated with visible light ($\lambda > 420$ nm), ZnO-t and ZnO-ev show very little activity (Figure 6.8a inset), which may be attributed to limited absorption of these materials at this wavelength range. Loading these materials with gold nanoparticles produced an increase in kinetics of the photocatalytic process, and R_{kapp} values of 1.6 and 4.2 were obtained for Au/ZnO-t and Au/ZnO-ev, respectively.

Despite being very active when irradiated at $\lambda > 365$ nm (Figure 6.8a), ZnO-cvd and Au/ZnO-cvd did not produce any phenol degradation under visible light irradiation (Figure 6.8a inset).

In addition, when 546 nm radiation was used (Figure 6.8b), neat ZnO-t and ZnO-ev did not show any activity, while the gold loaded materials produced 4 and 23% of phenol removal at the end of 2 h of irradiation, respectively.

The results suggest the existence of different activation mechanisms depending on the type of ZnO materials and irradiation wavelength used (UV or visible). It is generally accepted that semiconductor loading with noble metal nanoparticles may enhance the photocatalytic activity by increasing the amount and lifetime of photogenerated electron/hole pairs and by avoiding charge recombination [31]. Nevertheless, in the case of gold-loaded semiconductors, it has been shown that different photo-excitation mechanisms may occur depending on the irradiation wavelength used [11, 29]. The most reasonable rationalization of the photocatalytic mechanism under UV light assumes the direct photoexcitation of ZnO. As the Fermi level of gold is lower than that of ZnO, photo-excited electrons may be transferred from the conduction band of the semiconductor to metal particles deposited on its surface,

while photo-generated valence band holes remain on ZnO. Nevertheless, not all of the photogenerated electrons migrate from the semiconductor to the metal, with some remaining in the semiconductor particle as the two systems attain Fermi-level equilibration [32]. This charge effect is expected to be the main mechanism occurring for Au/ZnO-cvd, since no activity was observed when irradiated with visible light (Figure 6.8a inset).

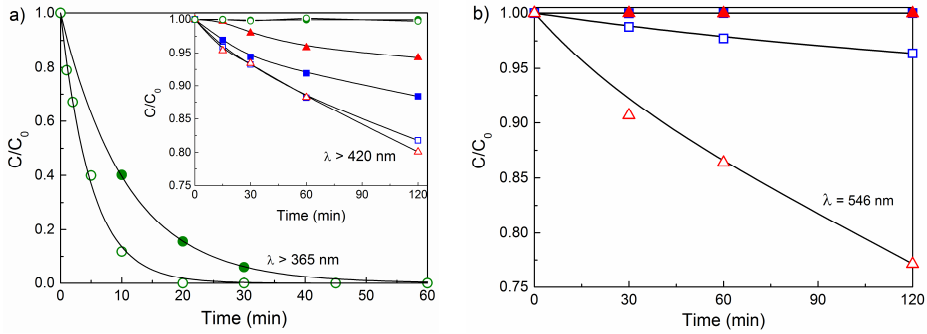

Figure 6.8 – Photocatalytic oxidation of phenol under λ > 365 nm (a), λ > 420 nm (a, inset) and λ = 546 nm (b) using ZnO-cvd (-●-), Au/ZnO-cvd (-○-), ZnO-t (-■-), Au/ZnO-t (-□-), ZnO-ev (-▲-) and Au/ZnO-ev (-△-).

On the other hand, a plasmonic effect is expected to occur upon visible light photoexcitation of gold nanoparticles by irradiation at λ = 546 nm, very close to the absorption maxima of gold plasmon band, as in the case of Au/ZnO-ev and Au/ZnO-t materials. In this case, electrons from Au are injected into the ZnO conduction band leading to the generation of positive charges in the Au nanoparticles [11, 29]. This different behavior observed in the photoactivation mechanism of the gold loaded ZnO materials may be related to the different sizes of the gold nanoparticles loaded on the ZnO materials [33].

It has been reported that gold nanoparticles with diameter below 5 nm do not show surface plasmon resonance due to the quantum-size limitations [34]. It should be the case of Au/ZnO-cvd, whose gold particles have an average diameter of 2.9 nm. Moreover, the higher efficiency of Au/ZnO-ev compared to that of Au/ZnO-t under 546 nm excitation may be attributed to the higher percentage of gold loaded on the ZnO-ev material. Another interesting observation is the difference in the k_{app} values (Table 6.3) for the reactions using Au/ZnO-ev upon excitation at λ > 420 nm (0.18×10^{-2} min^{-1}) and at λ = 546 nm (0.23×10^{-2} min^{-1}).

Table 6.3 – First order kinetic rate constants (k_{app}) for the photocatalytic degradation of phenol under different irradiation wavelengths.

	k_{app} ($\times 10^{-2}$ min^{-1})			
Catalyst	> 365 nm	> 420 nm	= 546 nm	Solar
ZnO-cvd	12.6	n.d.	-	9.26
Au/ZnO-cvd	63.0	n.d.	-	20.0
ZnO-t	0.28	-	n.d.	5.07
Au/ZnO-t	0.45	-	0.033	9.86
ZnO-ev	0.043	-	n.d.	6.48
Au/ZnO-ev	0.18	-	0.23	7.78

n.d.: no degradation observed; "-" not measured

Besides the higher irradiation intensity at $\lambda > 420$ nm (2.17 mW cm^{-2} comparing to 0.65 mW cm^{-2} for $\lambda = 546$ nm), the efficiency of Au/ZnO-ev catalyst was lower, as a result of the simultaneous electron transfer between the semiconductor and the metal nanoparticles, since both are being irradiated at this wavelength range.

6.3.4. Photocatalytic phenol oxidation pathway using ZnO and Au/ZnO materials

The photocatalytic pathway of phenol oxidation was studied using ZnO-t, ZnO-cvd and the respective gold-loaded materials under simulated solar light using ethylenediaminetetraacetic acid **(**EDTA) and *tert*-butanol (*t*-BuOH) as hole and radical scavengers, respectively [20, 35, 36]. Results show the phenol concentration evolution in the photocatalytic experiments using bare (Figures 6.9a and 6.9c) and Au-loaded (Figure 6.9b and 6.9d) materials in the presence of scavengers. The corresponding pseudo-first order rate constants are presented in Table 6.4.

Table 6.4 – First order kinetic rate constants (k_{app}) for the photocatalytic degradation of phenol under solar light irradiation in the presence of EDTA or *t*-BuOH.

Catalyst	$k_{app,EDTA}$ ($\times 10^{-2}$ min^{-1})	$k_{app,t\text{-}BuOH}$ ($\times 10^{-2}$ min^{-1})
ZnO-cvd	1.96	7.02
Au/ZnO-cvd	4.89	14.4
ZnO-t	1.04	3.66
Au/ZnO-t	2.30	9.59

It was observed in all cases that the addition of EDTA or *t*-BuOH produced a decrease in the rate of phenol degradation, which indicates that both radical species and photogenerated holes are involved in the phenol degradation mechanism.

The introduction of EDTA led to a noticeable decrease, in the same order of magnitude, in k_{app} of 79 and 77% for ZnO-t and Au/ZnO-t, and of 79 and 75% for ZnO-cvd and Au/ZnO-cvd, respectively. When *t*-BuOH was added to the system, a similar decrease in k_{app} was observed for the reactions with ZnO-cvd (24%), Au/ZnO-cvd (28%) and ZnO-t (28%). Yet, a very different behavior was observed for Au/ZnO-t, the addition of the radical scavenger leading to a mere 3% decrease in k_{app}.

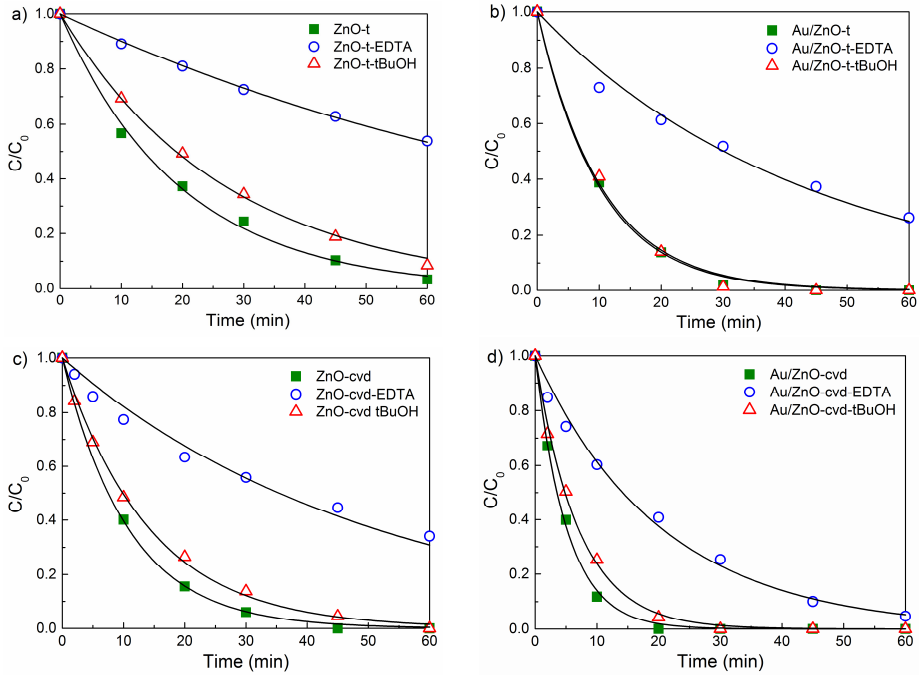

Figure 6.9 – Effect of hole/radical scavengers (1 mM EDTA/t-BuOH) on the photocatalytic degradation of phenol using ZnO-t (a), Au/ZnO-t (b), ZnO-cvd (c) and Au/ZnO-cvd (d) catalysts under simulated solar light irradiation. Curves represent the fitting of the pseudo-first order rate equation to the experimental data.

The above results suggest that photogenerated holes play a major role in the mechanism of phenol degradation (both direct oxidation and through formation of reactive radicals such as hydroxyl radical, $HO^{\bullet}$), but free radicals produced by photoexcited electrons (such as superoxide radical, $O_2^{\bullet-}$) also participate in this mechanism particularly when ZnO-cvd, Au/ZnO-cvd and ZnO-t are used. However, when Au/ZnO-t is used, a minor effect is observed when using *t*-BuOH as radical scavenger, which indicates that in this case the main reaction pathway is through direct oxidation of phenol by the photogenerated holes.

As discussed in the previous section, it is expected that the main mechanism of Au/ZnO-cvd activation occur by direct photo-excitation of ZnO-cvd, with Au

nanoparticles acting as electron sinks, while in the case of Au/ZnO-t both semiconductor and metal nanoparticle excitation may occur simultaneously upon solar light irradiation. This may increase the availability and the lifetime of holes formed on both ZnO and Au particles, which are easily quenched by phenol, leading to its oxidation through a “photo-Kolbe-like” process [37].

6.4. Effect of silver on the photocatalytic activity of ZnO materials

In the next section Ag was loaded on ZnO-n, ZnO-t and ZnO-ev taking into account their efficiency for phenol oxidation. The effect of Ag content and the efficiency of the photocatalysts was assessed for phenol degradation. Then, the study was extend for the degradation of a mixture of phenolic compounds using the best catalyst in powder form and immobilized on glass Raschig rings.

6.4.1. Characterization of Ag/ZnO photocatalysts

As already seen before (Table 6.1), the specific surface area (S_{BET}) of the bare ZnO materials were 2, 6 and 26 $m^2\ g^{-1}$ for ZnO-n, ZnO-t and ZnO-ev, respectively. *Melián et al.* [18] have reported that the deposition of silver in semiconductors may enhance the adsorption capacity of the photocatalyst by increasing its surface area. On the other hand, other studies show that during the preparation method the Ag nanoparticles can aggregate forming small clusters, thus reducing the surface area of the resulting material [38]. In this study, no change on the S_{BET} of the ZnO materials was observed after Ag loading, which may be attributed to the small amount of Ag deposited in the ZnO materials.

Representative HRTEM images of Ag spheroidal particles deposited on ZnO-n and ZnO-t are given in Figures 6.10a and 6.10b, respectively. The HRTEM images suggest a good distribution of Ag particles with similar size (5 nm) over the ZnO materials.

SEM images of commercial ZnO-ev and Ag/ZnO-t film are also shown in Figures 6.10c and 6.10d, respectively. The ZnO-ev consists mainly of small (50-100 nm), cylindrical, and spherical particles. When the Ag/ZnO-t material was immobilized in glass rings a relatively homogeneous film at the microscale was observed.

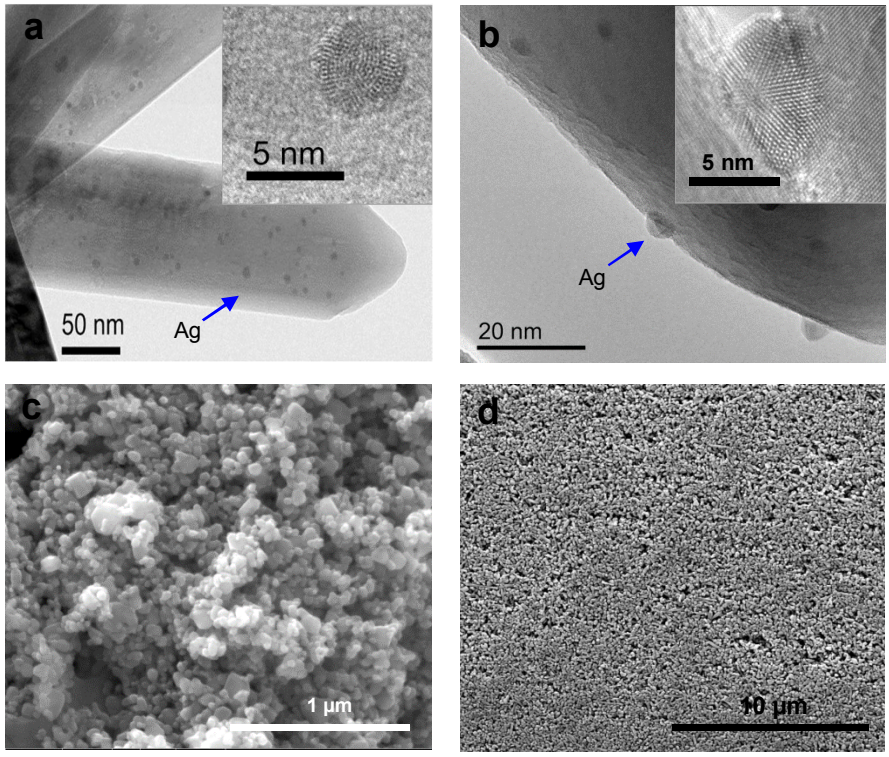

Figure 6.10 – HRTEM micrographs of Ag/ZnO-n (a), Ag/ZnO-t (b), and SEM image of Ag/ZnO-t immobilized on glass rings.

The DRUV-Vis spectra of the photocatalysts are shown in Figure 6.11. The presence of Ag nanoparticles on ZnO materials leads to the increase of the absorption in the visible light range between 400 and 600 nm, due to the Ag surface plasmon band [39], as already seen for Au/ZnO materials. The band gap energy values obtained were 3.20, 3.22 and 3.24 eV for ZnO-n, ZnO-t and ZnO-ev, respectively. For low content of silver (0.25 *at.%*) the band gap energy is similar to those of bare ZnO materials. However, when the Ag amount was increased a slight decrease in the band gap was detected. This observation was more pronounced for the Ag/ZnO-ev catalysts, decreasing from 3.24 eV to 3.12 eV for bare ZnO-ev and 1.0%Ag/ZnO-ev, respectively. This decrease in the band bap on Ag/ZnO-ev materials suggests a better distribution of Ag nanoparticles on ZnO-ev surface, which hold the highest S_{BET} (26 m^2 g^{-1}), than ZnO-n and ZnO-t, resulting in an increase of the absorption in the entire visible spectrum range (Figure 6.11c).

Regarding the position of the surface plasmon resonance band for Ag/ZnO-n and Ag/ZnO-t materials (Figures 6.11a and 6.11b inset, respectively), the maximum absorption occurs at 454 nm, while for Ag/ZnO-ev a red-shifted band with a maximum

peaking at 476 nm is observed (Figure 6.11b inset). This shift may be attributed to the presence of Ag nanoparticles with different size and shape [40]. As expected, the absorption in the visible spectral range is directly proportional to the amount of Ag loaded in the different ZnO materials.

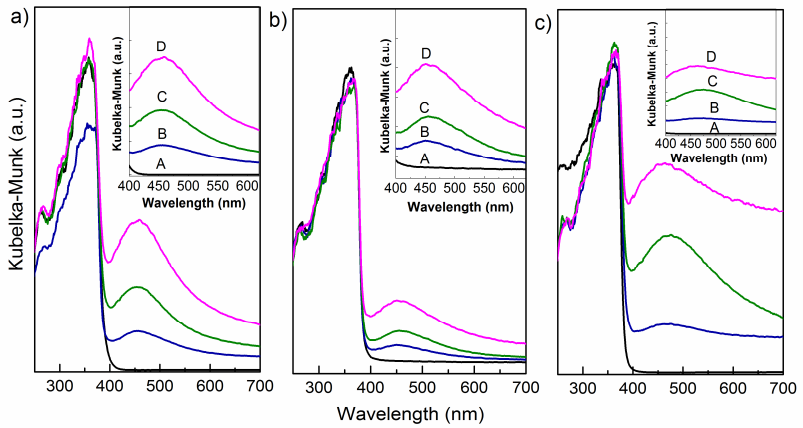

Figure 6.11 – Diffuse reflectance UV-Vis spectra of Ag/ZnO-n (a), Ag/ZnO-t (b) and Ag/ZnO-ev (c) materials. A, B, C and D correspond to 0, 0.25, 0.5 and 1.0 *wt.%* of Ag.

XPS analysis 1%Ag/ZnO-t material is shown in Figure 6.12a. The reference binding energies (BE) reported for $3d_{3/2}$ and $3d_{5/2}$ levels of Ag with a spin-orbital splitting photoelectrons (6.0 eV) are 368.1 eV and 374.1 eV, respectively [41, 42]. If the peaks in the 3d level are shifted to lower BE ($\leq$ 0.6 eV), Ag could be at different states (Ag, Ag_2O and AgO). Deconvolution fitting of the XPS spectrum showed two peaks in the $3d_{5/2}$ level, at 367.8 and 368.2 eV and for $3d_{3/2}$ level, at 373.9 and 374.2 eV, corresponding to oxidized Ag (AgO) and to Ag^0 state, respectively.

It has been reported that $AgNO_3$, used as silver precursor, can be easily decomposed at low temperatures to give Ag_2O [43]. However, Ag_2O is very unstable above ~120 ºC, being converted to AgO at temperatures between 100 and 200 ºC, while AgO starts to decompose into Ag above 400 ºC. The TPR analyzes were carried out in order to identify the decomposition temperature of Ag species in 1%Ag/ZnO-t (Figure 6.12b) before and after the calcination treatment at 400 ºC. The TPR profile of bare ZnO-t was also evaluated as control. Two peaks in the 100-220 ºC range were observed for the non-calcined material, which could be assigned to the decomposition of Ag_2O to form AgO and also to the formation of NO_2 resulting from the $AgNO_3$ decomposition [43]. After the thermal treatment at 400 ºC, the peaks corresponding to the decomposition of Ag_2O and NO_2 are absent indicating that this temperature is

adequate to guarantee the elimination of NO_2 from the silver precursor. From TPR analysis no signal was detected for ZnO confirming the stability of the material among the temperatures tested.

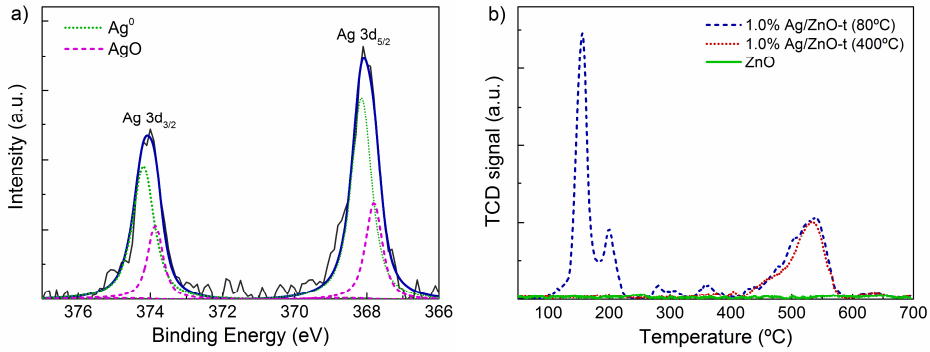

Figure 6.12 – XPS spectrum of 1%Ag/ZnO-t (a) and TPR analysis of both ZnO-t and 1%Ag/ZnO-t (b).

6.4.2. Photocatalytic activity of Ag/ZnO materials

The effect of silver deposition on the efficiency of ZnO materials was studied for the photocatalytic oxidation of phenol in water under simulated solar light. As mentioned, in section 6.3.2, in the absence of catalyst a decrease in phenol concentration of 5% after 60 min irradiation is observed. It was also observed that a maximum of 5% decrease in phenol concentration after the dark adsorption period was obtained for both ZnO and Ag/ZnO materials.

Different behaviors were observed depending on the ZnO materials used (Figure 6.13). Among the bare ZnO materials, ZnO-n was the less active catalyst, while ZnO-ev was the most efficient, with k_{app} of 9.8×10^{-3} and 6.5×10^{-2} min^{-1}, respectively. Nevertheless, when silver was loaded on ZnO-ev, a significant decrease in k_{app} was observed being more pronounced for the sample containing 1.0 *at.*% ($k_{app} = 3.3\times10^{-2}$ min^{-1}). In fact, some authors have shown that the deposition of noble metals not always improves the photoactivity of semiconductors. Depending on the structure of the photocatalyst, the Ag deposition may result in the blockage of the active centers of the metal oxide semiconductor, thus reducing its photocatalytic activity [18, 40].

In the case of ZnO-t materials the addition of Ag leads to an increase in the photocatalytic activity. It was found that the lowest amount of silver (0.25 *at. %*) led to the highest phenol degradation efficiency ($k_{app} = 7.7\times10^{-2}$ min^{-1}). However, when the

amount of Ag is increased the photoefficiency of the ZnO-t materials declined. This may suggest that the effective quantity of holes and electrons when 0.25 *at. %* Ag is added is adequate for oxidize an initial concentration of 20 mg L^{-1} of phenol and any increase in the silver load may lead to a surplus charge separation state which is not efficiently contributing to the reaction.

For Ag/ZnO-n materials an increase in k_{app} with increasing Ag load was observed, with a k_{app} of 3.34×10^{-2} min^{-1} being obtained using 1%Ag/ZnO-n catalyst, corresponding to a 3.4 fold increase compared with bare ZnO-n. A ZnO-ev sample with 1.4 *at.%* Ag was also tested, a decrease in the efficiency for phenol degradation was obtained (k_{app} = 2.61×10^{-2} min^{-1}).

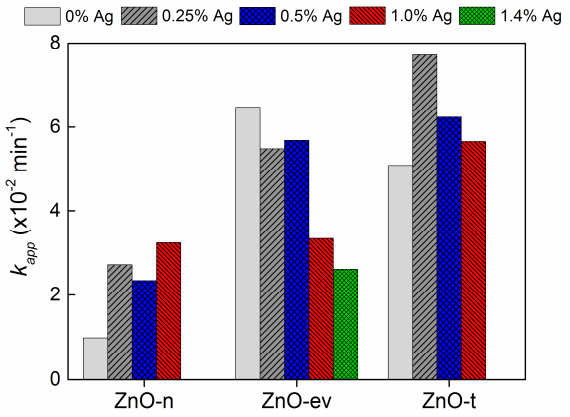

Figure 6.13 – First order apparent rate constants (k_{app}) for the photocatalytic reactions using neat and Ag-loaded ZnO materials.

It is worth mentioning that Ag nanoparticles were also deposited on ZnO-cvd (the most efficient ZnO found), however no beneficial effect was observed for low amounts of Ag (Appendix, Figure A.8).

Total organic carbon (TOC) measurements were also performed for evaluating the degree of mineralization achieved by the photocatalytic treatment of the phenol containing solutions. In general, an increase in the TOC removal was obtained when Ag nanoparticles were incorporated in the ZnO materials. The mineralization efficiency was quantified by using a synergy factor (R_{TOC}), defined as:

$$R_{TOC} = \frac{X_{TOC,\,60\,min(Ag/ZnO)}}{X_{TOC,\,60\,min(ZnO)}} \qquad (6.3)$$

where X_{TOC} corresponds to the TOC conversion. The highest R_{TOC} was obtained for 1.0%Ag/ZnO-n (R_{TOC} = 33.8). For 0.25%Ag/ZnO-ev and 0.25%Ag/ZnO-t R_{TOC} values

of 1.5 and 1.4 were obtained, which indicate a 33% and 26% increase in the mineralization capacity comparing with the respective bare ZnO materials.

6.4.3. Photocatalytic degradation pathway using Ag/ZnO-t materials

Reports have been show that loading Ag onto ZnO induces the formation of a Schottky barrier at the metal-semiconductor interphase surface [44, 45]. Due to the higher Fermi level energy of ZnO compared with Ag, the electrons can easily flow from the photoexcited metal oxide to Ag. The transfer of electrons to the Ag nanoparticles is normally faster than the electron-hole (e^-/h^+) recombination process occurring in the ZnO phase, and thus high amounts of electrons (e^-) from ZnO can be stored in the Ag nanoparticles. Ag particles act as electron sinks where adsorbed oxygen may be reduced yielding superoxide radical ($O_2^{\bullet -}$). As a result, more holes (h^+), which are strongly oxidizing species, are available to drive oxidation reactions, namely the formation of hydroxyl radicals ($HO^\bullet$) from hydroxyl anions and/or also direct oxidation of phenol.

The main routes occurring during the photocatalytic phenol degradation were investigated by using EDTA and *t*-BuOH. Figure 6.14 shows the evolution of phenol concentration during the photocatalytic experiments using bare ZnO-t (Figure 6.14a) and 0.25%Ag/ZnO-t (Figure 6.14b) catalysts in the presence of electron/hole scavengers.

It was observed for the two materials that the addition of EDTA or *t*-BuOH leads to a decrease in the phenol degradation rate, which indicates that both radical species and photogenerated holes are involved in the phenol degradation process. For ZnO-t the presence of *t*-BuOH led to a decrease in k_{app}, from 5.07×10^{-2} to 3.66×10^{-2} min^{-1}. This decrease was even more pronounced in the presence of EDTA ($k_{app} = 1.04\times10^{-2}$ min^{-1}). A similar behaviour was observed for 0.25%Ag/ZnO-t (Figure 6.14b), where the presence of t-BuOH and EDTA led to a decrease in the k_{app} from 7.7×10^{-2} min^{-1} to 4.3×10^{-2} min^{-1} and 1.8×10^{-2} min^{-1}, respectively.

The results indicate that, although reactive species, such as hydroxyl ($HO^\bullet$), superoxide ($O_2^{\bullet -}$) and/or hydroperoxyl ($HOO^\bullet$) radicals, are responsible for part of the photocatalytic phenol degradation, photogenerated holes on the catalyst surface (h^+) seem to play the main role, since k_{app} was much more reduced when EDTA was used as hole scavenger.

Yet, in the presence of 0.25%Ag/ZnO-t the contribution of radical species in the phenol degradation reaction is more pronounced comparing with bare ZnO-t, since 45% and 28% decrease in k_{app} was observed when *t*-BuOH was added to

0.25%Ag/ZnO-t and ZnO-t suspensions, respectively. These results may be related to the more efficient charge separation occurring upon photoexcitation of 0.25%Ag/ZnO-t, leading to a higher availability of surface electrons and holes and the formation of higher amounts of radical species.

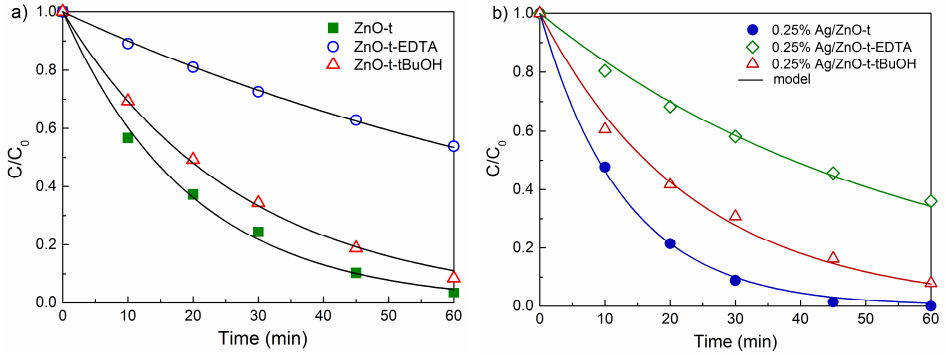

Figure 6.14 – Effect of hole/radical scavengers (1 mM EDTA/t-BuOH) on the photocatalytic degradation of phenol using ZnO-t (a), 0.25%Ag/ZnO-t (b).

6.4.4. Reutilization tests

The photostability of ZnO and 0.25%Ag/ZnO-t was investigated by reusing these materials in consecutive phenol degradation reactions, at natural pH conditions (pH = 6.1), under simulated solar light. Before each run the catalyst was washed with deionized water and dried at 110 ºC. Figure 6.15 shows the phenol concentration evolution in 4 consecutive cycles of photocatalytic reactions using ZnO and 0.25%Ag/ZnO-t.

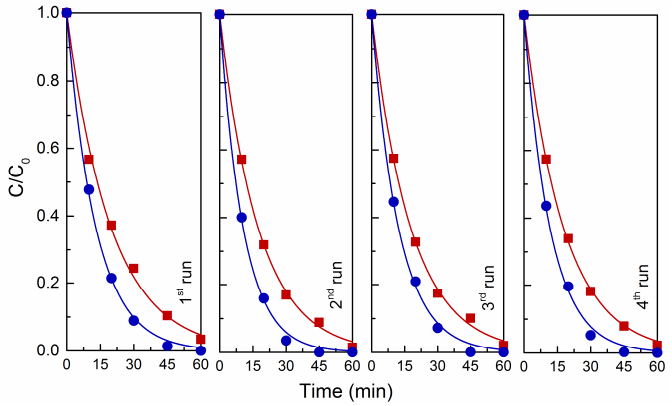

Figure 6.15 – Reusability assessment for ZnO-t (■) and 0.25%Ag/ZnO-t (●) for phenol degradation.

The results show that ZnO-t maintains its activity during four cycles of utilization, which indicate good stability of this material within the reaction conditions used.

For the reactions using 0.25%Ag/ZnO-t a slight improve in the kinetics of phenol degradation were observed for the second run. This may be attributed to partial photoreduction of Ag species during the previous photocatalytic reaction. The presence of oxidize Ag species was confirmed by XPS analysis. These species may change to its reduced form upon irradiation. In fact, several studies reported the use of the photo-impregnation method to deposit and reduce Ag nanoparticles on catalysts increasing their activity and stability [18, 46, 47]. In terms of mineralization, a slight decrease (18% and 10% for ZnO and 0.25%Ag/ZnO-t, respectively) in the TOC removal capacity was observed after four uses.

6.4.5. Photocatalytic degradation of a mixture of phenolic compounds

Taking into account the photocatalytic efficiency observed for ZnO-t and 0.25%Ag/ZnO-t in the degradation of phenol, the photocatalytic treatment of a mixture containing four phenolic compounds was studied. Phenol (PH), resorcinol (RC), 4-methoxyphenol (MP) and 4-chlorophenol (CP) were selected as model compounds. The separation of catalyst powders from the treated water requires separation steps that should be taken into account for technological applications. Thus, a set of experiments were also performed using the catalysts immobilized on glass Raschig rings. A dark period for each experiment was carried out for 30 min before irradiation. No significant decrease in the initial concentration for the different compounds was observed during the dark period. The experimental results indicate that the degradation of the individual compounds in the mixture obeys a pseudo-first-order rate law. Using the information from the kinetic curves (Appendix, Figure A.9) it was determined the half life time ($t_{1/2}$) for each compound. The relationship between the $t_{1/2}$ and the individual compounds for the experiments using ZnO-t and 0.25%Ag/ZnO-t in the form of powder and immobilized on glass Raschig rings are shown in Figure 6.16.

The results show that, in general the deposition of Ag improves the photocatalytic efficiency of the resulting material. Shorter half life time is needed for each compound be converted in 50% when 0.25%Ag/ZnO-t was used, either as a powder or film. It was also observed that the individual compounds present in the mixture are converted simultaneously, indicating that no competition occurs between each compound during the photocatalytic reaction.

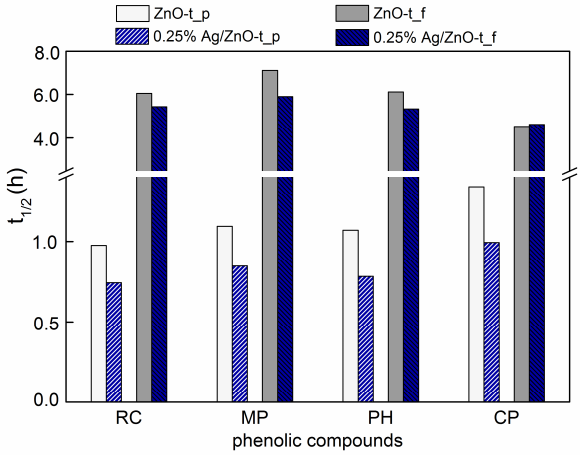

Figure 6.16 – Half life time ($t_{1/2}$) degradation as a function of each phenolic compound using powder (_p) and films (_f) of bare ZnO-t and 0.25%Ag/ZnO-t.

As expected, the use of a catalyst in the form of powder leads to a faster conversion, *i.e.* a shorter half-life compared to that of the immobilized photocatalyst. This is obviously expected since the contact surface is larger in the suspended material, due to the larger amount of catalyst per unit of volume. Nevertheless, several practical aspects arise from the use of a catalyst powder form. Those include the need for post-separation techniques, as well as the difficulty to recover the catalyst in continuous flow reaction systems. This recovery is more important as the cost of the catalyst increases with the deposition of noble metals. Thus a compromise must be established between the desired conversion and the need of recycling the catalyst.

In terms of TOC removal, the presence of Ag revealed to be advantageous, being of 6% and 27% using ZnO, and 14% and 42% using 0.25%Ag/ZnO-t with the photocatalyst immobilized and in powder form, respectively.

Globally, the results show that the deposition of Ag nanoparticles on ZnO materials may improve their photocatalytic efficiency by increasing the photocatalytic degradation rate as well as the mineralization capacity. Moreover, when applied to near to real field conditions (*i.e.*, mixture of compounds that may be encountered in waste waters and the possibility of using the catalyst immobilized on physical support to be employed in continuous systems) the use of Ag/ZnO photocatalysts could be of major relevance for solar applications.

6.5. Conclusions

ZnO materials synthesized by different techniques were successfully used for the photocatalytic oxidation of aqueous solutions of phenol under simulated solar light irradiation. The higher efficiency observed for ZnO-cvd, ZnO-t and ZnO-ev samples was attributed to the presence of isolated hydroxyl surface groups in higher amount.

The amounts of Au loaded depend on the nature of the ZnO support. For a 1 *wt.*% the yield of deposition varied from 0.29 to 0.9 *wt.*% depending on the material.

Gold particles with the smallest dimensions (2.9 nm average size) were found for Au/ZnO-cvd, which was attributed to an exceptionally high aspect ratio of the ZnO-cvd crystals, and to an epitaxial Au growth on the ZnO support.

Au/ZnO-t and Au/ZnO-cvd were the most active materials in terms of both phenol oxidation kinetics and mineralization extent, under solar light irradiation.

Au/ZnO photoexcitation mechanisms varied depending on the wavelength of irradiation, the intrinsic optical properties of catalyst and on gold nanoparticle size. In the case of Au/ZnO-cvd, the main mechanism was found to be by direct photoexcitation of the semiconductor and electron transfer to the gold nanoparticles. With Au/ZnO-t and Au/ZnO-ev, photoexcitation of gold nanoparticles also occurs due to the surface plasmon resonance effect.

Photogenerated holes play a major role in the photodegradation mechanism, particularly in the case of the reaction using Au/ZnO-t, but free radicals produced by photoexcited electrons are also important for the very active Au/ZnO-cvd.

In case of Ag/ZnO materials prepared by liquid impregnation it was observed an increase in the efficiency of the photocatalysts when Ag was added on ZnO materials with exception for commercial ZnO-ev. In terms of phenol mineralization the incorporation of Ag nanoparticles produced an increase in the performance of all the photocatalysts when compared to the respective bare metal oxides.

The highest efficiency was obained when Ag was deposited on ZnO-t, 0.25%Ag/ZnO-t being the most active photocatalyst. The increase in the activity was ascribed to the role of Ag nanoparticles as electrons sinks, thus increasing the efficiency and lifetime of charge separation in the semiconductor.

For the reactions using 0.25%Ag/ZnO-t, the contribution of radicals to the phenol degradation mechanism was more evident than for bare ZnO-t, as a result of the higher amount of electrons and holes at the surface of the metal-loaded catalyst.

The reutilization tests proved that both ZnO and 0.25%Ag/ZnO-t materials have good stability under the reaction conditions tested.

In addition, both ZnO and 0.25%Ag/ZnO-t performed efficiently (the latter being superior) in the photocatalytic treatment of a mixture of phenol, resorcinol, 4-methoxyphenol and 4-chorophenol, using the photocatalyst suspended or immobilized on glass rings. The latter form is of particular interest for technological applications.

References

[1] S. Anas, R.V. Mangalaraja, S. Ananthakumar, Studies on the evolution of ZnO morphologies in a thermohydrolysis technique and evaluation of their functional properties, J.Hazard. Mater., 175 (2010) 889-895.

[2] R. Bacsa, Y. Kihn, M. Verelst, J. Dexpert, W. Bacsa, P. Serp, Large scale synthesis of zinc oxide nanorods by homogeneous chemical vapour deposition and their characterisation, Sur. Coat. Technol., 201 (2007) 9200-9204.

[3] J.Q. Hu, Q. Li, N.B. Wong, C.S. Lee, S.T. Lee, Synthesis of Uniform Hexagonal Prismatic ZnO Whiskers, Chem. Mater., 14 (2002) 1216-1219.

[4] A. Kołodziejczak-Radzimska, E. Markiewicz, T. Jesionowski, Structural characterisation of ZnO particles obtained by the emulsion precipitation method, J. Nanomaterials, 2012 (2012) 15-15.

[5] A. Di Paola, E. García-López, G. Marcì, L. Palmisano, A survey of photocatalytic materials for environmental remediation, J.Hazard. Mater., 211-212 (2012) 3-29.

[6] S. Bouhadoun, C. Guillard, F. Dapozze, S. Singh, D. Amans, J. Bouclé, N. Herlin-Boime, One step synthesis of N-doped and Au-loaded TiO_2 nanoparticles by laser pyrolysis: Application in photocatalysis, Appl. Catal. B: Environ., 174–175 (2015) 367-375.

[7] L. Xiang, X. Zhao, C. Shang, J. Yin, Au or Ag nanoparticle-decorated 3D urchin-like TiO2 nanostructures: Synthesis, characterization, and enhanced photocatalytic activity, J. Colloid Inter. Sci., 403 (2013) 22-28.

[8] V.M. Daskalaki, M. Antoniadou, G. Li Puma, D.I. Kondarides, P. Lianos, Solar Light-Responsive Pt/CdS/TiO_2 Photocatalysts for Hydrogen Production and Simultaneous Degradation of Inorganic or Organic Sacrificial Agents in Wastewater, Environ. Sci. Technol., 44 (2010) 7200-7205.

[9] S. Shen, L. Guo, X. Chen, F. Ren, C.X. Kronawitter, S.S. Mao, Effect of noble metal in CdS/M/TiO_2 for photocatalytic degradation of methylene blue under visible light, International Journal of Green Nanotechnology: Mater. Sci. Eng., 1 (2010) M94-M104.

[10] A. Primo, A. Corma, H. Garcia, Titania supported gold nanoparticles as photocatalyst, Phys. Chem. Chem. Phys., 13 (2011) 886-910.

[11] H. Yu, H. Ming, H. Zhang, H. Li, K. Pan, Y. Liu, F. Wang, J. Gong, Z. Kang, Au/ZnO nanocomposites: Facile fabrication and enhanced photocatalytic activity for degradation of benzene, Mater. Chem. Phys., 137 (2012) 113-117.

[12] X. Wang, G. Liu, Z.-G. Chen, F. Li, L. Wang, G.Q. Lu, H.-M. Cheng, Enhanced photocatalytic hydrogen evolution by prolonging the lifetime of carriers in ZnO/CdS heterostructures, Chem. Commun., (2009) 3452-3454.

[13] N. Takeda, T. Torimoto, S. Sampath, S. Kuwabata, H. Yoneyama, Effect of Inert Supports for Titanium Dioxide Loading on Enhancement of Photodecomposition Rate of Gaseous Propionaldehyde, J. Phys. Chem., 99 (1995) 9986-9991.

[14] R. Leary, A. Westwood, Carbonaceous nanomaterials for the enhancement of TiO_2 photocatalysis, Carbon, 49 (2011) 741-772.

[15] F. Sun, F. Tan, W. Wang, X. Qiao, X. Qiu, Facile synthesis of Ag/ZnO heterostructure nanocrystals with enhanced photocatalytic performance, Mater. Res. Bulletin, 47 (2012) 3357-3361.

[16] C. Tian, Q. Zhang, A. Wu, M. Jiang, Z. Liang, B. Jiang, H. Fu, Cost-effective large-scale synthesis of ZnO photocatalyst with excellent performance for dye photodegradation, Chem. Commun., 48 (2012) 2858-2860.

[17] M. Bowker, A. Nuhu, J. Soares, High activity supported gold catalysts by incipient wetness impregnation, Catal. Today, 122 (2007) 245-247.

[18] E. Pulido Melián, O. González Díaz, J.M. Doña Rodríguez, G. Colón, J.A. Navío, M. Macías, J. Pérez Peña, Effect of deposition of silver on structural characteristics and photoactivity of TiO2-based photocatalysts, Appl. Catal. B: Environ., 127 (2012) 112-120.

[19] L.M. Pastrana-Martínez, J.L. Faria, J.M. Doña-Rodríguez, C. Fernández-Rodríguez, A.M.T. Silva, Degradation of diphenhydramine pharmaceutical in aqueous solutions by using two highly active TiO_2 photocatalysts: Operating parameters and photocatalytic mechanism, Appl. Catal. B: Environ., 113–114 (2012) 221-227.

[20] N. Serpone, I. Texier, A.V. Emeline, P. Pichat, H. Hidaka, J. Zhao, Post-irradiation effect and reductive dechlorination of chlorophenols at oxygen-free TiO_2/water interfaces in the presence of prominent hole scavengers, J. Photochem. Photobiol. A: Chem., 136 (2000) 145-155.

[21] S.A.C. Carabineiro, B.F. Machado, R.R. Bacsa, P. Serp, G. Dražić, J.L. Faria, J.L. Figueiredo, Catalytic performance of Au/ZnO nanocatalysts for CO oxidation, J. Catal., 273 (2010) 191-198.

[22] S. Bhattacharyya, A. Gedanken, A template-free, sonochemical route to porous ZnO nano-disks, Microporous Mesoporous Mater., 110 (2008) 553-559.

[23] H. Noei, H. Qiu, Y. Wang, E. Loffler, C. Woll, M. Muhler, The identification of hydroxyl groups on ZnO nanoparticles by infrared spectroscopy, Phys. Chem. Chem. Phys., 10 (2008) 7092-7097.

[24] A. Kolodziejczak-Radzimska, E. Markiewicz, T. Jesionowski, Structural Characterisation of ZnO Particles Obtained by the Emulsion Precipitation Method, J. Nanomater., 2012 (2012) 9.

[25] J. Araña, J.M. Doña-Rodríguez, D. Portillo-Carrizo, C. Fernández-Rodríguez, J. Pérez-Peña, O. González Díaz, J.A. Navío, M. Macías, Photocatalytic degradation of phenolic compounds with new TiO2 catalysts, Appl. Catal. B: Environ., 100 (2010) 346-354.

[26] R. Shi, P. Yang, J. Wang, A. Zhang, Y. Zhu, Y. Cao, Q. Ma, Growth of flower-like ZnO via surfactant-free hydrothermal synthesis on ITO substrate at low temperature, Cryst. Eng. Comm., 14 (2012) 5996-6003.

[27] S.A.C. Carabineiro, B.F. Machado, G. Dražić, R.R. Bacsa, P. Serp, J.L. Figueiredo, J.L. Faria, Photodeposition of Au and Pt on ZnO and TiO_2, in: M.D.S.H.P.A.J.J.A.M. E.M. Gaigneaux, P. Ruiz (Eds.) Stud. Surf. Sci. Catal., Elsevier, 2010, pp. 629-633.

[28] S.A.C. Carabineiro, L.M.D.R.S. Martins, M. Avalos-Borja, J.G. Buijnsters, A.J.L. Pombeiro, J.L. Figueiredo, Gold nanoparticles supported on carbon materials for cyclohexane oxidation with hydrogen peroxide, Appl. Catal. A: General, 467 (2013) 279-290.

[29] C. Gomes Silva, R. Juárez, T. Marino, R. Molinari, H. García, Influence of Excitation Wavelength (UV or Visible Light) on the Photocatalytic Activity of Titania Containing Gold Nanoparticles for the Generation of Hydrogen or Oxygen from Water, J. Am. Chem. Soc., 133 (2011) 595-602.

[30] Y. Hu, H.-J. Chen, Preparation and characterization of nanocrystalline ZnO particles from a hydrothermal process, J. Nanopart. Res., 10 (2008) 401-407.

[31] E. Kowalska, O.O.P. Mahaney, R. Abe, B. Ohtani, Visible-light-induced photocatalysis through surface plasmon excitation of gold on titania surfaces, Phys. Chem. Chem. Phys., 12 (2010) 2344-2355.

[32] H. Choi, W.T. Chen, P.V. Kamat, Know Thy Nano Neighbor. Plasmonic versus Electron Charging Effects of Metal Nanoparticles in Dye-Sensitized Solar Cells, ACS Nano., 6 (2012) 4418-4427.

[33] M.A. El-Sayed, Some Interesting Properties of Metals Confined in Time and Nanometer Space of Different Shapes, Acc. Chem. Res., 34 (2001) 257-264.

[34] K. Yamada, K. Miyajima, F. Mafuné, Thermionic Emission of Electrons from Gold Nanoparticles by Nanosecond Pulse-Laser Excitation of Interband, J. Phys. Chem. C, 111 (2007) 11246-11251.

[35] L.M. Pastrana-Martínez, S. Morales-Torres, V. Likodimos, J.L. Figueiredo, J.L. Faria, P. Falaras, A.M.T. Silva, Advanced nanostructured photocatalysts based on reduced graphene oxide-TiO_2 composites for degradation of diphenhydramine pharmaceutical and methyl orange dye, Appl. Catal. B: Environ., 123-124 (2012) 241-256.

[36] C. Minero, G. Mariella, V. Maurino, D. Vione, E. Pelizzetti, Photocatalytic Transformation of Organic Compounds in the Presence of Inorganic Ions. 2. Competitive Reactions of Phenol and Alcohols on a Titanium Dioxide−Fluoride System, Langmuir, 16 (2000) 8964-8972.

[37] B. Kraeutler, A.J. Bard, Heterogeneous photocatalytic decomposition of saturated carboxylic acids on titanium dioxide powder. Decarboxylative route to alkanes, J. Am. Chem. Soc., 100 (1978) 5985-5992.

[38] R. Georgekutty, M.K. Seery, S.C. Pillai, A Highly Efficient Ag-ZnO Photocatalyst: Synthesis, Properties, and Mechanism, J. Phys. Chem. C, 112 (2008) 13563-13570.

[39] Z. Xuming, C. Yu Lim, L. Ru-Shi, T. Din Ping, Plasmonic photocatalysis, Rep. Prog. Phys., 76 (2013) 046401.

[40] M. Rycenga, C.M. Cobley, J. Zeng, W. Li, C.H. Moran, Q. Zhang, D. Qin, Y. Xia, Controlling the Synthesis and Assembly of Silver Nanostructures for Plasmonic Applications, Chem. Reviews, 111 (2011) 3669-3712.

[41] T. Liu, B. Li, Y. Hao, F. Han, L. Zhang, L. Hu, A general method to diverse silver/mesoporous–metal–oxide nanocomposites with plasmon-enhanced photocatalytic activity, Appl. Catal. B: Environ., 165 (2015) 378-388.

[42] R.K. Sahu, K. Ganguly, T. Mishra, M. Mishra, R.S. Ningthoujam, S.K. Roy, L.C. Pathak, Stabilization of intrinsic defects at high temperatures in ZnO nanoparticles by Ag modification, J. Colloid Inter. Sci., 366 (2012) 8-15.

[43] K.H. Stern, High Temperature Properties and Decomposition of Inorganic Salts Part 3, Nitrates and Nitrites, J. Phys. Chem. Reference Data, 1 (1972) 747-772.

[44] Y. Dong, S. Zhan, P. Wang, A facile synthesis of Ag Modified ZnO nanocrystals with enhanced photocatalytic activity, J. Wuhan Univ. Technol. Mat. Sci. Edit., 27 (2012) 615-620.

[45] N. Sobana, M. Muruganadham, M. Swaminathan, Nano-Ag particles doped TiO_2 for efficient photodegradation of Direct azo dyes, J. Mol. Catal. A: Chem., 258 (2006) 124-132.

[46] M.A. Behnajady, N. Modirshahla, M. Shokri, A. Zeininezhad, H.A. Zamani, Enhancement photocatalytic activity of ZnO nanoparticles by silver doping with optimization of photodeposition method parameters, J. Environ. Sci. Health, Part A, 44 (2009) 666-672.

[47] C. Ren, B. Yang, M. Wu, J. Xu, Z. Fu, Y. lv, T. Guo, Y. Zhao, C. Zhu, Synthesis of Ag/ZnO nanorods array with enhanced photocatalytic performance, J. Hazard. Mater., 182 (2010) 123-129.

Part IV

Chapter 7

Final remarks and suggestions for future work

This final chapter highlights the breakthroughs described over the preceding chapters. Suggestions for a future work as follow up on these achievements are also proposed.

7.1. Final remarks

In this dissertation, wide nanostructured architectures based on TiO_2 and ZnO were synthetized and used for water treatment by heterogeneous photocatalysis. Model compounds for these studies included methylene blue, phenolic organics and a cyanotoxin. Selected photocatalysts were bounded to glass slides and glass Raschig rings using different immobilization techniques. In order to confirm the photocatalytic activity and stability of these immobilized catalysts a wide range of experimental conditions was tested.

To understand the photochemical oxidative degradation ability of the developed photocatalysts, complete characterization was thoroughly carried out using different techniques. Following, is a description of the main conclusions retained during this research work.

When different TiO_2 materials were immobilized on glass Raschig rings it was observed that the photoefficiency of the system depended on the nature of the TiO_2. By carefully controlling the number of TiO_2 layers and considering the results on the reutilization tests, it was found that TiO_2-coated Raschig rings with 3 layers constituted the best compromise between photocatalytic performance and film stability for phenol degradation under simulated solar light. Among the films tested, the EP-coated rings were the more stable up to 3 layers. The activity of SA and SG-coated rings markedly decreased after the first use. This was ascribed to the fact that very fine particles are released in the initial cycles, which contribute to light dispersion and consequent lower the photocatalytic efficiency in the following cycles.

Taking into account the stability of EP-3L films the study was extended by varying the operation conditions: number of EP-3L coated-Raschig rings, H_2O_2 concentration, irradiation intensity and initial phenol concentration. An empirical kinetic model was developed in terms of the reaction rate dependency on the operating conditions. By using the developed model was possible to predict the reaction rate of phenol degradation at different operating conditions.

Regarding the photocatalytic degradation of a mixture containing seven phenolic derivatives it was observed that the degradation depended on the substituent group to the aromatic ring, with gallic acid baring 3 very strong activating groups (–OH) and a strong deactivating group (–COOH) being the easiest degraded compound.

The next step was the introduction of CNT into a TiO_2 matrix with the objective of enhancing photocatalytic activity. In this case, TiO_2 materials and TiO_2/CNT

composites were prepared by hydration-dehydration and sol-gel methods, immobilized by doctor blade technique and used for methylene blue degradation under near-UV to visible light irradiation. In general, the presence of adequate CNT loading on the TiO_2 matrix led to an increase of the photocatalytic efficiency. The level of interaction between CNT and TiO_2 phases in the composite materials strongly depends on TiO_2 particle size, TiO_2 crystal phase composition and surface chemistry of both CNT and TiO_2. The presence of the oxygenated surface groups in CNT revealed to be a key aspect, acting as anchoring points to TiO_2 nanoparticles. Consequently, this resulted in an increase of the S_{BET} of the composite materials and better dispersion of TiO_2 particles (avoiding the formation of aggregates).

The relationship found between the Hammett constant of four *para*-substituted phenols and the respective initial reaction rates using TiO_2 and TiO_2/CNT materials may constitute a useful tool to predict the behavior of the materials when used for the photocatalytic degradation of other phenolic molecules.

Composite materials containing carbon nanotubes, graphene oxide and nanodiamonds as carbon phase were also combined with TiO_2, and used as powders for degradation of microcystin-LA under simulated solar light and visible light irradiation. Once again the presence of the carbon phase proved beneficial when combined with TiO_2. Among the composite materials, graphene oxide-TiO_2 photocatalyst showed the highest photocatalytic activity under simulated solar light and visible light irradiation. In this case the excellent performance of this composite was attributed to the optimal self-assembly between the graphene oxide sheets and the TiO_2 particles.

TiO_2-nanodiamonds composites revealed high activity under simulated solar light. However, under visible light showed no activity for the photocatalytic degradation of microcystin-LA, which can be explained by the wide band gap of the nanodiamonds.

With this study was found that TiO_2-carbon composites may be promising materials for the detoxification of cyanotoxin-contaminated surface water and freshwaters under simulated solar light, and in particular graphene oxide-TiO_2 materials under visible light.

Good efficiency for photocatalytic oxidation of phenol under simulated solar light was observed using ZnO with different morphologies. The introduction of carbon materials on ZnO tetrapods prepared by CVD resulted in higher photocatalytic reaction rates. The efficiency of the photocatalyst depends on the nature and on the surface chemistry of the carbon material. Among the tested photocatalysts, the higher

performance was obtained with the composite containing nitrogen doped-CNT. The presence of the electron rich nitrogen groups on the CNT's surface acts as an effective electron scavenger for ZnO, inhibiting the recombination of photoexcited electron-hole pairs improving the photoactivity.

When noble metal nanoparticles were deposited on ZnO materials, a beneficial effect on their activity was observed. The morphology of ZnO and the amount of noble metal nanoparticles were crucial for the activity of the catalysts.

To elect the most promising catalyst for photocatalytic water treatment developed under this research program, a final set of experiments was performed using the most efficient photocatalysts referred in chapters 4, 5 and 6 (*i.e.*, GO-TiO_2-4, N-CNT/ZnO-cvd, Au/ZnO-cvd and 0.25%Ag/ZnO-t). Their efficiency was compared against the corresponding bare phases, and also to TiO_2 P25, the benchmark photocatalyst. The photocatalytic performances were compared under the same conditions of catalyst load, pH, phenol concentration, radiation source and intensity, by using phenol as a model compound. The results are compiled in Figure 7.1.

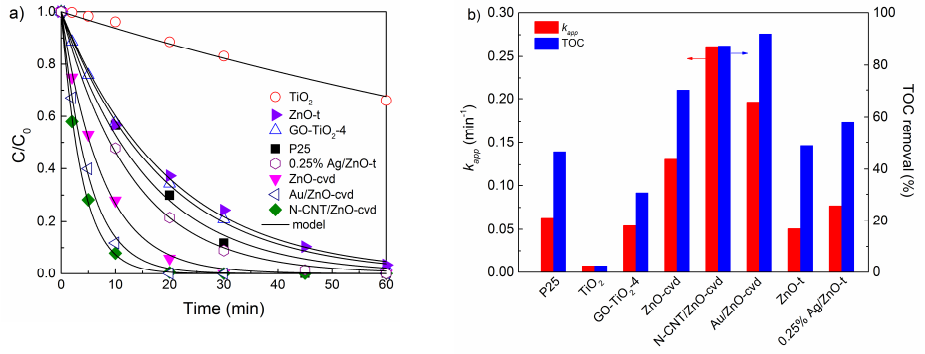

Figure 7.1 – (a) Normalized concentration (C/C_0), and (b) k_{app} and TOC removal obtained for the photocatalytic degradation of phenol under simulated solar light irradiation in a slurry reactor ($[PhOH]_0$ = 20 mg L^{-1}; I = 30.9 mW cm^{-2}; 1 g L^{-1} of catalyst load; pH= 6.1) using selected photocatalysts.

For the above-mentioned system, ZnO-cvd based materials appear as the most promising photocatalysts, with performances largely exceeding the benchmark TiO_2 P25.

In summary, with this study it was found that the efficiency of the photocatalytic process is strongly influenced by the physical-chemical and optical properties of the catalysts. Technical parameters such as the irradiation source, the geometry of the reactor and the catalyst state (powder or immobilized) play also a crucial role in the

photoefficiency of the process. The nature of the target organic pollutant and the irradiation source strongly influences the photocatalysts' performance. For instance, ZnO-cvd, N-CNT/ZnO-cvd and Au/ZnO-cvd materials show higher efficiencies for phenol degradation under simulated solar light; however under visible light irradiation their activity was negligible. In opposition, GO-TiO_2-4 is an active photocatalyst under visible light irradiation, as shown in the experiments with microcystin-LA.

7.2. Suggestions of future work

Considering the findings from this research, and taking advantage of the good performance obtained with metal oxides/carbon-based composites, some suggestions of future work are given in the following.

A carefully study on the immobilization of metal oxides/carbon-based composites and the optimization of the operation conditions (*e.g.*, reactor design and light irradiation) would be some of the paths to explore in order to enhance the photocatalytic process.

On the other hand, it will be interesting to study the activity of these catalysts using realistic waste water samples rather than model compounds in distilled water. This task would be hardest to perform due to the large amount of pollutants that an effluent may contain. Nevertheless, a detailed study on the reaction mechanisms of the different organic pollutants would be of upmost importance, in particular considering reaction intermediates that can have higher toxicity than the parent pollutant.

Another approach is to use metal oxides/carbon-based composites in the field of water disinfection caused by pathogenic microorganisms. Moreover, the advantage of using these materials immobilized as antibacterial surfaces that can be recycled and don't require additional chemical treatment, makes the large-scale use more practicable. The additional deposition of Ag nanoparticles on the composites with the aim of enhance the efficiency of the materials may be other option, since currently metal oxides doped with Ag nanoparticles have been extensively studied and used to inactivate many microorganisms.

Appendix

Appendix

A.1 The effect of reuse EP-3L films for phenol degradation is discussed in chapter 2, section 2.3.6.

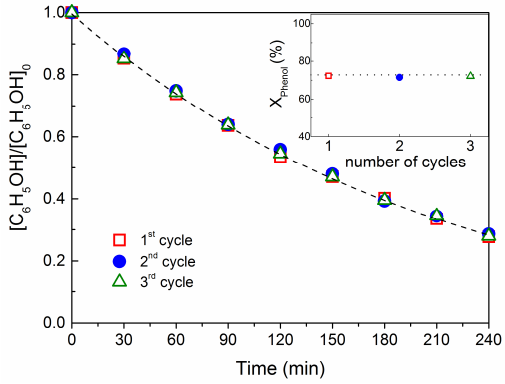

Figure A.1 – Effect of number of cycles using fresh EP-3L films on the degradation of phenol.

A.2 The colorimetric method using the Folin–Ciocalteu's phenolic reagent was used for the determination of total phenolic content. Comments on this results are included in chapter 2, section 2.5.

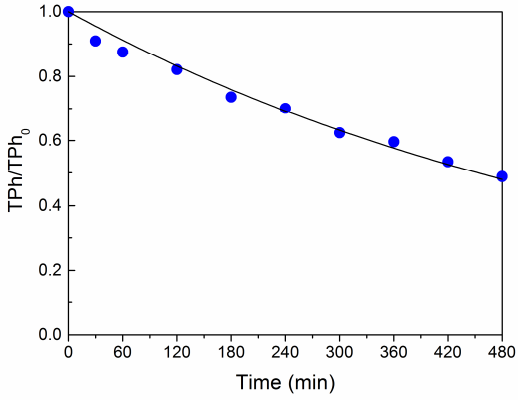

Figure A.2 – Normalized total phenolic content during photocatalytic treatment of the synthetic effluent using EP-3L.

A.3 Experiments under dark conditions using the different materials were performed. Comments on these results are included in chapter 4, section 4.3.2.

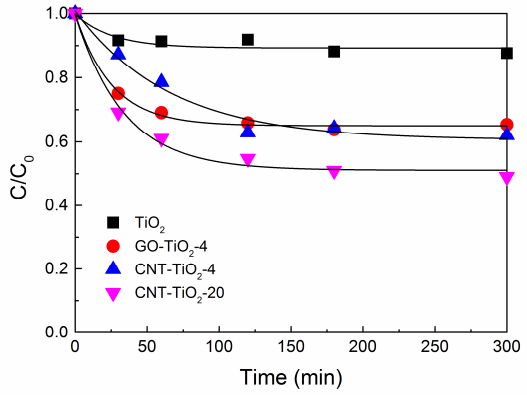

Figure A.3 Experiments under dark conditions using TiO_2, GO-TiO_2-4, CNT-TiO_2-4 and CNT-TiO_2-20.

A.4 To avoid an excess of catalyst a preliminary study on the effect of ZnO load was performed, which results are included in chapter 5,section

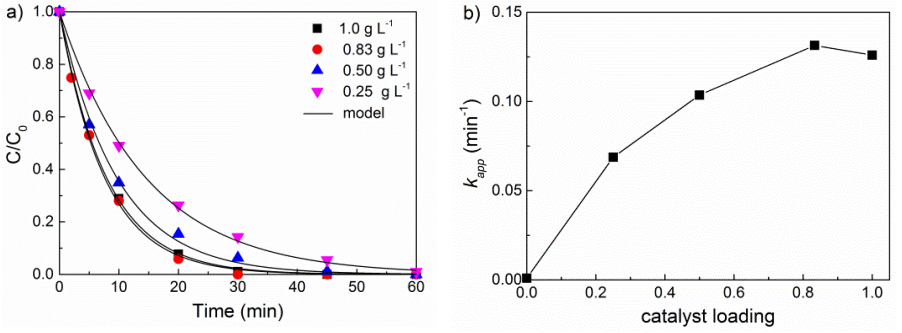

Figure A.4 – (a) Normalized concentration of phenol (C/C_0) *vs.* time using different ZnO loadings, and (b) the respective apparent first order rate constants (k_{app}).

A.5 The TPD of nanodiamond sample show larger amount of released CO and CO_2 (1966 and 6637 µmol g^{-1}, respectively). Comments on this material are included on chapter 5, section 5.3.1.

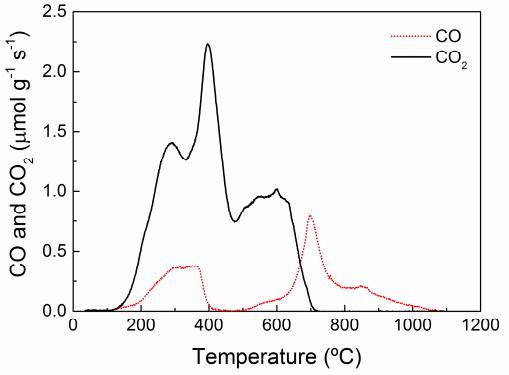

Figure A.5 – CO and CO_2 TPD profiles of ND sample.

A.6 The XPS analysis show the presence of 31% pyrrolic nitrogen, 29% pyridinic nitrogen, 12% quaternary nitrogen, and 28% nitrogen. Comments on this figure are included in chapter 5, section 5.3.1.

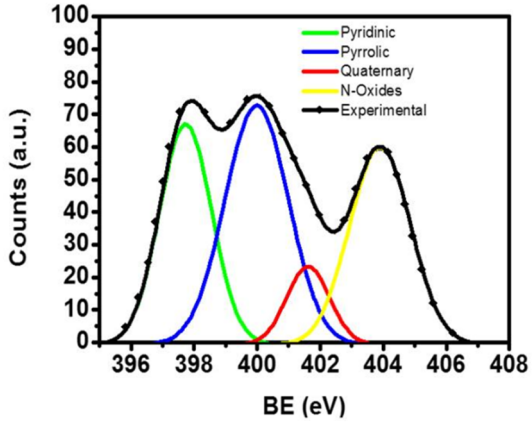

Figure A.6 – N 1s XPS spectrum of N-CNTs.

A.7 The N-doped carbon nanotubes (N-CNT) were tested on photocatalytic degradation of phenol. The results are comment in chapter 5, section 5.3.2.

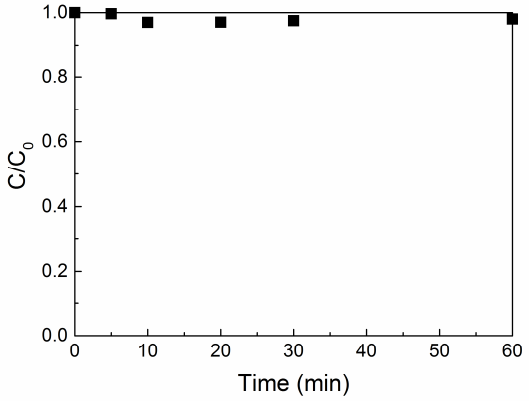

Figure A.7 – Photocatalytic oxidation of phenol using bare N-CNT.

A.8 The role of Ag nanoparticles deposited on ZnO prepared by CVD was study. The results shown in Figure A.6 are discussed in chapter 6, section 6.4.2.

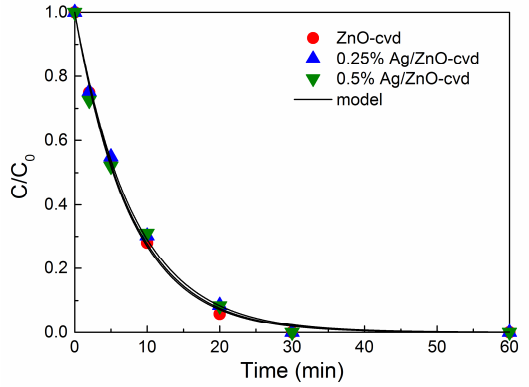

Figure A.8 – Normalized concentration of phenol (C/C_0) using neat ZnO-cvd and Ag/ZnO-cvd materials under simulated solar light.

A.9 The half life time ($t_{1/2}$) for each compound was determined from the kinetic curves. With this information was possible to compare the efficiency between the materials when were in the powder form and immobilized on glass raschig rings. This results are discussed in chapter 6, section 6.4.5.

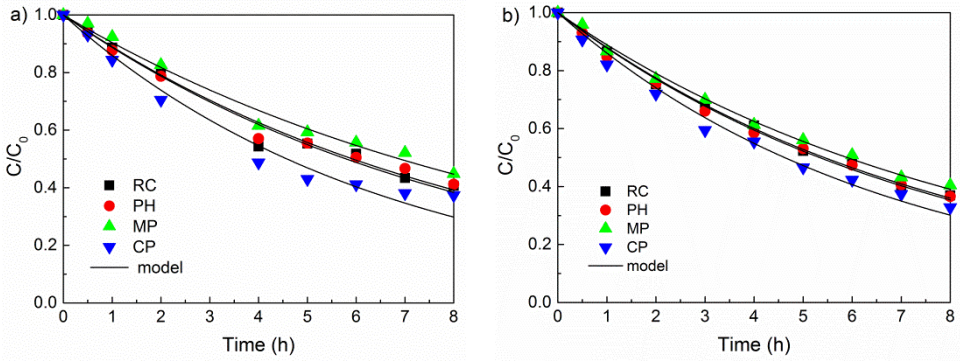

Figure A.9 – Kinetic profiles of each phenolic compound of the mixture using: (a) ZnO-t (-■-, R^2 = 0.982; -●-, R^2 = 0.989; -▲-, R^2 = 0.987; -▼-, R^2 = 0.974), and (b) 0.25%Ag/ZnO-t (-■- R^2 = 0.996; -●-, R^2 = 0.995; -▲-, R^2 = 0.996; -▼-, R^2 = 0.987) films, respectively.